

ALMA MATER STUDIORUM - UNIVERSITÀ DI
BOLOGNA

DOTTORATO DI RICERCA IN INGEGNERIA
CIVILE, CHIMICA, AMBIENTALE E DEI
MATERIALI

XXIX CICLO

Settore Scientifico Disciplinare ICAR/o8

Settore Concorsuale o8/B2

MODELLING AND ANALYSIS OF
MECHANICAL EFFECTS INDUCED BY
SALT CRYSTALLISATION IN POROUS
BUILDING MATERIALS: A TWO-SCALE
APPROACH

Presentata da:

Lisa GREMENTIERI

Relatore:

Prof. Francesco UBERTINI

Coordinatore Dottorato:

Prof. Luca VITTUARI

Correlatore:

Prof. Stefano DE MIRANDA

Prof. Federica DAGHIA

Dr. Luisa MOLARI

Esame finale anno 2017

Lisa GREMENTIERI : *Modelling and analysis of mechanical effects induced by salt crystallisation in porous building materials: a two-scale approach* , Ph.D Dissertation, Alma Mater Studiorum - Università di Bologna © March 2017

*To my family and Edoardo
for their love and encouragement.*

ABSTRACT

Salt crystallisation can induce high stresses in the micro-structure of building materials constituting historic buildings and monuments.

This dissertation combines numerical methods at different scales to model and analyse the mechanical effects induced by salt crystallisation in porous building materials. Two different scales are considered: the macro-scale, in which the porous building material is seen as a homogeneous continuum, and the micro-scale, being the scale in which can be distinguished the material matrix and the pores.

Regarding the macro-scale, a new Hygro-Thermo-Chemical (HTC) model is presented. A suitable modelling of the crystallisation/dissolution and hydration/dehydration processes allows considering salts with multiple crystallised forms involving hydrous and anhydrous crystals. The HTC model presented is specialised for sodium sulphate solutions and sodium chloride solutions. The predictive capabilities of the model are validated on some experiments available in the literature, involving fired-clay bricks. Moreover, an enriched version of the HTC model is presented in order to describe different drying kinetics, taking into account the kind of efflorescence formation. The validation is performed through two different extensive campaigns on drying of Prague sandstone in presence of sodium chloride salt solution. The HTC modelling results show a good agreement with the experimental data, proving the effectiveness of the proposed model.

Concerning the micro-scale, a micro-mechanical model is developed on the base of the real 3D micro geometry of a porous material, coming from X-ray Micro Computed Tomography (X-ray μ CT) images. The micro-mechanical model is obtained by automatically converting the images into a finite element mesh. Some hypotheses on the loading condition of the micro-mechanical model, accounting for dif-

ferent crystallisation physics, are introduced. Moreover, a procedure to obtain a simplified micro-mechanical model of a porous material is conceived to define the most suitable micro simplified geometry representing the real material. As case study, the proposed approaches are applied to the Prague sandstone. Moreover, it is shown that the micro-mechanical loading scheme adopted influences the macro-scale mechanical effects and that some approaches commonly used in the literature for their evaluation can lead to their underestimation.

In order to establish a link between the micro and the macro scales, a multi-scale approach, based on numerical homogenisation, is presented. It allows to predict the effects of salt crystallisation occurring at the scale of the structure. Finally, the results of the proposed approach are incorporated in a Hygro-Thermo-Chemo-Mechanical (HTCM) model, which combines hygro-thermo-chemical aspects and the mechanical ones, to perform a structural computation with environmental and mechanical loadings to forecast the most probable damage scenarios.

These results about the modelling and the analysis of the mechanical effect of salt crystallisation in porous media at two different scale aim at shedding some light on the still open issue of the relationship between the crystallisation physics and its mechanical effects on porous building materials.

PUBLICATIONS

Some ideas and figures have appeared previously in the following publications:

L. Grententieri, F. Daghia, L. Molari, G. Castellazzi, H. Derluyn, V. Cnudde, and S. de Miranda. A multi-scale approach for the analysis of the mechanical effects of salt crystallisation in porous media. 2017. Submitted

G. Castellazzi, S. de Miranda, L. Grententieri, L. Molari, and F. Ubertini. Multiphase model for hygrothermal analysis of porous media with salt crystallization and hydration. *Materials and Structures/Materiaux et Constructions*, 49(3):1039–1063, 2016. doi: 10.1617/s11527-015-0557-y

J. Desarnaud, H. Derluyn, L. Grententieri, L. Molari, S. de Miranda, V. Cnudde, and N. Shahidzadeh. Salt weathering of sandstone during drying: Effect of primary and secondary crystallisation. In *Science and Art: A Future for Stone: Proceedings of the 13th International Congress on the Deterioration and Conservation of Stone*, page 299, 2016b

H. Derluyn, M.A. Boone, J. Desarnaud, L. Grententieri, L. Molari, S. de Miranda, N. Shahidzadeh, and V. Cnudde. Quantifying salt crystallization dynamics in sandstone using 4D laboratory X-ray micro-CT. In *Science and Art: A Future for Stone: Proceedings of the 13th International Congress on the Deterioration and Conservation of Stone*, 2016

S. de Miranda, L. Grententieri, L. Molari, V. Cnudde, H. Derluyn, J. Desarnaud, and N. Shahidzadeh. Drying of salt contaminated building sandstones: from experiments to numerical modelling. In *VI International Conference on Coupled Problems in Science and Engineering - COUPLED PROBLEMS 2015, Venice, Italy, May 18-20, 2015*

G. Castellazzi, S. de Miranda, L. Grententieri, L. Molari, and F. Ubertini. Modelling of non-isothermal salt transport and crystallization in historic masonry. *Key Engineering Materials*, 624:222–

229, 2015c. doi: 10.4028/www.scientific.net/KEM.624.222

G. Castellazzi, S. de Miranda, L. Grementieri, L. Molari, and F. Ubertini. Assessment of salt crystallization through numerical modelling. In A. Troi and E. Lucchi, editors, *Cultural Heritage Preservation: Proceedings; EWCHP-2013, 3rd European Workshop on Cultural Heritage Preservation*, pages 89–95. Bozen/Bolzano, Italy, 16th-18th September 2013b

*[...] eterno studente,
perché la materia di studio sarebbe infinita
e soprattutto perché so di non sapere niente [...]*

"Addio", F. Guccini

ACKNOWLEDGEMENTS

The financial support of the Joint Heritage European Programme grant JPI-JHEP: project KISADAMA is gratefully acknowledged.

Thanks to Professor Ubertini for the opportunity to take part to the DICAM PhD program. The KISADAMA team and the research group of the Laboratory of Computational Mechanics (LAMC), in particular Prof. Stefano de Miranda, Luisa Molari, PhD and Giovanni Castellazzi, PhD, are gratefully acknowledged for their support.

A special thank to Federica Daghia, HDR for the invitation at Laboratoire de Mécanique et Technologie (LMT) Cachan for her teaching and advice and to DICAM, which provided the "Marco Polo" scholarship for the research period in France. I wish to thank all the LAMC PhD colleagues for their friendship and help and LMT - Cachan's technicians for their support in performing numerical simulations.

Finally, thanks to people from all over the world I have the opportunity and the privilege to meet in Italy and France during the last three years, who enriched my life.

Lisa Grementieri
March 2017

CONTENTS

1	INTRODUCTION	1
2	STATE OF THE ART	9
2.1	Salt transport and crystallisation	9
2.1.1	Crystallisation dynamics	10
2.1.2	Pressure exerted by growing crystals	14
2.1.3	Modelling of hygro-thermal issues, salt transport and crystallisation	16
2.1.4	Needs for further research	18
2.2	Mechanical effects in multiphase porous media	19
2.2.1	Coupled modelling of salt transport and damage	20
2.2.2	Multi-scale approaches	22
2.2.3	Microporomechanics basics	33
2.2.4	Needs for further research	46
i	HYGRO-THERMO-CHEMICAL ASPECTS	49
3	THE HYGRO THERMAL CHEMICAL MODEL	51
3.1	Introduction	51
3.2	Assumptions	52
3.3	Balance equations	55
3.4	Constitutive relations	58
3.5	Sorption/desorption curves	63
3.6	Kinetic laws	64
3.7	Source and sink terms	69
3.8	Summary of the HTC model equations	70
3.9	Concluding Remarks	72
4	SODIUM SULPHATE SOLUTION	73
4.1	Specialisation	73
4.2	Numerical applications	77
4.3	Results and discussion	77
4.3.1	Test at constant humidity: crystallisation of mirabilite	77
4.3.2	Test at constant temperature: hydration of thenardite	83

4.3.3	Test with varying temperature and humidity	86
4.4	Concluding Remarks	89
5	SODIUM CHLORIDE SOLUTION	93
5.1	Specialisation	93
5.2	Thermal Effects	95
5.3	Numerical applications	99
5.4	Concluding Remarks	103
6	INSIGHT ON BOUNDARY CONDITIONS	105
6.1	Introduction	105
6.2	Experimental campaigns	106
6.3	Specialisation	109
6.4	Convective humidity coefficient	110
6.5	Simulation of drying experiments	111
6.5.1	Parameters used	113
6.5.2	Definition of γ_w	113
6.5.3	Simulation of the drying at 50% RH	115
6.5.4	Simulation of the drying at 20% RH	117
6.5.5	Simulation of the drying at 40% RH	119
6.5.6	Crystallization pattern	120
6.5.7	Salt amount: global estimation in time	122
6.6	Discussion	127
6.7	Concluding Remarks	129
ii	MECHANICAL ASPECTS	131
7	HOMOGENISATION APPROACH	133
7.1	The numerical homogenisation approach	133
7.2	The Mori-Tanaka scheme: application to porous media	137
7.3	Concluding remarks	143
8	POROUS MEDIA SATURATED WITH ONE SPECIES	149
8.1	The choice of the Representative Elementary Volume	149
8.1.1	The case study	150
8.1.2	Overall Porosity	150
8.1.3	Geometry of the pore space	153
8.1.4	Average Mechanical Properties	157
8.2	Calculation of the Biot's Tensor	158
8.2.1	Theoretical framework	158

8.2.2	The Finite Element Modelling	162
8.3	Results and Discussion	165
8.4	Concluding Remarks	166
9	DEFINITION OF SIMPLIFIED PORE GEOMETRIES	169
9.1	The procedure	169
9.2	Numerical evaluation	170
9.3	Calibration of the analytical model and validation	170
9.4	Concluding remarks	172
10	POROUS MEDIA SATURATED WITH MULTIPLE SPECIES	175
10.1	The model	175
10.1.1	Hypotheses	175
10.1.2	Equations	176
10.1.3	The law of partial pressures	178
10.2	Computation of partial Biot's tensors	180
10.2.1	From crystallisation's physics to the mechanical model	180
10.3	Results and Discussion	184
10.3.1	Partial Biot's tensor	184
10.3.2	Stress distributions at the micro-scale	188
10.4	Concluding Remarks	189
iii	COUPLING HTC-MECHANICS	193
11	THE HYGRO THERMO CHEMO MECHANICAL MODEL	195
11.1	Introduction	195
11.2	Mechanics	197
11.2.1	Momentum Balance Equation	197
11.2.2	Strain-displacement Equation	197
11.2.3	Constitutive Law	197
11.2.4	Fundamental equation	202
11.3	Numerical application	203
11.4	Concluding remarks	208
12	CONCLUSIONS AND PERSPECTIVES	213
iv	APPENDIX	219
A	TABLES	221
A.1	Thermal Conductivity of the liquid water function of temperature	221
A.2	Molar dissolution enthalpy at infinite dilution	222

A.3	Molar latent heat of hydration/ dehydration for H ₂ O-Na ₂ SO ₄ solutions	222
B	COEFFICIENTS OF THE HTC MODEL	223
B.1	Latent heat of crystallization for an anhydrous salt	223
B.2	Kinetic hydration/dehydration parameter for sulphate solutions	224
B.3	Coefficients of the system of equations	224
C	COEFFICIENTS OF THE HTC MODEL FOR CHLO- RIDES	227
	BIBLIOGRAPHY	231

LIST OF FIGURES

Figure 1.1	Example of efflorescences and sub-florescences	4
Figure 2.1	Voigt's and Reuss' bounds: 1D example	24
Figure 2.2	Self-consistent scheme	26
Figure 2.3	The iterative construction process of the differential scheme	27
Figure 2.4	Comparison of effective bulk moduli of an idealised porous material as predicted by different micromechanical schemes	28
Figure 2.5	Schematic diagram of the FE ² model .	33
Figure 2.6	Reference systems and characteristic lengths for the macro- and micro- scales.	35
Figure 2.7	Porous media: micro-mechanical model	36
Figure 2.8	Relation between micro and macro-scale quantities in kinematic homogenization	41
Figure 3.1	Definition of the REV.	52
Figure 3.2	Porous medium: REV	53
Figure 3.3	Degree of saturation of a salt solution function of water activity.	64
Figure 3.4	Representation of the nucleation of \bar{n} nuclei in the REV pore volume	65
Figure 4.1	Na ₂ SO ₄ aqueous solution: solubility diagram and the phase diagram	74
Figure 4.2	Test at constant humidity: geometry, boundary conditions and mesh	78
Figure 4.3	Test at constant humidity: temperature	82
Figure 4.4	Test at constant humidity: dissolved salt concentration and supersaturation ratio	83

Figure 4.5	Test at constant humidity: saturation degree of precipitated mirabilite and rate of liquid water trapped in hydrated salt crystal	84
Figure 4.6	Problem domain – geometry and mesh	85
Figure 4.7	Test at constant temperature – humidity in point S and environmental humidity	86
Figure 4.8	Test at constant temperature	87
Figure 4.9	Test with varying temperature and humidity 1	88
Figure 4.10	Test with varying temperature and humidity 2	90
Figure 5.1	Sorption isotherms from 273 K to 323 K for pure water	96
Figure 5.2	Trend of C_{hT}^g , C_{hT}^l and C_{hT} with relative humidity in a range of temperatures from 273 K to 323 K	97
Figure 5.3	Trend of C_{TT}^g , C_{TT}^l , C_{TT}^{g+l} with equivalent relative humidity in a range of temperatures from 273 K to 323 K for $\omega = 0$	98
Figure 5.4	Geometry of the masonry column and Boundary Conditions	99
Figure 5.5	Evolution of temperature	100
Figure 5.6	Equivalent relative humidity in isothermal regime and non-isothermal regime	101
Figure 5.7	Supersaturation ratio ω/ω_{sat} in isothermal regime and non-isothermal regime	102
Figure 5.8	Precipitated NaCl in isothermal regime and non-isothermal regime	103
Figure 6.1	Drying at 50% RH: SEM pictures	107
Figure 6.2	Drying at 20% RH: SEM pictures	108
Figure 6.3	Water activity of a sodium chloride solution	110
Figure 6.4	Geometry and mesh of the specimen.	112
Figure 6.5	First experimental campaign. Drying at 50% RH	116

Figure 6.6	Second experimental campaign. Drying at 50% RH	117
Figure 6.7	First experimental campaign. Drying at 20% RH	118
Figure 6.8	Second experimental campaign. Drying at 20% RH	119
Figure 6.9	First experimental campaign. Drying at 40% RH	120
Figure 6.10	First experimental campaign. Crystallization pattern at RH 20 % and RH 50%.	121
Figure 6.11	First experimental campaign. Crystallized salt map at the end of the process in the case of drying at RH 20% and RH 50%	121
Figure 6.12	Second experimental campaign. Salt volume ratio and saturation versus time for the specimen dried at RH 20 % and RH 50 %	123
Figure 6.13	Second experimental campaign. Salt volume ratio versus the time in hours for drying test at 20% and 50% RH . .	124
Figure 6.14	Model results of crystallised salt volume fraction versus time	125
Figure 6.15	Comparison between trends of drying curve and crystallised salt	126
Figure 6.16	Representation of adopted trend of γ_w as a function of S_s^s	128
Figure 7.1	Reference systems and characteristic lengths for the macro- and micro- scales.	134
Figure 7.2	Characteristic quantities at the micro- and macro-scales and energy equivalence	135
Figure 7.3	Biot coefficient b computed with Mori-Tanaka (MT) scheme using different pore shapes and aspect ratios	142
Figure 7.4	Biot coefficient b function of porosity ϕ_0 and Poisson's Coefficient ν computed with MT scheme using different pore shapes	145

Figure 7.5	Biot coefficient b computed with MT scheme function of the aspect ratio r	146
Figure 7.6	Shear modulus ratio μ^{MT}/μ_m computed with MT scheme using different pore shapes and aspect ratios	146
Figure 7.7	Shear modulus ratio μ^{MT}/μ_m function of porosity ϕ_0 and Poisson's Coefficient ν computed with MT scheme using different pore shapes	147
Figure 8.1	Slice of 3D reconstructed volume of the Prague sandstone	151
Figure 8.2	EVs' porosities function of the EV size	152
Figure 8.3	Sketch of the method to compute the volume associated to each distance d_i and representation of distances between matrix voxels	155
Figure 8.4	Geometry indicators histograms for EVs of 5 different sizes	156
Figure 8.5	Geometry indicators for 3 different EVs of 1.1875 mm	157
Figure 8.6	Notation in REV's definition.	159
Figure 8.7	Boundary Conditions and loading scheme adopted for the numerical calculation of the Biot's Tensor	162
Figure 8.8	Comparison between images	163
Figure 8.9	Comparison between the geometry indicators $f_w(d_i)$ computed for the two different resolution for REV #73	164
Figure 8.10	Workflow for calculation of Biot's tensor.	165
Figure 8.11	Calibration and validation of the Mori-Tanaka scheme with data of Table 8.3	167
Figure 9.1	Calibration of the analytical model with simplified micro-geometries for Prague sandstone	173
Figure 9.2	Validation of the analytical model	174
Figure 9.3	Surface representing the Biot's coefficient	174
Figure 10.1	Notation in partially saturated REV	177

Figure 10.2	Comparison between the physical meaning of the proposed approach and the "Law of Partial Pressures"	179
Figure 10.3	Workflow for calculation of Biot's tensor and of partial Biot's tensor.	181
Figure 10.4	Exemplification of zones where it can be assumed that crystallisation pressure acts	183
Figure 10.5	Saturation degree S_s^π according to the HSP REV #73 ($v = 9.5 \mu\text{m}$).	184
Figure 10.6	Partial Biot's coefficient function of degree of saturation assuming different crystal growth models: HSP vs. LPP.	185
Figure 10.7	Partial Biot's coefficient function of degree of saturation assuming different crystal growth models: HSP vs. LPP.	186
Figure 10.8	The influence of Poisson's coefficient of the material matrix on the partial Biot's coefficient	187
Figure 10.9	Hypothesis of smaller pores filled first: maximum principal local stresses $\sigma_{III}(\underline{x})$ at $S_\alpha^\pi = 4.15\%$ and $S_\alpha^\pi = 30.58\%$	189
Figure 10.10	Hypothesis of smaller pores filled first: maximum principal local stresses $\sigma_{III}(\underline{x})$ at $S_\alpha^\pi = 71.34\%$ and $S_\alpha^\pi = 100.00\%$	190
Figure 10.11	Comparison between the law of partial pressure and REV's maximum (σ_{III}) and minimum (σ_I) values of principal stresses for $v_m = 0.2$	191
Figure 11.1	Multi-scale procedure for the evaluation of mechanical effects induced by salt crystallisation.	196
Figure 11.2	Assumptions made for the constitutive law in the case of salts with one crystallised form: representation of a pore.	199
Figure 11.3	Trend of crystallisation pressure of Halite (NaCl) as a function of supersaturation ratio	202

Figure 11.4	Geometry	204
Figure 11.5	Trend of the partial Biot's coefficient as a function of the saturation degree of precipitated Halite	206
Figure 11.6	Supersaturation ratio	207
Figure 11.7	Precipitated NaCl	208
Figure 11.8	Magnitude of displacements	209
Figure 11.9	Magnitude of displacements (partic- ular)	210
Figure 11.10	Damaged areas	211
Figure 11.11	Trend of the maximum spherical ef- fective stress as a function of time. . .	212

LIST OF TABLES

Table 3.1	Phases and species of the model . . .	53
Table 4.1	Test at constant humidity - Summary of model parameters for a sodium sul- phate solution	79
Table 6.1	Parameters used in the simulations. .	114
Table 6.2	Parameters adopted for γ_w in the two experimental campaigns.	127
Table 7.1	Nomenclature of the ellipsoidal pore shapes as a function of the aspect ra- tio r	138
Table 7.2	Expressions of α and β for spherical, needle-shaped, disk-shaped pores and penny cracks.	141
Table 8.1	Porosity of EVs chosen among those of 1.1875 mm	153
Table 8.2	Comparison between porosities	163
Table 8.3	Biot's coefficients	166
Table 9.1	Numerical assessment of Biot's coef- ficients	171
Table 11.1	Parameters used in the simulations. .	205
Table A.1	Thermal Conductivity of the liquid water function of temperature	221
Table A.2	Molar dissolution enthalpy at infinite dilution in J mol^{-1}	222
Table A.3	Molar latent heat of hydration/ de- hydration for $\text{H}_2\text{O-Na}_2\text{SO}_4$ solutions function temperature	222

ACRONYMS

BC	boundary condition
BCs	boundary conditions
CRP	constant drying rate period
EDS	Energy Dispersive Spectroscopy
EDX	Energy-Dispersive X-ray
EV	Elementary Volumes
FEM	Finite Element Method
FFT	fast Fourier transform
HAM	Heat, Air and Moisture
HLP	"Hypothesis of Large Pores first"
HSP	"Hypothesis of Small Pores first"
HTC	Hygro-Thermo-Chemical
HTCM	Hygro-Thermo-Chemo-Mechanical
LPP	"Law of Partial Pressures"
MT	Mori-Tanaka
X-ray μCT	X-ray Micro Computed Tomography
REV	Representative Elementary Volume
RH	Relative Humidity
RUC	Repeated unit cell
SEM	Scanning Electron Microscopy
SH	Statistical Homogeneity
VOI	Volume Of Interest

NOTATION

The mathematical notation adopted is reported here:

s Scalar

\underline{v} Vector

\mathbf{M} Matrix | 2nd order tensor

\mathbf{A} 3th order tensor

\mathbf{T} 4th order tensor

LIST OF SYMBOLS

This list of symbols is not exhaustive. Symbols that only appear locally in the text, or are self-explanatory, are not included.

ROMAN SYMBOLS

SYMBOL	UNIT	DESCRIPTION
A	$\text{kg}/\text{m}^2/\text{s}^{1/2}$	water adsorption coefficient
$\mathbb{A}(\underline{X}, \underline{x})$	-	strain localization tensor
a_w	-	water activity of salt solution
$\mathbb{B}(\underline{X}, \underline{x})$	-	stress localization tensor
\mathbf{B}	-	Biot's tensor
\mathbf{B}_α^π	-	partial Biot's tensor
b	-	Biot's coefficient
b_α^π	-	partial Biot's coefficient
$\mathbf{C}(\underline{X}, \underline{x})$	Pa	local elasticity tensor
$\mathbf{C}^{\text{hom}}(\underline{X})$	Pa	Homogenised stiffness tensor
C_i	m/s	growth rate constant of the i^{th} crystallized form
c_w	kg/m^3	concentration of moisture
c_w^{ls}	kg/m^3	concentration of the liquid water trapped in hydrated crystals
c_α^π	kg/m^3	concentration of α in π -phase
D_l	s	liquid conductivity of pure water
D_s	m^2/s	diffusion coefficient of a salt free solution
D_v	m^2/s	vapour permeability coefficient
D_v^{air}	m^2/s	vapour permeability coefficient for the dry air

SYMBOL	UNIT	DESCRIPTION
d	μm	characteristic lengths of local heterogeneities
e	J/m^3	total enthalpy per unit volume of porous medium
e_{α}^{π}	J/kg	enthalpy of α in π -phase
$\mathbf{E}(\underline{X})$	Pa	macroscopic strain
E_{a_i}	J/mol	activation energy of the i -th crystallized form
E_m	Pa	elastic modulus of the solid skeleton
f_l, f_s, f_v	-	correction functions
g_l, g_v, g_{ω}	-	correction factors
h	-	pore relative humidity
h_{α}	-	environmental humidity
h^*	-	equilibrium relative humidities for the transition due to the hydration/dehydration process
\bar{h}	-	relative humidity prescribed at the boundary
H_{cry_i}	J/kg	latent heat of crystallization of the i -th crystallized form
H_{eva}	J/kg	latent heat of evaporation
$H_{\text{hyd}_{ij}}$	J/kg	latent heat of hydration/dehydration from the j -th crystallized form to the i -th one
h_{hyd}	J/mol	molar latent heat of hydration/dehydration
ΔH_L	J/mol	excess crystallization enthalpy per unit mole of crystallized salt
$\overline{\Delta_{\text{sol}}H^{\infty}}$	J/mol	molar dissolution enthalpy at infinite dilution of the anhydrous salt
j_{w}^g	$\text{kg}/\text{m}^2/\text{s}$	flux of vapour water
j_{w}^l	$\text{kg}/\text{m}^2/\text{s}$	flux of liquid water

SYMBOL	UNIT	DESCRIPTION
\underline{j}_s^i	kg/m ² /s	flux of dissolved salt
\underline{j}_{ws}^l	kg/m ² /s	flux of the liquid phase
$\underline{j}_{s,diff}^l$	kg/m ² /s	diffusive flux of dissolved salt
$\underline{j}_{w,diff}^l$	kg/m ² /s	diffusive flux of liquid water
\underline{j}_e	J/m ² /s	enthalpy flux
\underline{j}_q	J/m ² /s	heat flux
\underline{j}_w	kg/m ² /s	moisture flux
K_{c_i}	m/s	growth rate coefficient of the i-th crystallized form
$K_{H_{ij}}$	m/s	kinetic hydration parameter
$K_{H_{ji}}$	m/s	kinetic dehydration parameter
K_g	s	vapour permeability
K_l	s	liquid conductivity of the salt solution
K_s	m ² /s	salt diffusion coefficient
ℓ	mm	characteristic lengths of the representative elementary volume
L	m	characteristic lengths of the structure
L_i	μm	average length of the i-th crystal in a certain instant t
\hat{L}	J/kg	excess enthalpy of a electrolytic solution containing 1 kg of water
m	mol/kg	molality of the liquid phase
m_α^π	kg	mass of α in π -phase
M_α^π	g/mol	molar mass of α in π -phase
M_{H_2O}	g/mol	molar mass of pure water
M_s^l	g/mol	molar mass of salt mixture solute
N	-	number of crystallized forms
N_A	mol ⁻¹	Avogadro constant $6,022 * 10^{23}$
\underline{n}	-	outward unit normal to the boundary
n	m ⁻³	total amount of nuclei per unit volume of solution

SYMBOL	UNIT	DESCRIPTION
n_i	m^{-3}	amount of nuclei of the i -th crystallized form per unit volume of solution
\bar{n}	-	total number of nuclei in the REV
\bar{n}_i	-	number of nuclei in the REV of the i -th crystallized form
P_{cry_i}	-	crystallization process order of the i -th crystallized form
$P_{hyd_{ij}}$	-	hydration process order
$P_{hyd_{ji}}$	-	dehydration process order
p_α^π	Pa	partial pressure of α in π -phase
p_c	Pa	capillary pressure
p_v	Pa	vapour pressure
$p_{v,sat}$	Pa	saturation vapour pressure of the salt mixture
p_{v,sat_w}	Pa	saturation vapour pressure of the pure water
q_w	$kg/m^2/s$	prescribed normal flux of moisture
q_ω	$kg/m^2/s$	prescribed normal flux of salt
q_T	$kg/m^2/s$	prescribed normal flux of heat
R	$J/mol/K$	ideal gas constant
R_v	$J/kg/K$	gas constant of water vapour
r_p	μm	average pore radius
S_α^π	m^3/m^3	degree of saturation of α in π -phase (volume occupied by α in π -phase per unit volume of pores)
S_{ws}^l	m^3/m^3	degree of saturation of the solution (volume occupied by the solution per unit volume of pores)
t	s	time
T	K	temperature
\bar{T}	K	prescribed temperature at the boundary
T_α	K	prescribed environmental temperature

SYMBOL	UNIT	DESCRIPTION
$\underline{U}(\underline{X})$	m	macro-scale displacement
$\underline{u}(\underline{X}, \underline{x})$	m	micro-scale displacement
V_{cell}^i	m^3	unit cell volume of the i -th crystallized form
$(V_m)_{\alpha}^{\pi}$	m^3/mol	molar volume of the α in the π -phase
\underline{X}	m	position vector at the structure's scale
\underline{x}	m	position vector at the REV's scale
X_w	-	mole fraction of the pure water
Z_i	-	number of formula units in the unit cell of the i -th crystal

GREEK SYMBOLS

SYMBOL	UNIT	DESCRIPTION
$\alpha(\underline{X})$	K^{-1}	thermal expansion tensor of the porous material
α_0	-	threshold value at which the dissolution starts
β_α^π	$J/kg/K$	specific heat capacity of α in π -phase
β_{eff}	$J/kg/K$	effective specific heat capacity of the porous medium
ϕ_0	m^3/m^3	total open porosity (volume of voids per unit volume of porous medium)
ϕ_{eff}	m^3/m^3	effective porosity
γ	-	mean activity coefficient of the dissolved salt
γ_w	$kg/m^2/s$	humidity convective coefficient
γ_T	$kg/m^2/s$	thermal convective coefficient - convective heat transfer coefficient
$\varepsilon(\underline{X}, \underline{x})$	-	microscopic strain tensor
λ_{eff}	$J/s/m/K$	effective thermal conductivity
λ_m^{dry}	$J/s/m/K$	thermal conductivity of dry material
λ_w	$J/s/m/K$	thermal conductivity of the liquid water
λ_{s_i}	$J/s/m/K$	thermal conductivity of salt in i -th crystallized form
μ_w^{ls}	$kg/m^3/s$	rate of liquid water trapped in hydrated salt crystals
μ_w^{lg}	$kg/m^3/s$	water evaporation rate
ν_0	-	number of water molecules trapped per salt mole
ν_m	-	Poisson's coefficient of the solid skeleton
ρ_α^π	kg/m^3	mass density of α in π -phase
ρ_{ws}^l	kg/m^3	mass density of the liquid phase

SYMBOL	UNIT	DESCRIPTION
ρ_{eff}	kg/m^3	effective mass density of the porous media
$\Sigma(\underline{X})$	Pa	macroscopic stress tensor
$\Sigma'(\underline{X})$	Pa	macroscopic effective stress tensor
$\sigma(\underline{X}, \underline{x})$	Pa	microscopic stress tensor
τ_v	-	vapour resistance factor
τ_l	-	tortuosity
v	mm	length of voxel's side
ω	kg/kg	mass of the dissolved salt per unit mass of liquid phase
ω_{sat}	kg/kg	mass of the dissolved salt per unit mass of liquid phase at the saturation
$\bar{\omega}$	kg/kg	mass of the dissolved salt per unit mass of liquid phase prescribed at the boundary

INTRODUCTION

Motivation

Centuries of masonry construction have left a wide heritage of historic buildings and monuments, which are often of extraordinary architecture and design. Their structures are usually made of masonry constituted by bricks or natural stones and mortar, *i. e.* porous building materials. During their lifetime, they are subjected to different types of loading, *e. g.* static service loads and cyclic mechanical loadings, like earthquakes and vibrations. In addition to these loads, historic buildings are subjected to chemical degradation processes. They can be considered as loadings causing a reduction in mechanical properties and affecting the durability of the constituting material. They usually are not considered because their influence can be seen in the long period, but they become important when dealing with historic structures exposed to aggressive environments. Understanding the deterioration processes in a unified framework, involving not only mechanical causes but also the environmental ones inducing mechanical effects, is necessary to conserve these structures. Among factors of degradation in porous building materials, heat, moisture and salt transport combined with salt crystallisation strongly influence the durability of structural systems like masonry.

In particular, salts inside masonry structures – like sodium chloride (NaCl) and sodium sulfate (Na₂SO₄) – can be naturally present or absorbed from the atmosphere or groundwater during the life of the structure. Indeed, the source of salt may be one or a combination of the following (Abu Bakar et al., 2009): (1) saline soils and groundwater, (2) sea spray, (3) air-borne salt, (4) air pollutants, (5) animal excretion, micro-organism, leaking sewers, (6) salt naturally occurring in the stone, brick clay or mortar sand (7) salt water used for puddling brick clay or mixing mortar, (8) salts used for

de-icing roads in cold climates, (9) inappropriate cleaning compounds. Water and dissolved salt ions can penetrate into building materials through the porous matrix and existing cracks. Due to water evaporation or a temperature change, the supersaturation ratio – *i.e.* the ratio between salt concentration in the pore saline solution and the one at saturation – increases; when the concentration exceeds the saturation threshold, salts can precipitate in different forms depending on the local hygro-thermal conditions. If the salts precipitate on the outer surface of the material efflorescences may appear, if the salts precipitate beneath the surface sub-florescences or crypto-florescences will be generated (Rodríguez-Navarro and Doehne, 1999). Several experimental evidences demonstrate that growing crystal can exert a pressure, generated by solution supersaturation and interfacial energies. Indeed, salt crystallisation induces high stresses in the material micro-structure enhancing the damage process and for this reason is recognized as one of the major factors of degradation in porous building materials. In the worst cases, these processes can cause complete structural disintegration of the material, leading to structural problems and there is compelling evidence that its influence will increase due to the global climate change and human impacts (Goudies and Viles, 1997; Wüst and McLane, 2000).

Therefore, to conserve these structures the challenge for structural engineers is to understand how salt crystallisation affect the structural integrity of historic structures made of porous building materials. The physical mechanisms governing salt related problems in porous building materials are: the diffusion – *i.e.* salt and moisture transport – the chemistry of crystallisation, the thermodynamics and the mechanics of material, including the damage induced by salt crystallisation. This physical phenomenon is affected by the salt in solution and the material micro-structure. It is evident that it involves different scales: the macro-scale, in which the porous building material is seen as a homogeneous continuum, and the micro-scale, being the characteristic scale of the microporomechanics in which can be distinguished the material matrix and the pores. Indeed, salt

transport and crystallisation phenomena are influenced by the geometry at the micro-scale but their effects – *e.g.* efflorescences, subflorescences, material pulverization, blistering – can be seen at the macro-scale and, sometimes, at the scale of the building, as depicted in Figure 1.1.

Despite many efforts, to date the kinetics of in-pore crystallisation is not completely understood (Espinosa-Marzal and Scherer, 2010a). Moreover, we are still facing with several open issues (Espinosa-Marzal and Scherer, 2010b; Scherer et al., 2001), concerning where nucleation and crystal growth take place within a pore network; what is the effect of pore site distribution on stress; under what conditions salt crystallisation leads to crack and failure of the material.

The modelling of these phenomena is necessary to forecast the most probably damage scenarios in the long term. However, the prediction of mechanical effects induced by salt crystallisation is still a challenge, since the process involves several physics. Moreover, an accurate modelling of such phenomenon, ranging from the hygro-thermal behaviour to mechanical issues, should include the effects of the material micro-structure. Indeed, almost all materials possess heterogeneous structures at a certain scale of observation: in particular, as it is well-known, porous building materials can be modelled as a composite material constituted by the microstructural matrix and voids. Understanding the behaviour of such media is not an easy task as their physical properties depend entirely on their underlying micro-structures which may differ in morphology, porosity and properties of the material matrix. The complexity of the micro-structural behaviour is further pronounced by incorporating the presence inside the voids of different species in different phases, like in the case under discussion, or damage, caused by local fractures of the matrix, when the stress in the material matrix exceeds the material strength. Therefore, the prediction of the mechanical response of porous materials requires appropriate methods, able to link the micro and the macro-scale, taking into account the influence of geometry and the behaviour of the material at the micro-scale. This is necessary because conducting experiments on

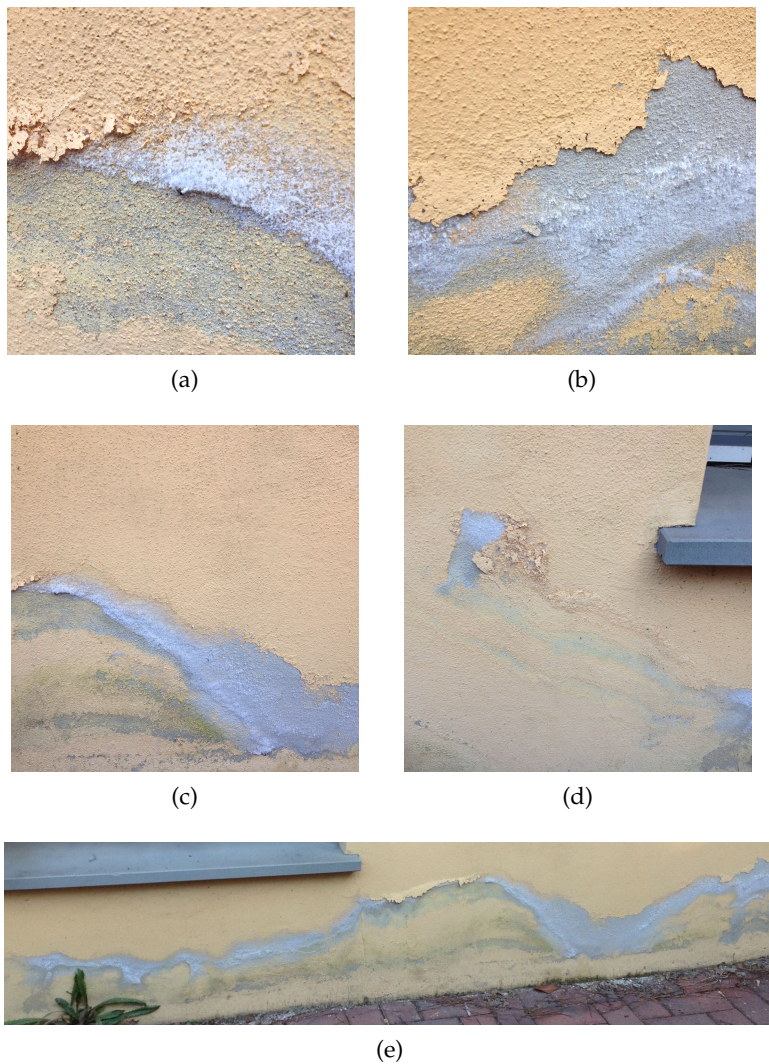


Figure 1.1: Example of efflorescences and subflorescences developed in ten years on a building due to capillary rising of groundwater in winter: (a)-(d) Details of plaster bulges; (e) Overview of plaster bulges and marks of previous level of efflorescences.

a large number of porous building materials with different physical and geometrical properties is nearly impossible from time and cost point of views. Also, performing a direct numerical simulation of the entire body including the whole real micro-geometry leads to a huge problem whose solution is computationally expensive and demands high memory storage requirements, which cannot be fulfilled for common engineering applications.

The scope of this dissertation is to give some contributions on the modelling and analysis of mechanical effects induced by salt crystallisation in porous building materials employing a two-scale approach, in order to better understand the relationship between the crystallisation physics and its mechanical effects. Much has been written on transport processes of salts and hicro-thermal behaviour of structures. Therefore this thesis is focused on the mechanical effects due to salt crystallisation. To do so it is very important to understand the physics of the problem and the contribution already made in the literature to be able to develop an appropriate mechanical model. To date, all contributions in the literature are limited to make a rough estimate of the stress induced at the macro-scale by salt crystallisation and to compare it with a tensile sigma saying that the failure is reached. The objective is to go further with a more sophisticated mechanical approach that takes into account the real micro-structure of the material and the distribution of the crystallisation pressure.

To this aim, the coupled multiphase model for the hygro-thermal analysis of hystoric masonry, presented in Castellazzi et al. (2013a) is improved and extended, in order to develop a general framework to include the crystallisation/dissolution and the hydration/dehydration processes of salts with N crystallised forms. In the proposed model thermal effects are fully considered. In particular, the dependency on temperature of sorption/desorption curves as well as of other material parameters, neglected in Castellazzi et al. (2013a), are taken into account. In addition, it is specialised for the most common and destructive salts: sodium chloride

*Objectives and
Contributions*

and sodium sulfate. It is also enriched to describe different drying kinetics and take into account diverse efflorescence formations. This HTC model and its validation constitutes the first part of the dissertation and it is the first step to proceed in the modelling and analysis of mechanical effects induced by salt crystallisation.

The second part of the dissertation focuses on modelling of mechanical effects employing a two-scale approach, in order to take into account the micro-mechanical features of the real porous media. Indeed, advanced experimental techniques, like X-ray μ CT, allow to obtain images of the real micro structure of materials. These experimental techniques combined with finite element analysis open new scenarios on the possibility to simulate the local stress in the material micro-structures and to upscale it at the scale of the structure, allowing to refine macroscopic relations, which estimate the mechanical effect induced by salt crystallisation in the material matrix. In particular, this analysis is pursued proposing a multi-scale approach, based on numerical homogenisation, which exploit the geometry of the porous material at the micro-scale. The input data of the proposed multi-scale approach are (i) the macro-scale distribution of the crystallised salt or, equivalently, its saturation degree and (ii) the real 3D geometry of the porous material at the micro-scale. The former is the output of the HTC model, which is developed and validated in the first part of the dissertation. As regards the real 3D micro-geometry, in this dissertation, we refer to images coming from X-ray μ CT of the porous material. In particular, inspired by the approach recently proposed in Castellazzi et al. (2015a, 2017), we developed a procedure that enables the automatic transformation of the X-ray μ CT images into a three-dimensional finite element mesh. This constitutes the basis of the micro-mechanical finite element model used to perform the numerical homogenisation. On this regards, the challenge is to translate the physics of crystallisation in a mechanical interaction between the phases filling the pores and the material matrix, at the scale of the material micro-structure. Thus, some hypotheses on the loading scheme of the micro-

mechanical model, based on the knowledge of crystallisation physics, are made and their effects in terms of mechanical response at the macro-scale are compared. Moreover, a procedure to obtain a simplified micro-mechanical model of a porous material is conceived to define the most suitable micro simplified geometry representing the real material. In the third part of the dissertation results deriving from the proposed numerical procedure are incorporated in a structural computation with environmental-mechanical loadings to forecast the most probable damage scenarios. In particular, a Hygro-Thermo-Chemo-Mechanical (HTCM) model, combining hygro, thermal, chemical aspects and the mechanical ones, is proposed and further specialised for sodium chloride solutions. The model considers an elastic porous material, isotropic at the macroscopic scale and described by the simplified micro-mechanical model developed in the second part of the dissertation.

*Outline of the
dissertation*

The dissertation is organized as follows. It consists in three parts and it starts with a concise state of the art in Chapter 2. In the first part the Hygro-Thermo-Chemical aspects are investigated. In Chapter 3 a new fully coupled multiphase model for hygro-thermal analysis and prediction of salt diffusion and crystallisation in porous building materials – called briefly HTC model – is presented. The model is specialised for sodium sulphate solutions – Chapter 4 – and for sodium chloride solutions in Chapter 5. Chapter 6 treats the extension of the HTC model to describe the drying kinetics leading to different efflorescence formations and its validation through two distinct extensive campaigns on drying in presence of NaCl salt solution.

In the second part of the dissertation a multi-scale approach for the analysis of mechanical effects induced by salt crystallisation in porous media, based on numerical homogenisation, is presented. Chapter 7 gives some details about the homogenisation approach adopted. Chapter 8 deals with porous media saturated with one species: a general procedure to find the size of a porous medium Representative Elementary Volume (REV) and to compute

the Biot's tensor, starting from a X-ray Micro Computed Tomography (X-ray μ CT) dataset, is presented. On the other hand, Chapter 9 is devoted to the development of a procedure to obtain a simplified micro-mechanical model of a porous material. Porous media saturated with multiple species are treated in Chapter 10. In particular, a multi-scale approach for the analysis of mechanical effects induced by salt crystallisation in porous media is presented.

In the last part of the dissertation – Chapter 11 – a Hygro-Thermo-Chemo-Mechanical (HTCM) model, combining hygro-thermal-chemical aspects and the mechanical ones, is developed. In the final Chapter 12, the conclusions of the work are formulated, and an outlook for future developments is given.

STATE OF THE ART

In this dissertation, the modelling and analysis of mechanical effects induced by salt crystallisation in porous building materials is investigated employing a two-scale approach. As outlined, the growth and dissolution of salt crystals is sensitive to temperature and relative humidity changes. Therefore, the study of this problem can be subdivided in three main steps:

1. the development of a general Hygro-Thermo-Chemical (HTC) model which is able to predict how much salt precipitates, where it crystallises and in which conditions for different types of salt;
2. the development of a micro-mechanical model which is able to model the mechanical effect induced by salt crystallisation and a strategy which is able to link the micro-macro scale;
3. the development of a HTCM model able to include both HTC aspects and the mechanical ones.

In this Chapter an overview of the state of the art to date is given.

2.1 SALT TRANSPORT AND CRYSTALLISATION : FROM EXPERIMENTAL EVIDENCES TO THE MODELLING

The action of salts on weathering of porous media and the physics of crystallisation are widely treated in the literature: however, to date, they remain incompletely understood. Experimental studies, at different scales, help to understand these complex processes: they are necessary either to develop a model of the physical phenomenon or to provide input data and to validate numerical codes.

In this Section a concise state of the art to date on all Hygro-Thermo-Chemical aspects will be given both from the experimental and the modelling side. In particular, the background on the physics of crystallisation will be presented. Nevertheless, it is worth noting that to date some open questions about crystallisation physics remain unanswered.

2.1.1 *Crystallisation dynamics*

With the variation of climatic conditions such as relative humidity, temperature or rain followed by drying, the salts present in porous media crystallise because of the pore solution supersaturation, either in the form of efflorescence (at the surface) or subflorescence (within the pore network) (Rodriguez-Navarro and Doehne, 1999). Moreover, some salts – *e. g.* sodium sulfate (Na_2SO_4) – have different crystallised forms (Steiger and Asmussen, 2008); in particular, they can precipitate in two kind of forms: hydrate, if some water molecules are included in the crystal (*e. g.* mirabilite $\text{Na}_2\text{SO}_4 \cdot 10\text{H}_2\text{O}$) or anhydrous, if no water molecule is included in the crystal (*e. g.* thenardite Na_2SO_4). Once crystallised, salts can re-dissolve in two different ways: by contact with liquid water (dissolution) or by contact with water vapour (deliquescence). The latter is due to the hygroscopic properties of salts. For example, the fog can enhance the deliquescence process, while the rain the dissolution one. The resulting salt solution is then mobilized in the porous network and salt subsequently re-crystallises on drying or under certain temperature conditions. Depending on whether the salt re-precipitation occurs directly from an homogeneous solution or from pre-existing crystallites present in the solution, different growth rates and crystallisation patterns can result. It is proven that the presence of salt changes the internal structure of a porous material (Lubelli et al., 2006) and pore size distribution (Koniorczyk and Gawin, 2008; Koniorczyk et al., 2016), affecting the properties of both solid skeleton and liquid phase, *e. g.* sorption isotherms, solution density, and dy-

dynamic viscosity (Koniorczyk and Wojciechowski, 2009; Majid Hassanizadeh and Leijnse, 1995).

The effect of the crystal growth on the drying behaviour of porous media with NaCl solution has been recently experimentally investigated in sandstone (Desarnaud et al., 2015), and in fired clay bricks (Eloukabi et al., 2013; Gupta et al., 2014). In all the cases, it has been noted that the formation of salt crystal on the external surface deeply influences the evaporation.

The most recent complete experimental study on the crystallisation dynamics is reported in Desarnaud et al. (2015). It is conducted in the frame of the JPI-JHEP European Project KIDADAMA (de Miranda et al., 2013), aiming at studying the Kinetic of Salt Crystallization and Mechanical Damage in Historic Masonry. This study sheds some light on crystallisation dynamics at different scales and can be useful to develop or validate numerical models that predict salt damage risks in building materials. In this study, the authors perform a multi-scale study on the behaviour of sodium chloride contaminated sandstones, exposed to different Relative Humidity (RH) conditions, roughly representative of winter and summer ones. Sodium chloride is chosen because its solubility is only weakly temperature dependent, so that the main driving forces for (re-)crystallisation are RH variations. Macro-scale experiments involve samples of three different sizes and evaporative surface ratios: they allow the studying of crystallisation patterns and of drying kinetics of saturated sandstones. In particular, samples of cylindrical shape are initially saturated with a saturated NaCl solution and subsequently dried at 20% or 50% RH in a climatic chamber at constant temperature. The experimental drying tests show different kinetics for the different drying environmental humidities. The monitoring of the drying process is carried out by measuring the weight change of the sample. In particular, drying at 20% RH is found to take longer than at 50% RH due to the formation of a crusty efflorescence on the surface. The experiments conducted in Gupta et al. (2014) on the drying behaviour of fired-clay brick saturated of NaCl solution lead to the same conclusions. At

very low relative humidity (0% RH) the drying process is very slow comparing with the drying at higher relative humidity (55% and 70% RH). These different kinetics depend on the different efflorescences that are formed on the external surface. In particular, in Eloukabi et al. (2013) the efflorescences are classified as crusty or patchy (also referred to as "cauliflower" in Shahidzadeh-Bonn et al. (2008)). The crusty efflorescences block the pores, while the patchy ones leave some pores space. In the first case the drying kinetics of the evaporation is strongly slowed down. The formation of patchy or crusty efflorescence has been found to depend on the characteristic of the porous media (for example the pore radius) (Eloukabi et al., 2013) and on the environmental conditions (Desarnaud et al., 2015; Gupta et al., 2014). Moreover, in Desarnaud et al. (2015) the recrystallisation behaviour and the drying of the salt contaminated sandstones once they are rewetted with liquid water or brought in contact with water vapour (RH \sim 100%) is investigated. In general, recrystallisation that results from cycling differs from the initial crystallisation (Desarnaud and Shahidzadeh-Bonn, 2011): if the nucleation is primary, *i.e.* directly from solution, high supersaturations can be achieved (De Yoreo and Vekilov, 2003; Mullin, 2001) which is the case for the evaporation of homogeneous salt solutions in confined systems (Desarnaud et al., 2014); on the contrary, the secondary nucleation, from pre-existing crystallites present in the solution, typically happens around the saturation concentration (De Yoreo and Vekilov, 2003). In the study is shown that deliquescence-drying cycles at 20% RH induce a movement of the salt precipitation, *i.e.* the salt skin partly disappears, salt precipitates in the pores and the drying is faster than the first drying. At 50% RH, deliquescence-drying cycling does not cause any changes with respect to the first drying.

On the other hand, in Desarnaud et al. (2015) micro-scale experiments are used to investigate the crystallisation pattern in the core of the stone and at the surface in more detail, after the samples has dried out. These experiments are carried out using high resolution X-ray Micro Computed

Tomography (X-ray μ CT), optical and Scanning Electron Microscopy (SEM) combined with Energy-Dispersive X-ray (EDX).

The study presented in Desarnaud et al. (2015) is completed by experiments performed into square microcapillaries, which simply model systems for a single pore within a porous medium. They are conducted to investigate the kinetics of dissolution and deliquescence of crystals, followed by recrystallisation, and to quantify small-scale features, in order to improve the understanding of the underlying basis of macroscopic fluid and solute transport behaviour. Other previous studies reported in the literature deal either with unidirectional (1D) evaporation of a porous material that is permanently supplied with the salt solution or with evaporation-wicking experiments (Eloukabi et al., 2013; Shokri, 2014), revealing the impact of the pore size and the relative humidity on the type of crystallisation.

The results obtained in Desarnaud et al. (2015) for NaCl are in good agreement with a previous work of Desarnaud et al. (2013) on sodium sulfate for which humidity cycling and rewetting/drying also leads to different crystallisation mechanisms due to the difference between the primary or secondary nucleation and the related supersaturation reached in the solution during drying.

In order to improve the understanding of coupled drying - crystallisation, or deliquescence - dissolution dynamics, an experimental study (Derluyn et al., 2016) has been performed recently to obtain data of the simultaneous measurement of drying/deliquescence and salt precipitation/dissolution. In particular, data on the kinetics of drying and deliquescence, and on the precipitation and distribution of salt crystals within the pore space of Mšené (Prague) sandstone are derived from quantitative image analysis on laboratory X-ray Micro Computed Tomography (X-ray μ CT) scans, obtained developing climatic chambers compatible with X-ray μ CT scanners. This allows for inducing crystallisation under controlled temperature and relative humidity, and for dynamically visualizing salt weathering phenomena in building materials, by simultaneously imaging the transport and crystallisation process during consecutive scanning. Cylindrical

sandstone samples are initially capillary saturated with a saturated NaCl-solution and subsequently dried at 20% RH and at 50% RH, at room temperature. During drying, the samples are scanned at defined moments in time, confirming the kinetics reported in Desarnaud et al. (2015). Furthermore, X-ray μ CT scans are acquired during subsequent cycles of deliquescence, *i.e.* exposure to high RH, and drying at 20% RH. The resolution of X-ray μ CT scans results in 10 μ m. During the deliquescence, the salt efflorescence dissolves first, followed by the subflorescence dissolution and the pore space filling with saline fluid at a constant rate. The X-ray μ CT datasets reveal the direct coupling between the transport and crystallisation dynamics through quantitative image analysis of the simultaneous visualization of both processes in 4D. These data can be helpful for numerical models that predict salt damage risks in building materials, as model parameters for the transport and crystallisation kinetics need to be defined, as well as for the validation of model which aim the prediction of the distribution of crystals within the pore space.

It is clear from the literature contributions to date that the crystallisation dynamics in a porous medium depends on both thermodynamic and transport processes; these will have also a direct impact on the evaporation rate of the solvent (water) from the porous network. Moreover, some advanced experimental techniques – such as Scanning Electron Microscopy and X-ray Micro Computed Tomography – allow to have some insight on the quantification of the simultaneous drying/crystallisation kinetics, as well as the deliquescence/dissolution kinetics.

2.1.2 *Pressure exerted by growing crystals*

Since the mid-19th century, several experiments demonstrated that a growing crystal can exert pressure (Becker and Day, 1905, 1916; Correns, 1926; Correns and Steinborn, 1939; Lavallo, 1853; Taber, 1916). The general consensus in the literature is that this pressure is a thermodynamic interaction, due to

a non-equilibrium state, generated by solution supersaturation (Coussy, 2006; Flatt, 2002; Flatt et al., 2007; Scherer, 1999, 2004; Steiger, 2005a,b) and interfacial energies, which develops if a liquid film between the crystal and the confining surface is present (Espinosa-Marzal and Scherer, 2010b; Scherer, 1999, 2004). The crystal is thus subjected to different pressures on its different faces: the faces in contact with the liquid solution are thought to be under the pressure of the pore solution, while those in contact with the confining surface (through the liquid film) are assumed to be under the crystal pressure. It follows that the crystal pressure results higher than the one of the surrounding solution (Scherer et al., 2001; Steiger, 2005a), thus the crystallisation pressure is generally defined as the overpressure induced by the growing crystal, or, in other words, as the difference between the crystal pressure acting on the loaded crystal face - the pressure across the liquid film - and the liquid pressure of the bulk solution, acting on the unloaded crystal face (Steiger, 2005a). Recent experiments confirm that the pressure originates from a repulsive interaction between charged surfaces separated by the liquid film and the maximum force is achieved when there is no more solution around the sides of the crystal (Desarnaud et al., 2016a).

Correns (1949) was the first who proposed a relationship to evaluate the crystallisation pressure. However, throughout years the literature proposed expressions more and more refined to compute the crystal pressure acting on the pore wall, based on experimental evidences and analytical models (Correns, 1949; Desarnaud et al., 2016a; Espinosa-Marzal and Scherer, 2010a; Flatt et al., 2014; Steiger, 2005a,b). According to those expressions, the crystallisation pressure depends on:

- A. the solution temperature;
- B. the supersaturation ratio, which is defined as the ratio between the concentration of the solution and the one at saturation;

- c. the kind of precipitated crystal: *e.g.* crystals exerting the highest value of crystallisation pressure are halite and thenardite (Steiger, 2005a).

For these reasons, the determination of solubility diagrams is necessary. Solubility diagrams and the estimation of crystallisation pressures can be found in the literature for a great range of salt solutions (Steiger, 2005a; Steiger and Asmussen, 2008; Steiger et al., 2008). Recently, also the crystallisation behaviour of salt mixtures have been investigated (Lindström et al., 2015, 2016) and compared to a single salt behaviour.

2.1.3 *Modelling of hygro-thermal issues, salt transport and crystallisation*

The problem of the hygro-thermal behaviour of porous media in presence of salt solution is very complex from the modelling point of view because the diffusion and crystallisation of the salt in porous media depends not only on the transport of water and salt in different forms (gas, solid, liquid) but also on the phase transitions between them and furthermore on the interactions between the various processes. In the literature the modelling of hygro-thermal issues, salt transport and crystallisation is generally carried out from a macroscopic point of view, *i.e.* idealising the porous medium filled with air, water, salt in solution, *etc...* as a multiphase homogeneous continuum. This underlies the implicit definition of a Representative Elementary Volume (REV) which is generally defined as the minimum window allowing to obtain an homogeneous value of the considered property which is independent of the window size. The definition of a REV ensure each material point of the considered domain is representative of the porous material.

In order to model these processes in a macroscopic framework, the starting point is an accurate transient Heat, Air and Moisture (HAM) transfer model, since, as explained previously, the hygrothermal environmental conditions strongly influence the salt precipitation. The numerical simulation of

heat and moisture transport phenomena has been widely investigated in the literature and many models have been developed (see, for example, Castellazzi et al. (2015b); Grunewald et al. (2003); Hansen (1986); Häupl et al. (1997); Lewis and Schrefler (1998); Pel (1995); Tariku et al. (2010)); these models do not take into account the presence of salts, assuming that pores contain only water in different phases.

Whether salts are in solution or in solid phase, the hygrothermal behaviour of building materials is strongly modified. Thus, some extended HAM models, embedding salt diffusion and crystallisation, have been proposed in literature (Castellazzi et al., 2013a; Derluyn, 2012; Koniorczyk and Gawin, 2008, 2011; Koniorczyk and Konca, 2013; Nicolai, 2007). Castellazzi et al. (2013a) developed a coupled multiphase model for hygrothermal analysis of masonry structures contaminated with sodium chloride salt, adopting the description of porous material proposed by Schrefler (2002) and Gawin and Schrefler (1996). In order to validate the proposed model, they simulated salt transport and crystallisation in a 2D slice of a wall subjected to ageing for several months in isothermal conditions and taking into account the measured environmental relative humidity variation. Koniorczyk and Gawin (2008, 2011), respectively for sodium sulfate and sodium chloride solutions, extended the model previously formulated for a general porous medium by Lewis and Schrefler (1998) including the salt mass balance equation and the kinetics of the salt crystallisation/dissolution. In Koniorczyk and Konca (2013) a mathematical model of salt, moisture and energy transport concerning the salt phase change kinetics for sodium sulfate solutions is derived on the base of an experimental set-up constructed to measure the thermal effect of the salt crystallisation/dissolution process in building materials containing sodium sulphate. Finally, Derluyn, in her PhD dissertation (Derluyn, 2012), develops a numerical model covering heat, water and salt transport processes, salt crystallisation, deformation and cracking for sodium chloride and sodium sulfate; experimental results for the validation of the proposed model are ob-

tained using neutron radiography and X-ray Micro Computed Tomography.

These models are generally limited to the crystallisation/dissolution process. Some efforts in the direction of modelling and simulating also the transition from a hydrate crystallised form to an anhydrous one and reverse the have been attempted only in Nicolai (2007).

2.1.4 *Needs for further research*

Despite some models dealing with salt transport and crystallisation at the macro-scale have been proposed, either for sodium chloride solution or sodium sulfate solution, a general framework in the modelling the phenomenon, able to take into account several types of salt has not been proposed yet. Indeed, these models are generally limited to the crystallisation/ dissolution process and neglect the hydration/dehydration one, *i.e.* they do not account for the transition from a hydrate form to an anhydrous one and reverse. Moreover, in these models thermal effects are described through the energy equation. However, numerical simulations based on these models are often performed in isothermal regime, particularly when dealing with salts having the mass fraction at saturation constant with temperature, like for example the sodium chloride (Castellazzi et al., 2013a). Despite many studies in the literature, we are still facing with several open issues (Espinosa-Marzal and Scherer, 2010b; Scherer et al., 2001), concerning where nucleation and crystal growth take place within a pore network; what is the effect of pore site distribution on stress; under what conditions salt crystallisation leads to crack and failure of the material. Finally, all numerical models proposed until now cannot account for the different formations of efflorescences according to environmental conditions and their influence in the drying of salt contaminated porous media.

In this dissertation a general framework to model hygro-thermal-chemical aspects, including the crystallisation/dissolution and the hydration/dehydration processes of salts

with N crystallised forms, is developed and thermal effects are fully considered. The proposed model is specialised for the most common and destructive salts: sodium chloride and sodium sulfate. Then it is enriched to describe different drying kinetics and take into account diverse efflorescence formations.

2.2 MECHANICAL EFFECTS IN MULTIPHASE POROUS MEDIA

Crystallisation phenomena take place in the porous medium's voids, leading to the development of a crystallisation pressure which is exerted on the material matrix. It follows that the matrix of the porous medium is subjected to a stress state. It is evident that salt transport, crystallisation and mechanical effects are strictly related and that the geometry at the micro-scale plays a crucial role in the determination of the latter.

Porous building materials, like masonry, mortar and natural stones, are composite materials (Dormieux et al., 2006; Dormieux and Kondo, 2016; Dormieux and Ulm, 2005). The most prominent heterogeneity of such natural composite materials is of course the porosity, *i. e.* the space left in between the different solid phases at various scales, ranging from interlayer spaces in between minerals, to the macropore space in between microstructural units of the material in the micrometer to millimetre range. The porosity and the shape of the voids, which depends on the geometry of the micro-structure, are the two ingredients to understand and predict the macroscopic material behaviour, in particular the mechanical one and the permeability. The mechanical behaviour of multiphase porous materials was perceived early on in the ground-breaking work of M.A. Biot (1941) and K. Terzaghi (1923), who developed the macroscopic basis of what is now known as '*poromechanics*', *i. e.* a branch of continuous mechanics which studies the mechanical behaviour of porous materials. In the 1970s, a breakthrough was achieved with pioneering works that relates macroscopic laws to mi-

crostructural properties. It was the birth of 'micromechanics of porous media', or in short '*microporomechanics*'.

The assessment of the mechanical response of porous materials subjected to salt crystallisation requires appropriate methods, able to link the micro and the macro-scale, taking into account the influence of geometry and the behaviour of the material at the micro-scale. For these reasons, it is fruitful to treat the problem with multi-scale techniques, which are employed when at least two different scales co-exist. These models are based on the physics of the microstructures and are usually employed to predict the macroscopic behaviour of heterogeneous materials, with random or periodic micro-structures.

In this section the state of the art on the coupled modelling of salt transport and damage due to salt crystallisation is presented. Moreover, basic principles of multi-scale techniques and, in particular, of homogenisation theories and microporomechanics are illustrated.

2.2.1 *Coupled modelling of salt transport and damage due to salt crystallisation*

Some contributions on the modelling of the mechanical effects induced by salt crystallisation either at macro scale (Coussy, 2006; Derluyn et al., 2014a; Flatt et al., 2014; Koniorczyk and Gawin, 2012) or at the microscopic one (Scherer, 1999, 2004) can be found in literature.

In the pioneer work of Coussy (2006) the deformation and the fracture of porous solids from internal crystallisation of salt is explored in the framework of the thermodynamics of unsaturated brittle poroelasticity, with the aim of combining the mechanics of porous solids and the physical chemistry of confined crystallisation under drying. In particular, the usual theory of crystal growth in confined conditions is further developed in order to include both the deformation and the drying of the porous solid. This information is up-scaled at the macroscopic scale on the base of an homogenisation scheme with simplified pore geometries. The approach is

used to perform a quantitative analysis of the role of the pore size distribution on the crystal growth under repeated imbibition-drying cycles. The deformation and the fracture of the porous solid from drying-induced crystallisation are then considered in the context of brittle poroelasticity. The adoption of a fracture criterion based on the elastic energy that the solid matrix can ultimately store finally leads to the determination of how long a stone can resist repeated cycles of drying-induced crystallisation of salt.

Nicolai (2007) included salt transport and crystallisation in the porous micromechanics theory by Coussy (2006, 2004). Indeed, in order to deal with real structures, it is necessary to scale up to the macro level, as attempted in Koniorczyk and Gawin (2012) and Derluyn et al. (2014a).

In Koniorczyk and Gawin (2012) a novel mathematical model of chemo-hydro-thermo-mechanical behaviour of porous building materials considering salt transport and crystallisation is presented. The model describes salt transport and crystallisation in a non-isothermal, partly saturated deformable porous material. It allows to investigate the total stress in the building elements exploiting in the realistic environment, considering the external load, the stress induced by moisture migration (capillary pressure), thermal stress and the stress generated during crystal growth. The additional pressure, which is generated during the salt crystallisation, is taken into account by means of the effective stress principle. The properties of the solution and the magnitude of crystallisation pressure depends on the internal pore structure of the material. Moreover, some efforts are made towards the investigation of the influence of pore micro-structure on the salt transport and crystallisation.

Derluyn et al. (2014a) present a computational model coupling heat, water and salt ion transport, salt crystallisation, deformation and damage in porous materials, focused on crystallisation-induced damage. The theory of poromechanics is employed to relate stress, induced by crystallisation processes or hygro-thermal origin, to the material's mechanical response. In this model, a non-local formulation is developed to describe the crystallisation kinetics. The model per-

formance is illustrated by simulating the damage caused by sodium chloride crystallisation in a porous limestone, comparing the results with experimental observations based on neutron and X-ray imaging.

In all these studies the modelling of salt transport and its mechanical effects is performed employing a macro-scale approach, without using up-scaling methods based on the real microstructure of the considered material.

2.2.2 *Multi-scale approaches*

Multi-scale techniques are traditionally categorised into the *homogenisation method*, where the length scales of micro- and macro-problems are sufficiently separate, and the *concurrent method*, which considers strong coupling between the scales.

Homogenisation
Method

The main objective of the classical *homogenisation method* is to estimate the effective macroscopic properties of a heterogeneous material from the response of its underlying microstructure, thereby allowing to substitute the heterogeneous material with an equivalent homogeneous one. In particular, it enforces the relation between homogenised quantities, *i. e.* the homogenised constitutive law.

It was conceived to describe polycrystalline or composite materials, but recently it has been successfully applied to describe macroscopic properties of porous materials (Dormieux et al., 2006). Historically homogenisation methods were applied because of (i) the impossibility to carry out calculations which account for the whole micro-structure and (ii) the lack of knowledge on the real micro-structure. It consists in four main steps:

1. the defining of an observation window in the heterogeneous material, which ensures the principle of scale separation: the Representative Elementary Volume (REV);
2. the defining of the equivalence between the heterogeneous and homogeneous material;

3. the introduction of some hypotheses in the writing of the micromechanical boundary value problem, in particular, on the choice of the boundary condition;
4. the analysis at the REV level;
5. the determination of the macroscopic behaviour from the average mechanical response of the REV;
6. the expression of the microscopic solution in terms of macroscopic variables. This is the so-called re-localization step and it is optional.

Homogenisation methods can be classified in: analytical, semi-analytical and computational or numerical homogenisation. A detailed historical review on analytical, semi-analytical and computational homogenisation can be found in Saeb et al. (2016). Here, we recall the classic basic concepts.

2.2.2.1 *Analytical and Semi-Analytical Homogenization*

Preliminary steps in homogenization date back to the 19th century when Voigt (1889) proposed to assume a uniform strain within the heterogeneous material. This assumption was later followed by Reuss (1929) in a dual manner. Indeed, Reuss approximated the stress field within the material as uniform. They are called *kinematic and static constant field methods*, respectively, since they are based on a very strong assumption, that is the strain or stress, respectively, are constant over the entire REV. These two opposite hypotheses can be easily illustrated with a 1D example consisting in a beam with two materials in parallel or in series subjected to an imposed displacement or force, respectively (Figure 2.1).

*Voigt's and
Reuss' bounds*

This example assumes two extreme micro-structures, *i. e.* materials in series and in parallel. However, the real micro-structure is usually something in the middle. Therefore, these two approximations, when applied to multiphase composites in pure mechanical problems, yield two bounds for the elastic strain energy (Hill, 1952). The Voigt's assumption, as the upper bound, violates the equilibrium of the stress field.

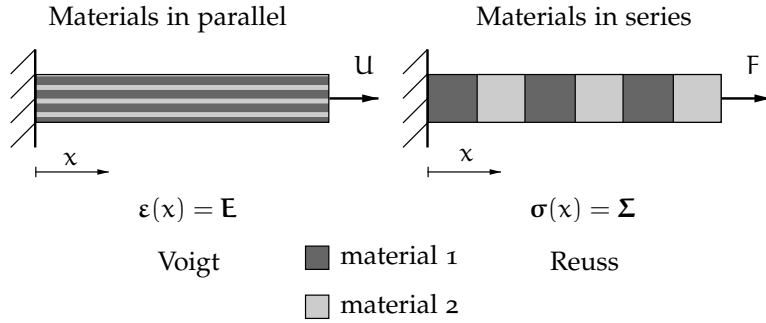


Figure 2.1: Voigt's and Reuss' bounds: 1D example

Also, the Reuss' assumption, as the lower bound, violates the compatibility of the strain field. The bounds are typically quite wide (Babuska, 1976) and are valid only for linear material properties.

*Taylor's and
Sachs' bounds*

The non-linear equivalents to Voigt's and Reuss' assumptions are usually referred to as Taylor's and Sachs' bounds (Sachs, 1928; Taylor, 1938), respectively, originally derived for polycrystals (Bishop and Hill, 1951). While universal and very simple, these bounds do not carry any information of the micro-structural morphology and take only the inhomogeneity volume fraction into account.

*Hashin's and
Shtrikman's
bounds*

Some decades later, Hashin and Shtrikman presented an extension of the method, based on variational formulations, to obtain bounds on bulk and shear moduli (Hashin and Shtrikman, 1963) for isotropic composites consisting of isotropic constituents. These bounds are expressed in terms of phase volume fractions and phase moduli but are independent of the phase geometry. Their proposed bounds were later generalized by Walpole (1966), Milton and Kohn (1988) for anisotropic media, and by Zimmerman (1992) to obtain bounds on the Poisson's ratio of the composites. Nevertheless, it is worth noting that Hashin-Shtrikman bounds and their improvements yield very wide bounds for the case of considerable mismatch in phase properties (Ostoja-Starzewski, 2007), *e.g.* porous materials.

The generalization of the Hashin-Shtrikman variational approach to predict tighter bounds compared to the Voigt's and Reuss' bounds was made in Bornert et al. (1996); Li and

Dunn (2001); Nemat-Nasser et al. (1993), mainly by taking into account the geometrical information of the phases, like inclusion shape, orientations and locations.

*Analytical
micro-
mechanical
models*

A more sophisticated approach consists in estimating the effective properties of heterogeneous media by making some assumption on the geometry of the micro-structure and obtaining the homogenised mechanical properties in a closed form. The first was established by Eshelby (1957) based on *dilute family methods* assuming that the inhomogeneities are so dilutely distributed that their interactions might be neglected. So, the problem is reformed into the analysis of a single inclusion embedded in an infinite matrix (Kanouté et al., 2009). The Eshelby scheme can be adopted to model porous media with porosity up to 10%. However, neglecting the interaction of particles is an unrealistic assumption of Eshelby for materials with randomly dispersed particulate micro-structure, even at a few percent volume fraction (Zohdi and Wriggers, 2001). Further proposed models such as Mori-Tanaka (Benveniste, 1987; Mori and Tanaka, 1973), the self-consistent scheme (Hill, 1965; Kröner, 1958; Willis, 2000), the generalized self-consistent scheme (Huang et al., 1994), and the differential method (McLaughlin, 1977; Norris, 1985) are mainly based on the mean-field approximation (Pierard et al., 2004) and approximate the interaction between the phases.

Mori and Tanaka in their most popular work published in 1973 (Mori and Tanaka, 1973) discussed a method of calculating the average internal stress in the matrix of a material containing inclusions with transformation strain. This achievement was an improvement of the Eshelby's problem (Eshelby, 1957), since the proposed scheme takes into account the mechanical interaction between inclusions. Later, Benveniste (Benveniste, 1987) reconsidered and reformulated the Mori-Tanaka's theory in its application to the computation of effective properties of composites. In particular, he analysed two-phase composites with anisotropic elastic constituents and an inclusion phase consisting of aligned or randomly oriented ellipsoidal particles. Before him, Berryman and other authors (Berryman, 1980; Kuster and Toksöz,

1974; Walpole, 1969; Walsh, 1969; Wu, 1966) found analytical solutions concerning randomly oriented ellipsoidal particles for any aspect ratio of the ellipsoid as well as for the special cases of spheres, needles, disks and penny shaped cracks. This scheme is expected to be relevant for a morphology of the porous medium's micro-structure, where the pores can be regarded as inclusions embedded in a solid matrix.

In contrast, the main idea of the self-consistent method is to replace the problem of the interaction among many particles by the problem of interaction of one particle, which is assumed to have spherical or ellipsoidal shape, and an infinite matrix: but now the unbounded domain is made of the effective medium. Unfortunately, the self-consistent method can produce negative effective bulk and shear responses, for voids, for volume fractions of 50% and higher.

To overcome this issue, the generalized self consistent methods encase the particle in a shell of matrix material, surrounded by the effective medium; despite this improvement, some problems have been detected and discussed in Hashin (1983). The difference between self-consistent schemes are sketched in Figure 2.2.

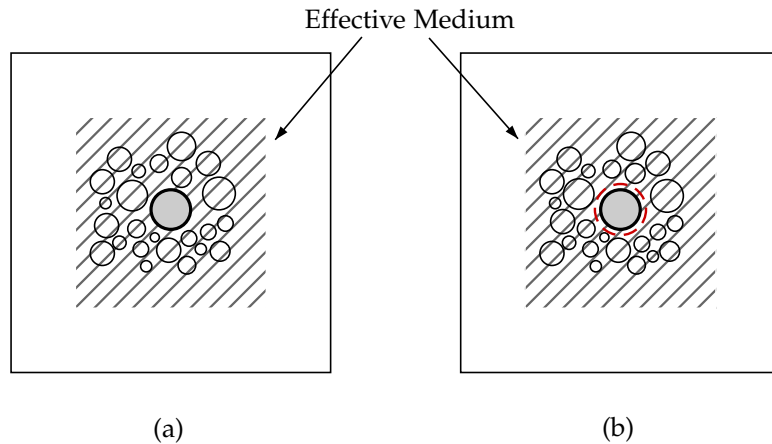


Figure 2.2: Self-consistent scheme: (a) first version, and (b) generalized version (Hashin, 1983).

On the other hand, the differential scheme has the advantage that it always distinguishes between the two phases

and, in contrast to the self-consistent scheme, no effective medium is defined. This is advantageous when the ratios of phase moduli are extreme as in the case of a porous medium (McLaughlin, 1977). The method is based on the idea that the heterogeneous material is constructed explicitly from an initial material through a series of incremental additions. The construction process is uniquely specified by parametrising the volume fractions of the included phases. The properties of the final material depend upon the construction path taken and not just on the final volume fractions. The result is a system of ordinary differential equations for the moduli, which is integrated along the path (Norris, 1985). Thus, the homogenised properties are computed in a iterative way as illustrated in Figure 2.3.

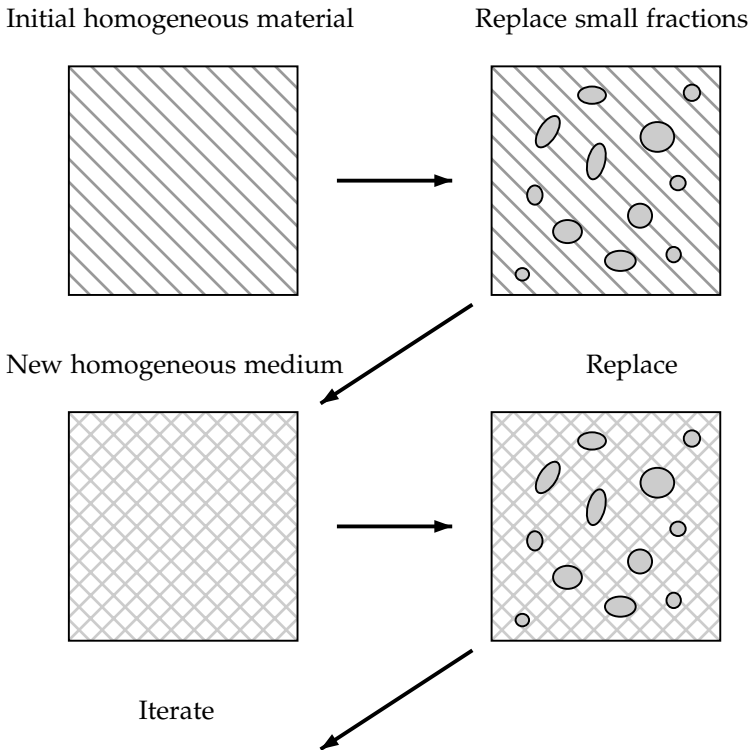


Figure 2.3: The iterative construction process of the differential scheme (Norris, 1985).

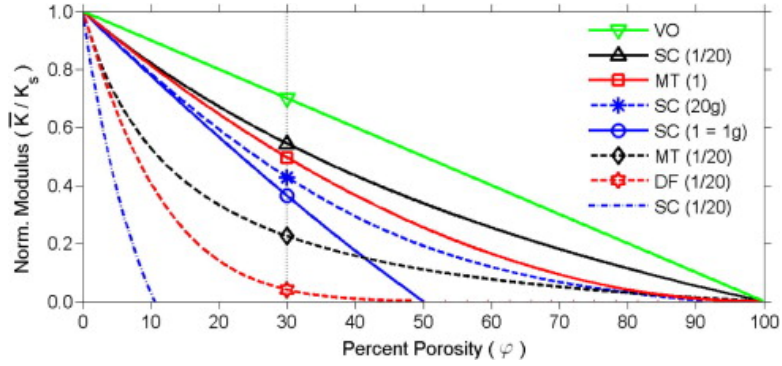


Figure 2.4: Comparison of effective bulk moduli of an idealized porous material as predicted by following micromechanical schemes: Mori-Tanaka (MT), self-consistent (SC), differential (DF), and Voigt (VO). The number in the legend indicates the aspect ratio a that is common to all randomly oriented spheroidal inclusions, while the letter 'g' next to a number indicates that the solid properties are assigned to the solid inclusions (rather than to the matrix), representing a material composed of grains or crystals. Modulus values are normalized with respect to the elastic properties of the microstructure, with the Poisson ratio of the microstructure assumed to be 0.25 (Vlahinić et al., 2011).

Finally, Hori and Nemat-Nasser (1993) proposed the double-inclusion model which is a unified generalization of the self-consistent and Mori-Tanaka schemes and takes the interaction between the phases into account more appropriately. The extension of the application of the analytical homogenization to non-linear composites and finite deformation elasticity was studied in the pioneering works of Hill (1972) and Ogden (1974). A detailed review and comparisons of analytical models of micro-mechanics can be found in Mura et al. (1996). On the other hand, Vlahinić et al. (2011) compares Mori-Tanaka (MT), self-consistent (SC), differential (DF), and Voigt (VO) schemes specialised for idealised porous media with different pore shapes, as reported in Figure 2.4.

2.2.2.2 Numerical Homogenisation: a literature overview

In the past two decades, substantial progress has been made in the numerical homogenization of complex multiphase materials. Detailed reviews on computational homogenisation can be found in Geers et al. (2010) and Nguyen et al. (2011). These approaches allow to take into account the microstructure geometry, even in detail, and use numerical methods to perform the homogenisation. One of the widely used approaches in modelling heterogeneous materials is the *unit-cell method* which leads to a global macroscopic constitutive model for a heterogeneous material based on detailed modelling of the micro-structure, which is usually assumed periodic. In the literature, the micro-scale sample is referred to as Representative Elementary Volume (REV) for geometrically irregular micro-structures and to Repeated unit cell (RUC) for periodic ones. The equivalence between the heterogeneous and homogeneous material is enforced by means of an energy equivalence between the two scales, known as Hill's lemma or Hill-Mandel condition (Hill, 1972; Mandel, 1972). The transition between the two scales is obtained via averaging the internal fields within the REV.

The three key points in computational homogenisation are:

- A. the choice of the boundary condition;
- B. the size and morphology of the REV;
- C. the analysis at the REV level.

CHOICE OF THE BOUNDARY CONDITION The more common options in the choice of boundary condition for the micromechanical boundary value problem are: (i) linear displacement boundary conditions, (ii) constant traction boundary conditions, and (iii) periodic displacement and anti-periodic traction boundary conditions. The first and the second ones are sometimes referred to as homogeneous boundary conditions (Hashin, 1983) or uniform boundary condition (Dormieux et al., 2006): these are defined based on the hypothesis of constant strain or stress on the boundary of

the REV, respectively. If the former boundary condition is enforced in the micromechanical boundary value problem, we speak of *kinematic homogenisation*; if the latter is adopted, the approach is named *static homogenisation*. Generally speaking, kinematic hypotheses yield a behaviour which is stiffer than the real one, whereas static hypotheses yield a behaviour which is more compliant than the real one.

On the other hand, the periodic boundary conditions involve a mix of kinematic and static hypotheses. The displacements of couples of points in the boundary are linked to each other, but their value is not specified. This leads to stresses which are equal and opposite in the same couple of points. Periodic boundary conditions simulate an infinite medium constituted of repetitions of the REV in all directions. In pure mechanical linear and non-linear problems, the effective behaviour derived under periodic boundary conditions is bounded by linear displacement boundary conditions from above and constant traction boundary conditions from below for a finite size of the REV (Kanit et al., 2003; Nemat-Nasser and Hori, 1995; Perić et al., 2011; Van Der Sluis et al., 2000). However, as remarked in Shen and Brinson (2006), periodic boundary conditions require the continuity of the inclusions on opposite boundaries to ensure the periodicity of the micro-structure. Since real heterogeneous materials – *e.g.* porous materials – are seldom periodic, they are not appropriate for finite element models developed by cutting out fragments of actual micro-structures. Moreover, Pecullan et al. (1999) demonstrated that linear displacement boundary conditions produce a stiffness tensor closer to the effective stiffness tensor for materials with stiff matrix and compliant inclusions, like porous materials. In contrast, constant traction boundary conditions yield better estimates for composites with compliant matrix and stiff inclusions.

For more details on the aspects of the numerical solution and computational cost associated with different types of boundary conditions the interested reader can refer to (Fritzen and Böhlke, 2010).

SIZE AND MORPHOLOGY OF THE REV The choice of the REV for heterogeneous materials with complex micro-structures is a delicate task. Ideally, one would like to reach the maximum accuracy with the least computational effort. The REV must be large enough to be statistically representative of the material so that it effectively includes a sampling of all micro-structural heterogeneities that occur in the material (Drugan and Willis, 1996). On the other hand, it must remain sufficiently small to be considered as a material point of continuum mechanics (Kanit et al., 2003).

The *first-order computational homogenization scheme* – e.g. periodic and kinematic homogenization – critically relies on the principle of separation of scales: this assumption is particularly valid when macro-gradients remain small and material failure does not occur. The *second-order computational homogenization* partly alleviates the assumption of scale separation by taking the gradient of the macro-deformation gradient tensor into account (Geers et al., 2007; Gitman et al., 2005; Kouznetsova et al., 2002, 2004; Nguyen et al., 2013).

Strictly speaking, the response of the material must be independent of the choice of boundary conditions imposed on the REV (Ostoja-Starzewski, 1998; Sab, 1992). According to Hill (1963), a REV is well defined when it contains a sufficient number of inclusions and the responses under linear displacement and constant traction boundary conditions coincide.

More details on the choice and morphology of a porous material REV will be given in Chapter 8.

ANALYSIS AT THE REV LEVEL To date, numerous schemes have been introduced to perform various analyses over the Representative Elementary Volume (REV). Renard and Marmonier (1987) first introduced the idea of using a finite element discretization at the microstructure. In the classic approach for linear elastic materials, the analysis at REV level is employed to assess elastic properties of homogenised continuum at the macro-scale. If non-linearities are present – non-linear constitutive behaviour, damage, etc... – it is possible to follow two distinct paths: (i) the building of a macro-

FE² method

scopic non-linear behaviour, making some hypotheses on kinetic at the micro-scale; (ii) the employing of a multilevel finite element approach.

Feyel (1999) introduced a multilevel finite element (FE^2) approach, in which the stress-strain relationship is evaluated at each point of the macro-scale through solving the boundary value problem associated with the micro-scale. These models are constructed using three main ingredients (Feyel, 2003): (i) a modeling of the mechanical behaviour at the micro-scale (the REV); (ii) a localization rule which determines the local solutions inside REV, for any given overall strain; (iii) a homogenization rule giving the macroscopic stress tensor, knowing the micromechanical stress state. Indeed, in the general method of FE^2 , the constitutive equations are written only on microscopic scale and homogenization and localisation equations are used to compute the macroscopic strains and stresses knowing the mechanical state at microscopic level. In particular, a spatially resolved REV discretised by finite elements corresponds to the macro-scale integration points of finite elements at the macro-scale, and separate finite element computations are performed simultaneously at the two scales. A schematic diagram of the FE^2 is illustrated in Figure 2.5

Although this method is known to be computationally expensive, it is trivially parallelisable as the computations at the micro-scale are completely independent of each other (Feyel, 1999; Mosby and Matouš, 2015; Unger, 2013; Šolinc and Korelc, 2015). Also, a number of methods have been recently developed aiming at reducing the computational cost and increasing the accuracy of multi-scale analysis (Abdulle and Bai, 2012; Otero et al., 2015; Somer et al., 2009; Terada et al., 2003; Yadegari et al., 2015).

FFT method

The other technique recently developed to perform analysis at the REV level, as an alternative of the Finite Element Method, is fast Fourier transform (FFT) proposed originally by Moulinec and Suquet (1998). The initial idea of the method was to make direct use of the digital images of the real micro-structure in the numerical simulation which

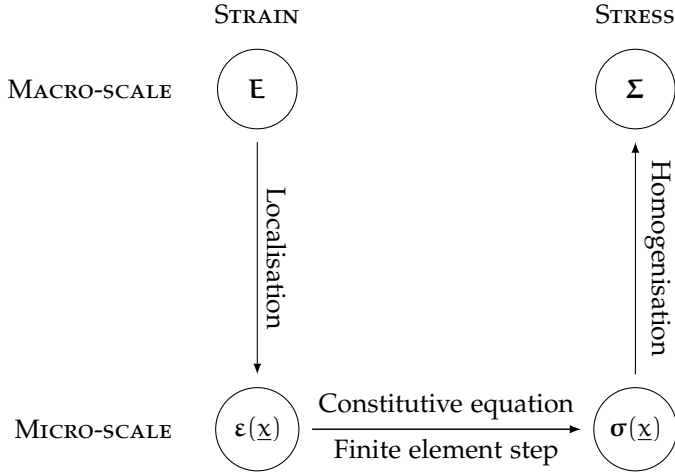


Figure 2.5: Schematic diagram of the FE² model (Feyel, 1999, 2003; Feyel and Chaboche, 2000).

reduces the effort to generate compatible micro-structural finite element discretisations (Moulinec and Suquet, 1998). Michel et al. (1999) compared and reviewed the analysis of REV using the finite element method and FFT. They concluded that the FFT method is computationally superior for linear composites given that the contrast between the phases is not too large. However, the basic model of FFT fails to produce reasonable results in the presence of voids – *e.g.* porous media – or rigid heterogeneities as its rate of the convergence is proportional to the contrast between the phases. Recently, Monchiet and Bonnet (2012) proposed a polarization-based FFT iterative scheme to determine the overall properties of multiphase composites with arbitrary phase contrast, see also Brisard and Dormieux (2010); Michel et al. (2000); Willot et al. (2014).

2.2.3 Microporomechanics basics

The goal of this Section is to give some basic elements of the linear micromechanics of porous media, in short linear microporomechanics. This technique will be used in the sec-

ond part of this dissertation, so these concepts are preparatory. In microporomechanics, the porous medium can be treated as a particulate composite (Hashin, 1983) having inclusions with zero stiffness. More specifically, Hashin defines a *particulate composite* when one phase is in the form of particles embedded in the second matrix phase. Indeed, the pore space can be considered as an elastic material with null stiffness values (Dormieux et al., 2006).

In particular, according to Hashin (1983), it is necessary

- A. to define a Representative Elementary Volume (REV), ensuring the scale separation;
- B. that the Statistical Homogeneity (SH) holds, *i. e.* all global geometrical characteristics such as volume fractions, two-point correlations, etc. are the same in any REV, irrespective of its position. In particular, this implies that body averages and REV averages are the same.

2.2.3.1 Geometrical and micromechanical modelling

Referring to a porous medium depicted in Figure 2.6, if L , ℓ and d are the characteristic lengths of the structure, elementary volume and local heterogeneities, respectively, the conditions that allow defining the Representative Elementary Volume (REV) are:

$$d \ll \ell \ll L; \quad (2.1)$$

The macro-scale is defined as the one in which the porous material can be seen as a homogeneous continuum, while the micro-scale is designated as the one in which can be distinguished the material matrix and the pores. In particular, \underline{X} is the position vector associated to the macroscopic reference system, while \underline{x} is the one identifying the microscopic reference system. Analogously, $\sigma(\underline{X}, \underline{x})$ and $\varepsilon(\underline{X}, \underline{x})$ are the micro-scale stress and strain, respectively, while $\Sigma(\underline{X})$ and $\mathbf{E}(\underline{X})$ are the macroscopic ones.

Referring to the porous medium sketched in Figure 2.7, if we denote by $\mathbf{C}(\underline{x})$ the microscopic linear elasticity tensor at

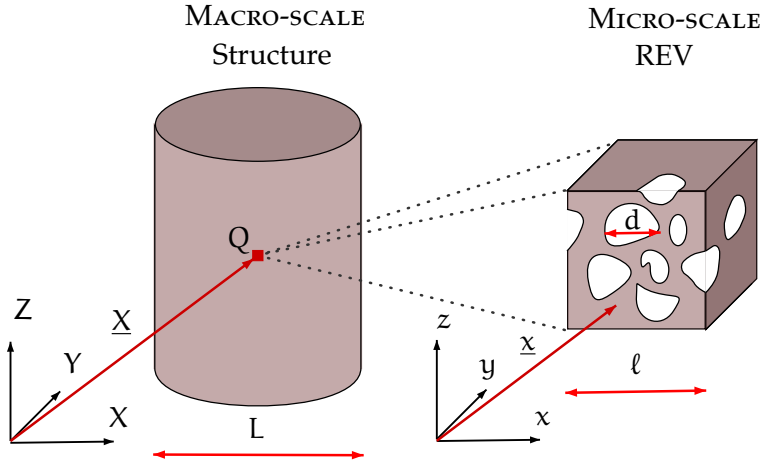


Figure 2.6: Reference systems and characteristic lengths for the macro- and micro- scales.

the micro-scale point \underline{x} , and by $\mathbb{S}(\underline{x}) = \mathbb{C}(\underline{x})^{-1}$ the compliance tensor, we can write:

$$\underline{x} \in \Omega_p \quad \mathbb{C}(\underline{x}) = \mathbb{C}_p = 0 \quad \mathbb{S}(\underline{x}) = \mathbb{S}_p \rightarrow \infty \quad (2.2a)$$

$$\underline{x} \in \Omega_m \quad \mathbb{C}(\underline{x}) = \mathbb{C}_m^{-1} \quad \mathbb{S}(\underline{x}) = \mathbb{S}_m = (\mathbb{C}_m)^{-1} \quad (2.2b)$$

where

$$|\Omega_p| = |\Omega| \phi_0, \quad |\Omega_m| = |\Omega| (1 - \phi_0), \quad (2.3)$$

$\Omega = \Omega_p \cup \Omega_m$ is the considered microscopic REV domain and ϕ_0 is porosity (volume of voids per unit volume of porous medium), *i. e.* the volume fraction of the pore space.

2.2.3.2 Micromechanical boundary value problem formulation

The micromechanical boundary value problem formulation can be stated for the porous media as:

$$\nabla \cdot \boldsymbol{\sigma} = 0^2 \quad \text{in } \Omega, \quad (2.4a)$$

$$\boldsymbol{\sigma} = \mathbb{C}(\underline{x}) : \boldsymbol{\varepsilon} \Leftrightarrow \boldsymbol{\varepsilon} = \mathbb{S}(\underline{x}) : \boldsymbol{\sigma} \quad \text{in } \Omega, \quad (2.4b)$$

$$\boldsymbol{\varepsilon} = \text{sym}(\nabla \underline{\mathbf{u}}) \quad \text{in } \Omega, \quad (2.4c)$$

¹ \mathbb{C}_m is a positive definite fourth-order tensor

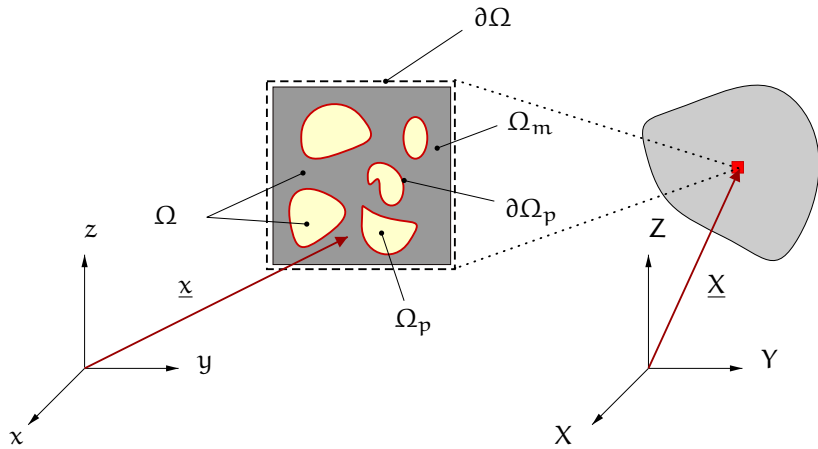


Figure 2.7: Porous media: multi-scale mechanical model.

where $\boldsymbol{\sigma}(\underline{x})$ and $\boldsymbol{\varepsilon}(\underline{x})$, are the micro-scale stress and strain, respectively, and $\underline{\mathbf{u}}(\underline{x})$ is the displacement at the micro-scale. It is worth noting that the micromechanical problem formulation (2.4) is an ill-posed problem: it has no unique solution, without additional constraints, like the boundary conditions.

As seen in Section 2.2.2.2, there are different options in the choice of boundary conditions. To ensure a statistical homogeneous field in composite material some special boundary conditions are required. These are called Uniform Boundary Conditions and produce homogeneous field in a homogeneous body. Indeed, the fundamental postulate of the theory of elastic heterogeneous media by Hashin (Hashin, 1983) states:

Fundamental Postulate (of elastic heterogeneous media). *The stress and strain fields in a large Statistical Homogeneity heterogeneous body subjected to uniform boundary conditions are statistical homogeneous, except in a boundary layer near the external surface.*

² It is possible to demonstrate that the mechanical effects of the micromechanical body forces can be neglected at the scale of REV, with regard to the effects of the heterogeneity (Dormieux et al., 2006).

For elastic bodies, Uniform Boundary Conditions are either one of:

$$\underline{\sigma}(\underline{x}) \cdot \underline{n}(\underline{x}) = \underline{\Sigma}_0 \cdot \underline{n}(\underline{x}) \quad \text{on } \partial\Omega, \quad (2.5a)$$

$$\underline{u}(\underline{x}) = \underline{E}_0 \cdot \underline{x} \quad \text{on } \partial\Omega. \quad (2.5b)$$

where $\underline{\Sigma}_0$ and \underline{E}_0 are constant second order tensors, which characterise the stress or the strain on the REV boundary, respectively.

Equation (2.5a) is the so-called uniform stress boundary condition or constant traction boundary condition. The micromechanical boundary value problem (2.4) can be restated in the form of a standard problem of linear elasticity imposing Eq. (2.5a). The resulting micromechanical boundary value problem is typical of *static homogenisation*. The solving of this system yields the response of the REV subjected to the stress state $\underline{\Sigma}_0$ at its boundary. However, it is worth noting that in the case of the static approach it is necessary to restrain the rigid body motions. Instead of the uniform stress boundary condition (2.5a), it is possible to apply the uniform strain boundary condition also called linear displacement boundary condition (2.5b). The resulting micromechanical boundary value problem is typical of *kinematic homogenisation*. It is worth noting that \underline{E}_0 has replaced $\underline{\Sigma}_0$ as the loading parameter, in comparison to (2.5a).

*Uniform stress
boundary
condition*

*Uniform
strain
boundary
condition*

Another option is to enforce periodic boundary conditions:

$$\underline{u}(\underline{x}_1) = \underline{u}(\underline{x}_2) \quad \forall (\underline{x}_1, \underline{x}_2) \text{ on } \partial\Omega \text{ in periodic position.} \quad (2.6)$$

However, they can be successfully applied only on periodic micro-structures, so they are not suitable for the investigation of real porous media. Moreover, if the REV size is sufficiently big with respect of the characteristic length of the heterogeneity, there is a small difference between the kinematic and periodic approaches, since the resulting microscopic fields are diverse only on the boundary.

2.2.3.3 Energetic equivalence: the Hill's lemma

The equivalence between the heterogeneous and equivalent homogeneous material is established in terms of energy:

$$\langle \boldsymbol{\sigma}(\underline{X}, \underline{x}) : \boldsymbol{\varepsilon}(\underline{X}, \underline{x}) \rangle = \boldsymbol{\Sigma}(\underline{X}) : \mathbf{E}(\underline{X}), \quad (2.7)$$

where $\langle \bullet \rangle$ is the average operator on the REV domain Ω , defined as follows:

$$\langle \bullet \rangle = \frac{1}{|\Omega|} \int_{\Omega} \bullet \, dV_x; \quad (2.8)$$

and $\boldsymbol{\Sigma}(\underline{X})$ and $\mathbf{E}(\underline{X})$ are the macroscopic stress and strain respectively. This energy equivalence is named the Hill's lemma (Hill, 1967): it imposes the same energy density at the two scales. This equivalence needs to be fulfilled by the homogenized material. Moreover, by imposing its satisfaction, it is possible to derive (i) the expression of the macroscopic stresses and strains as functions of the corresponding microscopic quantities and (ii) the homogenised behaviour.

STATIC HOMOGENISATION When a uniform stress state $\boldsymbol{\Sigma}_0$ is imposed along the REV boundary, it is possible to prove that the microscopic stress field $\boldsymbol{\sigma}(\underline{X}, \underline{x})$ satisfies the following relation:

$$\langle \boldsymbol{\sigma}(\underline{X}, \underline{x}) \rangle = \boldsymbol{\Sigma}_0, \quad (2.9)$$

where $\langle \boldsymbol{\sigma} \rangle$ is the average microscopic stress field on the REV. The macroscopic stress $\boldsymbol{\Sigma}(\underline{X})$ is thus naturally identified as $\boldsymbol{\Sigma}_0$. The verification of the Hill's lemma leads to the following definition of the macroscopic strain: $\mathbf{E}(\underline{X}) = \langle \boldsymbol{\varepsilon}(\underline{X}, \underline{x}) \rangle$.

KINEMATIC HOMOGENISATION When a uniform strain state \mathbf{E}_0 is imposed along the REV boundary, it is possible to demonstrate that the microscopic strain field $\boldsymbol{\varepsilon}(\underline{X}, \underline{x})$ satisfies the following relation:

$$\langle \boldsymbol{\varepsilon}(\underline{X}, \underline{x}) \rangle = \mathbf{E}_0, \quad (2.11)$$

where $\langle \boldsymbol{\varepsilon} \rangle$ is the average microscopic strain field on the REV. The macroscopic strain $\mathbf{E}(\underline{X})$ is thus naturally identified as

\mathbf{E}_0 . The verification of the energy equivalence expressed in Eq. (2.7) leads to the following definition of the macroscopic stress:

$$\boldsymbol{\Sigma}(\underline{\mathbf{X}}) = \langle \boldsymbol{\sigma}(\underline{\mathbf{X}}, \underline{\mathbf{x}}) \rangle. \quad (2.12)$$

2.2.3.4 The homogenised stiffness tensor

In this section derive the macroscopic constitutive law for a dried porous material, defining the homogenised stiffness tensor \mathbf{C}^{hom} starting from the micromechanical boundary value problem (2.4), (2.5b).

Let us consider the definition of the micromechanical problem (2.4), (2.5b). Since it is linear, the relation between microscopic $\boldsymbol{\varepsilon}(\underline{\mathbf{x}})$ and macroscopic \mathbf{E} is linear, too. In particular, this link is captured by a fourth-order strain localisation tensor $\mathbb{A}(\underline{\mathbf{x}})$:

$$\boldsymbol{\varepsilon}(\underline{\mathbf{x}}) = \mathbb{A}(\underline{\mathbf{x}}) : \mathbf{E} \quad (2.13)$$

*Localization
step*

The components of $\mathbb{A}(\underline{\mathbf{x}})$ satisfy the symmetry relations $A_{ijkl}(\underline{\mathbf{x}}) = A_{jikl}(\underline{\mathbf{x}}) = A_{ijlk}(\underline{\mathbf{x}})$, since tensors $\boldsymbol{\varepsilon}(\underline{\mathbf{x}})$ and \mathbf{E} are symmetric. The averaging of the strain field in Eq. (2.13) leads to:

$$\mathbf{E} = \langle \boldsymbol{\varepsilon} \rangle = \langle \mathbb{A} : \mathbf{E} \rangle = \langle \mathbb{A} \rangle : \mathbf{E} \quad \Leftrightarrow \quad \langle \mathbb{A} \rangle = \mathbb{I}, \quad (2.14)$$

where \mathbb{I} is the fourth-order identity tensor. Following a different path, we get:

$$\begin{aligned} \mathbf{E} = \langle \boldsymbol{\varepsilon} \rangle &= \frac{1}{|\Omega|} \int_{\Omega} \boldsymbol{\varepsilon}(\underline{\mathbf{x}}) \, dV \\ &= \frac{(1 - \phi_0)}{|\Omega_m|} \int_{\Omega_m} \mathbb{A}(\underline{\mathbf{x}}) : \mathbf{E} \, dV_m + \\ &+ \frac{\phi_0}{|\Omega_p|} \int_{\Omega_p} \mathbb{A}(\underline{\mathbf{x}}) : \mathbf{E} \, dV_p \\ &= [(1 - \phi_0) \langle \mathbb{A} \rangle_m + \phi_0 \langle \mathbb{A} \rangle_p] : \mathbf{E}. \end{aligned} \quad (2.15)$$

This expression is convenient to work with a composite and separate the contributions of the matrix and the ones of the inclusions. It follows that:

$$(1 - \phi_0) \langle \mathbb{A} \rangle_m + \phi_0 \langle \mathbb{A} \rangle_p = \mathbb{I}, \quad (2.16)$$

where:

$$\begin{aligned}\langle \bullet \rangle_m &= \frac{1}{|\Omega_m|} \int_{\Omega_m} \bullet \, dV_x, \\ \langle \bullet \rangle_p &= \frac{1}{|\Omega_p|} \int_{\Omega_p} \bullet \, dV_x.\end{aligned}\tag{2.17}$$

Combining the constitutive equation (2.4b) with the strain concentration rule (2.13) yields:

$$\boldsymbol{\sigma}(\underline{x}) = \mathbf{C}(\underline{x}) : \mathbf{A}(\underline{x}) : \mathbf{E}.\tag{2.18}$$

*Macroscopic
constitutive
law*

Finally, we adopt an upscaling procedure based on the stress average rule (2.12) to translate the microscopic stress field into a macroscopic stress state. Relation (2.12) can be expanded as follows:

$$\begin{aligned}\boldsymbol{\Sigma} &= \frac{1}{|\Omega|} \int_{\Omega} \boldsymbol{\sigma}(\underline{x}) \, dV \\ &= \frac{(1 - \phi_0)}{|\Omega_m|} \int_{\Omega_m} \boldsymbol{\sigma}(\underline{x}) \, dV_m + \frac{\phi_0}{|\Omega_p|} \int_{\Omega_p} \boldsymbol{\sigma}(\underline{x}) \, dV_p.\end{aligned}\tag{2.19}$$

Substituting (2.18) in (2.19) leads to the macroscopic constitutive law:

$$\boldsymbol{\Sigma} = \mathbf{C}^{\text{hom}} : \mathbf{E},\tag{2.20}$$

where the homogenised stiffness tensor \mathbf{C}^{hom} reads:

$$\mathbf{C}^{\text{hom}} = (1 - \phi_0) \mathbf{C}_m : \langle \mathbf{A} \rangle_m + \phi_0 \mathbf{C}_p : \langle \mathbf{A} \rangle_p.^3\tag{2.21}$$

Taking into account the definition of mechanical properties of a porous medium (2.2), the expression of \mathbf{C}^{hom} can be simplified as follows:

$$\mathbf{C}^{\text{hom}} = (1 - \phi_0) \mathbf{C}_m : \langle \mathbf{A} \rangle_m = \mathbf{C}_m : (\mathbf{I} - \phi_0 \langle \mathbf{A} \rangle_p),\tag{2.22}$$

exploiting the identity (2.16).

A graph resuming the quantities involved in homogenisation approaches and their relations is reported in Figure 2.8.

³ This relation is valid for any composite material with inclusions

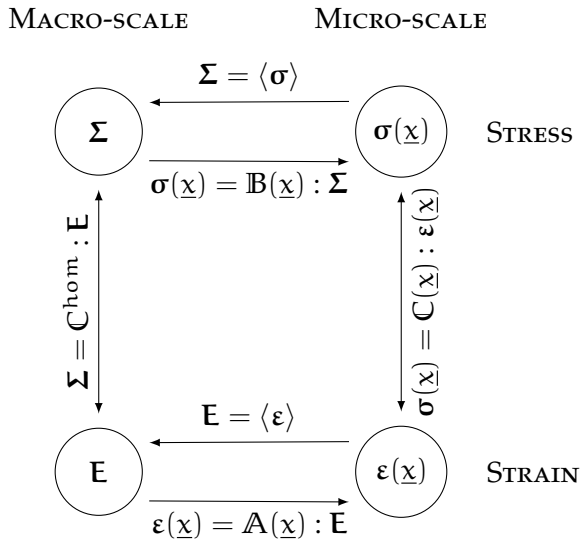


Figure 2.8: Relation between micro and macro-scale quantities in kinematic homogenization: $\mathbb{A}(\underline{x}) = A_{ijkl}(\underline{x})$ and $\mathbb{B}(\underline{x}) = B_{ijkl}(\underline{x})$ are respectively the strain and the stress localization tensors, $\mathbb{C}(\underline{x}) = C_{ijkl}(\underline{x})$ is the local elasticity tensor.

ENERGY POINT OF VIEW The same problem can be examined with an energy approach. This is based on the average theorem of virtual work, which when specialized to heterogeneous elastic bodies with Uniform Boundary Conditions (2.5a), gives the elastic strain energy supplied to the REV W^E :

$$W^E = \frac{1}{2} \mathbf{E} : \mathbf{C}^{\text{hom}} : \mathbf{E} |\Omega|, \quad (2.23)$$

where

$$\mathbf{C}^{\text{hom}} = \langle \mathbf{A}^t : \mathbf{C} : \mathbf{A} \rangle, \quad (2.24)$$

showing that \mathbf{C}^{hom} is a symmetric tensor. This approach allows to establish the bounds for the homogenised stiffness tensor. In particular, it is possible to demonstrate that:

$$(\forall \mathbf{E}) \quad \mathbf{E} : \mathbf{C}^{\text{hom}} : \mathbf{E} \geq 0, \quad (2.25a)$$

$$(\forall \mathbf{E}) \quad \mathbf{E} : (\mathbf{C}^{\text{hom}} - \langle \mathbf{C} \rangle) : \mathbf{E} \leq 0. \quad (2.25b)$$

They can be formally summarized by:

$$\mathbf{C}^{\text{hom}} \geq 0, \quad (2.26a)$$

$$\mathbf{C}^{\text{hom}} \leq \langle \mathbf{C} \rangle = (1 - \phi_0) \mathbf{C}_m. \quad (2.26b)$$

The inequality ⁴ (2.26b) is a writing of the Voigt bound. It is associated with the uniform strain boundary condition (2.5b).

*Isotropic
macroscopic
behaviour*

In the case of isotropic macroscopic behaviour \mathbf{C}^{hom} can be expressed as a function of the homogenised shear and bulk moduli μ^{hom} and κ^{hom} :

$$\mathbf{C}^{\text{hom}} = 3\kappa^{\text{hom}} \mathbb{J} + 2\mu^{\text{hom}} \mathbb{K}, \quad (2.27)$$

where the fourth-order tensors \mathbb{J} and \mathbb{K} are defined as:

$$\mathbb{J} = \frac{1}{3} \mathbf{I} \otimes \mathbf{I}, \quad \mathbb{K} = \mathbb{I} - \mathbb{J}, \quad (2.28)$$

representing the spherical and deviator tensors, respectively. From inequalities (2.26), it is readily seen that bounds of elastic constants μ^{hom} and κ^{hom} are:

$$0 \leq \kappa^{\text{hom}} \leq (1 - \phi_0) \kappa_m, \quad (2.29a)$$

$$0 \leq \mu^{\text{hom}} \leq (1 - \phi_0) \mu_m. \quad (2.29b)$$

⁴ In the sense of quadratic forms in the space of second-order symmetric tensors.

In this section we have derived the macroscopic constitutive law for a dried porous material, defining the homogenised stiffness tensor \mathbb{C}^{hom} starting from the micromechanical boundary value problem (2.4). Different expressions of \mathbb{C}^{hom} are examined, finding that it depends on:

1. the mechanical properties of the material matrix (\mathbb{C}_m);
2. the porosity ϕ_0 , *i. e.* the volume fraction of voids;
3. the geometry of the microstructure or pore space, which is included in the definition of the average of the localisation tensor \mathbb{A} .

In addition, the bounds of the homogenised stiffness tensor are given and specified for the isotropic macroscopic behaviour.

2.2.3.5 *The principle of effective stress*

For porous media, whose pore space is saturated with a pressured fluid phase, it is possible to retrieve the principle of effective stress using a micro-mechanical approach. In particular, given the constitutive behaviour of the porous material matrix, we are interested in evaluating the mechanical effect of the pore pressure. Assuming that the microscopic and macroscopic pressure gradients are of the same order of magnitude, the mechanical interaction between the fluid and the solid at the microscopic level can be taken into account through a uniform pressure P that is equal to the macroscopic one, which is applied at the solid-fluid interface. Thus, the macroscopic pressure P plays the role of an additional loading parameter acting on the REV.

Let us consider that the pressure P , which is also the constant pressure in the fluid, is acting along the whole solid-pore interface. The loading applied to the matrix of the porous medium Ω_m is defined by the pressure P and tensors \mathbb{E} or $\mathbb{\Sigma}$ representing respectively the strain and stress state of the REV at macroscopic scale. From this point on, we choose to work with kinematic homogenisation, but of course it is possible the writing of this problem in terms of

*Boundary
value problem
formulation*

static homogenisation. The most general form of the boundary value problem, written on the solid phase only, can be stated as:

$$\nabla \cdot \boldsymbol{\sigma} = 0 \quad \text{in } \Omega_m, \quad (2.30a)$$

$$\boldsymbol{\sigma} = \mathbf{C}_m : \boldsymbol{\varepsilon} \quad \text{in } \Omega, \quad (2.30b)$$

$$\boldsymbol{\varepsilon} = \text{sym}(\nabla \underline{\mathbf{u}}) \quad \text{in } \Omega_m, \quad (2.30c)$$

$$\underline{\mathbf{u}}(\underline{\mathbf{x}}) = \mathbf{E} \cdot \underline{\mathbf{x}} \quad \text{on } \partial\Omega, \quad (2.30d)$$

$$\underline{\mathbf{T}} = -P \underline{\mathbf{n}}(\underline{\mathbf{x}}) \quad \text{on } \partial\Omega_p, \quad (2.30e)$$

*The
homogenised
state equation*

From (2.30) follows that the strain and stress fields $\boldsymbol{\varepsilon}(\underline{\mathbf{x}})$ and $\boldsymbol{\sigma}(\underline{\mathbf{x}})$ are linear functions of the loading parameters. The strain field can be written as:

$$\boldsymbol{\varepsilon}(\underline{\mathbf{x}}) = \mathbb{A} : \mathbf{E} - \mathbf{A}'(\underline{\mathbf{x}})P \quad (2.31)$$

where the fourth-order tensor \mathbb{A} takes into account the local strain induced by the macroscopic strain \mathbf{E} while the second-order tensor \mathbf{A}' takes into account the local strain induced by the pressure P . Substituting (2.31) in (2.30b) yields the expression of the microscopic stress field $\boldsymbol{\sigma}(\underline{\mathbf{x}})$:

$$\boldsymbol{\sigma}(\underline{\mathbf{x}}) = \mathbf{C}_m : \mathbb{A} : \mathbf{E} - \mathbf{C}_m : \mathbf{A}'(\underline{\mathbf{x}})P \quad (2.32)$$

The macroscopic stress tensor $\boldsymbol{\Sigma}$ is derived from the microscopic stress field using the average rule (7.6):

$$\begin{aligned} \boldsymbol{\Sigma} &= \frac{1}{|\Omega|} \int_{\Omega} \boldsymbol{\sigma}(\underline{\mathbf{x}}) dV = \frac{(1 - \phi_0)}{|\Omega_m|} \int_{\Omega_m} \boldsymbol{\sigma}(\underline{\mathbf{x}}) dV_m + \\ &+ \frac{\phi_0}{|\Omega_p|} \int_{\Omega_p} -P \mathbf{I} dV_p = \\ &= (1 - \phi_0) \mathbf{C}_m : \langle \mathbb{A} \rangle_m : \mathbf{E} - [(1 - \phi_0) \mathbf{C}_m : \langle \mathbf{A}' \rangle_m + \phi_0 \mathbf{I}] P. \end{aligned} \quad (2.33)$$

Remembering the definition of \mathbf{C}^{hom} reported in Eq. (2.22) and defining the Biot second order tensor \mathbf{B} as:

$$\mathbf{B} = (1 - \phi_0) \mathbf{C}_m : \langle \mathbf{A}' \rangle_m + \phi_0 \mathbf{I}, \quad (2.34)$$

yields the principle of effective stress:

$$\boldsymbol{\Sigma} = \mathbf{C}^{\text{hom}} : \mathbf{E} - \mathbf{B}P, \quad (2.35)$$

which can be seen also as a macroscopic constitutive behaviour of saturated porous media. This equation represents the principle of effective stress, according to the Biot's theory (Biot, 1941, 1962), stated for the first time by Terzaghi (1923), long before the microporomechanics was conceived. In particular, we found that the term $\mathbf{B}\mathbf{P}$ is a measure of the mechanical effects induced by a pressurised phase inside the saturated porous medium.

2.2.3.6 The Biot Tensor

The Biot tensor can be written in a different way applying the Betti theorem (Dormieux et al., 2006):

$$\mathbf{B} = \mathbf{I} - (1 - \phi_0)\mathbf{I} : \langle \mathbf{A} \rangle_{\mathbf{m}} . \quad (2.36)$$

Moreover, remembering (2.16) it reduces to:

$$\mathbf{B} = \phi_0 \mathbf{I} : \langle \mathbf{A} \rangle_{\mathbf{p}} . \quad (2.37)$$

Equating (2.34) and (2.36) we get the link between $\langle \mathbf{A}' \rangle_{\mathbf{m}}$ and $\langle \mathbf{A} \rangle_{\mathbf{m}}$:

$$\mathbf{C}_{\mathbf{m}} : \langle \mathbf{A}' \rangle_{\mathbf{m}} = \mathbf{I} - \mathbf{I} : \langle \mathbf{A} \rangle_{\mathbf{m}} \quad (2.38)$$

THE ISOTROPIC CASE. Let us consider that the solid behaviour is isotropic and defined by the elasticity tensor:

$$\mathbf{C}_{\mathbf{m}} = 3\kappa_{\mathbf{m}}\mathbb{J} + 2\mu_{\mathbf{m}}\mathbb{K} \quad (2.39)$$

where $\kappa_{\mathbf{m}}$ and $\mu_{\mathbf{m}}$ are respectively the bulk and shear modulus of the solid phase and \mathbb{J} , \mathbb{K} the fourth-order tensors defined by (2.28). Let us further consider, a porous medium composed of an anisotropic solid phase which is randomly distributed at the microscopic scale. Since it entails a macroscopic isotropic behaviour, the average strain concentration tensor $\langle \mathbf{A} \rangle_{\mathbf{m}}$ can be divided into a spherical and a deviatoric part:

$$\langle \mathbf{A} \rangle_{\mathbf{m}} = (\mathbf{A}_{\mathbf{m}})^{\mathbf{v}}\mathbb{J} + (\mathbf{A}_{\mathbf{m}})^{\mathbf{d}}\mathbb{K} . \quad (2.40)$$

Substituting (2.39) and (2.40) in (2.22) yields:

$$\kappa^{\text{hom}} = (1 - \phi_0)\kappa_{\mathbf{m}} (\mathbf{A}_{\mathbf{m}})^{\mathbf{v}} , \quad (2.41a)$$

$$\mu^{\text{hom}} = (1 - \phi_0)\mu_{\mathbf{m}} (\mathbf{A}_{\mathbf{m}})^{\mathbf{d}} . \quad (2.41b)$$

It is worth noting that $(A_m)^v$ and $(A_m)^d$ capture the discrepancy between homogenised bulk κ^{hom} and shear moduli μ^{hom} with respect to the Voigt bounds (2.29). Under these hypotheses and remembering (2.41a), the Biot tensor can be written as:

$$\mathbf{B} = b\mathbf{I}, \quad b = 1 - (1 - \phi_0) (A_m)^v = 1 - \frac{\kappa^{\text{hom}}}{\kappa_m}. \quad (2.42)$$

where b is called Biot's coefficient. Moreover, applying (2.29) obtained in the isotropic case leads to the derivation of upper and lower bounds for the Biot's coefficient b :

$$\phi_0 \leq b = 1 - \frac{\kappa^{\text{hom}}}{\kappa_m} \leq 1, \quad (2.43)$$

where the Voigt bound constitutes the lower bound of the inequality (2.43). From the Voigt bound also follows that $0 \leq (A_m)^v \leq 1$.

In this Section we have found some interesting relations regarding the Biot's tensor; different writings are examined and it is found that it depends on:

1. the porosity of the porous medium ϕ_0 , *i.e.* the volume fraction of voids;
2. the geometry of the microstructure or pore space, which is included in the definition of the average of the localisation tensor \mathbb{A} .

This proves that mechanical effects due to a pressurised phase saturating the porous medium depend on the porosity and the geometry of the pore space. In addition, the Biot's tensor is derived for the isotropic macroscopic behaviour, defining the Biot's coefficient. Finally, we derive the bounds for the Biot's coefficient.

2.2.4 Needs for further research

Contributions on the modelling of the mechanical effects induced by salt crystallisation in multiphase porous media either at macro scale or at the microscopic one can be found

in the literature. Nevertheless, mechanical effects are not investigated from a rigorous micro-mechanical point of view. Moreover, there is no application to real porous media, because, until now, there were few experimental tools capable of capturing the real three-dimensional micro-structure of the porous material and simulation computational costs were prohibitive.

Indeed, a rigorous mechanical approach to the analysis of porous media imposes to apply multi-scale techniques (Coussy, 2004; Dormieux et al., 2006), in order to properly account for the effects of the micro-structure in a macro-scale computation.

However, the approaches proposed in the frame of linear microporomechanics, are generally based on simplified pore geometries and analytical schemes (Coussy, 2006; Flatt et al., 2014; Vlahinić et al., 2011), like for example the Mori-Tanaka's (Mori and Tanaka, 1973) one, which require strong assumptions on the pore shape.

We have seen that the Biot's tensor is used to describe at the macro-scale the mechanical effect induced by the presence of a pressure acting on pore walls for saturated porous media. For porous media saturated with different phases, a partial Biot's tensor can be defined, which can be generally written as a function of the degree of saturation of the considered phase. On this regards, the challenge is to translate the crystallisation's physics in a mechanical interaction between the phases

filling the pores and the material matrix, at the scale of the material micro-structure.

Advanced experimental techniques, like X-ray μ CT, combined with numerical methods and open new scenarios on the possibility to simulate the local stress in the material micro-structures and to upscale it at the scale of the structure, allowing to refine relations linking the mechanical effect induced by salt crystallisation with the degree of saturation of the considered phase.

Part I

HYGRO-THERMO-CHEMICAL ASPECTS

A new fully coupled multiphase model for hygro-thermal analysis and prediction of salt diffusion and crystallisation in porous building materials – called briefly HTC model – is presented. A suitable modelling of the crystallisation/dissolution and hydration/dehydration processes allows considering salts with hydrous and anhydrous crystals. The model is specialised for sodium sulphate solutions and for sodium chloride solutions. The predictive capabilities of the model are validated on some experiments available in the literature, involving fired-clay bricks and sodium sulphate solutions. As regards sodium chloride solutions, the role of temperature in modelling and simulation of the whole phenomenon is investigated. Moreover, the salt diffusion and crystallisation process in a masonry column exposed to weather conditions is simulated both in isothermal and non-isothermal regime. Finally, the model is extended to describe the drying kinetics leading to different efflorescence formations. The extended version of the model is then validated through two different extensive campaigns on drying in presence of sodium chloride salt solution.

THE HYGRO THERMAL CHEMICAL MODEL

A new Hygro-Thermo-Chemical (HTC) model is presented. It consists in a fully coupled multiphase model for hygro-thermal analysis and prediction of salt diffusion and crystallisation in porous building materials.

The equivalent relative humidity, the temperature, the concentration of the dissolved salt and the concentration of precipitated salts are assumed as independent variables. The governing equations are: moisture mass conservation, salt mass conservation, energy balance and evolution equations describing salt crystallisation/dissolution and salt hydration/dehydration kinetics. The equations are highly non-linear and fully coupled.

A suitable modelling of the crystallisation/dissolution and hydration/dehydration processes allows considering salts with multiple crystallised forms involving hydrous and anhydrous crystals.

3.1 INTRODUCTION

We will develop a new fully coupled multiphase numerical model to describe the macroscopic behaviour of porous building materials contaminated with salts and subjected to environmental loadings. Its formulation derives from the model proposed in Castellazzi et al. (2013a).

We employ the concept of a Representative Elementary Volume (REV), in which each point of the total volume of the porous medium is considered to be the centre of a REV. The position of the centre of the REV in a global coordinate system is described by the position vector at macroscopic scale \underline{X} . The size of the REV depends on the studied problem and it is generally defined as an infinitesimal part of the structure under consideration, large enough to be representative

of the constitutive material (Figure 3.1).

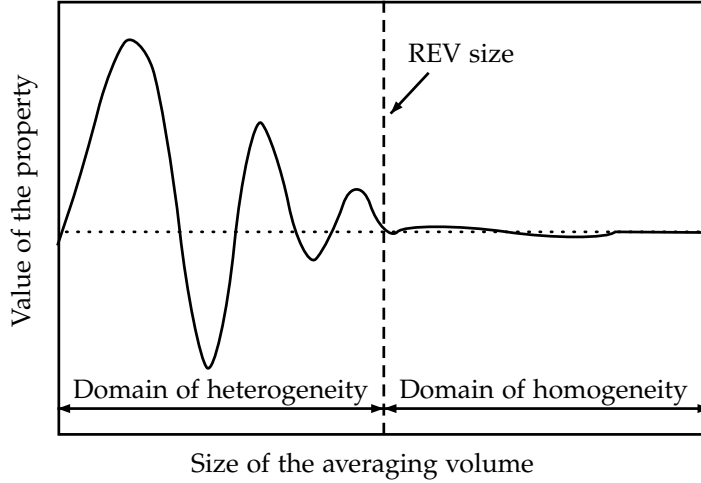


Figure 3.1: Definition of the Representative Elementary Volume.

If L , ℓ and d are the characteristic lengths of the structure, elementary volume and local heterogeneities respectively, the conditions that allow the defining of REV are:

$$d \ll \ell \ll L. \quad (3.1)$$

More details on the determination of REV's size will be given in Chapter 8.

3.2 ASSUMPTIONS

A multiphase continuous porous medium (Gawin and Schrefler, 1996; Schrefler, 2002) is considered. It is represented as a superimposition of continuous media. The porous medium consists of a network of interconnected voids (pores) inside a solid skeleton. The voids are filled partly with a liquid phase, partly with a gaseous phase and partly with solid phase. The liquid phase is modelled as non-ideal solution consisting of liquid water and dissolved salt. Only one salt is assumed to be dissolved in the solution. The gaseous phase is a perfect gas consisting of dry air and water vapour. For

simplicity, the presence of dry air is not explicitly considered in the model. Moreover, N salt solid phases are considered. All the phases and species that constitute the porous medium are summarized in Table 3.1.

In the following, gaseous, liquid and solid phases are de-

PHASES (π)	SPECIES(α)
Gaseous phase g	Water vapour w
Liquid phase l (salt solution)	Liquid water w Dissolved salt s
Solid phase s	Matrix material m Precipitated salt s_i (i -th crystallised form $i=1\dots N$)

Table 3.1: Phases and species of the model

noted by superscripts g , l and s , respectively. The material matrix, water, dissolved salt and precipitated salt are denoted by subscripts m , w , s and s_i , respectively. Subscript i refers to the specific crystallised form of the dissolved salt. The REV is sketched in Figure 3.2, in the hypothesis of two precipitated salts. The pores are considered cylindrical with isotropic distribution (Castellazzi et al., 2013a; Espinosa et al., 2008a). The effect of the deformation of the material matrix on the transport of various phases (de Miranda et al., 2009) is neglected as well as the gravitational effects. The content of each component is described by the

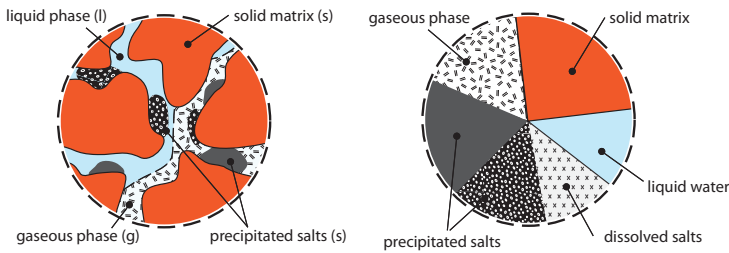


Figure 3.2: Porous medium: Representative Elementary Volume (REV)

concentration c_{α}^{π} , defined as the mass of α in π -phase m_{α}^{π}

per unit volume of porous medium, or by the corresponding saturation degree S_α^π , defined as the pore volume occupied by α in π -phase. The concentration c_α^π and the correspondent saturation degree S_α^π can be related as:

$$c_\alpha^\pi = (\phi_0 \cdot S_\alpha^\pi) \cdot \rho_\alpha^\pi, \quad (3.2)$$

where ρ_α^π is the mass density of α in π -phase and ϕ_0 is the total open porosity defined as the volume of voids per unit volume of porous medium. The degrees of saturation of all the components satisfy the relation:

$$S_w^g + S_w^l + S_s^l + S_s^s = 1, \quad (3.3)$$

where the saturation degree of the precipitated salts S_s^s is defined as the sum of the saturation degrees of the different crystallised forms: $S_s^s = \sum_{i=1}^N S_{s_i}^s$. The concentration of the precipitated salt in the i -th crystallised form, $c_{s_i}^s$, can be written as the sum of two contributes:

$$c_{s_i}^s = (c_{s_i}^s)_{\text{cry}} + (c_{s_i}^s)_{\text{hyd}}, \quad (3.4)$$

where $(c_{s_i}^s)_{\text{cry}}$ is the amount of precipitated salt due to crystallisation/dissolution process and $(c_{s_i}^s)_{\text{hyd}}$ is the amount of precipitated salt due to hydration/dehydration process.

For simplicity, an instantaneous thermodynamic equilibrium is assumed between liquid phase and gaseous phase. Based on this assumption, it is convenient to combine liquid water concentration c_w^g and vapour water concentration c_w^l into moisture concentration $c_w = c_w^g + c_w^l$. Note that water bound in hydride phases is not included in the moisture definition. In order to keep the model simple, whereas useful, the concentration of liquid water can be approximated to the concentration of moisture $c_w \simeq c_w^l$.

Finally, the mass fraction ω of the dissolved salt per unit mass of liquid phase can be used to describe the content of dissolved salt. The mass fraction ω is defined by the following expression:

$$\omega = \frac{m_s^l}{m_s^l + m_w^l} = \frac{m_s^l}{m_{sw}^l} = \frac{c_s^l}{c_{sw}^l}. \quad (3.5)$$

It follows that the relation between ω and c_s^l is:

$$c_s^l = \frac{\omega}{1 - \omega} c_w^l. \quad (3.6)$$

3.3 BALANCE EQUATIONS

In this section, the balance equations of moisture mass, salt mass and total stored energy are presented. Making reference to the REV in Figure 3.2, at the macroscopic scale the mass conservation equations of water vapour, liquid water and salt can be written respectively as:

$$\frac{\partial c_w^g}{\partial t} + \nabla \cdot \underline{j}_w^g = \mu_w^{lg}, \quad (3.7)$$

$$\frac{\partial c_w^l}{\partial t} + \nabla \cdot \underline{j}_w^l = \mu_w^{lg} - \mu_w^{ls}, \quad (3.8)$$

$$\frac{\partial c_s^l}{\partial t} + \nabla \cdot \underline{j}_s^l + \sum_{i=1}^N \frac{\partial c_{s_i}^s}{\partial t} = \mu_w^{ls}. \quad (3.9)$$

being \underline{j}_w^g the flux of vapour water, \underline{j}_w^l the flux of liquid water, \underline{j}_s^l the flux of dissolved salt, μ_w^{ls} the rate of liquid water consumed by crystallisation of hydrated salt crystals or by the hydration/dehydration process and μ_w^{lg} the water evaporation rate. The derivative of $c_{s_i}^s$ respect to the time in Eq. (3.9) accounts for crystallisation/dissolution and hydration/dehydration rates. The moisture balance equation can be obtained summing Eqs. (3.7) and (3.8):

$$\frac{\partial c_w}{\partial t} + \nabla \cdot \underline{j}_w = -\mu_w^{ls}, \quad (3.10)$$

where $\underline{j}_w = \underline{j}_w^g + \underline{j}_w^l$ denotes the moisture flux.

Since all the components of the liquid phase are convected by the liquid phase velocity, mass fractions can be used to relate the flux of the individual component to the flux of the phase. In particular, the flux of liquid water \underline{j}_w^l and the flux of dissolved salt \underline{j}_s^l can be described based on the typical expressions for binary solutions:

$$\underline{j}_w^l = (1 - \omega) \underline{j}_{ws}^l + \underline{j}_{w,diff}^l = (1 - \omega) \underline{j}_{ws}^l - \underline{j}_{s,diff}^l, \quad (3.11)$$

$$\underline{j}_s^l = \omega \underline{j}_{ws}^l + \underline{j}_{s,diff}^l, \quad (3.12)$$

where \underline{j}_{ws}^l is the flux of the liquid phase, $\underline{j}_{s,diff}^l$ is the diffusive flux of dissolved salt and $\underline{j}_{w,diff}^l$ is the diffusive flux of liquid water. It is worth noting that $(1 - \omega)$ is the mass fraction of liquid water per unit mass of the liquid phase and the diffusive flux of liquid water $\underline{j}_{w,diff}^l$ is simply the opposite of the diffusive flux of dissolved salt $\underline{j}_{s,diff}^l$.

The conservation equation for the total stored energy within the REV accounts for the energy transport by conduction and transport of enthalpy associated with the mass flux of each individual component:

$$\frac{\partial e}{\partial t} + \nabla \cdot \underline{j}_e = 0, \quad (3.13)$$

with:

$$e = c_m^s e_m^s + c_w^g e_w^g + c_w^l e_w^l + c_s^l e_s^l + \quad (3.14a)$$

$$+ \sum_{i=1}^N [(c_{s_i}^s)_{cry} (e_{s_i}^s)_{cry} + (c_{s_i}^s)_{hyd} (e_{s_i}^s)_{hyd}] ,$$

$$\underline{j}_e = \underline{j}_q + e_w^g \underline{j}_w^g + e_w^l \underline{j}_w^l + e_s^l \underline{j}_s^l. \quad (3.14b)$$

In the above expressions, e is the total enthalpy per unit volume of porous medium, e_α^π is the enthalpy of α in π -phase and \underline{j}_q is the heat flux and c_m^s is the bulk density of material matrix $c_m^s = (1 - \phi_0) \rho_m^s$.

For sake of simplicity no heat source/sink are considered. The enthalpies of various components are expressed with respect to a reference state at $T = 0$ in the following forms:

$$e_m^s = \beta_m^s T, \quad (3.15a)$$

$$e_m^s = \beta_m^s T + H_{eva}, \quad (3.15b)$$

$$e_w^l = \beta_w^l T, \quad (3.15c)$$

$$e_s^l = \beta_s^l T, \quad (3.15d)$$

$$e_m^s = \beta_m^s T + H_{eva}, \quad (3.15e)$$

$$(e_{s_i}^s)_{cry} = \beta_{s_i}^s T + H_{cry_i}, \quad (3.15f)$$

$$(e_{s_i}^s)_{hyd} = \beta_{s_i}^s T + H_{hyd_{ij}}. \quad (3.15g)$$

where β_α^π is the specific heat capacity of α in π -phase, H_{eva} is the latent heat of evaporation, H_{cry_i} is the latent heat of crystallisation of the i -th crystallised form, $H_{hyd_{ij}}$ is the latent heat of hydration/dehydration from the j -th crystallised form to the i -th one. In general, β_α^π and H_{eva} depend on the temperature. Here, for the sake of simplicity, the dependency of β_α^π from temperature is neglected. Substituting expressions (3.15), (3.14) into Eq. (3.13) and making use of Eqs. (3.7)-(3.9), it is possible to write the energy balance in the form:

$$\begin{aligned}
& \rho_{eff} \beta_{eff} \frac{\partial T}{\partial t} + \nabla \cdot \underline{j}_q + \\
& + \left(\beta_w^g j_w^g + \beta_w^l j_w^l + \beta_s^l j_s^l \right) \cdot \nabla T + \\
& + \mu_w^{lg} [(\beta_w^g - \beta_w^l) T + H_{eva}] + \mu_w^{ls} (\beta_s^l - \beta_w^l) T + \\
& + \sum_{i=1}^N \left(\frac{\partial c_{s_i}^s}{\partial t} \right)_{cry} [(\beta_{s_i}^s - \beta_s^l) T + H_{cry_i}] + \\
& + \left(\frac{\partial c_{s_i}^s}{\partial t} \right)_{hyd} [(\beta_{s_i}^s - \beta_s^l) T + H_{hyd_{ij}}] = 0,
\end{aligned} \tag{3.16}$$

where μ_w^{lg} is the water evaporation rate, ρ_{eff} and β_{eff} are the effective mass density and the effective specific heat capacity of the porous medium:

$$\rho_{eff} = c_m^s + c_w + c_s^l + \sum_{i=1}^N c_{s_i}^s, \tag{3.17}$$

$$\begin{aligned}
\beta_{eff} = & \frac{\beta_m^s c_m^s + c_w^g \left(\beta_w^g + \frac{\partial H_{eva}}{\partial T} \right) + c_w^l \beta_w^l + c_s^l}{\rho_{eff}} + \\
& + \frac{\sum_{i=1}^N (c_{s_i}^s)_{cry} \left(\beta_{s_i}^s + \frac{\partial H_{cry_i}}{\partial T} \right)}{\rho_{eff}} + \\
& + \frac{\sum_{i=1}^N (c_{s_i}^s)_{hyd} \left(\beta_{s_i}^s + \frac{\partial H_{hyd_{ij}}}{\partial T} \right)}{\rho_{eff}}.
\end{aligned} \tag{3.18}$$

3.4 CONSTITUTIVE RELATIONS

The following relations are assumed as constitutive equations for the gas flow and the capillary liquid flow, respectively:

$$\begin{aligned} j_{\omega}^g &= -K_g \nabla p_v, \\ j_{\omega s}^l &= -K_l \nabla p_c, \end{aligned} \quad (3.19)$$

where K_g is the vapour permeability, K_l the liquid conductivity of the salt solution, p_v the vapour pressure, p_c the capillary pressure. The vapour permeability K_g can be written as:

$$K_g = \frac{D_v}{R_v T}. \quad (3.20)$$

where D_v is the vapour permeability coefficient and R_v is the gas constant of water vapour. The vapour permeability coefficient D_v is given by:

$$D_v = \frac{D_v^{\text{air}}}{\tau_v} f_v (S_w^g), \quad f_v = (S_w^g)^{n_g}, \quad (3.21)$$

where D_v^{air} is the vapour permeability for the dry air, τ_v is a material reduction factor, f_v a scaling factor which takes into account the influence upon moisture, based on the reduction of available pore space through a scaling factor in terms of S_w^g (Scheffler and Plagge, 2010), n_g a saturation exponent that ranges from 1 to 3 (Koniarczyk and Gawin, 2011). Below a certain critical value of saturation, the gas flow does not take place any more. Here, for simplicity, this critical threshold is neglected. An expression to compute D_v^{air} [m²/s] is proposed in Sýkora et al. (2012):

$$D_v^{\text{air}} = 2.306 \cdot 10^{-5} \left(\frac{T}{273.15} \right)^{1.81}. \quad (3.22)$$

Regarding the flux of the liquid phase given in Eq. (3.19), the liquid conductivity can be expressed as:

$$K_l = g_\omega(\omega) D_l f_l (S_w^l), \quad f_l = (S_w^l)^{n_l}. \quad (3.23)$$

where D_l is the liquid conductivity of pure water, g_ω is a correction function which takes into account the presence of salt and is function of the dissolved salt concentration, f_l is a correction factor which accounts for the water saturation degree and the exponent n_l ranges from 1 to 6 (Koniorczyk and Gawin, 2011). The liquid flow is no longer possible when the water saturation degree is lower than a critical threshold, because the liquid phase is disrupted. Here, for simplicity, the threshold is set to zero. According to Sýkora et al. (2012), an empirical expression for the salt-free conductivity is:

$$D_l = \frac{h}{\rho_w^l R_v T} \left[3.8 \left(\frac{A}{\phi_0 \rho_w^l} \right)^2 10^{3(S_w^l - 1)} \right] \frac{\partial c_w}{\partial h}, \quad (3.24)$$

where A is a parameter called water adsorption coefficient and ρ_w^l is the mass density of liquid water. An expression for the correction function g_ω is proposed in Nicolai (2007):

$$g_\omega = \frac{\rho_{ws}^l}{\rho_w^l} (1 - 0.03m), \quad (3.25)$$

where m is the molality, $m = \frac{\omega}{1 - \omega} \frac{1000}{M_s^l}$ being M_s^l [g/mol] the molar mass of the solute, and ρ_{ws}^l is the mass density of the liquid phase which is function of ω and can be evaluated as discussed in Derluyn (2012). Precipitated salt diminishes the effective porosity and, as a consequence, influences the intrinsic permeability of the porous medium. This effect can be taken into account by modifying coefficients D_v and D_l through a correction function depending on the effective porosity ϕ_{eff} :

$$D_v \leftarrow g_v(\phi_{eff}) D_v, \quad D_l \leftarrow g_l(\phi_{eff}) D_l, \quad (3.26)$$

with:

$$\phi_{eff} = \phi_0 \left(1 - \sum_{i=1}^N S_{si}^s \right). \quad (3.27)$$

A simple choice for the correction functions is $g_v = (1 - S_s^s)^{n_v^s}$, $g_l = (1 - S_s^s)^{n_l^s}$, where n_v^s and n_l^s are material dependent parameters that, in the absence of experimental data,

can be set equal to 1. The vapour pressure and the capillary pressure in Eq. (3.19) can be expressed in terms of equivalent relative humidity h , which takes into account for the reduction of vapour pressure over a salt solution, as:

$$p_v = p_{v,sat} h, \quad p_c = \rho_w^l R_v T \ln(h), \quad (3.28)$$

where $p_{v,sat}$ is the saturation vapour pressure of the salt mixture, that depends on temperature as well as on dissolved salt concentration. In particular, the saturation vapour pressure of salt mixture can be taken as:

$$p_{v,sat} = p_{v,sat w}(T) \cdot a_w(\omega), \quad (3.29)$$

where $p_{v,sat w}$ is the saturation vapour pressure of the pure water and a_w is the water activity of salt solution. This latter quantity is defined as:

$$a_w = \gamma X_w. \quad (3.30)$$

where γ is the mean activity coefficient of the dissolved salt using the mole fraction scale, that can be evaluated by the ion interaction approach as illustrated in Marliacy et al. (2000) and Steiger et al. (2008), and X_w is the molar fraction of the solvent, that is pure water. The latter quantity can be expressed in terms of the mass fraction ω as follows:

$$X_w(\omega) = \frac{(1 - \omega)M_s^l}{(1 - \omega)M_s^l + \omega M_{H_2O}}, \quad (3.31)$$

where M_{H_2O} (g/mol) is molar mass of the pure water. Under the hypothesis of ideal solution, γ is equal to 1. It is worth noting that the equivalent relative humidity is related to the relative humidity h_0 as follows:

$$h_0 = a_w h. \quad (3.32)$$

Indeed, the relative humidity for thermodynamic reasons (Coussy, 2006; Nguyen et al., 2008) is generally defined as:

$$h_0 = \frac{p_v}{p_{v,sat w}(T)}; \quad (3.33)$$

note that when there is no salt the two humidity measures coincide.

The diffusive flux of the dissolved salt, $\underline{j}_{s,diff}^l$ is assumed as follows:

$$\underline{j}_{s,diff}^l = -\rho_{ws}^l K_s \nabla \omega, \quad (3.34)$$

where K_s is the diffusion coefficient and ρ_{ws}^l is the mass density of the liquid phase. The diffusion coefficient K_s can be written as:

$$K_s = \frac{D_s}{\tau_l} f_s (S_w^l), \quad f_s = (S_w^l)^{n_s}, \quad (3.35)$$

where D_s is the diffusion coefficient of a salt-free solution and τ_l is the tortuosity. Based on the same arguments as those used to derive the expression for liquid conductivity, f_s is a correction factor that takes into account the actual cross section available for diffusion. A limit value of liquid water content below which the diffusive process becomes impossible should be taken into account, but, for simplicity, such a limit value is neglected.

According to the Fourier's Law, the heat flux \underline{j}_q is taken as:

$$\underline{j}_q = -\lambda_{eff} \nabla T, \quad (3.36)$$

where λ_{eff} is the effective thermal conductivity of the porous material. It accounts for the heat conduction through the skeleton and the mobile phases. The thermal conductivity of a salt solution is approximately proportional to its water content, so λ_{eff} can be evaluated based on the following relation:

$$\lambda_{eff} = \lambda_m^{dry} + \phi_0 \left(S_w^l \lambda_w + \sum_{i=1}^N S_{s_i}^s \lambda_{s_i} \right), \quad (3.37)$$

where λ_w^{dry} is the thermal conductivity of the dry material, considering only the material matrix and empty pores, λ_w is the thermal conductivity of the liquid water and λ_{s_i} is the thermal conductivity of precipitated salt in the i -th crystallised form. Both λ_w and λ_{s_i} depend on the temperature. The thermal conductivity of the liquid water is reported in Appendix A. The dependency of λ_m^{dry} on the temperature

can be neglected.

As regards the latent heat of evaporation H_{eva} , the expression proposed in Sýkora et al. (2012) is adopted (H_{eva} is expressed in [J/kg]):

$$H_{eva} = 2.5008 \cdot 10^6 \left(\frac{273.15}{T} \right)^{(0.167+3.67 \cdot 10^{-4}T)} . \quad (3.38)$$

The latent heats H_{cry_i} and $H_{hyd_{ij}}$ depend on temperature T and on salt concentration and can be calculated through the method described in Derluyn (2012) and Marliacy et al. (2000). According to Marliacy et al. (2000) and to the Pitzer's model, the latent heat of crystallisation for an anhydrous salt, H_{cry_j} , is given by:

$$H_{cry_j} = - \frac{\overline{\Delta_{sol}H^\infty} + \Delta H_L}{M_{s_j}^s} . \quad (3.39)$$

where $M_{s_j}^s$ is the molar mass of the j crystallised form, $\overline{\Delta_{sol}H^\infty}$ is the molar dissolution enthalpy at infinite dilution of the anhydrous salt and ΔH_L is a correction term which takes into account for the excess of enthalpy of a solution containing 1 kg of water. The derivation of the above expression is reported in Appendix B. $\overline{\Delta_{sol}H^\infty}$ depends on temperature T and a possible correlation is reported in Marliacy et al. (2000):

$$\begin{aligned} \overline{\Delta_{sol}H^\infty} &= a_\infty + b_\infty(T - T_0), \\ T_0 &= 298,15 \text{ K}, \\ 273,15 &< T < 373,15 \text{ K}, \end{aligned} \quad (3.40)$$

with a_∞ and b_∞ parameters tabled in Appendix A for chloride and sulphate solutions. If i is a hydrated crystallised form and j is the anhydrous one, it is possible to write (Derluyn, 2012; Marliacy et al., 2000):

$$H_{hyd_{ij}} = \frac{h_{hyd}}{M_{s_i}^s}, \quad H_{hyd_{ji}} = - \frac{h_{hyd}}{M_{s_j}^s} . \quad (3.41)$$

where h_{hyd} is the molar enthalpy of hydration/dehydration which depends on temperature. A possible correlation is reported in Appendix A for sulphate solutions.

3.5 SORPTION/DESORPTION CURVES

In this work, the instantaneous equilibrium between liquid and vapour water is assumed. Accordingly, the moisture content at a certain temperature can be expressed as a function of the relative humidity. This relation, known as sorption/desorption isotherm, can be considered as a material property and can be obtained by experimental testing (Garrecht et al., 2013; Hansen, 1986; Karoglou et al., 2005; Treschler, 2001). In general, the desorption isotherm lies above the sorption one, so that the two curves show a hysteresis loop (Karoglou et al., 2005; Koniorczyk and Gawin, 2008). For the sake of simplicity, this phenomenon is neglected. The sorption isotherm is commonly determined for pure water, but it is influenced by the dissolved salt because of the changing contact angle and the surface tension of the solution (Garrecht et al., 2013; Koniorczyk and Gawin, 2008), and can be conveniently expressed in terms of saturation degree of the solution S_{ws}^l as a function of the equivalent relative humidity. Moreover, the extension to a non-isothermal regime can be made by the so-called modified Oswin model as proposed in Karoglou et al. (2005). In particular, the analytical expression for sorption/desorption curves proposed in Sýkora et al. (2012) for isothermal regime is here extended to non-isothermal regime as:

$$S_{ws}^l = \frac{\Psi(T) - 1}{\Psi(T) - h} h \left(1 - \sum_{i=1}^N S_{si}^s \right), \quad (3.42)$$

where Ψ is the sorption isotherm parameter, which depends on the temperature, and it is obtained by fitting experimental data or the predicted data provided by the modified Oswin model, for example by enforcing the value of water content at a certain value of relative humidity.

The relation (3.42) for sorption curves takes into account for the presence of precipitated salt inside the pores and, indirectly, the effect of the presence of dissolved salt. In fact, denoting by h_0 the relative humidity, the equivalent relative humidity h can be written as $\frac{h_0}{a_w}$ or, for an ideal solution,

as $\frac{h_0}{X_w}$. Then, the saturation degree of the solution, supposing that $\sum_{i=1}^N S_{s_i}^s = 0$, can be expressed in terms of relative humidity h_0 as:

$$S_{ws}^l = \frac{\Psi(T) - 1}{a_w \Psi(T) - h_0} h_0. \quad (3.43)$$

The trend of $S_{ws}^l(h_0)$ while varying the water activity is represented in Figure 3.3. Finally, the moisture content c_w and the water saturation degree S_w^l can then be expressed in terms of S_{ws}^l as:

$$c_w = \phi_0(1 - \omega)\rho_{ws}^l S_{ws}^l, \quad (3.44a)$$

$$S_w^l = (1 - \omega) \frac{\rho_{ws}^l}{\rho_w^l} S_{ws}^l. \quad (3.44b)$$

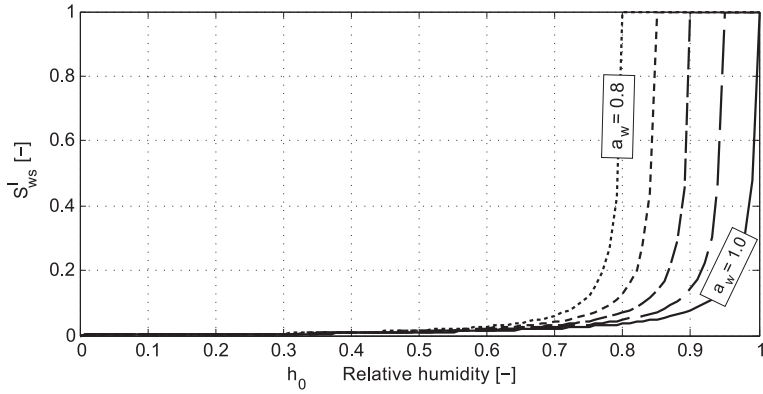


Figure 3.3: Degree of saturation of a salt solution function of water activity.

3.6 KINETIC LAWS

The kinetic law quantifies the amount of salt that precipitates in a certain crystallised form. The crystallisation/dissolution as well as the hydration/dehydration process are considered. For simplicity the deliquescence process is not explicitly considered. As already outlined, reference is made

to a pore model that considers cylindrical pores with isotropic distribution (Espinosa et al., 2008a). In the conditions proper to crystallisation we assume that a certain amount of nuclei is present in the solution and, to keep the mathematical model as simple as possible, nuclei are assumed of cylindrical form with radius r_p (Figure 3.4) (Castellazzi et al., 2013a; Espinosa et al., 2008a). The concentration of precipitated salt

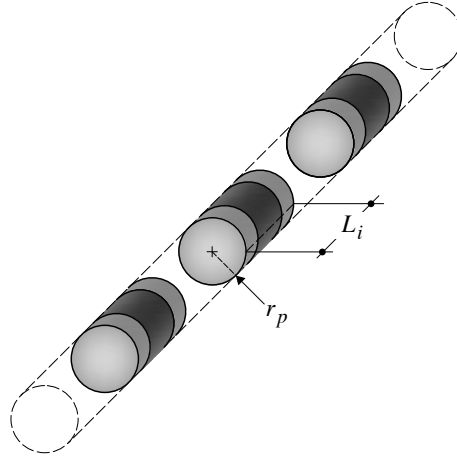


Figure 3.4: Representation of the nucleation of \bar{n} nuclei in the REV pore volume

in the i -th crystallised form can be expressed as:

$$c_{s_i}^s = \frac{m_{s_i}^s}{V_{\text{tot}}} = \frac{\pi r_p^2 L_i \rho_{s_i}^s \bar{n}_i}{V_{\text{tot}}}. \quad (3.45)$$

where L_i is the length of a crystal and n_i is the number of nuclei of the i -th kind of crystal in the REV, at a certain instant t (see Figure 3.4). Through simple steps, it is possible to show that:

$$\frac{\bar{n}_i}{V_{\text{tot}}} = \phi_0 S_{sw}^l n_i, \quad (3.46)$$

where n_i is the amount of nuclei per unit volume of solution of the i -th crystallised form and S_{sw}^l is the saturation degree of the solution, $S_{sw}^l = S_w^l + S_s^l$.

During the kinetic processes we assume that the total amount

of nuclei in the REV \bar{n} does not change. Hence the following constraint holds:

$$\frac{\partial \bar{n}}{\partial t} = 0, \quad \bar{n} = \sum_{i=1}^N \bar{n}_i. \quad (3.47)$$

In the numerical applications, \bar{n}_i has been taken proportional to the number of precipitated moles of salt as:

$$\bar{n}_i = \bar{n} \frac{\frac{c_{s_i}^s}{M_{s_i}^s}}{\sum_{k=1}^N \frac{c_{s_k}^s}{M_{s_k}^s}}. \quad (3.48)$$

Differentiating $c_{s_i}^s$ with respect to the time yields:

$$\frac{\partial c_{s_i}^s}{\partial t} = \pi r_p^2 \rho_{s_i}^s \frac{\bar{n}_i}{V_{\text{tot}}} \frac{\partial L_i}{\partial t} + \frac{\pi r_p^2 \rho_{s_i}^s L_i}{V_{\text{tot}}} \frac{\partial \bar{n}_i}{\partial t}, \quad (3.49)$$

In Eq. (3.49), the first term of the sum accounts for the crystallisation/dissolution process:

$$\begin{aligned} \left(\frac{\partial c_{s_i}^s}{\partial t} \right)_{\text{cry}} &= \pi r_p^2 \rho_{s_i}^s \frac{\bar{n}_i}{V_{\text{tot}}} \frac{\partial L_i}{\partial t} \\ &= \pi r_p^2 \rho_{s_i}^s \phi_0 S_{sw}^l n_i \frac{\partial L_i}{\partial t}, \end{aligned} \quad (3.50)$$

the second term accounts for the hydration/dehydration process,

$$\begin{aligned} \left(\frac{\partial c_{s_i}^s}{\partial t} \right)_{\text{hyd}} &= \frac{\pi r_p^2 \rho_{s_i}^s L_i}{V_{\text{tot}}} \frac{\partial \bar{n}_i}{\partial t} \\ &= \pi r_p^2 \rho_{s_i}^s \phi_0 S_{sw}^l L_i \frac{\partial n_i}{\partial t}. \end{aligned} \quad (3.51)$$

The outlined model, which considers cylindrical pores with the same radius, could be further improved by imaging the material pore microstructure subdivided in a number of pore classes. To complete the definition of the kinetic laws we need to define the growth rate of the length of the crystal for the crystallisation/dissolution process and rate of hydration/dehydration process. The supersaturation ratio,

defined as the current concentration of dissolved salt ω divided by the concentration at saturation ω_{sat} , is assumed as the driving force of salt crystallisation or dissolution. Crystallization starts when the supersaturation ratio is greater than the threshold α_0 and dissolution starts when the supersaturation ratio is less than one:

$$\frac{\omega}{\omega_{sat}} > \alpha_0 \rightarrow \text{crystallisation,}$$

$$\frac{\omega}{\omega_{sat}} < 1 \rightarrow \text{dissolution.}$$

For primary crystallisation $\alpha_0 > 1$ and depends on porosity and salt, further crystallisation proceeds at $\alpha_0 = 1$. According to Koniorczyk and Gawin (2011) and Derluyn (2012), the growth rate of the i -th crystal characteristic length can be written as:

$$\frac{\partial L_i}{\partial t} = K_{C_i} \left| \frac{\omega}{\omega_{sat}} - 1 \right|^{P_{cry_i}}. \quad (3.52)$$

where both the growth rate coefficient, K_{C_i} , and the crystallisation process order, P_{cry_i} , depend on the properties of porous material and salt. An expression for K_{C_i} is reported in Derluyn (2012):

$$K_{C_i} = C_i \exp\left(-\frac{E_{a_i}}{RT}\right). \quad (3.53)$$

with C_i the growth rate constant, E_{a_i} the activation energy of the specific process, R the universal gas constant and T the temperature. When in the REV there is a precipitated salt in its i -th crystallised form, a variation of humidity or temperature could lead to a hydration/dehydration of the salt. The salt hydration describes the absorption of water molecules in the salt crystal to build an hydrated salt. The salt dehydration is the reverse process, and the hydration rate can be defined as:

$$L_i \frac{\partial \bar{n}_i}{\partial t} = K_{H_{ij}} \left| \frac{h_0}{h^*(T)} - 1 \right|^{P_{hyd_{ij}}}, \quad (3.54)$$

where $h^*(T)$ gives the equilibrium relative humidity at which the phase change between hydrate and anhydrous salt starts, $K_{H_{ij}}$ is the kinetic hydration/dehydration parameter, which is the velocity needed by the j precipitated salt to transform into the i -precipitated salt, $P_{hyd_{ij}}$ is the process order which can be assumed equal to 1 for a diffusion forced hydration (Espinosa et al., 2008b). The rate of hydration is different from the rate of dehydration, since the kinetic hydration parameter, $K_{H_{ij}}$, and the kinetic dehydration parameter, $K_{H_{ji}}$, are related by the following expression:

$$K_{H_{ji}} = \frac{L_j}{L_i} K_{H_{ij}}. \quad (3.55)$$

This relation can be derived by considering that in a certain point and at a certain instant there is a unique value of relative humidity and temperature. Moreover, we assume that the number of salt nuclei that dehydrates is equal to the one that hydrates, *i.e.* $\frac{\partial \bar{n}_i}{\partial t} = \frac{\partial \bar{n}_j}{\partial t}$. The ratio $\frac{L_j}{L_i}$ can be calculated taking into account the isotropic cylindrical pore model and the fact that from 1 mol of hydrous salt, 1 mol of anhydrous salt is obtained through the hydration/dehydration process:

$$\frac{\pi r_p^2 L_i \rho_{s_i}^s}{M_{s_i}^s} = \frac{\pi r_p^2 L_j \rho_{s_j}^s}{M_{s_j}^s}. \quad (3.56)$$

Consequently:

$$\frac{L_j}{L_i} = \frac{M_{s_i}^s \rho_{s_i}^s}{M_{s_j}^s \rho_{s_j}^s} = \frac{(V_m)_{s_j}^s}{(V_m)_{s_i}^s}. \quad (3.57)$$

where $(V_m)_{s_i}^s$ is the molar volume of the salt in the i -th crystallised form. This can be evaluated using the following expression:

$$(V_m)_{s_i}^s = \frac{N_A V_{cell}^i}{Z_i}. \quad (3.58)$$

where N_A is the Avogadro constant, V_{cell}^i is the unit cell volume of the i -th crystallised form and Z_i is the number of formula units in the unit cell of the i -th crystal.

3.7 SOURCE AND SINK TERMS

The water evaporation rate μ_w^{lg} in the porous medium can be evaluated as:

$$\mu_w^{lg} = -\nabla \cdot (K_g \nabla p_v). \quad (3.59)$$

Taking into account the dependency of $p_{v,sat}$ on T and ω , it is possible to obtain the relation between the water evaporation rate and the independent variables h , T , ω :

$$\begin{aligned} \mu_w^{lg} = & - \left[\left(\frac{\partial K_g}{\partial T} p_{v,sat} + 2 K_g \frac{\partial p_{v,sat}}{\partial T} \right) \nabla T \cdot \nabla h \right] + \\ & - \left[2 K_g \frac{\partial p_{v,sat}}{\partial \omega} \nabla \omega \cdot \nabla h + K_g p_{v,sat} \nabla^2 h \right] + \\ & - \left[\left(\frac{\partial K_g}{\partial T} h \frac{\partial p_{v,sat}}{\partial \omega} + 2 K_g h \frac{\partial^2 p_{v,sat}}{\partial \omega \partial T} \right) \nabla \omega \cdot \nabla T \right] + \\ & \quad - \left[K_g h \frac{\partial^2 p_{v,sat}}{\partial \omega^2} \nabla \omega \cdot \nabla \omega \right] + \\ & - \left[\left(\frac{\partial K_g}{\partial T} h \frac{\partial p_{v,sat}}{\partial T} + K_g h \frac{\partial^2 p_{v,sat}}{\partial T^2} \right) \nabla T \cdot \nabla T \right] + \\ & - \left[k_g h \frac{\partial p_{v,sat}}{\partial T} \nabla^2 T + K_g h \frac{\partial p_{v,sat}}{\partial \omega} \nabla^2 \omega \right]. \end{aligned} \quad (3.60)$$

The rate of liquid water trapped in hydrated crystals μ_w^{ls} can be defined as:

$$\mu_w^{ls} = \frac{\partial c_w^{ls}}{\partial t}. \quad (3.61)$$

where c_w^{ls} is the concentration of the liquid water trapped in hydrated crystals that can be written as:

$$c_w^{ls} = M_{H_2O} \sum_{i=1}^N \nu_{0i} \frac{c_{s_i}^s}{M_{s_i}^s}, \quad (3.62)$$

being ν_{0i} the number of water molecules trapped per salt mole in order to form the i -th crystallised form. Substituting Eq. (3.62) in Eq. (3.61) yields the rate of liquid water trapped in hydrated crystals μ_w^{ls} , that can be written as:

$$\mu_w^{ls} = \sum_{i=1}^N \nu_{0i} \frac{M_{H_2O}}{M_{s_i}^s} \frac{\partial c_{s_i}^s}{\partial t}. \quad (3.63)$$

Using the latter expression, Eqs. (3.9) and (3.10) take the forms:

$$\frac{\partial c_w}{\partial t} + \nabla \cdot \underline{j}_w + \sum_{i=1}^N \nu_{0i} \frac{M_{H_2O}}{M_{s_i}^s} \frac{\partial c_{s_i}^s}{\partial t} = 0, \quad (3.64)$$

$$\frac{\partial c_s^l}{\partial t} + \nabla \cdot \underline{j}_s^l + \sum_{i=1}^N \left(1 - \nu_{0i} \frac{M_{H_2O}}{M_{s_i}^s}\right) \frac{\partial c_{s_i}^s}{\partial t} = 0. \quad (3.65)$$

Finally, remembering that:

$$M_{s_i}^s = M_s^l + \nu_{0i} M_{H_2O}, \quad (3.66)$$

Equation (3.65) can be rewritten as:

$$\frac{\partial c_s^l}{\partial t} + \nabla \cdot \underline{j}_s^l + \sum_{i=1}^N \frac{M_s^l}{M_{s_i}^s} \frac{\partial c_{s_i}^s}{\partial t} = 0. \quad (3.67)$$

3.8 SUMMARY OF THE HTC MODEL EQUATIONS

Considering the crystallisation of a salt solution with N crystallised forms and taking into account the dependencies outlined in the previous sections, the resulting governing equations of the model, that is the balance Eqs. (3.7), (3.8) and (3.13) together with the kinetic law, Eq. (3.49), can be written as:

$$\begin{aligned} & \varphi_h \frac{\partial h}{\partial t} + \nabla \cdot [-C_{hh} \nabla h - C_{hT} \nabla T - C_{hw} \nabla \omega] + \\ & + \varphi_{hw} \frac{\partial \omega}{\partial t} + \varphi_{hT} \frac{\partial T}{\partial t} + \sum_{i=1}^N \varphi_{hs_i} \frac{\partial c_{s_i}^s}{\partial t} + \mu_w^{ls} = 0, \end{aligned} \quad (3.68)$$

$$\begin{aligned} & \varphi_\omega \frac{\partial \omega}{\partial t} + \nabla \cdot [-C_{\omega h} \nabla h - C_{\omega T} \nabla T - C_{\omega\omega} \nabla \omega] + \\ & + \varphi_{\omega h} \frac{\partial h}{\partial t} + \varphi_{\omega T} \frac{\partial T}{\partial t} + \sum_{i=1}^N \varphi_{\omega s_i} \frac{\partial c_{s_i}^s}{\partial t} - \mu_w^{ls} = 0, \end{aligned} \quad (3.69)$$

$$\begin{aligned} & \varphi_T \frac{\partial T}{\partial t} + \nabla \cdot [-C_{TT} \nabla T - C_{Th} \nabla h - C_{T\omega} \nabla \omega] + \\ & -\mu_w^{ls} B_w^* + \mu_w^{lg} B_w + \sum_{i=1}^N (\varphi_{Ts_i})_{cry} \left(\frac{\partial c_{s_i}^s}{\partial t} \right)_{cry} + \\ & + \sum_{i=1}^N (\varphi_{Ts_i})_{hyd} \left(\frac{\partial c_{s_i}^s}{\partial t} \right)_{hyd} = 0, \end{aligned} \quad (3.70)$$

$$\frac{\partial c_{s_i}^s}{\partial t} = \pm C_{ss_i} \left| \frac{\omega}{\omega_{sat}} - 1 \right|^{P_{cry_i}} \pm C_{sh_i} \left| \frac{h}{h^*} - 1 \right|^{P_{hyd_i}}. \quad (3.71)$$

It is worth remarking that the following constraints hold:

$$S_\alpha^\pi > 0, \quad \sum S_\alpha^\pi = 1. \quad (3.72)$$

The expressions of coefficients φ_{ij} , C_{ij} , B_i for the system (3.68)-(3.71) are detailed in Appendix B.

The model equations are completed by the initial and boundary conditions. In particular, the boundary conditions on a certain portion of the domain boundary can be of Dirichlet type:

$$\begin{aligned} h &= \bar{h}, \\ \omega &= \bar{\omega}, \\ T &= \bar{T}, \end{aligned} \quad (3.73)$$

and of Neumann's or Robin's type:

$$\begin{aligned} \underline{j}_w \cdot \underline{n} &= q_w + \gamma_w (h_0 - h_\alpha), \\ \underline{j}_s^l \cdot \underline{n} &= q_\omega, \\ \underline{j}_e \cdot \underline{n} &= q_T + \gamma_T (T - T_\alpha), \end{aligned} \quad (3.74)$$

where \underline{n} is the outward unit normal to the boundary, \bar{h} , $\bar{\omega}$ and \bar{T} are the prescribed equivalent relative humidity, salt concentration and temperature, respectively, q_w , q_ω and q_T are the prescribed normal fluxes of moisture, salt and heat, h_α and T_α are the prescribed environmental humidity and temperature, and γ_w and γ_T are the convective humidity and thermal coefficients, respectively.

3.9 CONCLUDING REMARKS

A new coupled multiphase model for the hygrothermal analysis of porous building materials with salt crystallisation/dissolution and hydration/dehydration processes has been presented. The model is governed by three coupled, highly non-linear differential equations – moisture mass conservation, salt mass conservation and energy balance – completed by evolution equations that describe the kinetics of the salt precipitation.

The HTC model can be specialised for a great range of electrolytic salts. In the following chapters a specialisation of this Hygro-Thermo-Chemical (HTC) model for sodium sulfate solution and sodium chloride solutions will be presented.

SODIUM SULPHATE SOLUTION

The HTC model presented in Chapter 3 is specialised for sodium sulphate solutions. The predictive capabilities of the model are validated on some experiments available in the literature, involving fired-clay bricks and sodium sulphate solutions. In particular, firstly a constant humidity test is used to validate the crystallisation/dissolution kinetics. Then, the hydration/dehydration kinetics is validated through a constant temperature test. Finally, a test with variable hygro-thermal conditions is considered, where both the crystallisation/dissolution and hydration/dehydration processes are involved.

The illustrated numerical applications on fired-clay bricks show the effectiveness of the proposed approach.

4.1 SPECIALISATION

Here, the HTC model described in Chapter 3 is specialised for sodium sulphate solutions. A detailed experimental study on the phase diagram can be found in Steiger and Asmussen (2008). Under the assumptions of normal atmospheric conditions and temperature higher than 273 K, the sodium sulphate has two stable crystallised forms, mirabilite and thenardite V. Hereinafter, the subscript 1 denotes mirabilite and the subscript 2 denotes thenardite. The solubility and phase diagrams for sodium sulphate solution are reported in Figure 4.1. According to the hygrothermal conditions, the diagrams in Figure 4.1 can be simplified. In particular, in the numerical applications presented in the next section only the bold curves are considered. Moreover, the solubility experimen-

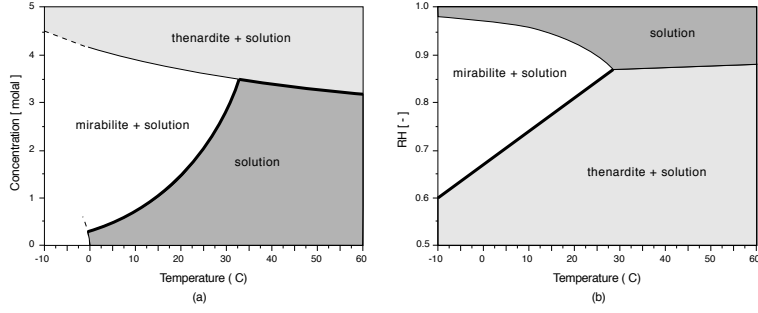


Figure 4.1: Solubility diagram (a) and the phase diagram (b); the curves considered in the numerical applications are highlighted

tal data are approximated by using the following function proposed in Koniorczyk and Gawin (2011):

$$\omega_{\text{sat}} = \begin{cases} 0.0488 \exp(0.0625(T - 273.15)) & T < 273.15 \text{ K} \\ 273.15 \leq T \leq 305.55 \text{ K} & (4.1) \\ 0.3697 & T \geq 305.55 \text{ K} \end{cases}$$

On the basis of the experimental data given in Steiger and Asmussen (2008), the equilibrium relative humidities for the mirabilite-thenardite V transition due to the hydration/dehydration process can be approximated using the following expression:

$$h^*(T) = 0.0082767T + 0.606 \quad 273.15 \leq T \leq 305.55 \text{ K} \quad (4.2)$$

with $T^* = 305.55 \text{ K}$.

Moreover, considering sodium sulphate solution, Eq. (3.63) can be written as:

$$\mu_w^{\text{ls}} = 10 \frac{M_{\text{H}_2\text{O}}}{M_{\text{S}_1}^s} \frac{\partial c_{\text{S}_1}^s}{\partial t}, \quad (4.3)$$

and the kinetic equation, Eq. (3.71), particularizes as:

$$\frac{\partial c_{s_1}^s}{\partial t} = \begin{cases} 0 & \omega \leq \omega_{\text{sat}} & c_{s_1}^s = 0, \\ -C_{ss_1} \left| \frac{\omega}{\omega_{\text{sat}}} - 1 \right|^{P_{\text{cry}_1}} & \omega \leq \omega_{\text{sat}} & c_{s_1}^s > 0, \\ C_{ss_1} \left| \frac{\omega}{\omega_{\text{sat}}} - 1 \right|^{P_{\text{cry}_1}} & \omega \geq \alpha_{01} \omega_{\text{sat}} & T < T^* \\ & h_0 \geq h^* & c_{s_2}^s = 0, \\ C_{ss_1} \left| \frac{\omega}{\omega_{\text{sat}}} - 1 \right|^{P_{\text{cry}_1}} + C_{sh_1} \left| \frac{h_0}{h^*} - 1 \right|^{P_{\text{hyd}_1}} & & \\ \omega \leq \alpha_{01} \omega_{\text{sat}} & T < T^* & h_0 \geq h^* & c_{s_2}^s > 0, \\ -C_{sh_1} \left| \frac{h_0}{h^*} - 1 \right|^{P_{\text{hyd}_1}} & \omega \geq \alpha_{01} \omega_{\text{sat}} & & \\ & T < T^* & h_0 < h^* & c_{s_1}^s > 0, \\ 0 & \omega \geq \alpha_{01} \omega_{\text{sat}} & T < T^* & h_0 < h^* \\ & & & c_{s_1}^s = 0, \\ -C_{sh_1} \left| \frac{h_0}{h^*} - 1 \right|^{P_{\text{hyd}_1}} & \omega \geq \alpha_{01} \omega_{\text{sat}} & & \\ & & T > T^* & c_{s_1}^s > 0, \\ 0 & \omega \geq \alpha_{01} \omega_{\text{sat}} & T > T^* & c_{s_1}^s = 0, \end{cases} \quad (4.4)$$

for mirabilite,

$$\frac{\partial c_{s_2}^s}{\partial t} = \begin{cases} 0 & \omega \leq \omega_{\text{sat}} & c_{s_2}^s = 0, \\ -C_{ss_2} \left| \frac{\omega}{\omega_{\text{sat}}} - 1 \right|^{P_{\text{cry}_2}} & \omega \leq \omega_{\text{sat}} & c_{s_2}^s > 0, \\ -C_{sh_2} \left| \frac{h_0}{h^*} - 1 \right|^{P_{\text{hyd}_2}} & \omega \geq \alpha_{02}\omega_{\text{sat}} \\ & T < T^* & h_0 \geq h^* & c_{s_2}^s > 0, \\ 0 & \omega \geq \alpha_{02}\omega_{\text{sat}} & T < T^* \\ & h_0 \geq h^* & c_{s_2}^s = 0, \\ C_{sh_2} \left| \frac{h_0}{h^*} - 1 \right|^{P_{\text{hyd}_2}} & \omega \geq \alpha_{02}\omega_{\text{sat}} \\ & T < T^* & h_0 < h^* & c_{s_1}^s > 0, \\ 0 & \omega \geq \alpha_{02}\omega_{\text{sat}} & T < T^* \\ & h_0 < h^* & c_{s_1}^s = 0, \\ C_{ss_2} \left| \frac{\omega}{\omega_{\text{sat}}} - 1 \right|^{P_{\text{cry}_2}} & \omega \geq \alpha_{02}\omega_{\text{sat}} \\ & T > T^* & c_{s_1}^s = 0, \\ C_{ss_2} \left| \frac{\omega}{\omega_{\text{sat}}} - 1 \right|^{P_{\text{cry}_2}} + C_{sh_2} \left| \frac{h_0}{h^*} - 1 \right|^{P_{\text{hyd}_2}} \\ \omega \leq \alpha_{02}\omega_{\text{sat}} & T > T^* & c_{s_1}^s > 0, \end{cases} \quad (4.5)$$

for thenardite. In the above equations:

$$C_{ss_1} = S_{ws}^l (n_1 \phi_0 \rho_{s_1}^s \pi r_p^2) K_{C_1}, \quad (4.6a)$$

$$C_{sh_1} = \frac{\rho_{s_1}^s \pi r_p^2}{V_{\text{tot}}} K_{H_{12}}, \quad (4.6b)$$

$$C_{ss_2} = S_{ws}^l (n_2 \phi_0 \rho_{s_2}^s \pi r_p^2) K_{C_2}, \quad (4.6c)$$

$$C_{sh_2} = \frac{\rho_{s_2}^s \pi r_p^2}{V_{\text{tot}}} K_{H_{21}}. \quad (4.6d)$$

The calculation of the kinetic parameters of Eq. (3.54) for a sodium sulphate solution and an expression for the molar enthalpy of hydration/dehydration are reported in Appendix B.

4.2 NUMERICAL APPLICATIONS

In this section, the predictive capabilities of the multiphase coupled model described in Chapter 3 and specialised for sodium chloride solutions in Section 4.1 are evaluated on some tests involving fired-clay bricks. Firstly, two benchmark tests taken from the literature are considered (Espinosa et al., 2008b; Koniorczyk and Konca, 2013). The first one (Koniorczyk and Konca, 2013) is a constant humidity test and serves to validate the crystallisation/dissolution kinetics. The second one (Espinosa et al., 2008b) is a constant temperature test and serves to validate the hydration/dehydration kinetics. Then, an example with varying conditions of temperature and humidity is considered. In this case the processes of crystallisation/dissolution and of hydration/dehydration are both involved. In these tests the liquid phase is modelled as an ideal solution.

In order to solve the model, the governing equations are discretized in space using the finite element method. The primary variables h , ω , T , $c_{s_1}^s$ and $c_{s_2}^s$ are interpolated based on standard Lagrangian shape functions. The time discretization is carried out by means of the backward finite difference method. A standard iterative strategy based on the Newton-Raphson method is applied to solve the non-linear system of equations. The implementation has been developed using COMSOL (2008).

4.3 RESULTS AND DISCUSSION

4.3.1 *Test at constant humidity: crystallisation of mirabilite*

The experiment proposed by Koniorczyk and Konca (2013) is used here to validate the crystallisation/dissolution kinetics. Two bricks, one saturated with pure water and one saturated with sodium sulphates solution (25% wt), are covered with hygral insulation and put into a climatic chamber, where they are cooled and warmed. The experiment starts at 303 K, then the cooling to 284 K induces the growth of

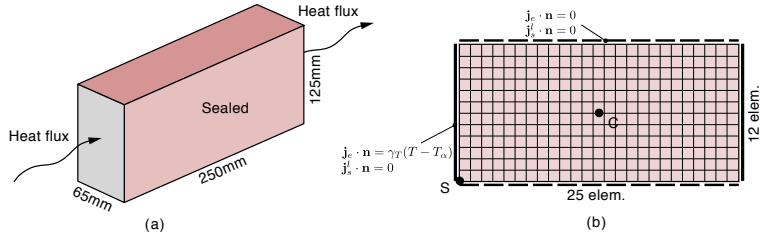


Figure 4.2: Test at constant humidity: geometry (a) ; boundary conditions and mesh (b)

mirabilite and, after, the warming up to 303 K causes the dissolution of mirabilite. Temperature sensors are placed in each brick, in the same position. However, temperature data from the two bricks are different because of the heat released or absorbed during the process of salt crystallisation/dissolution. The brick dimensions are 125 mm \times 250 mm \times 65 mm, see Figure 4.2a. The brick is completely sealed to humidity and dissolved salt. As regards the temperature, null Neumann boundary conditions are assumed on all the faces except for the two smallest ones, where Robin boundary conditions are assumed, Figure 4.2b. The initial conditions are: $T_0 = 303$ K, $h_0 = 1$, $\omega_0 = 0.25$, $c_{s_1}^s(0) = 0$ kg/m³, $c_{s_2}^s(0) = 0$ kg/m³. Owing to the geometry and boundary conditions, the brick is modelled as a bi-dimensional domain. Here and in the following tests, 8-node plane elements with quadratic shape functions are adopted. The finite elements mesh is shown in Figure 4.2b. The values of the model parameters used in the simulation are collected in Table 4.1.

Table 4.1: Test at constant humidity - Summary of model parameters for a sodium sulphate solution

QUANTITY		VALUE	UNITS	SOURCE
M_{H_2O}	Molar mass of pure water	18.015	g/mol	Literature
M_{mir}	Molar mass of mirabilite	322.196	g/mol	Literature
M_{the}	Molar mass of thenardite	142.043	g/mol	Literature
ϕ_0	Brick porosity	0.20	-	Koniorczyk and Konca (2013)
ρ_w^l	Density of the water in the liquid phase	1000	Kg/m ³	literature
ρ_{s1}^s	Density of the mirabilite	1460	Kg/m ³	Haynes (2012-2013)
ρ_{s2}^s	Density of the thenardite	2700	Kg/m ³	Haynes (2012-2013)
ψ	Sorption isotherm parameter	1.0094	-	Castellazzi et al. (2013a)
ρ_{brick}	Mass density of brick	1700	Kg/m ³	Koniorczyk and Konca (2013)
P_{cry1}	Mirabilite crystallisation process order	1	-	Derluyn (2012)
P_{cry2}	Thenardite V crystallisation process order	1.5	-	Derluyn (2012)
P_{hyd}	hydration process order	1	-	Espinosa et al. (2008b)

QUANTITY		VALUE	UNITS	SOURCE
C_1	Mirabilite growth rate constant	1.165×10^{14}	m/s	Derluyn (2012)
C_2	Thenardite V growth rate constant	4.75×10^2	m/s	Derluyn (2012)
E_{a1}	Mirabilite activation energy	113386	J/mol	Derluyn (2012)
E_{a2}	Thenardite activation energy	57321	J/mol	Derluyn (2012)
R_v	Gas constant of water vapour	461.5	J/kg/K	Literature
D_v	Vapour permeability	0.0039006	m^2/h	Sýkora et al. (2012)
D_s/τ_l	Diffusion coeff./tortuosity	0.499×10^{-9}	m^2/s	Haynes (2012-2013)
$\tau_{v\text{brick}}$	Vapour resistance factor	24.5325	-	Castellazzi et al. (2013a)
n	Number nuclei in solution	4×10^{-6}	$1/\mu m^3$	Espinosa et al. (2008a)
α_0	Crystallization threshold	1.7	-	Derluyn (2012)
A_{brick}	water adsorption coefficient	0.185	$kg/m^2 s^{1/2}$	Castellazzi et al. (2013a)
r_p	Average brick pore radius	0.7	μm	Castellazzi et al. (2013a)
H_{eva}	latent heat of evaporation	2451800	J/kg	Sýkora et al. (2012)
$H_{\text{cry}1}$	Mirabilite latent heat of crystallisation	-211100	J/kg	Derluyn (2012)

QUANTITY	VALUE	UNITS	SOURCE
$H_{\text{cry}2}$	Thenardite V latent heat of crystallisation	69200	J/kg Derluyn (2012)
$H_{\text{hyd}12}$	Latent heat of hydration	-241607	J/kg Calculated
$H_{\text{hyd}21}$	Latent heat of dehydration	548038	J/kg Calculated
$\beta_{\text{sbrick}}^{\text{m}}$	Specific heat capacity of brick	840	J/kg/K Tariku et al. (2010)
$\beta_{\text{g}}^{\text{w}}$	Specific heat capacity of water vapour	1847.7	J/kg/K Haynes (2012-2013)
$\beta_{\text{l}}^{\text{w}}$	Specific heat capacity of liquid water	4181.3	J/kg/K Literature
$\beta_{\text{s}1}^{\text{s}}$	Specific heat capacity of Mirabilite	1743	J/kg/K Ahl (2004)
$\beta_{\text{s}2}^{\text{s}}$	Specific heat capacity of Thenardite	891	J/kg/K Ahl (2004)
$\lambda_{\text{dry brick}}$	Thermal conductivity of dry brick	0.77	W/(mK) Derluyn (2012)
γ_{w}	Convective humidity coefficient	0.4	kg/(m ² s) Castellazzi et al. (2013a)
γ_{T}	Convective thermal coefficient	23	W/(m ² K) Derluyn (2012)

Figure 4.3(a) shows the temperature in the point S (see Figure 4.2(b)) in the two cases of pure water and of sulphate solution, together with the environmental temperature. As expected, there are differences between the curves of the temperature in the case of pure water and in the case of sulphate solution due to the heat released and adsorbed during the crystallisation/dissolution process. As it can be easily verified, the results obtained agree with the observed experimental results reported in Koniorczyk and Konca (2013). The temperature change inside the specimen is shown in Figure 4.3a. In particular, the temperatures in the point on

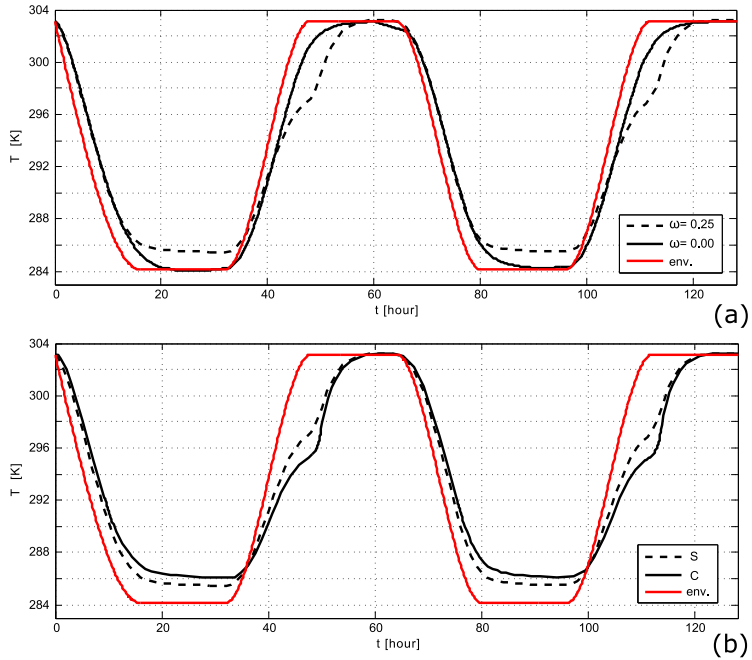


Figure 4.3: Test at constant humidity – temperature in the point S for the specimen saturated of pure water and of sulphate solution 25 %wt (a); temperature in points S and C for the case of sodium sulphate solution (b).

the surface and in the centre of the specimen (points S and C in Figure 4.2b) are given. The dissolved salt concentration and the supersaturation ratio in points S and C of the specimen saturated with sulphate solution are shown in Figure 4.4. Moreover, Figure 4.5 shows the saturation degree of precipitated mirabilite and the rate of trapped water in points S and C. The supersaturation ratio for the primary crystallisation is fixed at 1.7, in accordance with Koniorczyk and Konca (2013). Comparing Figures 4.4 and 4.5 it can be noted that the precipitation of mirabilite starts when the solution becomes supersaturated. After that, the dissolved salt concentration rapidly decreases, starting from the surface (Figure 4.4). Crystal growth starts from the surface and occupies the 5% of the pores, as shown in Figure 4.5a. Notice that the values of these peaks agree with those found

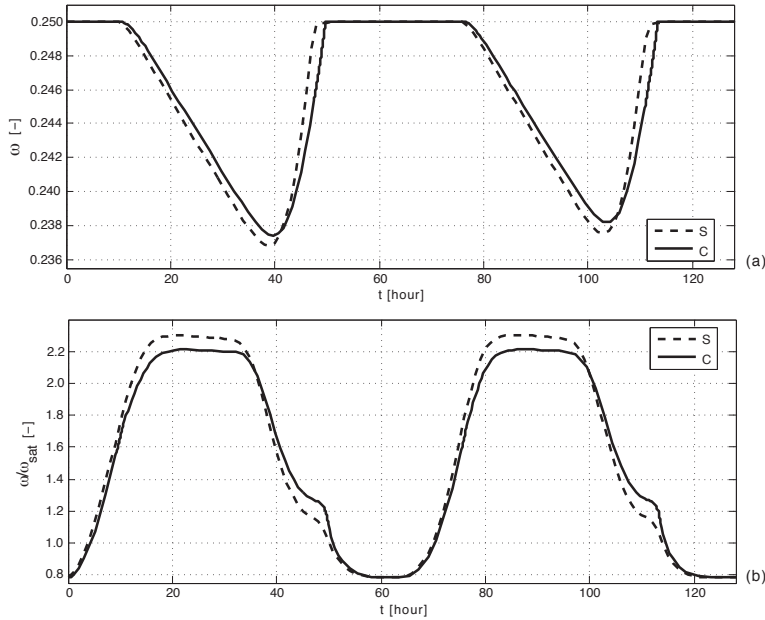


Figure 4.4: Test at constant humidity – dissolved salt concentration (a) and supersaturation ratio (b) in points S and C of the specimen saturated with sulphate solution 25 % wt

in Koniorczyk and Konca (2013). The volume of crystals that appear during cooling dissolves during warming up, so that the dissolved salt reaches the initial value. The cycle is repeated twice. The rate of liquid water trapped in hydrated salt crystal is shown in Figure 4.5b. As it can be noted, it is positive during the formation of mirabilite and negative during the dissolution process. As consequence, during the crystallisation of mirabilite the water content decreases because of the water trapped in the crystals, the reverse occurs during dissolution. Finally, the check on the mass balance in points S and C shows an error of 0.25%.

4.3.2 Test at constant temperature: hydration of thenardite

For the validation of the hydration kinetics, the experiment reported in Espinosa et al. (2008b) is studied. A specimen

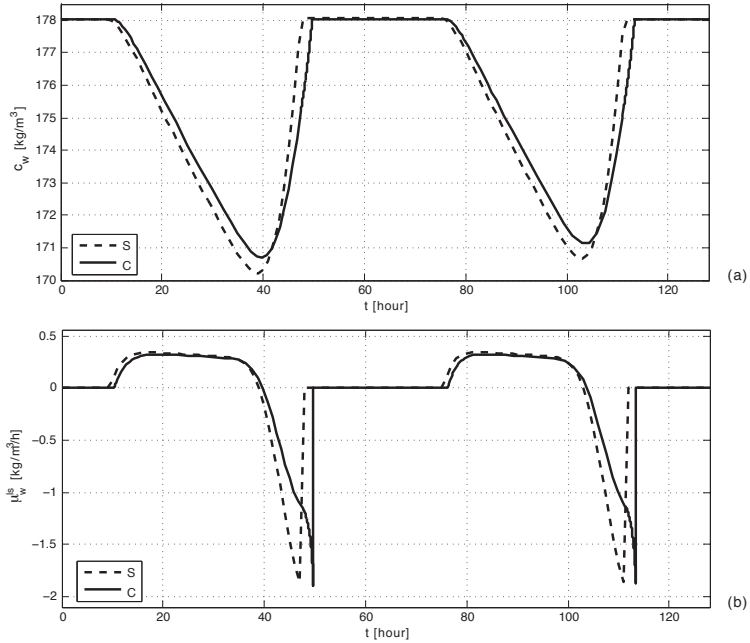


Figure 4.5: Test at constant humidity – saturation degree of precipitated mirabilite (a) and rate of liquid water trapped in hydrated salt crystal (b) in points S and C

of brick is posed in a climate chamber at constant temperature subjected to the change of humidity from 0.8 to 0.85. The hydration starts at humidity equal to 0.8 and proceeds slowly. When the humidity is increased to 0.85 the hydration goes on faster. Since during the hydration process water molecules are adsorbed or lost, the experiment is conducted with an automatic water adsorption measuring system to monitor the amount of water trapped or released. The experiment has been simulated with the proposed model. A cubic specimen with edge length of 1 cm is considered in the simulation. Null Neumann boundary conditions are imposed on all the faces for dissolved salt, while Robin boundary conditions are imposed for humidity. The temperature

is assumed to be constant. On all the edges of the domain (dashed line), boundary conditions are assumed as follows:

$$\underline{j}_w \cdot \underline{n} = \gamma_w(h_0 - h_\alpha), \quad \underline{j}_s^l \cdot \underline{n} = 0, \quad (4.7)$$

The problem domain and the finite element mesh are shown

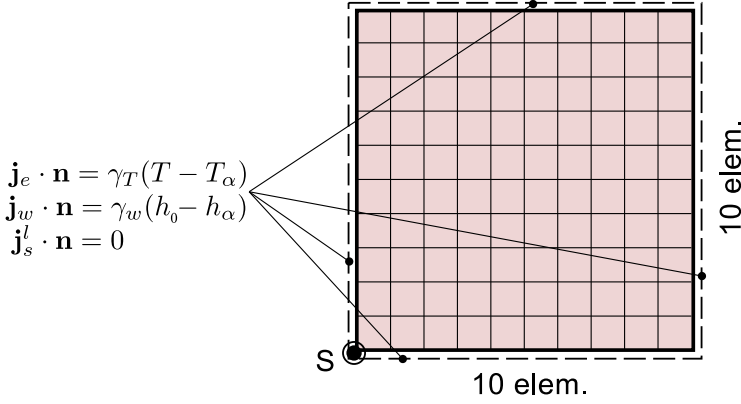


Figure 4.6: Problem domain – geometry and mesh

in Figure 4.6. The initial conditions are: $T_0 = 296.15$ K, $h_0 = 0.8$, $\omega_0 = 0.3$, $c_{s_1}^s(0) = 0$ kg/m³, $c_{s_2}^s(0) = 0.029(1 - \phi_0) \rho_{\text{brick}}$ kg/m³. The model parameters that are different from those used in the previous test are collected in Castellazzi et al. (2016). Figure 4.7 shows the environmental humidity together with the humidity of the specimen in point S (see Figure 4.6). Inspecting the graphs in Figures 4.7 and 4.8 reveals how the environmental humidity is reached in point S only after the end of the hydration process. Figure 4.8a, 4.8b shows the hydration process: the concentration of mirabilite $c_{s_1}^s$ increases and, in the meantime, the concentration of thenardite $c_{s_2}^s$ decreases. Moreover, it shows that, as expected, the concentration and the saturation degree of mirabilite obtained after the hydration process are higher than the thenardite one at the beginning. This is because mirabilite is a hydrous salt and its formation requires the adsorption of water molecules with a volume increase. In addition, it can be noted that, as expected, the precipitation rate of mirabilite

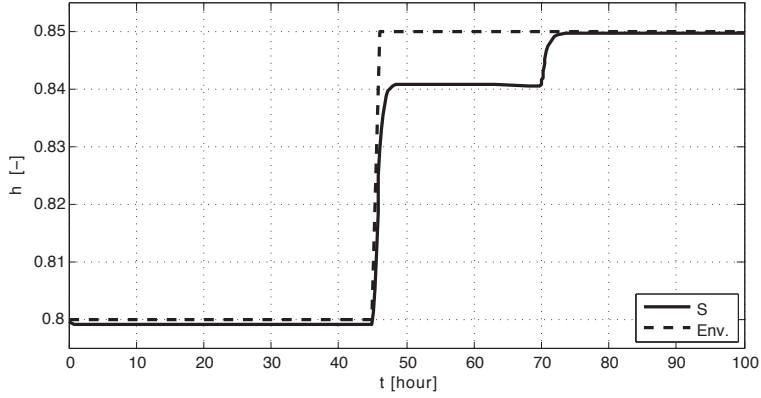


Figure 4.7: Test at constant temperature – humidity in point S and environmental humidity

is much faster upon increasing the environmental humidity. Obviously the same trend is followed by the saturation degree of the two crystallised forms. Finally, Figure 4.8c shows the rate of trapped liquid water and Figure 4.8d the water uptake referred to the dry mass of the brick. It is worth to note that the latter graph agrees with that reported in Espinosa et al. (2008b).

4.3.3 Test with varying temperature and humidity

A third example with variable conditions of temperature and humidity is presented here. The 1 cm edge square domain of Figure 4.6 is considered. It is assumed sealed to the dissolved salt. Robin boundary conditions for temperature and humidity are imposed on all the edges of the boundary:

$$\begin{aligned}
 \mathbf{j}_w \cdot \mathbf{n} &= \gamma_w (h_0 - h_\alpha), \\
 \mathbf{j}_s^l \cdot \mathbf{n} &= 0, \\
 \mathbf{j}_e \cdot \mathbf{n} &= \gamma_T (T - T_\alpha).
 \end{aligned} \tag{4.8}$$

The initial conditions are: $T_0 = 285$ K, $h_0 = 1$, $\omega_0 = 0.05$, $c_{s_1}^s(0) = 0$ kg/m³, $c_{s_2}^s(0) = 0$ kg/m³.

The material parameters used for the simulation are the same of the previous example. The environmental humid-

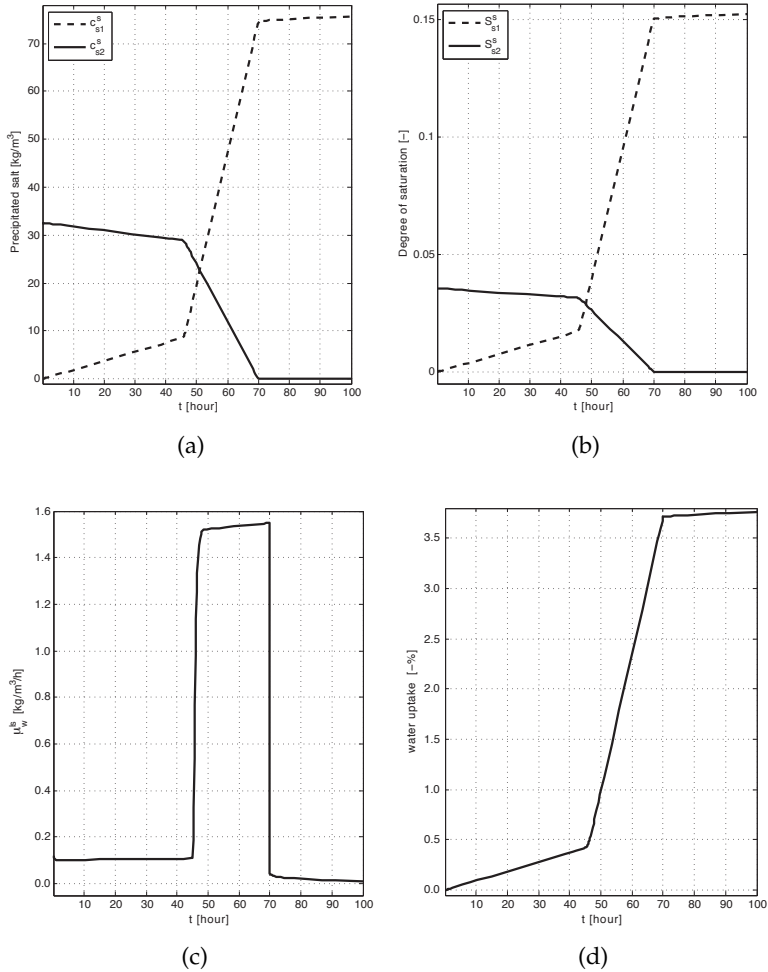


Figure 4.8: Test at constant temperature – concentration of precipitated mirabilite and thernardite (a) and the corresponding saturation degrees (b); rate of trapped liquid water (c) and water uptake referred to the dry mass of brick (d).

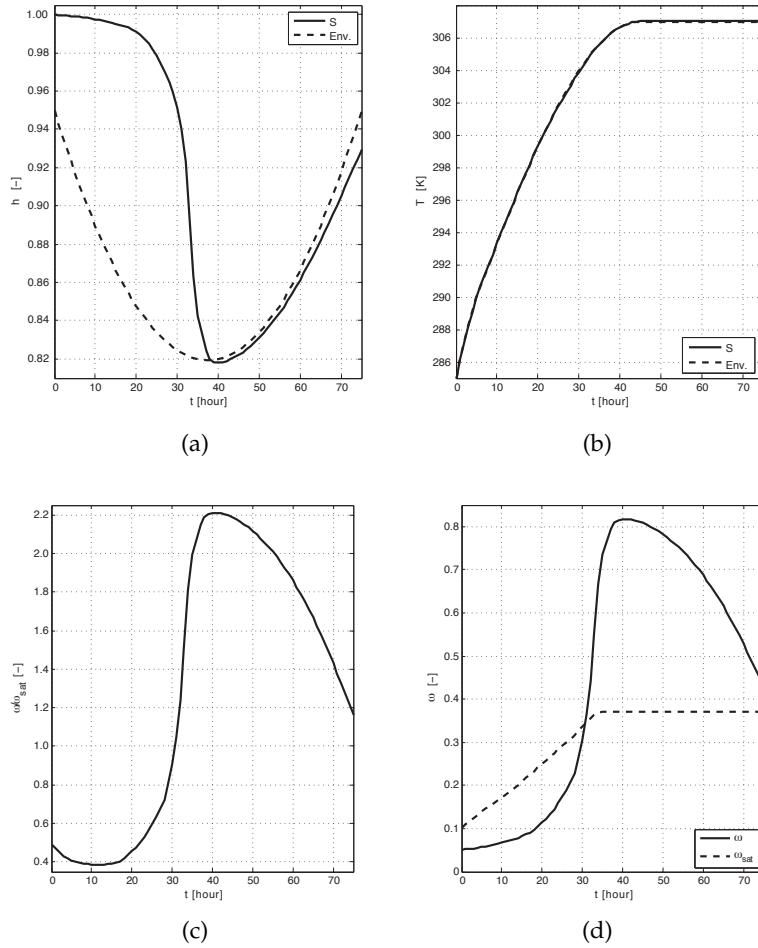


Figure 4.9: Test with varying temperature and humidity – humidity in point S and environmental humidity (a), temperature in point S and environmental temperature (b); supersaturation ratio (c), concentration of dissolved salt (d) in point S.

ity h_a and temperature T_a vary in time as illustrated in Figures 4.9a, 4.9b, dashed line. The environmental conditions have been chosen to comprehend both the processes, firstly the crystallisation and then the dehydration. The supersaturation ratio and the concentration of dissolved salt are shown in Figures 4.9c, 4.9d, while the concentration of precipitated mirabilite and thenardite and the saturation degree of precipitated mirabilite and thenardite in Figures 4.10a and 4.10b, respectively. Inspecting these graphs reveals that, due to the changing environmental conditions, at around 30 h the supersaturation ratio reaches 1 (see Figure 4.9a) and, since the temperature is under the temperature 303 K (see Figure 4.1a), the mirabilite starts to precipitate (see Figures 4.10a, 4.10b). After this, the conditions for dehydration are reached and the thenardite begins to form. Note that, as soon as the thenardite starts to form, the concentration of precipitated mirabilite decreases. Moreover, as expected, the concentration and the saturation degree of thenardite obtained after the dehydration process is lower than the mirabilite one at the beginning. Analogously to what observed for the precipitated salts concentrations, as soon as the amount of nuclei of the thenardite starts to increase, the one of the mirabilite decreases (Figure 4.10c). Finally, as expected, the rate of trapped water reveals a positive peak during the precipitation of mirabilite and a negative peak during the dehydration process (see Figure 4.10d).

4.4 CONCLUDING REMARKS

The Hygro-Thermo-Chemical (HTC) model proposed in Chapter 3 has been specialised for sodium sulphate solutions. The model has been validated through two benchmark tests taken from the literature, referred to sodium sulphate solutions and involving isothermal or isohygral conditions. Moreover, in order to show the potentialities of the model in more realistic cases, an example with non-isothermal and non-isohygral conditions has been discussed. In all, the numerical results, in very good agreement with the experimen-

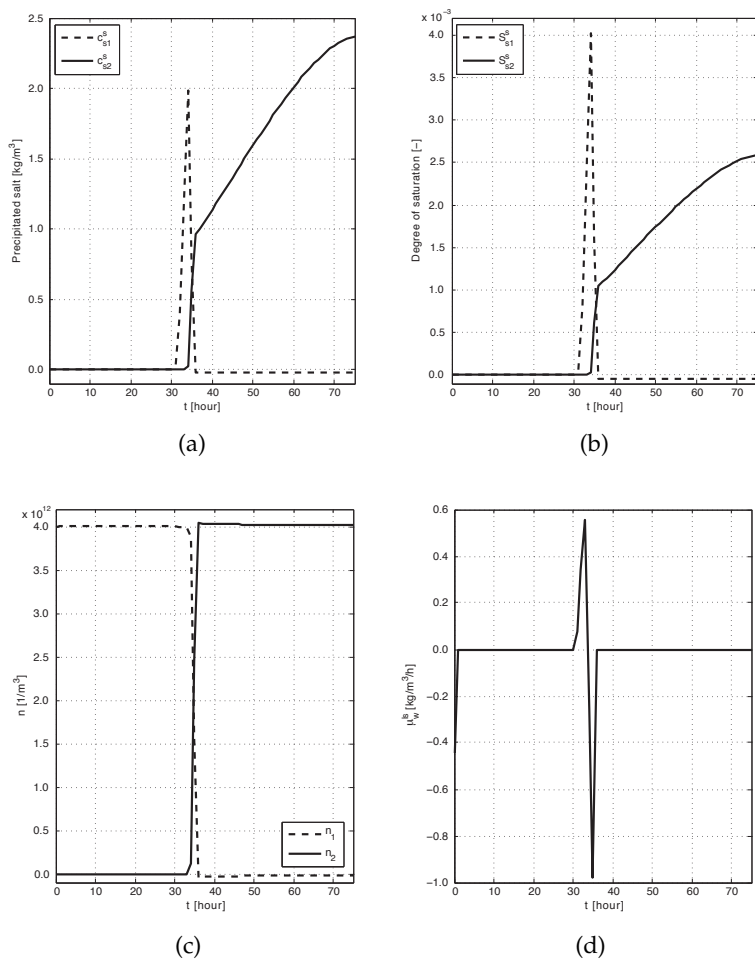


Figure 4.10: Test with varying temperature and humidity – concentration of precipitated mirabilite and thenardite (a), saturation degree of precipitated mirabilite and thenardite (b) in point S; number of nuclei of mirabilite (n_1) and of thenardite (n_2) (c), rate of trapped liquid water (d) in point S.

tal evidences, demonstrate the effectiveness of the proposed approach.

SODIUM CHLORIDE SOLUTION

The HTC Model is specialized for sodium chloride solutions. In addition, the role of temperature in modelling and simulation of the whole phenomenon is investigated, with emphasis on the precipitated salt. Thermal effects on sorption/desorption curves and on system coefficients are discussed. In particular, a correlation between sorption/desorption curves at various temperatures is presented and some system parameters depending on temperature are analysed. Moreover, the salt diffusion and crystallisation process in a masonry column exposed to weather conditions is simulated both in isothermal and non-isothermal regime and the results are compared and discussed.

5.1 SPECIALISATION

The HTC model presented in Chapter 3 can be specialised for a great range of electrolytic salts. Here, it is specialized for sodium chloride solutions. This leads to the same equations presented in Castellazzi et al. (2013a), which are a particular case of the HTC model.

According to the experimental solubility diagram of sodium chloride solution (Derluyn, 2012; Steiger et al., 2008) in which are shown solubility lines and expressing the equilibrium concentration in function of temperature for the specific salt crystal phase, when water is the solvent, under 273 K the salt crystallises into a hydrated form, but if we consider a range of temperatures greater than 273 K, halite is the only crystallised form (*i. e.* $N=1$).

In this case there are no hydration/ dehydration processes and ω_{sat} can be assumed constant with temperature. If we consider a sodium chloride solution in a range of temperature greater than 273 K, μ_w^{ls} can be set equal to zero, because in this case there are not hydrated forms.

Finally, the degrees of saturation of all the components satisfy the relation:

$$S_w^g + S_w^l + S_s^l + S_s^s = 1, \quad (5.1)$$

where S_s^s is the degree of saturation of the crystallised salt.

If we take into account the following dependencies:

$S_{ws}^l = S_{ws}^l(h, \omega, T)$, $p_{v,sat} = p_{v,sat}(\omega, T)$, $H_{eva}(T)$, $H_{cry}(T)$ and the contribution of effective porosity ϕ_{eff} , the resulting governing equations of the model (3.68)-(3.71) become:

$$\begin{aligned} \varphi_h \frac{\partial h}{\partial t} + \nabla \cdot [-C_{hh} \nabla h - C_{hT} \nabla T - C_{h\omega} \nabla \omega] + \\ + \varphi_{h\omega} \frac{\partial \omega}{\partial t} + \varphi_{hT} \frac{\partial T}{\partial t} + \varphi_{hs} \frac{\partial c_s^s}{\partial t} = 0 \end{aligned} \quad (5.2)$$

$$\begin{aligned} \varphi_\omega \frac{\partial \omega}{\partial t} + \nabla \cdot [-C_{\omega h} \nabla h - C_{\omega T} \nabla T - C_{\omega\omega} \nabla \omega] + \\ + \varphi_{\omega h} \frac{\partial h}{\partial t} + \varphi_{\omega T} \frac{\partial T}{\partial t} + \varphi_s \frac{\partial c_s^s}{\partial t} = 0 \end{aligned} \quad (5.3)$$

$$\begin{aligned} \varphi_T \frac{\partial T}{\partial t} \nabla \cdot [-C_{TT} \nabla T - C_{Th} \nabla h - C_{T\omega} \nabla \omega] + \\ + \varphi_{Ts} \frac{\partial c_s^s}{\partial t} + \mu_w^{lg} B_w = 0 \end{aligned} \quad (5.4)$$

$$\frac{\partial c_s^s}{\partial t} = \begin{cases} C_{ss} \left| \frac{\omega}{\omega_{sat}} - 1 \right|^p & \text{if } \omega \geq \alpha_0 \omega_{sat} \\ -C_{ss} \left| \frac{\omega}{\omega_{sat}} - 1 \right|^p & \text{if } \omega \leq \omega_{sat} \text{ and } c_s^s > 0 \end{cases} \quad (5.5)$$

Field equations are completed with the boundary and initial conditions. Here we recall the Dirichlet ones (3.73):

$$\begin{aligned} h &= \bar{h}, \\ \omega &= \bar{\omega}, \\ T &= \bar{T}, \end{aligned} \quad (5.6)$$

and the Neumann's or Robin's ones (3.74):

$$\begin{aligned} \underline{j}_w \cdot \underline{n} &= q_w + \gamma_w (h_0 - h_\alpha), \\ \underline{j}_s^l \cdot \underline{n} &= q_\omega, \\ \underline{j}_e \cdot \underline{n} &= q_T + \gamma_T (T - T_\alpha). \end{aligned} \quad (5.7)$$

5.2 THERMAL EFFECTS

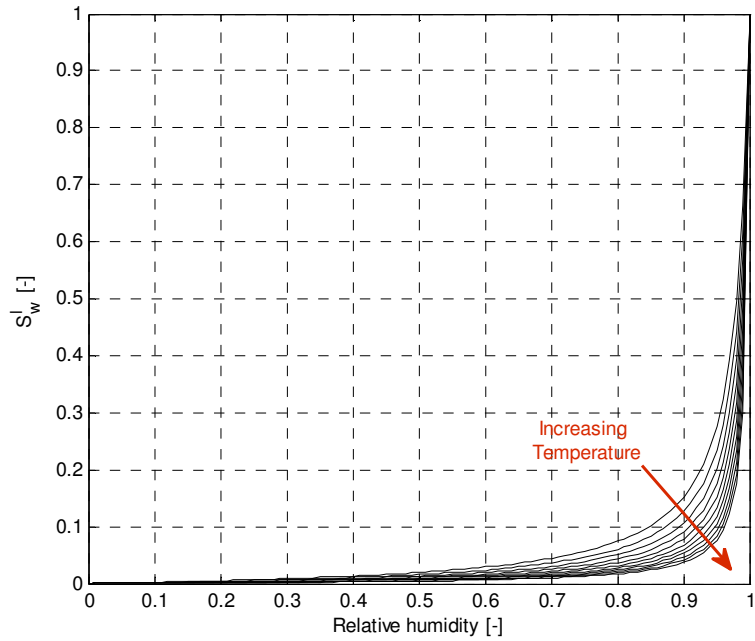
Considering thermal effects is essential for salts which have solubility and phase diagrams depending on temperature, like sulphates. Nevertheless, thermal effects are also relevant on salts which have the mass fraction of dissolved salt at saturation ω_{sat} nearly constant with temperature (*i.e.* sodium chloride) as will be shown in the following. In this section, thermal effects on sorption/desorption curves and on system coefficients are discussed. Starting from the assumption of instantaneous equilibrium between liquid and vapour water, the moisture content at a certain temperature can be expressed as a function of the relative humidity, through a sorption/desorption isotherm. The analytical expression for sorption/desorption curves for isothermal regime, proposed in Sýkora et al. (2012), is extended to non-isothermal regime with Eq. (3.42), where it has been assumed that Ψ depends on the temperature. The correlation between Ψ and T can be obtained fitting experimental data or using the modified Oswin model (Karoglou et al., 2005) which allows to investigate the dependency of S_{ws}^{l} on temperature:

$$c_w = c_m^s b_0 \exp\left(\frac{b_1}{T}\right) \left(\frac{h}{1-h}\right)^{b_2}, \quad (5.8)$$

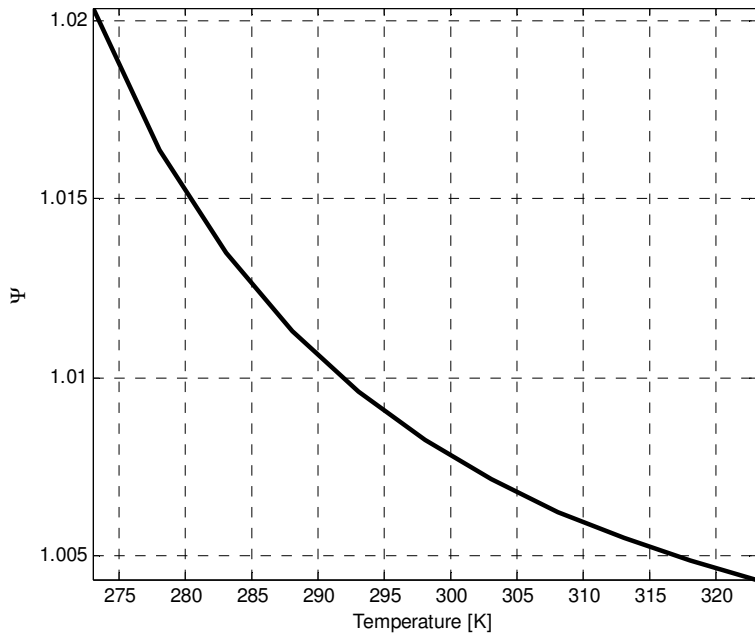
where b_0 , b_1 , b_2 are parameters which can be tuned experimentally. For a fired-clay brick, Figure 5.1a shows the sorption isotherms at different temperatures obtained using Eq. (3.42) for pure water, while the qualitative trend of $\Psi(T)$, obtained fitting the data predicted by the modified Oswin model, is depicted in Figure 5.1b. Note that increasing temperature, Ψ decreases.

In section 5.1 are shown the moisture balance equation (5.3) expressed in terms of the moisture diffusivity coefficients:

$$\begin{aligned} C_{hT}^{\text{l}} &= (1 - \omega) \rho_w^{\text{l}} R_v \ln(h) K_l, \\ C_{hT}^{\text{g}} &= \frac{D_v h}{R_v T} \frac{\partial p_{v,\text{sat}}}{\partial T}, \\ C_{hT} &= C_{hT}^{\text{l}} + C_{hT}^{\text{g}}, \end{aligned} \quad (5.9)$$



(a)



(b)

Figure 5.1: Sorption isotherms from 273 K to 323 K for pure water implementing Eq. (3.42) (a); trend of Ψ function of temperature (b)

and the energy equation in terms of the thermal conductivities:

$$\begin{aligned}
 C_{TT}^l &= (\beta_w^l(1 - \omega) + \beta_s^l) \rho_w^l R_v \ln(h) K_l T, \\
 C_{TT}^g &= (\beta_w^g T + H_{eva}) \frac{D_v h}{R_v T} \frac{\partial p_{v,sat}}{\partial T}, \\
 C_{TT}^{g+l} &= C_{TT}^l + C_{TT}^g.
 \end{aligned} \tag{5.10}$$

Figure 5.2 illustrates the moisture diffusivity coefficients

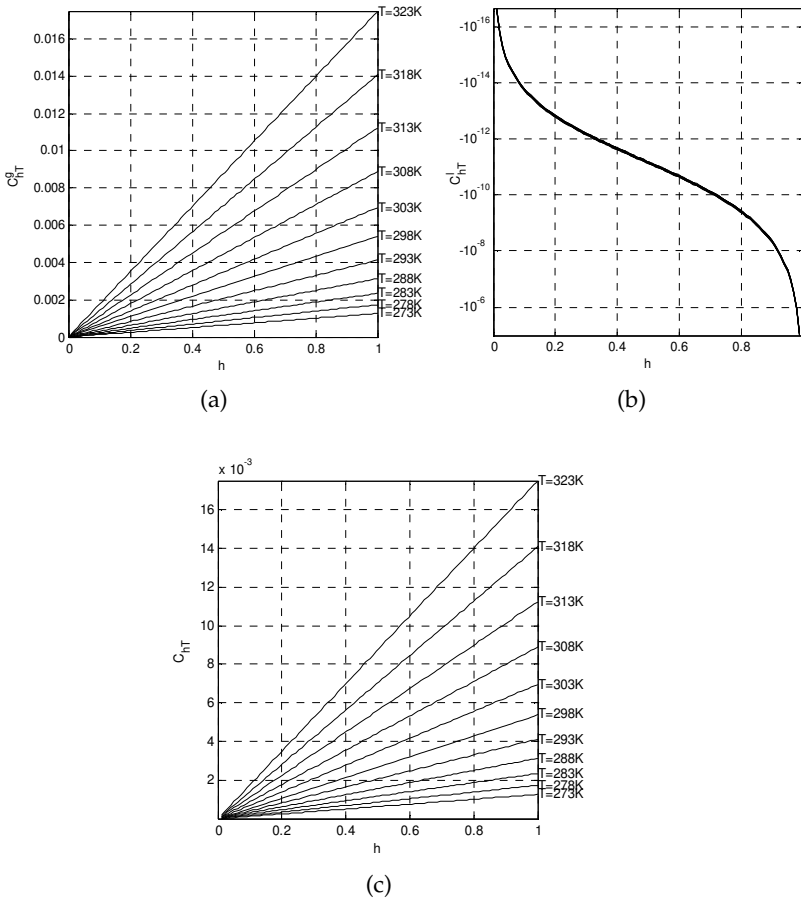


Figure 5.2: Trend of C_{hT}^g (a) , C_{hT}^l (b) , C_{hT} (c) with relative humidity in a range of temperatures from 273 K to 323 K.

C_{hT}^g , C_{hT}^l and C_{hT} against equivalent relative humidity for

different values of the temperature. As it can be noted, the variation of C_{hT}^g with temperature is remarkable, increasing with high temperature. In fact, increasing temperature increases the humidity diffusion. On the other hand, the variation with temperature of C_{hT}^l is very small and it is equal zero when $h=1$. Finally, the resultant C_{hT} coefficients is plotted in Figure 5.2c. Note that, as expected, the contribution of C_{hT}^g is predominant respect with C_{hT}^l . Figure 5.3 shows the

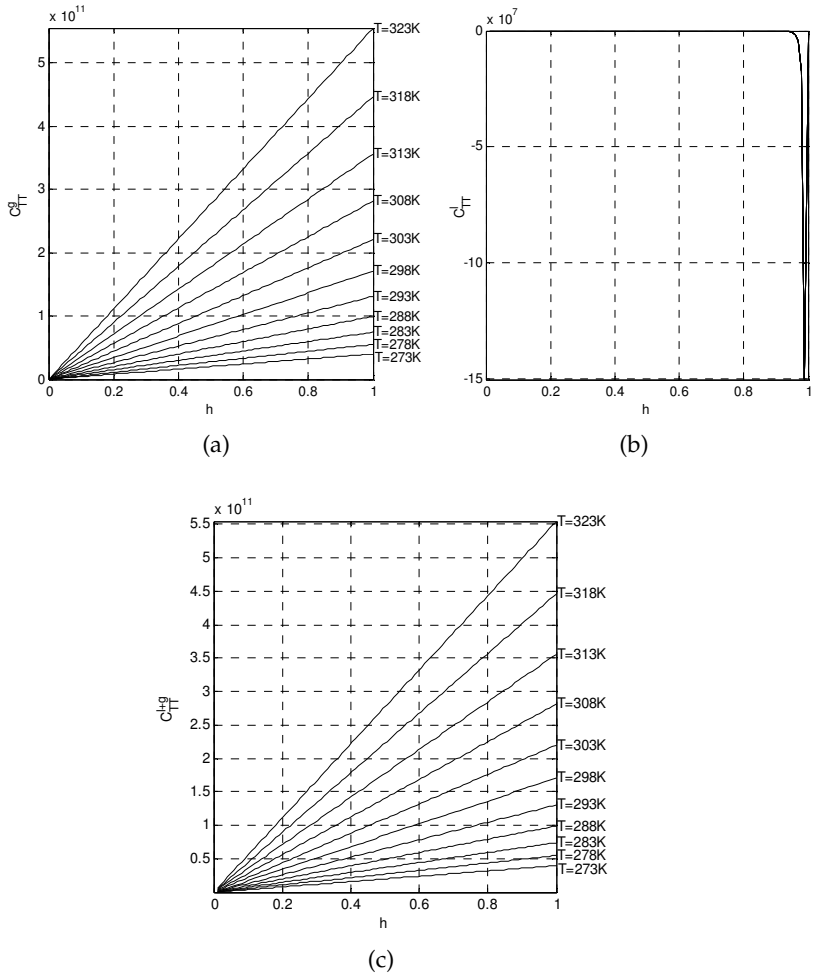


Figure 5.3: Trend of C_{TT}^g (a) , C_{TT}^l (b) , C_{TT}^{g+l} (c) with equivalent relative humidity in a range of temperatures from 273 K to 323 K, for $\omega = 0$.

thermal conductivity due to liquid water, C_{TT}^l , and water vapour, C_{TT}^g , against equivalent relative humidity for different temperatures and $\omega = 0$ (pure water). Analogously to what observed for the moisture diffusivity coefficients, the variation of C_{TT}^g with temperature is remarkable, increasing with high temperature. On the other hand the variation with temperature of C_{TT}^l is very small and it is equal zero when $h = 1$. This latter term makes C_{TT}^{g+l} almost discontinuous.

5.3 NUMERICAL APPLICATIONS

In this section, the predictive capabilities of the HTC model specialised for sodium chloride solutions, described in 5.1, are evaluated in a masonry column of $25 \times 25 \times 75$ cm exposed to weather conditions from June 2010 to the end of

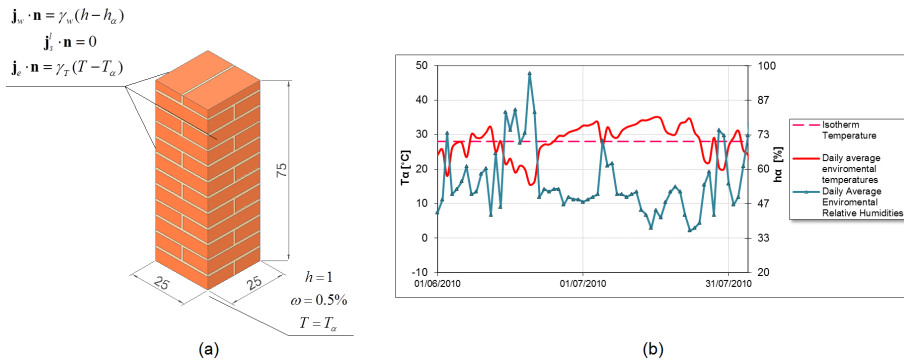


Figure 5.4: Geometry of the masonry column and Boundary Conditions (a); environmental temperatures and humidities in Bologna of June and July 2010 (b).

July 2010 in Bologna with the bottom face immersed in a NaCl aqueous solution with $\omega = 0.05\%$ (see Figure 5.4a). In these tests the masonry column is modelled as an equivalent homogeneous material and the liquid phase inside it is assumed an ideal solution.

Attention will be paid to effects of the temperature on the salt transport and crystallisation processes, thus NaCl salt is ideal because the mass fraction at saturation is nearly constant with temperature $\omega_{\text{sat}} = 0.264 \text{ kg}_{\text{salt}}/\text{kg}_{\text{solution}}$. In

particular, the same sample is studied in isothermal and non-isothermal regime. For simulations in non-isothermal regime, daily environmental average humidities and temperatures in Bologna from June 2010 to the end of July 2010 are chosen as boundary conditions (Figure 5.4). For the isothermal regime, the simulation is performed at the average temperature in the whole period of 2 months (28 °C), as shown in Figure 5.4b. In order to implement the model, the equations are discretized in space using the finite element method. The primary variables h , ω , c_s^s and T are interpolated based on standard Lagrangian shape functions. 27-node brick elements with quadratic shape functions are adopted. The time discretization is carried out by means of the backward finite difference method. A standard iterative strategy based on the Newton-Raphson method is applied to solve the non-linear system of equations. The implementation is developed using COMSOL MultiPhysics comsol2008. The typical element size for the finite element mesh is around 3.5 cm. The total number of degrees of freedom is 38,700. The wall is modelled as an equivalent brick Castella2013717. Figure 5.5 shows the maps of temperature in

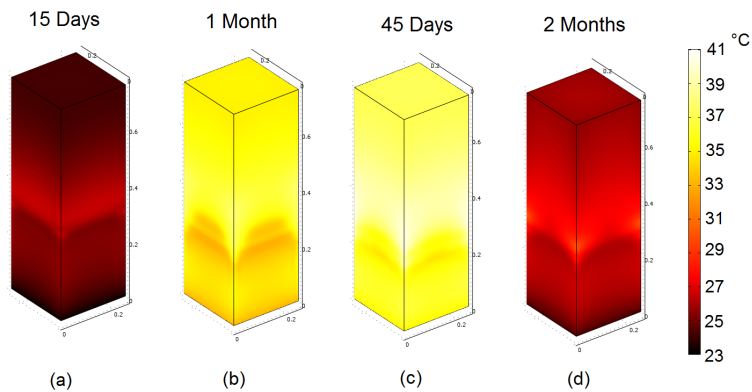


Figure 5.5: Evolution of temperature at 15 days (a), 1 month (b), 45 days (c) and 2 months (d).

non-isothermal regime after 15 days (b), 1 month (c), 45 days (d) and 2 months (e). Note that the rising water front is evident in the map of the temperature, in which it is possible to

see a lower temperature due to the hygro-thermal coupling. In Figure 5.6 a comparison between maps of equivalent rel-

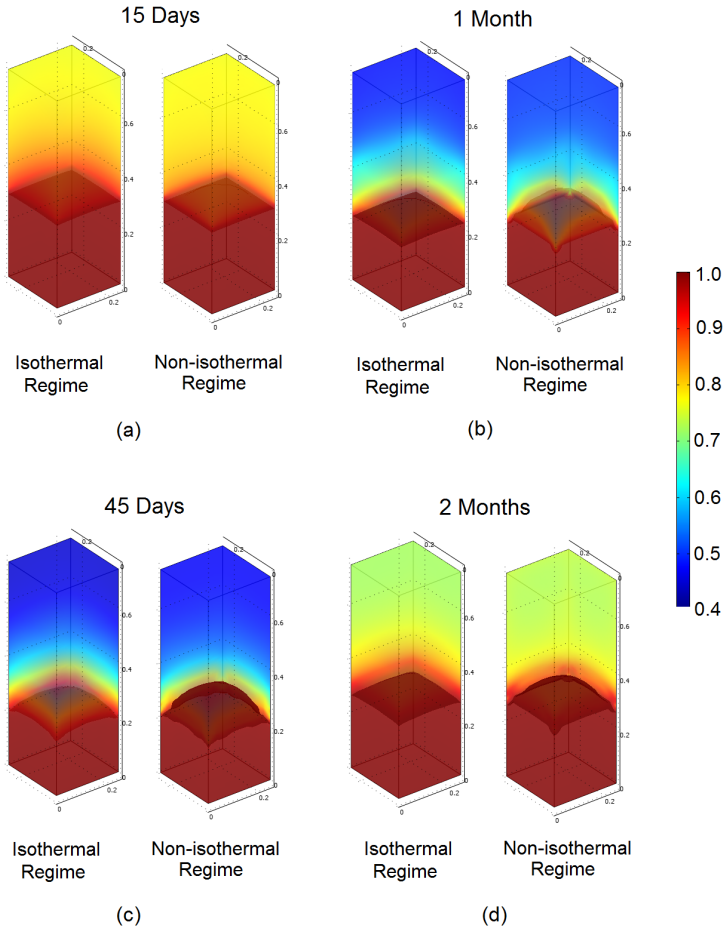


Figure 5.6: Relative humidity in isothermal regime and non-isothermal regime at 15 days (a), 1 month (b), 45 days (c) and 2 months (d).

ative humidity in isothermal and non-isothermal regime is made. The height of damp rising is the same, but in the case of isothermal regime the humidity is more diffused. Figure 5.7 shows that in non-isothermal regime higher values of supersaturation ratio are reached, leading to a greater amount of precipitated salt, as displayed in Figure 5.8. In particular, Figure 5.8 shows that the salt precipitation starts at the cor-

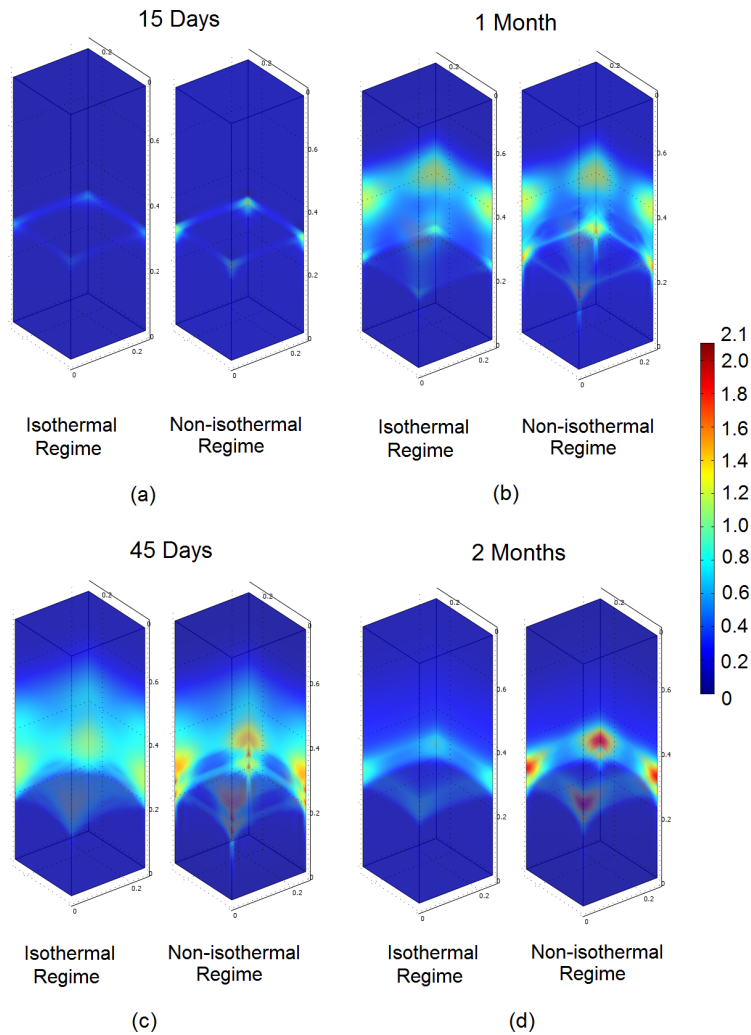


Figure 5.7: Supersaturation ratio ω/ω_{sat} in isothermal regime and non-isothermal regime at 15 days (a), 1 month (b), 45 days (c) and 2 months (d).

ners of the sample, proceeding on the faces and in the inner part of the masonry column. As it can be noted, the patterns of crystallised salt in isothermal and non-isothermal regime are considerably different.

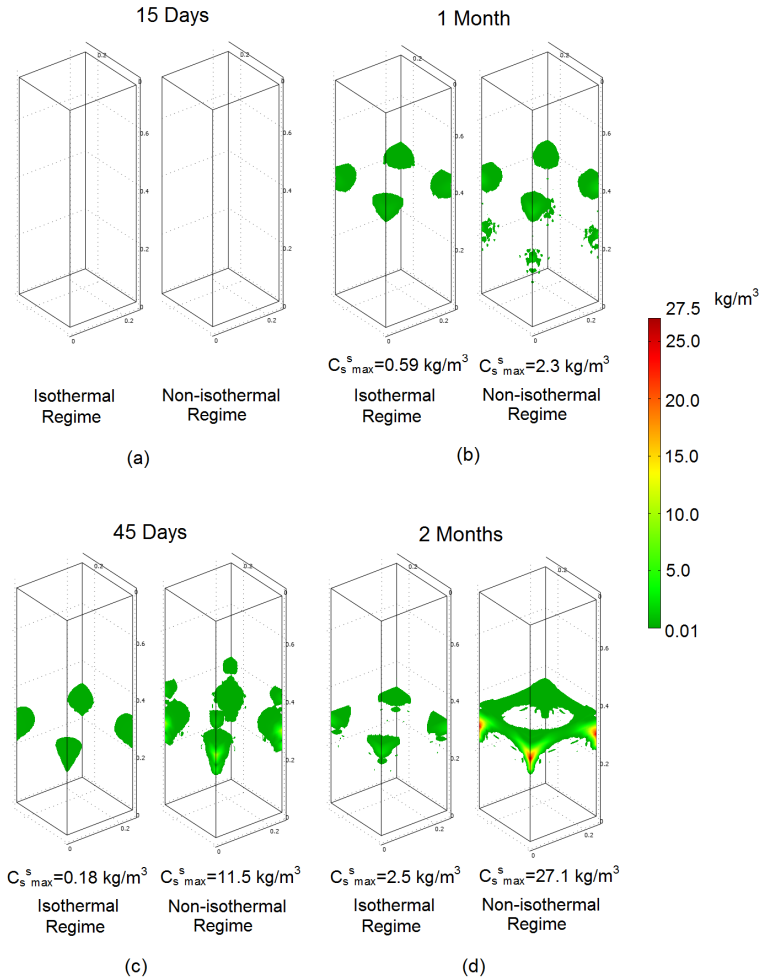


Figure 5.8: Precipitated NaCl in isothermal regime and non-isothermal regime at 15 days (a), 1 month (b), 45 days (c) and 2 months (d).

5.4 CONCLUDING REMARKS

The Hygro-Thermo-Chemical (HTC) model proposed in Chapter 3 has been specialised for sodium chloride solutions. Then, the influence of the thermal effects on salt transport and crystallisation in masonry structures has been investigated. A correlation between sorption/desorption curves at

various temperatures has been presented and some model parameters depending on temperature have been analysed. The HTC model specialised for sodium chloride solutions has been employed to simulate the capillary rising of a sodium chloride solution in a masonry column in isothermal and non-isothermal regime. The comparison between the results of isothermal and non-isothermal simulations shows that thermal effects have great influence on the transport process and can considerably alter the salt crystallisation pattern. Moreover, numerical results presented show how the HTC model is able to reproduce the physics of the phenomenon at the scale of the structure.

INSIGHT ON BOUNDARY CONDITIONS

In this Chapter the HTC model is enriched in order to describe different drying kinetics, taking into account the different efflorescence formations. Indeed, some experiments recently appeared in the literature about the drying of porous media in the presence of salt have shown that the kinetics of drying strongly depends not only upon the quantity of precipitated salt but also upon the form in which the salt precipitates. The enriched HTC model is then validated through two different extensive campaigns on drying in presence of sodium chloride salt solution.

6.1 INTRODUCTION

Drying of porous media in the presence of salt is a very common phenomenon, which causes the formation of salt crystals in the porous medium. Despite many contributions in the literature have dealt with the drying of salt contaminated porous materials, as illustrated in Section 2.1.1, this topic is still under discussion especially regarding the influence of salt crystallisation on drying. The problem of the evaporation in porous media filled with a salt solution is very complex from the modelling point of view because the diffusion and crystallisation of the salt in porous media depends not only on the transport of water and salt in different forms (gas, solid, liquid) but also on the phase transitions between them and furthermore on the interactions between the various processes. In order to describe this phenomenon we extend the HTC model presented in Chapter 3 and specialised for NaCl solutions in Chapter 5, taking into account for the different formations of efflorescences influenced by the environmental conditions. The model is then validated through two extensive experimental campaigns, illustrated

in the next Section (see also Section 2.1.1) and performed within the European project called KISADAMA (de Miranda et al., 2013).

6.2 EXPERIMENTAL CAMPAIGNS

We consider two parallel experimental campaigns on samples of cylindrical shape made by Prague (Mšené) sandstone with porosity $\phi_0 \sim 29\%$ and average pore diameter of $30 \mu\text{m}$. The specimens were initially saturated with a NaCl solution at saturation (6.1 M, $\omega = 0.264$) and subsequently dried at different RH-values.

The first campaign was partly conducted at Van der Waals-Zeeman Institute of the University of Amsterdam and partly at the Centre for X-ray Tomography at the Ghent University (UGCT) (Desarnaud et al., 2015); while the second one was totally performed at UGCT in Ghent.

During the first campaign the drying kinetics of cylindrical samples (diameter of 8.5 mm and height 8.5 mm) imbibed by a NaCl saturated solution were followed through automated balance with a precision of 0.001 g placed in a home-made, controlled climatic chamber at $T=21 \text{ }^\circ\text{C}$, at RH $\sim 20\%$, 40% and 50%.

The crystallisation in the core of the stone and at the surface were investigated for RH $\sim 20\%$ and 50% using high resolution X-ray μCT , optical and Scanning Electron Microscopy (SEM) combined with Energy Dispersive Spectroscopy (EDS). X-ray μCT performed at the Centre for X-ray Tomography at the Ghent University (UGCT) using the scanner HECTOR (Masschaele et al., 2013). The samples were initially scanned at the end of the drying process, and subsequently washed out to be scanned in their natural state.

At RH 50%, the typical drying behaviour is found with a constant drying rate during almost all the drying process. Only in the a very late stage a much slower drying kinetics is measured. At RH $\sim 20\%$ the drying behaviour of the sample consists of three regimes: first a constant drying rate until the residual saturation is roughly half of the initial sat-

uration, a second regime in which the drying kinetics follows an exponential decrease and a third regime in which the drying rate is much slower. The change in the drying kinetics is due to the different types of efflorescence formation arose in the surface of the specimen. In particular in the drying test performed at 50% RH, the efflorescences formed at the surface after drying is of "patchy" type and it allows the water evaporation, while in case of the drying test performed at 20% RH the formation is of "crusty" type and it drastically reduces the water evaporation. The different formations on the surface of the specimen are evident from the SEM pictures reported in Figure 6.1 and 6.2, for drying tests performed at environmental humidity equal to 50% RH and 20% RH, respectively. In the case of test performed at 20% RH, the salt skin which covers the outer surface of the sandstone is itself a porous medium with a mean pore size of about $3\ \mu\text{m}$, *i. e.* 10 times smaller than the pore diameter of sandstone.

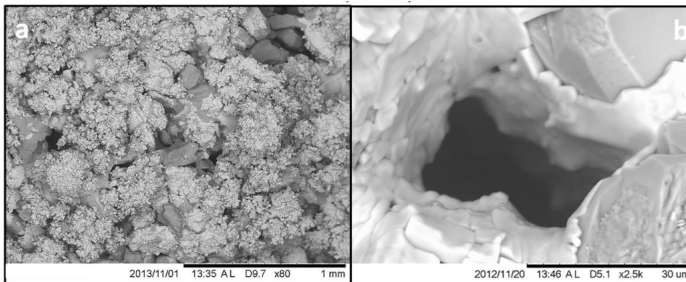


Figure 6.1: Drying at 50% RH. SEM pictures: (a) Patchy efflorescences formed at the surface after drying. (b) Crystallization of NaCl inside the wetting films at the corners of the pores. (Desarnaud et al., 2015)

In the second campaign, the drying kinetics has been investigated with a 4D X-ray μCT monitoring, the set-up is reported in Derluyn et al. (2016, 2015). Two cylindrical samples of 8 mm in diameter and 10 mm in height were cored from a Mšené sandstone specimen.

The samples were initially scanned in their dry state at the

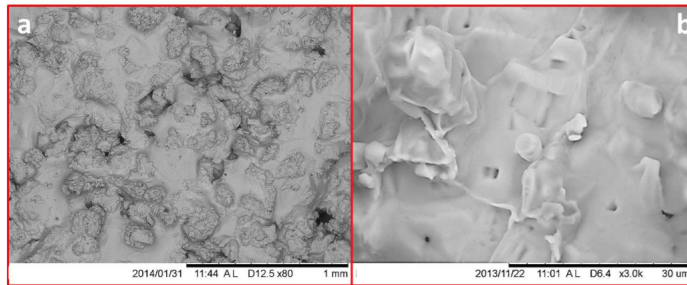


Figure 6.2: Drying at 20% RH. SEM pictures: (a) crust formed at the surface after drying. (b) details of the porous crust. (Desarnaud et al., 2015)

μ mCT scanner HECTOR of the UGCT. Next, the samples were capillary saturated by immersing them in a saturated NaCl solution for 30 minutes. The samples were then scanned in their wet state and during their drying every 30 minutes for the first 3 hours, and every hour during the succeeding 12 hours. Drying was controlled by placing the sample in a custom-built climatic chamber, compatible with the X-ray scanner, having an inner volume of $4 \times 4 \times 3 \text{ cm}^3$. Conditioned air is blown in the plexi-glass test chamber at a slow rate (3.3 ml/s). The drying was performed at the constant temperature of 19.2 °C and a RH of 20% for the first specimen and at RH 50% for the second one.

Each scan resulted in a 3D volume of the upper 6 mm of the sample with a reconstructed voxel size of 10 μ m. Due to the maximal spatial resolution aimed for, the complete height of the cylindrical samples could not be imaged in the field of view defined by the HECTOR set-up. The 3D volumes were further analysed with the software AVIZO (FEI). By working with differential images (Boone et al., 2014), the salt solution in the sample and the crystal precipitation could be segmented, allowing to simultaneously obtain quantitative data on the drying and the precipitation kinetics. These data were calculated as volumetric ratios, *i. e.*, the volume of solution/crystals with respect to the sample's volume. It needs to be remarked that the quantification based on the 4D X-ray μ CT imaging is limited in accuracy by

the spatial resolution of 10 μm and by the image analysis procedure, and as such can never be as precise as raw balance measurements to assess the drying kinetics. The added advantage however is that these dynamic imaging datasets provide also data on the crystallisation kinetics and enable the analysis of drying and precipitation at the pore scale level. The results of the experimental campaign confirmed the kinetics seen in the first experimental campaign with the added value to see the 4D map of whole process in terms of crystallised salt and of water lose.

6.3 SPECIALISATION

The model presented in Chapter 3 and specialised in Chapter 5 for sodium chloride solutions is extended in order to take into account the possible formation of superficial salt crust. The thermal part is not considered, since experiments are carried out in isothermal conditions.

Thus, the equations of the model can be summarized in the following form:

$$\varphi_h \frac{\partial h}{\partial t} + \nabla \cdot [-C_{hh} \nabla h - C_{hw} \nabla \omega] + \varphi_{hw} \frac{\partial \omega}{\partial t} + \varphi_{hs} \frac{\partial c_s^s}{\partial t} = 0, \quad (6.1a)$$

$$\varphi_\omega \frac{\partial \omega}{\partial t} + \nabla \cdot [-C_{\omega h} \nabla h - C_{\omega\omega} \nabla \omega] + \varphi_{\omega h} \frac{\partial h}{\partial t} + \varphi_s \frac{\partial c_s^s}{\partial t} = 0, \quad (6.1b)$$

$$\frac{\partial c_s^s}{\partial t} = \pm C_{ss} \left| \frac{\omega}{\omega_{\text{sat}}} - 1 \right|^p. \quad (6.1c)$$

The coefficients φ_i and C_{ij} , used in expressions (6.1), are reported in Appendix C. The equations describing the model are completed by the initial and boundary conditions. They can be of Dirichlet type:

$$h = \bar{h}, \quad (6.2)$$

$$\omega = \bar{\omega}, \quad (6.3)$$

and of Neumann's or Robin's type:

$$\underline{j}_w \cdot \underline{n} = q_w + \gamma_w (a_w h - h_\alpha) \quad (6.4)$$

$$\underline{j}_s^l = q_\omega, \quad (6.5)$$

where \underline{n} represents the outward unit normal to the boundary. It is worth noting that $a_w h = h_0$ takes into account the presence of salt: for sodium chloride solutions, a_w is equal to 1 when $\omega = 0$ and equal to 0.75 when $\omega = \omega_{\text{sat}}$ (see Barbosa-Canovas et al. (2007) and Figure 6.3).

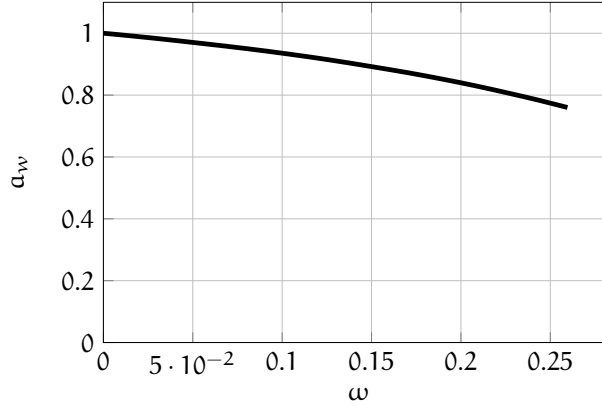


Figure 6.3: Water activity of a sodium chloride solution as a function of mass fraction (Barbosa-Canovas et al., 2007)

Moreover, \bar{h} and $\bar{\omega}$ represent the prescribed equivalent relative humidity and salt concentration, respectively; q_w and q_ω denote the prescribed normal fluxes of moisture and salt, respectively; h_α is the prescribed environmental relative humidity. Finally, γ_w is the convective humidity coefficient: a new expression will be proposed in the next section, on the basis of experimental evidences.

6.4 CONVECTIVE HUMIDITY COEFFICIENT

From the experimental evidences (Desarnaud et al., 2015), it is clear that the drying kinetics depends not only on the quantity of precipitated salt but also on the form in which the salt precipitates (for example patchy or crusty or something in between). The different forms of the precipitated salt are function of the gap between the initial relative humidity of the specimen surface and the environmental relative humidity, $\Delta h_0 = a_w h(0) - h_\alpha$.

Indeed, to describe the real physics of the drying kinetics, the convective humidity coefficient γ_w is considered not only function of the degree of saturation of the crystallised salt S_s^s but also of the relative humidity gap Δh_0 . In particular γ_w is considered constant and equal to the value of the convective coefficient in case of pure water, $\bar{\gamma}_w$, if the crystallised salt saturation degree does not reach a threshold value \bar{S}_s^s . Then, when the saturation degree of crystallised salt exceeds \bar{S}_s^s , γ_w generally decreases in relation to Δh_0 which influences the form of the crystallised salt. The convective coefficient can decrease till a residual value $\bar{\gamma}_{\text{crust}}$. This value is reached when $S_s^s = 1$ and takes into account that the salt crystal is itself a porous medium. The expression of γ_w can be formulated as:

$$\gamma_w = (\bar{\gamma}_w - \bar{\gamma}_{\text{crust}}) e^{-k \phi_0 \rho_s^s S_s^s} + \bar{\gamma}_{\text{crust}}. \quad (6.6)$$

where $k \geq 0$ is a linear function of the initial humidity gap Δh_0 :

$$k = \begin{cases} 0 & \text{if } S_s^s \leq \bar{S}_s^s, \\ k(\Delta h_0) & \text{if } S_s^s > \bar{S}_s^s. \end{cases} \quad (6.7)$$

The expression reduces to $\bar{\gamma}_w$ for $S_s^s = 0$ while for $S_s^s \geq 0$ the decreasing function is modulated by the parameter k .

Since the dependence of k on Δh_0 is considered linear, k can be tuned with two drying experiments named 1 and 2, and computed as follows:

$$k = \frac{k_1 - k_2}{\Delta h_0^{(1)} - \Delta h_0^{(2)}} \left(\Delta h_0 - \Delta h_0^{(2)} \right) + k_2 \quad \text{if } S_s^s > \bar{S}_s^s, \quad (6.8)$$

where k_1 and k_2 are coefficients tuned with two drying experiments having initial humidity gap $\Delta h_0^{(1)}$ and $\Delta h_0^{(2)}$, respectively. The effect of air velocity on the convective humidity coefficient is not explicitly considered in this model.

6.5 SIMULATION OF DRYING EXPERIMENTS

The model has been coded by means of COMSOL Multiphysics (COMSOL, 2008). The non-linear system of equations is solved through a standard iterative strategy, based

on Newton-Raphson method. The time discretisation is carried out by means of the backward finite difference method and the space discretisation is performed by the finite element method. Brick elements with standard Lagrangian quadratic shape functions are adopted. Each specimen has been spatially discretised with smaller finite elements in correspondence of the external surface, since it is the area in which there are the more pronounced gradients (see Figure 6.4). After a convergence study the mesh shown in Figure 6.4 has been adopted for all the simulations. The temperature is considered constant in the domain during the simulations. The initial conditions enforced in the simulations are:

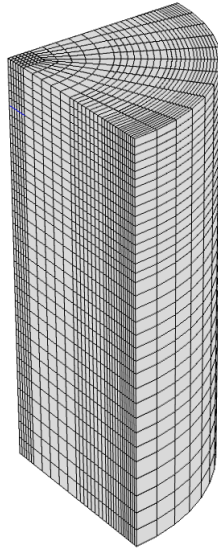


Figure 6.4: Geometry and mesh of the specimen.

$$\begin{aligned}h(t = 0) &= 1.0, \\ \omega(t = 0) &= 0.264 \text{ kg/m}^3 \\ c_s^s(t = 0) &= 0.\end{aligned}$$

Regarding the boundary conditions, null Neuman conditions:

$$\begin{aligned} \underline{j}_w^l \cdot \underline{n} &= 0, \\ \underline{j}_s^l \cdot \underline{n} &= 0, \end{aligned}$$

are enforced in the vertical planes of simmetry and on the bottom plane, while the conditions:

$$\begin{aligned} \underline{j}_w^l \cdot \underline{n} &= \gamma_w (a_w h - h_\alpha), \\ \underline{j}_s^l \cdot \underline{n} &= 0, \end{aligned}$$

are enforced on the remaining external surfaces.

6.5.1 Parameters used

The specimens are made of Prague sandstone (Pavlík et al., 2008), which has a unimodal pore system with an average pore diameter of 30 μm (Desarnaud et al., 2015). From the experimental evidences it is clear that the salt begins to precipitate almost soon, so the supersaturation threshold at which the crystallisation starts is close to the unity. In the numerical simulation we adopted 1.01. The sorption isotherm parameter Ψ is obtained by fitting the experimental data reported in Pavlík et al. (2008) by enforcing the measured value of water content at 0.8 relative humidity c_{w80} :

$$\Psi = 0.8 \frac{c_{w80} - \Phi_0 \rho_w^l}{c_{w80} - \Phi_0 \rho_w^l 0.8}. \quad (6.9)$$

The material parameters used are reported in Table 6.1.

6.5.2 Definition of γ_w

As described in Section 6.4, the expression of γ_w can be defined tuning some parameters. In particular, we assume a linear dependence of k on Δh_0 , so its trend can be defined with two experiments. We define the values of k_1 and k_2 in the Eq. (6.8) considering the drying tests performed with

PAR.	VALUE	UNIT	DESCRIPTION
D_v	$1.9 \cdot 10^{-6}$	m^2/s	Vapour permeability
Φ_0	0.29	-	Porosity
A	1.68	$kg\ m^{-2}s^{-0.5}$	Water adsorption coefficient
r_p	$15 \cdot 10^{-6}$	m	Average pore radius
K_c	$1.08 \cdot 10^{-4}$	m/h	Growth rate coefficient
n	$7 \cdot 10^{12}$	$1/m^3$	Nuclei in solution
p	1		Crystallization process order
ω_{sat}	0.264	kg/kg	Mass fraction ω at saturation
K_s	$2.2 \cdot 10^{-9}$	m^2/h	Diffusion coefficient
ρ_s^s	2170	kg/m^3	Mass density of precipitated NaCl
Ψ	1.0028	-	Sorption isotherm parameter

Table 6.1: Parameters used in the simulations.

saturated NaCl solution at RH 50% and RH 20%, in both experimental campaigns.

Since at RH 50% only one regime is observed till almost the end of the drying test, γ_w is considered constant and equal to $\bar{\gamma}_w$, *i.e.* considering $k = k_1 = 0.0$.

The simulation at RH 20% is used to define k_2 and the threshold value of S_s^s at which the drying kinetics changes.

Once values k_1 and k_2 are calibrated it is possible to define the expression of k . Since for all the experiments, the initial equivalent relative humidity is 1.0, the parameter k can be expressed by Eq. (6.8) as a linear function of the environmental relative humidity as:

$$k = \frac{k_1 - k_2}{0.5 - 0.2} (h_\alpha - 0.2) + k_2. \quad (6.10)$$

As regards the parameter $\bar{\gamma}_w$ in Eq. (6.6), it can be tuned with: (i) experimental results of drying tests after saturation by imbibition with pure water at different relative humidities at the same environmental conditions or (ii) considering

experimental results of drying with salt at RH 50%. Indeed, it is worth noting that the air velocity flow, that is not explicitly considered in the model, influences its value. For all the simulations of drying tests $\bar{\gamma}_{\text{crust}}$ is taken equal to 0.02.

6.5.3 Simulation of the drying at 50% RH

In this Section, the simulation of drying experiments at 50% RH for the two experimental campaigns is presented. As outlined in Section 6.5.2, according to experimental evidences the expression of the convective humidity coefficient reported in Eq. (6.6) results as:

$$\gamma_w = \bar{\gamma}_w \quad \forall S_s^s, \quad (6.11)$$

since k is assumed equal to zero.

6.5.3.1 First experimental campaign

We present the results of simulations of drying tests at 50% RH performed during the first experimental campaign. In particular the drying test after the saturation by imbibition with pure water are used to tune $\bar{\gamma}_w$, then the same value is assumed to simulate the drying after the imbibition with NaCl saturated solution. The comparison between numerical and experimental results is presented in terms of saturation versus the square root of time in hours. The saturation, sat , for the drying test with pure water is defined as follows:

$$\text{sat}(t) = \frac{m_w^l(t)}{m_w^l(0)} \quad (6.12)$$

where

$$m_\alpha^\pi(t) = \int_{V_{\text{spec}}} c_\alpha^\pi(t) dV. \quad (6.13)$$

On the other hand, the saturation for the test with salt solution is defined as:

$$\text{sat}(t) = \frac{m_w^l(t) + m_s^l(t) + m_s^s(t)}{m_w^l(0) + m_s^l(0) + m_s^s(0)}. \quad (6.14)$$

Figure 6.5 shows that the experimental curves are recovered by the proposed model considering a constant convective coefficient $\bar{\gamma}_w = 0.21$, in both the case of drying after imbibition of pure water and after the imbibition of salt solution.

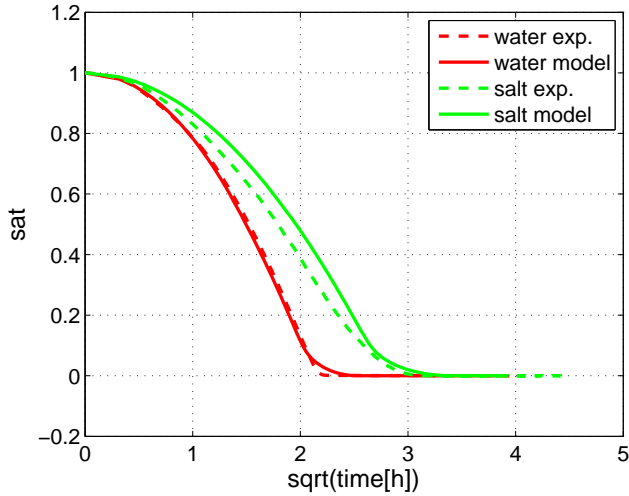


Figure 6.5: First experimental campaign. Drying at 50% RH: saturation versus the square root of time in hours for drying test performed with pure water and NaCl saturated solution, experimental data and results obtained with the proposed model.

6.5.3.2 *Second experimental campaign*

The second experimental campaign was performed with a smaller volume of the test cell which leads to different environmental conditions in terms of air flow velocity in respect to the first campaign. Indeed, in the second experimental campaign the drying is faster, thus $\bar{\gamma}_w$ increases. In this campaign pure water drying data are not available, thus we tuned the $\bar{\gamma}_w$ considering the drying with salt at 50% RH. The resulting $\bar{\gamma}_w$ is equal to 0.31. The comparison between numerical and experimental results, presented in terms of saturation versus the square root of time in hours, is reported in Figure 6.6.

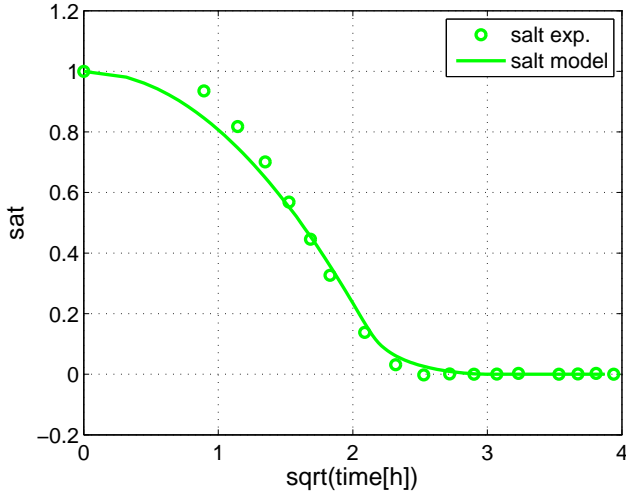


Figure 6.6: Second experimental campaign. Drying at 50% RH: saturation versus the square root of time in hours for drying test performed with NaCl saturated solution, experimental data and results obtained with the proposed model.

6.5.4 Simulation of the drying at 20% RH

In this Section, the simulation of drying experiments at 20% RH for the two experimental campaigns is presented. Since the saturation curve of the salt contaminated sandstone at RH 20% shows a double kinetics, it is necessary the calibration of the parameter $k = k_2$ and of the threshold value \bar{S}_s^s .

6.5.4.1 First experimental campaign

The drying tests at 20% RH performed during the first experimental campaign are simulated. Since $\bar{\gamma}_w$ does not depend on the environmental humidity, the value calibrated for the tests at 50% RH ($\bar{\gamma}_w = 0.21$) is assumed. Figure 6.7 shows the comparison between numerical and experimental results in terms of saturation versus the square root of time in hours according to Eqs. (6.12)-(6.14). In particular, the simulation is used to define $k = k_2$ and the threshold value of S_s^s at

which the drying kinetics changes. The value of $\bar{S}_s^s = 0.19$, corresponding to $c_s^s = 116 \text{ kg/m}^3$ is assumed for the first experimental campaign, and $k = 0.018$ is adopted for tests at RH 20%.

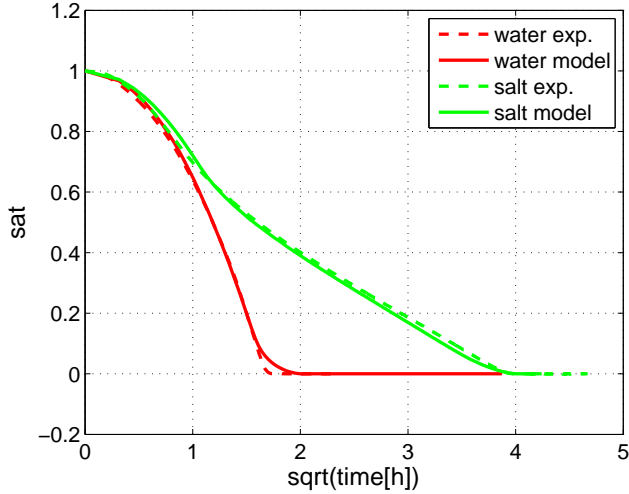


Figure 6.7: First experimental campaign. Drying at 20% RH: saturation versus the square root of time in hours for drying test performed with pure water and NaCl saturated solution, experimental data and results obtained with the proposed model.

6.5.4.2 Second experimental campaign

The same drying behaviour is confirmed in the second experimental campaign. In this campaign the parameter $\bar{\gamma}_w$ is tuned in Section 6.5.3.2 and assumed equal to 0.31. The comparison between numerical and experimental results, presented in terms of saturation versus the square root of time in hours, is reported in Figure 6.8. In particular, k , which depends on the humidity gap, is assumed also for the second experimental campaign equal to 0.018. However, the threshold value of \bar{S}_s^s at which the drying kinetics changes for the second experimental campaign is taken as $\bar{S}_s^s = 0.28$, corresponding to $c_s^s = 175 \text{ kg/m}^3$.

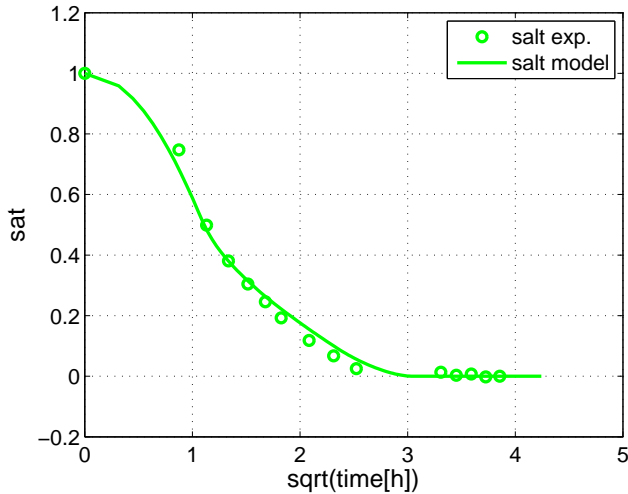


Figure 6.8: Second experimental campaign. Drying at 20% RH: saturation versus the square root of time in hours for drying test performed with NaCl saturated solution, experimental data and results obtained with the proposed model.

6.5.5 Simulation of the drying at 40% RH

The drying tests performed after the saturating by imbibition with saturated NaCl solution at 40% RH are available only for the first experimental campaign.

Once values k_1 and k_2 are fixed, it is possible to define the value of k at 40% RH using Eq. (6.10). Thus, k results equal to 0.006, while for the first experimental campaign the value of $\bar{S}_s^s = 0.19$, corresponding to $c_s^s = 116 \text{ kg/m}^3$ is adopted.

Figure 6.9 shows the comparison between numerical and experimental results in terms of saturation versus the square root of time in hours according to Eqs. (6.12)-(6.14), highlighting a very good agreement between numerical and experimental results.

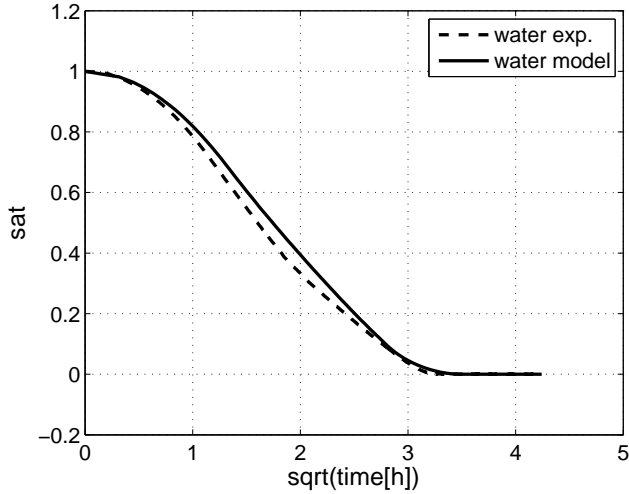


Figure 6.9: First experimental campaign. Drying at 40% RH: saturation versus the square root of time in hours for drying test performed with pure water and NaCl saturated solution, experimental data and results obtained with the proposed model.

6.5.6 Crystallization pattern

In order to investigate the crystallisation patterns obtained in the first experimental campaign (Desarnaud et al., 2015), the specimens were scanned once the drying process was completed and then the same specimen were washed and scanned again to have the reference state without the salt. The scans at the end of the drying process at 20% and 50% are reported in Figure 6.10. As it can be seen the salt is essentially localized at the external surface. The crystallisation pattern obtained by the model is reported in Figure 6.11, where maps of the crystallised salt in terms of c_s^s are depicted for simulations at 20% and 50% RH. In agreement with the experimental data, the crystallised salt is localized on the external surface. In particular the maximum localization is in the corner. It is impossible for the model to describe the outgoing of the salt from the domain to form the crust, so it is reasonable that the salt is located in a region

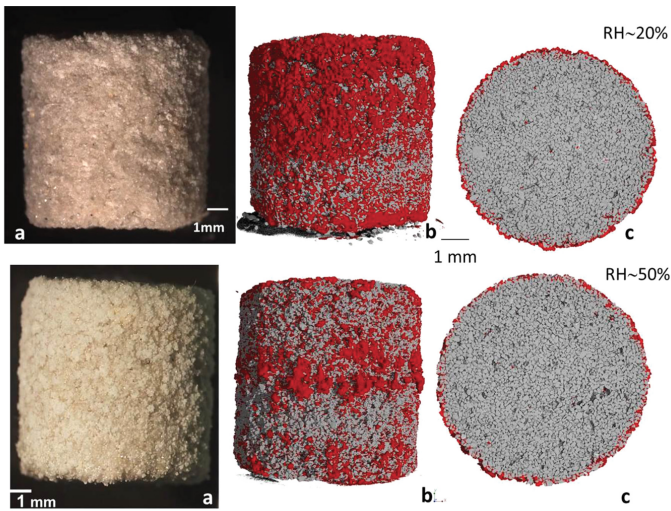


Figure 6.10: First experimental campaign. Crystallization pattern at RH 20 % (first raw) and RH 50% (bottom raw) (De-sarnaud et al., 2015).

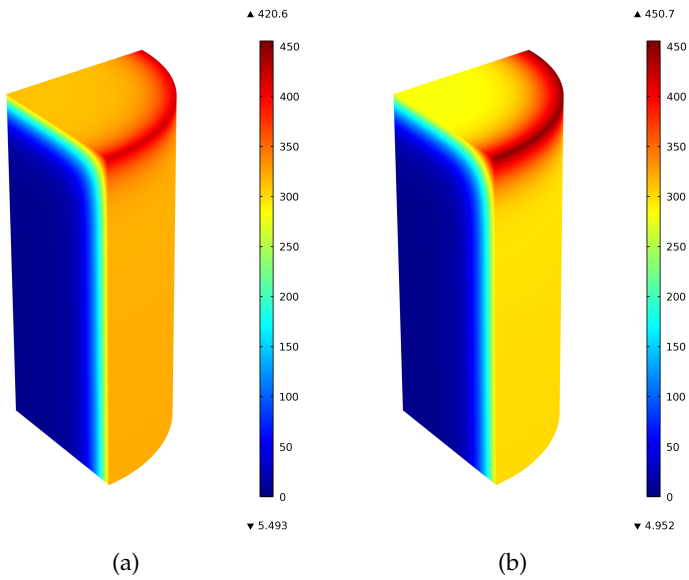


Figure 6.11: First experimental campaign. Crystallized salt (c_s^s) map at the end of the process in the case of drying at RH 20% (a) and RH 50% (b).

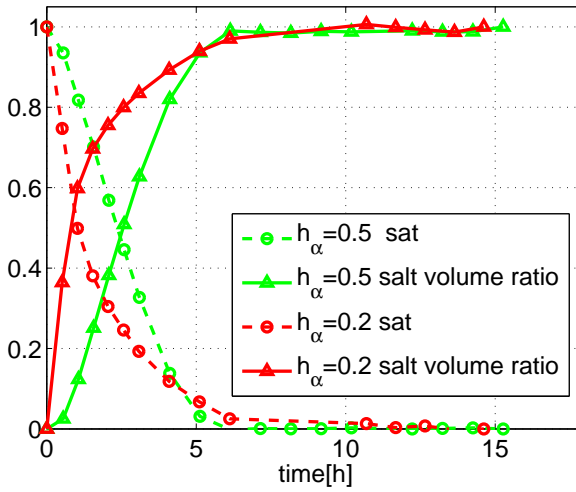
close to the surface with a sharp gradient. The second experimental campaign and its simulation confirm the results of the first one.

6.5.7 Salt amount: global estimation in time

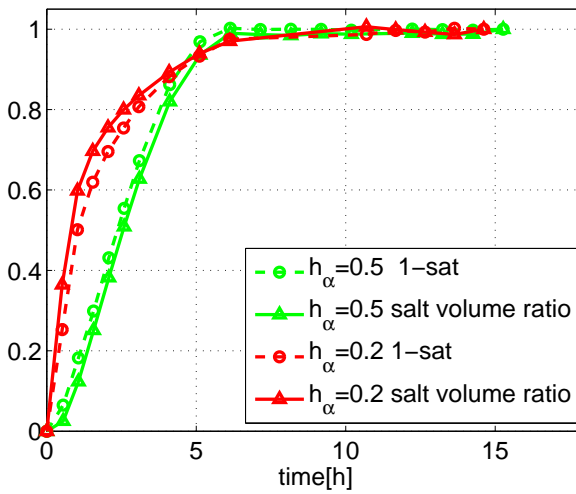
In order to estimate the global salt amount in time, we consider the second experimental campaign entirely performed at UGCT and described in Section 6.2 which allows the monitoring of the dried out solution and of the crystallised salt formation in time. In Figure 6.12 the curves of saturation and of salt volume ratio versus time, defined as $m_s^s(t)/m_s^s(t_{\text{end}})$, are reported for drying tests performed with environmental humidities equal to RH 20% and RH 50%. These results allow to visualise the trend of the amount of salt in respect to the trend of saturation in time. In particular, Figure 6.12a shows that the decreasing of the saturation is accompanied by an increasing of the precipitated salt. Furthermore, the normalisation of the total amount of precipitated salt, the salt volume ratio, and of the dried out solution reported in Figure 6.12b shows the same trend in time.

The comparison between model and experimental results of the salt volume ratio versus time at 20% and 50% RH is depicted in Figure 6.13, showing a very good agreement between numerical and experimental results.

The global amount of salt in terms of the volume fractions of precipitated salt versus time obtained with the model is reported in Figure 6.14 for the first (Figure 6.14a) and the second (Figure 6.14b) experimental campaigns. The curves obtained by the model, as expected, start to zero precipitated salt at $t = 0$ and arrive to a maximum final value for the precipitated salt of 4.23% for both experimental campaigns. This theoretical value can be calculated for a porous medium having a porosity equal to 29% saturated with a NaCl aqueous solution at $\omega = 0.264$ (6.1 M). We can remark that the trends shown by the curves obtained with the model for the two experimental campaigns are qualitatively similar: initially the curve related to the drying experiment



(a)



(b)

Figure 6.12: Second experimental campaign. Salt volume ratio and saturation versus time for the specimen dried at RH 20 % and RH 50 %.

at 20% RH shows a steeper slope in respect to the curve related to drying at 50% RH while, after sometimes, it shows a decreasing slope and reaches the maximum salt value af-

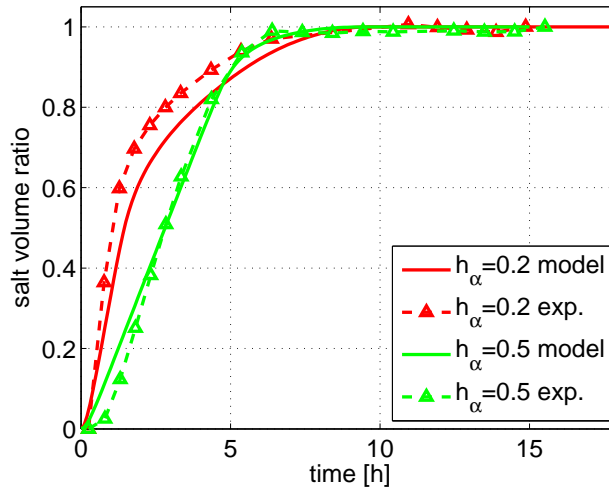


Figure 6.13: Second experimental campaign. Salt volume ratio versus the time in hours for drying test at 20% and 50% RH: experimental data and results obtained with the proposed model.

ter the curve related to the drying at 50% RH. The faster crystallisation of the simulation results of the second experimental campaign is due to the different conditions in which the specimen has been posed in the two campaigns. To better understand the effectiveness of the simulation results of the first experimental campaign, we can look at the trend of the amount of salt in respect to the trend of saturation in time. In Figure 6.12b the graphs show that the trends of salt volume ratio and of the saturation is the same in time. Exactly the same trends are obtained by the modelling results of the two experimental campaigns as illustrated in Figure 6.15.

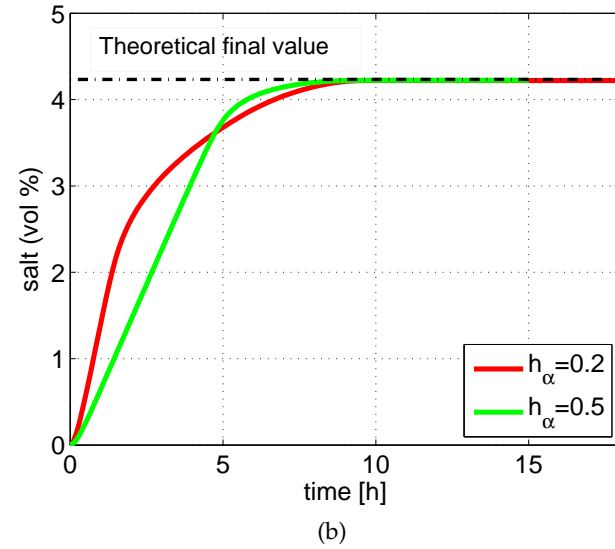
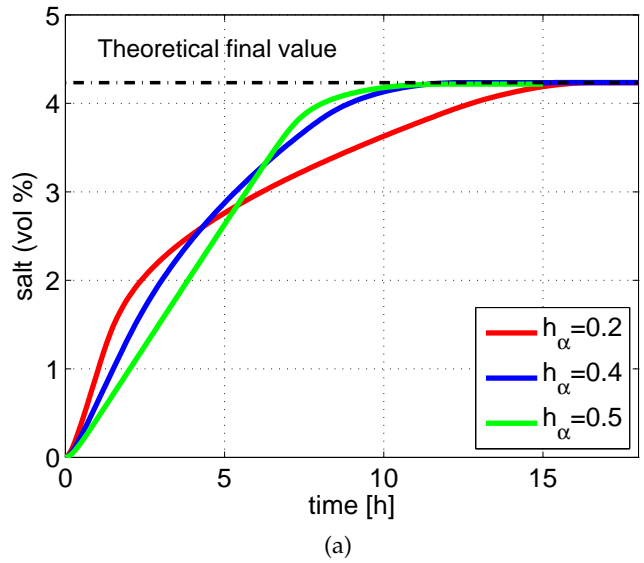


Figure 6.14: Model results of crystallised salt volume fraction versus time for (a) the first experimental campaign – specimen dried at RH 20%, 40% and 50% RH – and (b) the second one – specimen dried at RH 20% and 50% RH.

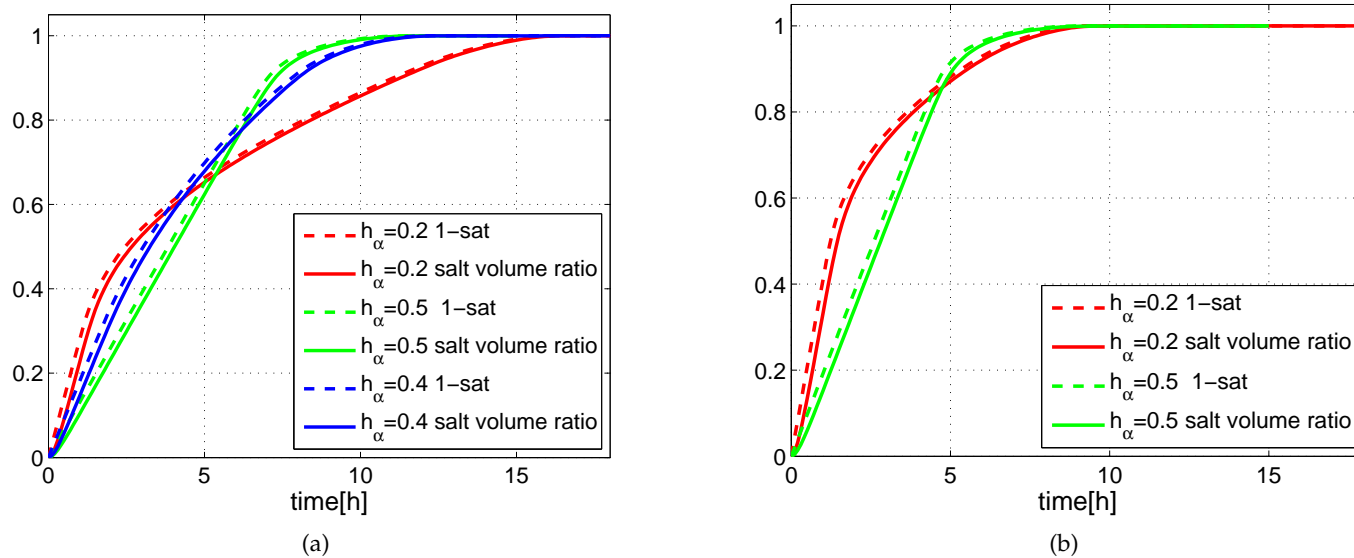


Figure 6.15: Comparison between trends of drying curve and crystallised salt for (a) the first experimental campaign and (b) the second one.

6.6 DISCUSSION

The proposed model, together with a suitable relation for the convective humidity coefficient γ_w has been validated through two experimental campaigns described in Section 6.2. The adopted parameters for Eqs. (6.6)-(6.7) are reported in Table 6.2 and the resulting trends of γ_w are depicted in Figure 6.16a and Figure 6.16b for the first and the second experimental campaigns, respectively.

PAR.	AMSTERDAM	GHENT
$\bar{\gamma}_w$	0.21	0.31
$\bar{\gamma}_{\text{crust}}$	0.02	0.02
\bar{S}_s^s	0.19	0.28
k_1	0.0	0.0
k_2	0.18	0.18

Table 6.2: Parameters adopted for the convective humidity coefficient γ_w in the two experimental campaigns.

As already outlined, the difference of $\bar{\gamma}_w$ for the two experimental campaigns is due to different environmental conditions in terms of air flow velocity.

On the other hand, the different values of the threshold at which crystals start to block the pores, \bar{S}_s^s , can be explained as follows (Derluyn, 2017): the different air flow velocity leads to a different drying velocities of the specimen. Indeed, if we consider the drying at 20% RH, for the first experimental campaign performed in Amsterdam, the starting of a different regime seems to be at a higher value of saturation, thus at a lower amount of salt, than for the second experimental campaign. If the drying is faster, the ratio of efflorescence/subflorescence at the surface will tend to change. As a consequence, you can keep on drying faster for a longer time before pores on the surface start to "close". In other words, not all the salt precipitates as efflorescence (which can form a crust), but there is also an amount of salt that precipitates below the surface. In particular, the

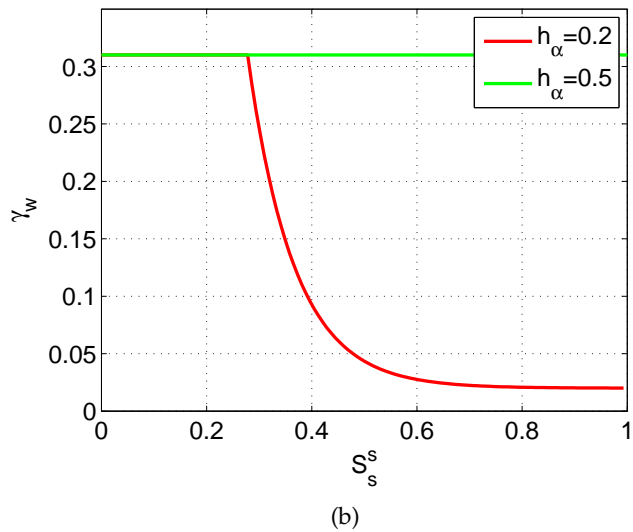
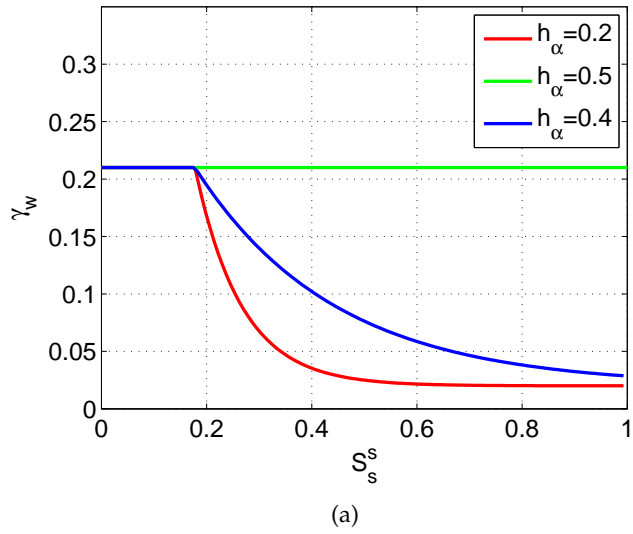


Figure 6.16: Representation of adopted trend of γ_w as a function of S_s^s : (a) first experimental campaign (Amsterdam), (b) second experimental campaign (Ghent).

more salt precipitates as subflorescence, the faster the drying will go. The same phenomenon can be observed also during deliquescence-drying cycles at 20% RH (Desarnaud

et al., 2015). Therefore, it seems that for this case, subflorescence does not block the pores so much.

Results of simulations prove that the model is able to capture the different drying kinetics at diverse values of relative humidity with respect of both experimental campaigns considered.

6.7 CONCLUDING REMARKS

The HTC model specialised for sodium chloride solutions has been extended to take into account the different kinetics of the drying process, due to different salt crystallisation at the external surface of the specimen examined. To this aim a law for the convective humidity coefficient is proposed. The model is used to simulate two experimental campaigns carried out in the framework of the European project KISADAMA (de Miranda et al., 2013). Numerical results show that the model is able to catch the different kinetics of drying (saturation curves), the amount of crystallised salt and, qualitatively, the position of the crystallised salt and the crystallisation pattern over time.

Part II

MECHANICAL ASPECTS

In microporomechanics a porous media can be treated as a particulate composite having inclusions with zero stiffness. In the frame of linear microporomechanics, it is found that the object describing the mechanical effect induced by the presence of a pressure acting on pore walls is the Biot's tensor, for saturated porous media, and the partial Biot's tensor, for porous media saturated with different phases, which can be generally written as a function of the degree of saturation of the considered phase. Approaches proposed in literature are generally based on homogenisation schemes with simplified pore geometries. On the other hand, here we present a multi-scale approach for the analysis of mechanical effects induced by salt crystallisation in porous media, based on numerical homogenisation. It allows to predict the effects of salt crystallisation occurring at the scale of the structure, based on the real 3D micro geometry of the porous material coming from Micro Computed Tomography images.

HOMOGENISATION APPROACH

In this Chapter the homogenisation approach adopted in this work is presented. In particular, the numerical homogenisation approach and the application of an analytical homogenisation approach – the Mori-tanaka scheme – to porous media are detailed.

7.1 THE NUMERICAL HOMOGENISATION APPROACH

In the second part of the dissertation, a multi-scale approach for the analysis of mechanical effects induced by salt crystallisation in porous media is presented. Basic concepts of multi-scale techniques have been detailed in Section 2.2.2. The multi-scale approach considered here is based on numerical homogenisation (see Section 2.2.2.2). To this aim, it is necessary to define a Representative Elementary Volume (REV), which is generally defined as the minimum window allowing to obtain an homogeneous value of the considered property which is independent of the window size. Referring to a porous medium depicted in Figure 7.1, if L , ℓ and d are the characteristic lengths of the structure, elementary volume and local heterogeneities, respectively, the conditions that allow defining the Representative Elementary Volume (REV) are:

$$d \ll \ell \ll L; \quad (7.1)$$

In order to pass from the micro-scale to the macro-scale, a linear microporomechanical approach which exploits homogenization theories (Coussy, 2006; Dormieux et al., 2006; Hashin, 1983) is adopted. The aim is to link the micro-scale stress $\boldsymbol{\sigma}(\underline{X}, \underline{x})$, strain $\boldsymbol{\varepsilon}(\underline{X}, \underline{x})$ and stiffness $\mathbf{C}(\underline{X}, \underline{x})$ tensors, which are heterogeneous at micro-scale, to macroscopic quantities which are homogeneous on the REV, *i.e.* the macroscopic stress $\boldsymbol{\Sigma}(\underline{X})$, strain $\mathbf{E}(\underline{X})$ and homogenised stiffness

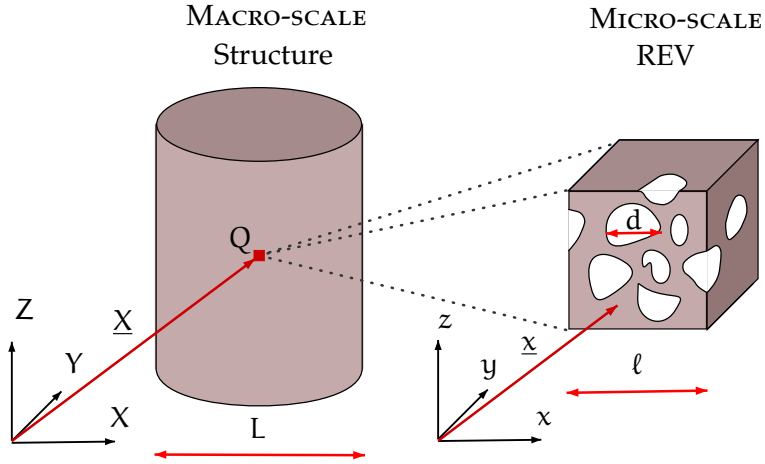


Figure 7.1: Reference systems and characteristic lengths for the macro- and micro- scales.

$\mathbb{C}^{\text{hom}}(\underline{X})$ tensors (see Figure 7.2). An energy equivalence between the micro-scale and the macro-scale is imposed:

$$\Sigma(\underline{X}) : \mathbf{E}(\underline{X}) = \langle \sigma(\underline{X}, \underline{x}) : \varepsilon(\underline{X}, \underline{x}) \rangle, \quad (7.2)$$

where $\langle \bullet \rangle$ is the average operator on the REV domain Ω_{REV} , defined as follows:

$$\langle \bullet \rangle = \frac{1}{|\Omega_{\text{REV}}|} \int_{\Omega_{\text{REV}}} \bullet \, dV_{\underline{x}}. \quad (7.3)$$

This enables one to define the macroscopic stress and strain as averages over the REV of the corresponding microscopic quantities, as well as to compute the homogenized stiffness tensor.

The macroscopic transformation of the REV is assumed infinitesimal and the response of REV at microscopic scale also meets the conditions of infinitesimal deformation and small displacements.

In this study, we refer to a first order homogenization procedure based on the solution of a boundary value problem on the REV. It consists in the following steps:

1. Geometrical and mechanical modelling of the material at the microscopic scale.

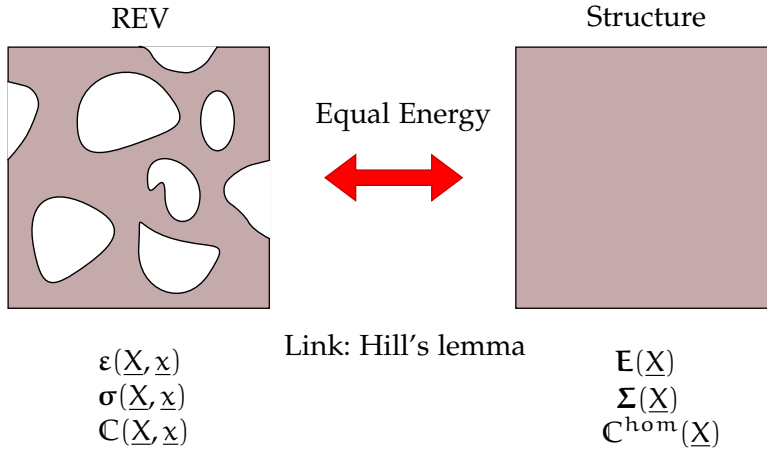


Figure 7.2: Characteristic quantities at the micro- and macro-scales and energy equivalence

2. Definition of an appropriate boundary condition on the REV (*i. e.* formulation of a micromechanical boundary value problem) and determination of the response of the REV at the microscopic scale, in terms of the corresponding microscopic strain and stress fields $\varepsilon(\underline{X}, \underline{x})$ and $\sigma(\underline{X}, \underline{x})$. This is the so-called localization step.
3. Determination of the macroscopic behaviour from the average mechanical response of the REV.

As regards point 1, the geometry of the REV can be obtained in several ways: from the assumption of simplified pore geometries to the measurements of REV's real geometry.

Regarding the point 2, as explained in Sections 2.2.2 and 2.2.3, there are different options in the defining of the boundary condition: here we choose kinematic homogenization, in which the linear displacement boundary condition is usually enforced. In kinematic homogenization, the linear displacement boundary condition ensure that the $\varepsilon = \mathbf{E}_0$ is constant on the REV's boundaries:

$$\underline{u}(\underline{X}, \underline{x}) = \mathbf{E}_0(\underline{X}) \cdot \underline{x} \quad \text{on} \quad \partial\Omega_{\text{REV}}, \quad (7.4)$$

where \mathbf{E}_0 is the applied macroscopic strain and $\partial\Omega_{\text{REV}}$ is the external REV boundary. It is possible to demonstrate that

$$\langle \varepsilon(\underline{X}, \underline{x}) \rangle = \mathbf{E}_0(\underline{X}), \quad (7.5)$$

where $\langle \varepsilon \rangle$ is the average microscopic strain field on the REV. Moreover, enforcing the Hill's Lemma (Hill, 1967) expressed in Eq. (7.2), which ensures the energy equality, it follows that

$$\langle \boldsymbol{\sigma}(\underline{X}, \underline{x}) \rangle = \boldsymbol{\Sigma}(\underline{X}). \quad (7.6)$$

For porous media, whose pore space is saturated with pressured phases, a further loading condition must be considered. Assuming that the microscopic and macroscopic pressure gradients are of the same order of magnitude, the mechanical interaction between the fluid and the solid at the microscopic level can be taken into account in a simplified way through a uniform pressure that is equal to the macroscopic one, which is applied at the solid-fluid interface. This enables us to solve a micro-scale problem only on the solid portion of the REV.

Finally, as regards point 3, the solution of the micromechanical boundary value problem together with Eq. (7.2) allow to write the macroscopic constitutive behaviour as:

$$\boldsymbol{\Sigma}(\underline{X}) = \mathbf{C}^{\text{hom}}(\underline{X}) : \mathbf{E}(\underline{X}) - \boldsymbol{\Sigma}_{p,c}(\underline{X}), \quad (7.7)$$

where $\boldsymbol{\Sigma}_{p,c}$ denotes the mechanical effect induced by pore pressures when the boundary of the REV is completely constrained and \mathbf{C}^{hom} is derived in Section 2.2.3.4. Equation (7.7) represents a general writing of the principle of effective stress, derived in Section 2.2.3.6.

This two scales approach is classical in microporomechanics (Dormieux et al., 2006). In this dissertation, the kinematic homogenization will be performed numerically, employing the real micro-structure of the material obtained from X-ray Micro Computed Tomography images. This method can be applied to porous media saturated with a single or multiple species: in the latter case, it enables us to test different loading schemes, deriving from different hypotheses on the way that crystals grow inside the porous medium. Indeed, changing the loading scheme – *i.e.* the model of crystal growth which determines the pore surfaces loaded by the pressure – and/or the volume of crystal occupying the pore space, the mechanical effects induced vary, both at the

micro-scale and at the macroscopic one. Since we want to investigate the role of the real pore geometry and of different loading schemes on the definition of the mechanical effects of salt crystallisation on the porous material, we assume in the following that the macroscopic strain $\mathbf{E} = \mathbf{0}$ so that the homogenised constitutive equation (7.7) reads as:

$$\Sigma(\underline{X}) = -\Sigma_{p,c}(\underline{X}). \quad (7.8)$$

In the literature, the calculation of the macroscopic mechanical properties is typically performed exploiting analytical schemes which require strong assumptions on the pore shape. In the following we present the specialisation for porous media of the Mori-Tanaka scheme (Mori and Tanaka, 1973), which we will use for comparison with our numerical scheme.

7.2 THE MORI-TANAKA SCHEME: APPLICATION TO POROUS MEDIA

The Mori-Tanaka (MT) scheme can be applied to porous materials. Since it takes into account mechanical interactions between inclusions, it can describe porous media with porosities up to 50%.

Analytical models, like the Mori-Tanaka scheme, still hold great importance in all those cases where it is not possible to have experimental information about the micro-structure of the material (mainly due to the attainment of the maximum resolution of the instruments). Moreover, the application of this scheme to porous media can also be useful to obtain a simplified micro-mechanical model of the porous material, which defines the most suitable micro simplified geometry representing the real one, as will be shown in Chapter 9. Here, we specialize the Mori-Tanaka's scheme in Benveniste (1987) for porous media, imposing the mechanical properties of the pore space equal zero ($\kappa_p = \mu_p = 0$). We assume that the porous medium has an elastic isotropic homogeneous material matrix with randomly oriented ellipsoidal pores. In particular, introducing an orthonormal frame $(\Gamma^i, \underline{t}_1^i, \underline{t}_2^i, \underline{n}^i)$, in which \underline{n}^i denotes the unit normal

to the pore orientation plane and Γ^i the centre of the pore, the pore shape is described by the equation of an ellipsoid of revolution, with aspect ratio r :

$$x^2 + y^2 + \frac{z^2}{r^2} = k^2, \quad (7.9)$$

being $x = \underline{x} \cdot \underline{t}_1^i$, $y = \underline{x} \cdot \underline{t}_2^i$ and $z = \underline{x} \cdot \underline{n}^i$. As shown in Table 7.1, r spans from 0 to ∞ , determining the pore shape.

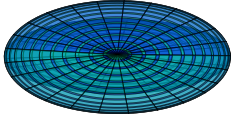
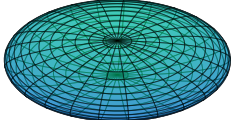
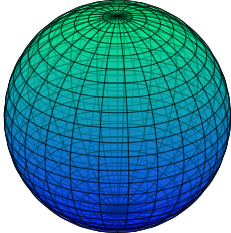
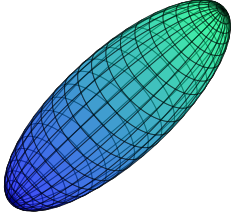
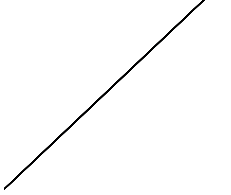
PORE SHAPE	ASPECT RATIO	
Disk	$r = 0$	
Oblate spheroid	$0 < r < 1$	
Sphere	$r = 1$	
Prolate spheroid	$r > 1$	
Needle	$r \rightarrow \infty$	

Table 7.1: Nomenclature of the ellipsoidal pore shapes as a function of the aspect ratio r .

In addition to pore shapes depicted in Table 7.1, we can mention also penny cracks as a particular case of oblate spheroid with $r \ll 1$.

For porous media, homogenised bulk and shear moduli κ^{MT} and μ^{MT} result as:

$$\kappa^{\text{MT}} = \kappa_m \frac{1 - \phi_0}{1 - \phi_0 (1 - \alpha)}, \quad (7.10a)$$

$$\mu^{\text{MT}} = \mu_m \frac{1 - \phi_0}{1 - \phi_0 (1 - \beta)}, \quad (7.10b)$$

where α and β are scalar quantities depending on the pore shape, which can be found in the literature for a wide range of inclusion's shapes (Berryman, 1980).

If the randomly oriented pores are oblate or prolate spheroids, the specialization of α and β for porous media reads respectively:

$$\alpha = \frac{F_1}{F_2}, \quad (7.11)$$

$$\beta = \frac{1}{5} \left(\frac{2}{F_3} + \frac{1}{F_4} + \frac{F_4 F_5 + F_6 F_7 - F_8 F_9}{F_2 F_4} \right), \quad (7.12)$$

where:

$$F_1 = 1 - \left(\frac{3}{2} (f + \theta) - \frac{1 - 2\nu_m}{2(1 - \nu_m)} \left(\frac{3}{2} f + \frac{5}{2} \theta - \frac{4}{3} \right) \right), \quad (7.13)$$

$$\begin{aligned} F_2 = & 1 - \left(1 + \frac{3}{2} (f + \theta) - \frac{1 - 2\nu_m}{4(1 - \nu_m)} (3f + 5\theta) \right) + \\ & + \frac{1}{2} \left(3 - \frac{2(1 - 2\nu_m)}{1 - \nu_m} \right) \\ & \left(f + \theta - \frac{1 - 2\nu_m}{2(1 - \nu_m)} (f - \theta + 2\theta^2) \right). \end{aligned} \quad (7.14)$$

$$F_3 = f + \frac{3}{2} \theta - \frac{1 - 2\nu_m}{2(1 - \nu_m)} (f + \theta), \quad (7.15)$$

$$F_4 = 1 - \frac{1}{4} \left(f + 3\theta - \frac{1 - 2\nu_m}{2(1 - \nu_m)} (f - \theta) \right), \quad (7.16)$$

$$F_5 = f - \frac{1 - 2\nu_m}{2(1 - \nu_m)} \left(f + \theta - \frac{4}{3} \right), \quad (7.17)$$

$$F_6 = \frac{1 - 2\nu_m}{2(1 - \nu_m)} (f + \theta) - f, \quad (7.18)$$

$$F_7 = 2 - \frac{1}{4} \left(3f + 9\theta - \frac{1-2\nu_m}{2(1-\nu_m)}(3f + 5\theta) \right), \quad (7.19)$$

$$F_8 = -1 + \frac{1-2\nu_m}{1-\nu_m} - \frac{f}{2} \left(\frac{1-2\nu_m}{2(1-\nu_m)} - 1 \right) + \quad (7.20)$$

$$-\frac{\theta}{2} \left(5 \frac{1-2\nu_m}{2(1-\nu_m)} - 3 \right),$$

and

$$F_9 = \frac{1-2\nu_m}{2(1-\nu_m)}\theta - \left(\frac{1-2\nu_m}{2(1-\nu_m)} - 1 \right) f. \quad (7.21)$$

The functions θ and f are given by:

$$\theta(r) = \begin{cases} \frac{r}{(1-r^2)^{\frac{3}{2}}} \left[\cos^{-1}(r) - r(1-r^2)^{\frac{1}{2}} \right] & 0 \leq r < 1, \\ \frac{r}{(r^2-1)^{\frac{3}{2}}} \left[r(1-r^2)^{\frac{1}{2}} - \cosh^{-1}(r) \right] & r > 1, \end{cases} \quad (7.22)$$

and

$$f(\theta, r) = \begin{cases} \frac{r^2}{1-r^2}(3\theta - 2) & 0 \leq r < 1, \\ \frac{r^2}{r^2-1}(2 - 3\theta) & r > 1. \end{cases} \quad (7.23)$$

Parameters α and β can also be found in the literature for spherical, needle-shaped, disk-shaped (Walpole, 1969; Wu, 1966) oblate, prolate (Kuster and Toksöz, 1974) and penny crack inclusions (Walsh, 1969). Here, these expressions are specialised for porous media. Coefficients α and β specialised for porous media function of matrix Poisson's coefficient are reported in Table 7.2 for pores having shape of spheres, needles, disks and penny cracks.

If pores are randomly oriented, the Biot's tensor results spherical, thus a scalar parameter, the Biot's coefficient, can be defined. According to the expression derived in Section 2.2.3.6 – Eq. (2.42) – and to Biot (1962); Geertsma (1957), the Biot's coefficient can be expressed as:

$$b = 1 - \frac{\kappa^{\text{hom}}}{\kappa_m}. \quad (7.24)$$

PORE SHAPE	α	β
Spheres ($r = 1$)	$\frac{3}{2} \frac{1-\nu_m}{1-2\nu_m}$	$\frac{10\nu_m-8}{5\nu_m-7}$
Needles ($r \rightarrow \infty$)	$\frac{2\nu_m}{1-2\nu_m} + \frac{5}{3}$	$\frac{8}{3} - \frac{8\nu_m}{5}$
Disks ($r \rightarrow 0$)	∞	∞
Penny Cracks ($r \ll 1$)	$\frac{2(1-\nu_m)}{(1-2\nu_m)\pi r}$	$\frac{1}{5} + \frac{8\nu_m^2-48\nu_m+40}{15\pi r(2-\nu_m)}$

Table 7.2: Expressions of α and β for spherical, needle-shaped, disk-shaped pores and penny cracks.

It follows that the Biot's coefficient for porous media with randomly oriented ellipsoidal pores according to the Mori-Tanaka's scheme and Eq. (7.10a) can be computed as:

$$b^{MT} = 1 - \frac{\kappa^{MT}}{\kappa_m} = 1 - \frac{1 - \phi_0}{1 - \phi_0(1 - \alpha)}, \quad (7.25)$$

where expressions of parameter α , specialised for porous media, are reported in Table 7.2 for pore shapes having notable values of aspect ratio r . Equation (7.25) remarks that the Biot's coefficient depends on the value of porosity, the Poisson's coefficient of the material matrix ν_m and the pore shape through α , but not on the elastic modulus of the matrix. Moreover, remembering the inequality (2.43), we remark that considering the Voigt bound, presented in Section 2.2.2, it is possible to estimate the Biot's coefficient as $b^V = \phi_0$, which constitute the lower bound for this parameter.

Assuming the solid skeleton of the porous media linear elastic and isotropic, the trend of the Biot's coefficient with respect to the Poisson's coefficient ν and the porosity ϕ_0 is investigated not only with the Mori-tanaka scheme, but also considering its lower bound, the Voigt's one.

Figure 7.3 shows the trend of the Biot's coefficient computed using the scheme of Voigt and Mori-Tanaka considering different forms of pores randomly oriented – spherical, prolate, oblate and penny-shaped cracks –, as a function of the Poisson's ratio and the porosity of the material. In particular, spherical pores, needle-shaped, oblate with aspect ratio $r = 0.05$, prolate with aspect ratio $r = 3$ and penny

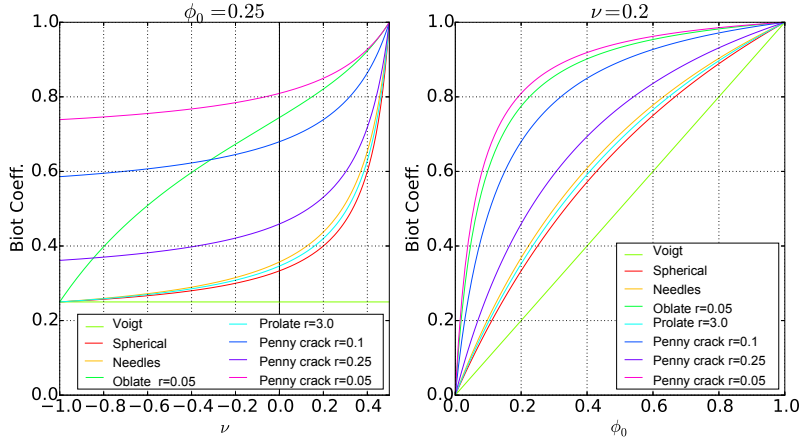


Figure 7.3: Biot coefficient b computed with MT scheme using different pore shapes

crack with three different aspect ratios are considered. As it can be noted, the Voigt estimation gives only a rough estimate of the Biot's coefficient, because it assumes that strain is uniform within the heterogeneous material, as pointed out in Section 2.2.2.1.

The complete surface representation of the Biot's coefficient as a function of the porosity of the material and of the Poisson's coefficient for the pore shapes considered above is illustrated in Figure 7.4. It is worth noting that graphs in Figure 7.3 are sections of the complete surfaces depicted in Figure 7.4 for different pore shapes. Moreover, both Figure 7.3 and Figure 7.4 highlight that the assumed pore shape can lead to very different results in terms of Biot's coefficient. For this reason it is interesting have some experimental information on the real geometry of the micro-structure.

Figure 7.5 represents the Biot's coefficient calculated with the Mori-Tanaka's scheme as a function of the aspect ratio r for assigned values of porosity and Poisson's ratio. Continuous black line represents the trend of the Biot's coefficient for oblate $0 < r < 1$, spherical $r = 1$ and prolate $r > 1$ pores. It is worth noting that the curve presents a minimum for the spherical pore and a horizontal asymptote for r tending to infinity (the needle-shaped pore). For $r = 0$, *i.e.* disk-

shaped pores, the Biot's coefficient has the maximum value, *i. e.* 1. The red dotted line represents the trend of the Biot's coefficient in the case of pores having a penny crack shape: these values are subjected to the condition $r \ll 1$.

Moreover, Figure 7.6 shows the trend of the shear modulus ratio μ^{MT}/μ_m computed using the scheme of Mori-Tanaka considering different forms of pores randomly oriented – spherical, prolate, oblate and penny-shaped cracks –, as a function of the Poisson's ratio and the porosity of the material. In particular, spherical pores, needle-shaped, oblate with aspect ratio $r = 0.05$, prolate with aspect ratio $r = 3$ and penny crack with three different aspect ratios are considered; the complete surface representation of the shear modulus ratio as a function of the porosity of the material and of the Poisson's coefficient for the pore shapes considered above is illustrated in Figure 7.7. Graphs in Figure 7.6 are sections of the complete surfaces depicted in Figure 7.7 for different pore shapes. Moreover, both Figure 7.6 and Figure 7.7 highlight that the assumed pore shape can lead to very different results also in terms of the shear modulus ratio μ^{MT}/μ_m .

7.3 CONCLUDING REMARKS

In this Chapter the numerical homogenisation approach that will be employed in this work is presented. In particular, the numerical homogenisation approach and the application of an analytical homogenisation approach – the Mori-Tanaka scheme – to porous media have been detailed. Regarding the former, the macroscopic constitutive behaviour for a porous media whose pore space is saturated with pressurised phases have been derived: it accounts for the mechanical effect induced by pore pressures. Regarding the latter, the specialisation of the Mori-Tanaka's scheme in for porous media has been shown. In particular, we have derived mechanical properties and the Biot's coefficient assuming a porous medium with randomly oriented ellipsoidal pores, having an aspect ratio r . Finally, the trend of Biot's

coefficient and shear modulus ratio as a function of porosity and Poisson's coefficient has been displayed.

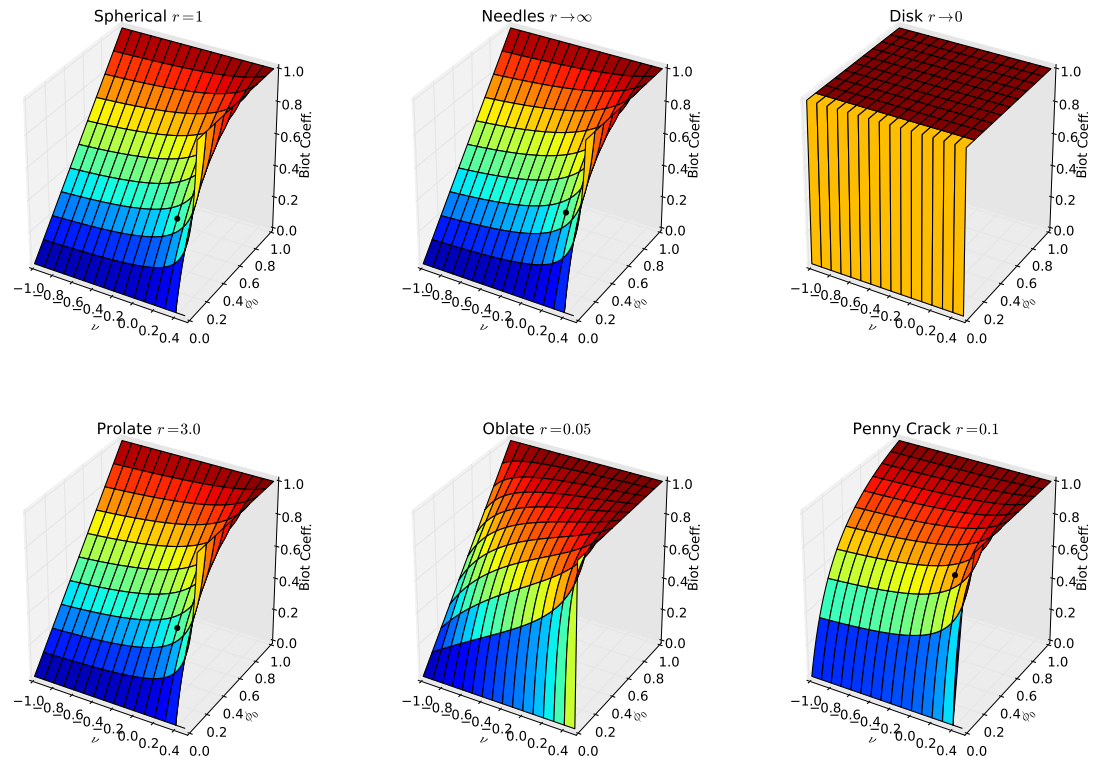


Figure 7.4: Biot coefficient b function of porosity ϕ_0 and Poisson's Coefficient ν computed with MT scheme using different pore shapes

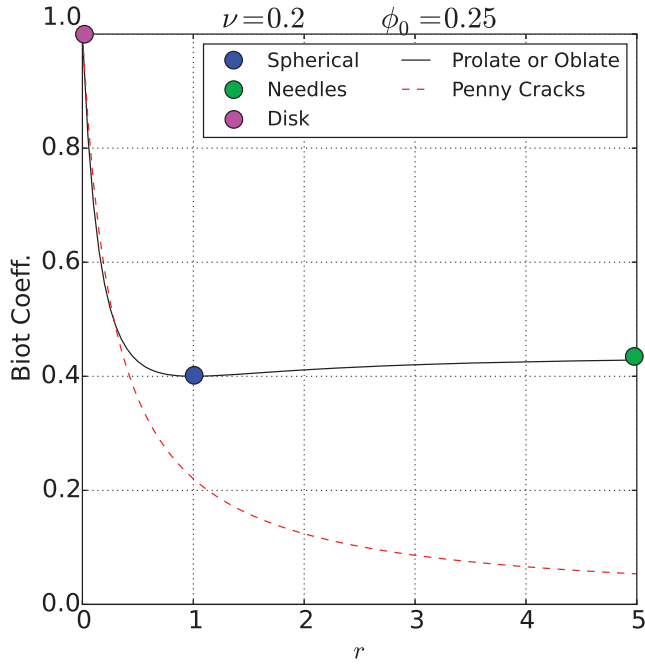


Figure 7.5: Biot coefficient b computed with MT scheme function of the aspect ratio r

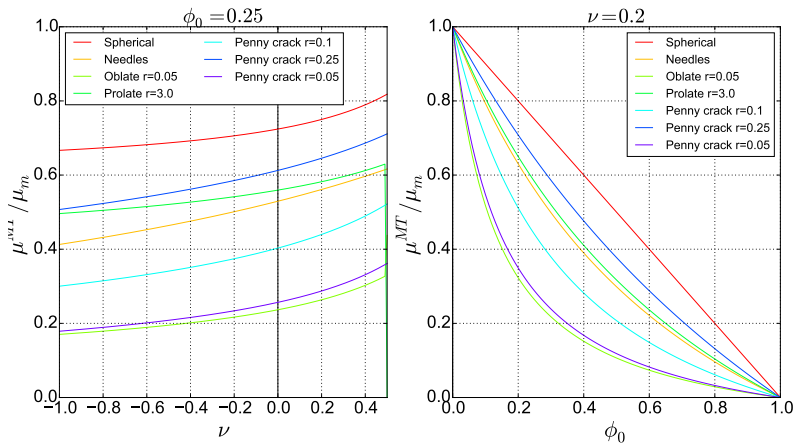


Figure 7.6: Shear modulus ratio μ^{MT}/μ_m computed with MT scheme using different pore shapes

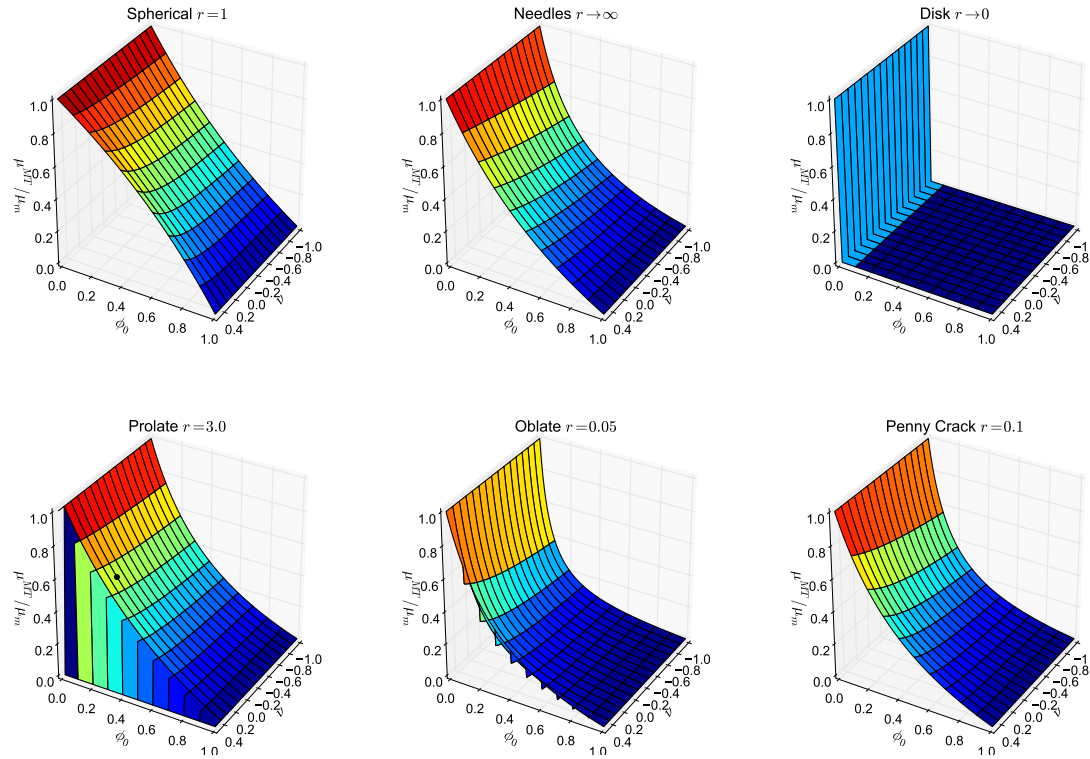


Figure 7.7: Shear modulus ratio μ^{MT}/μ_m function of porosity ϕ_0 and Poisson's Coefficient ν computed with MT scheme using different pore shapes

POROUS MEDIA SATURATED WITH ONE SPECIES

The aim of this Chapter is to illustrate a general procedure to (i) find the size of a porous medium Representative Elementary Volume (REV) and (ii) to compute the Biot's tensor, starting from a X-ray Micro Computed Tomography (X-ray μ CT) dataset. The micro-mechanical model is obtained by automatically converting the images into a finite element mesh. The proposed procedure is applied to a Prague sandstone. The results in terms of Biot's tensor are used to validate the size of the mechanical REV.

8.1 THE CHOICE OF THE REPRESENTATIVE ELEMENTARY VOLUME

The aim of this Section is to illustrate a general procedure to find the size of a porous medium REV starting from a X-ray μ CT dataset. In the framework of multi-scale approaches and, in particular, of homogenisation theories, the REV is defined as the minimum observation window allowing to obtain a homogenized behaviour which is independent of the window size. In particular, the REV for a porous medium has to be representative of:

- (a) the overall porosity;
- (b) the geometry of the pore space;
- (c) the average mechanical properties.

These three features define the mechanical REV, which ensures that $d \ll \ell$. In order to satisfy the second part of the inequality (7.1) ensuring the scale separation, the wave length of the load applied on the structure has to be much larger than the size of mechanical REV. It is worth noting that the

load considered can be of different natures: *e. g.* mechanical, thermal, chemical.

8.1.1 *The case study*

Here, the X-ray μ CT input dataset comes from a Prague sandstone (Pavlík et al., 2008) sample of 8 mm in diameter that was scanned at the HECTOR scanner (Masschaele et al., 2013) of the Centre for X-ray Tomography of the Ghent University (UGCT) (Derluyn et al., 2014b). The 3D volume was reconstructed using a filtered backprojection algorithm in the software Octopus (Inside Matters bvba, Belgium; Vlassenbroeck et al. (2007)), resulting in a dataset consisting of cubic voxels (3D equivalent of pixels) of $4.75 \mu\text{m}$ in size. Subsequently, a Volume Of Interest (VOI) of $5.225 \text{ mm} \times 5.225 \text{ mm} \times 4.755 \text{ mm}$ was selected and segmented using Morpho+, a software package currently distributed as Octopus Analysis (Inside Matters bvba, Belgium, Brabant et al. (2011)). The segmentation leads to a stack of 1001 binary images of 1100×1100 pixels (see Figure 8.1). Black pixels represent the solid matrix and the white ones the pore space. It is worth noting that segmented images are always affected by uncertainties due to the filtering and phase segmentation processes, depending on the filter chosen to reduce the image noise and on the choice of threshold value. These uncertainties can impact the material micro-structure 3D geometry which is treated in this study.

8.1.2 *Overall Porosity*

As pointed out, the REV has to be representative of the material porosity. To achieve this goal, a number of Elementary Volumes (EV) having different sizes are randomly extracted from the VOI. For each of them the overall porosity value is calculated. This parameter can be calculated by mean of software packages for 3D analysis, which usually can compute also the open and closed porosity. Here we compute the overall porosity by mean of a simple Python code. Since

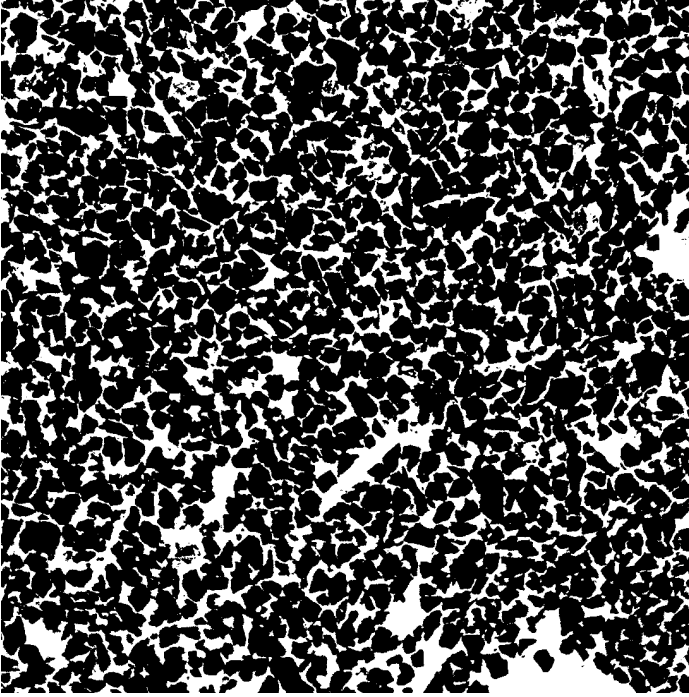


Figure 8.1: Segmented binary image of a horizontal slice of the 3D reconstructed volume of the Prague sandstone: solid matrix (black) and pore space (white) (Derluyn et al., 2014b).

voxels are cubic, we can imagine a voxel as the element a_{ijk} of a 3D array A having value 0 (black) or 1 (white). In other words:

$$a_{ijk} = \begin{cases} 1, & \text{if } a_{ijk} \in \text{pore} \\ 0, & \text{if } a_{ijk} \in \text{solid} \end{cases} \in \mathbb{N}_0^{n \times m \times l} \quad (8.1)$$

where n , m , l are the dimensions of array A . Thus, the calculation of the overall porosity ϕ_0 is straightforward:

$$\phi_0 = \frac{1}{n m l} \sum_{i=1}^n \sum_{j=1}^m \sum_{k=1}^l a_{ijk}, \quad (8.2)$$

resulting the arithmetic mean of the values associated with EV voxels.

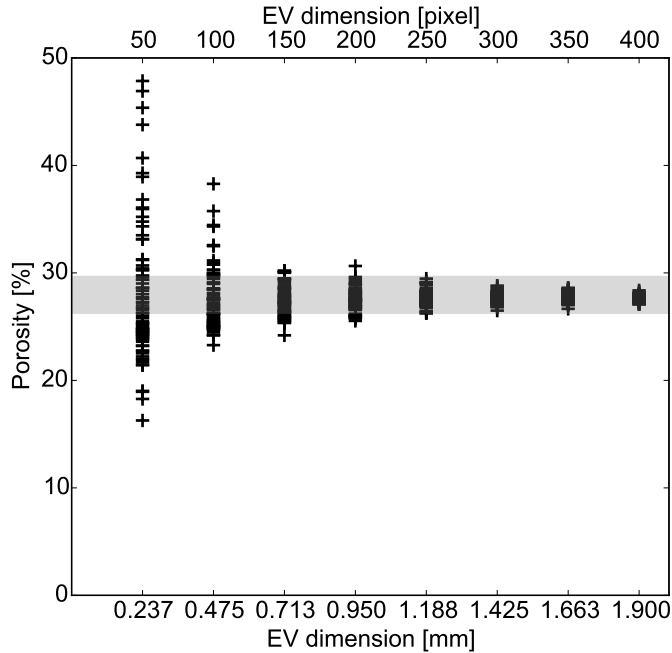


Figure 8.2: EVs' porosities function of the EV size: the porosity range 26.25-29.67% given for Prague Sandstone in Pavlík et al. (2008) is highlighted in light grey.

Different sizes of cubic EVs are chosen: from 0.2375 mm (50 pixels) to 1.9000 mm (400 pixels). For each size, 80 EVs are randomly extracted and for each of them the porosity is calculated. Figure 8.2 shows the porosities of different EVs obtained as a function of the EV size. Data are compared with the value of porosity given for the Prague Sandstone in Pavlík et al. (2008), ranging from 26.25% to 29.67%. It is worth noting that, for the sake of simplicity, here we assume that the overall porosity is equal to the total open porosity. As expected, increasing the EV size the range of porosities calculated gets narrower. Thus, inspecting Figure 8.2 it is possible to conclude that 1.1875 mm is the best EV size from a porosity point of view, ensuring representativeness and affordable computational cost for the further steps. Indeed, for this size the 80 EVs analysed have a range of porosities between 26.25% and 29.47%, which are in agreement with

Table 8.1: Porosity of EVs chosen among those of 1.1875 mm.

EV#	ϕ_0 [%]
9	26.25
73	27.85
21	29.47

the porosity range given in Pavlík et al. (2008).

In the following, among the EVs of 1.1875 mm, we analyse the geometry of the pore space and average mechanical properties of the ones having the maximum (29.47%), the minimum (26.25%) and the medium porosity (27.85%) values, to further assess the representativeness of this EV size. The overall porosity of analysed EVs is given in Table 8.1.

8.1.3 *Geometry of the pore space*

The pore space's geometry is usually investigated isolating and analysing each part of the volume which is not connected with another one. Thus, each detected object is modelled as an equivalent shape, based on the equivalence of geometrical indicators like moments of inertia or volume. This procedure is usually performed by software packages for 3D analysis (Brabant et al., 2011).

In this work, the geometry of the pore space is characterised in a non-standard way, which is related to the development of the mechanical model discussed in the rest of the dissertation. In order to model the interaction between the solid matrix and the different phases (water, moisture, salt, ...) contained in the pores, we need to associate the volume of pores filled by each phase with the contact surfaces between this phase and the solid matrix. In order to create a univocal link between the pores' volume (white voxels) and the contact surfaces (faces of the black voxels), the following scheme is adopted:

- the volume of each voxel, of side v , is split into six equal portions, each associated to one of the faces: this yields a unitary volume $V_u = v^3/6$ associated to each face of the voxel (see Figure 8.3a);
- for each face of the solid matrix voxels, the distance d_i to the face of the solid matrix voxel directly facing it is computed (see Figure 8.3b): this distance can be expressed as $d_i = k_i v$, where k_i is the number of pore voxels crossed;
- the volume associated to each face of the solid matrix voxels is the sum of the unitary volumes of each pore voxel crossed: this yields $V_i = k_i V_u = k_i v^3/6$.

The distances d_i and the volumes V_i enable us to define two indicators to analyse the geometry of the pore space:

- the frequency distribution of the distances d_i , calculated as

$$f(d_i) = \frac{n(d_i)}{\sum_i n(d_i)},$$

where $n(d_i)$ is the number of occurrences of the distance d_i within the considered sample;

- the weighted frequency distribution of the distances, calculated as

$$f_w(d_i) = \frac{n(d_i)V_i}{\sum_i n(d_i)V_i}.$$

It should be underlined that the second indicator also corresponds to the pore volume fraction associated to a given distance d_i . This indicator will be used in the following to compute the progressive filling of the pore space with the crystallised salt. Figure 8.4 shows the two defined geometry indicators for EVs of 5 different sizes, extracted from the VOI starting from the same seed: 0.2375 mm, 0.4750 mm, 0.7125 mm, 0.9500 mm, 1.1875 mm. It is worth noting that increasing the EV size, the shape of graphs become smoother. Moreover, only for dimensions of 0.9500 mm and larger it is possible to capture the whole range of pore dimensions.

Definitely, Figures 8.4a and 8.4b show that 1.1875 mm is a good choice for the REV dimension. Once the REV size is chosen, it is interesting to investigate its spatial variability. To this end, the two geometry indicators f and f_w are built for the three EVs of Table 8.1 of 1.1875 mm and depicted in Figures 8.5a and 8.5b. We observe that the trend of the different graphs is similar, meaning that the REV dimension chosen is not particularly affected by the spatial variability and, thus, it is representative of the pore space geometry.

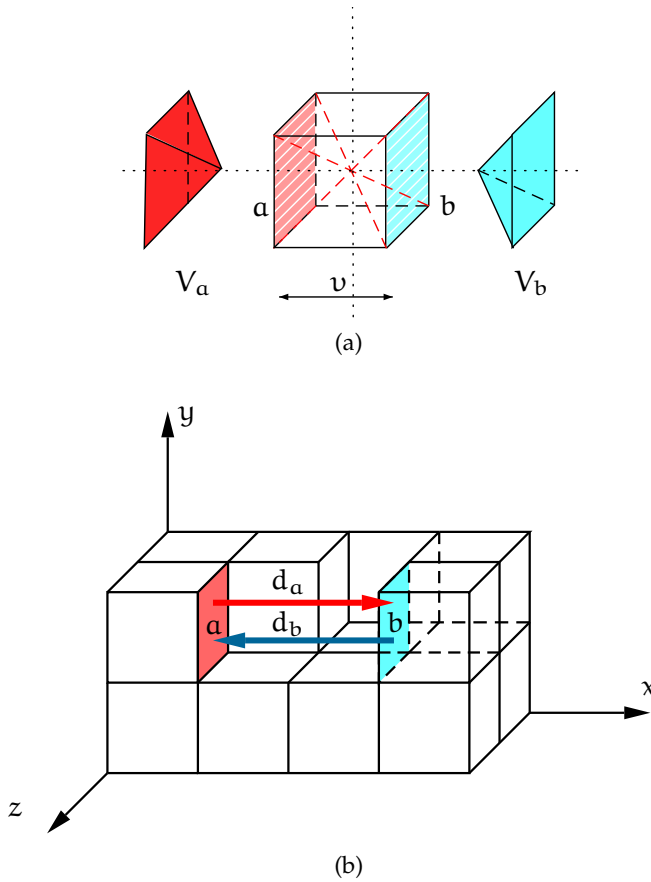
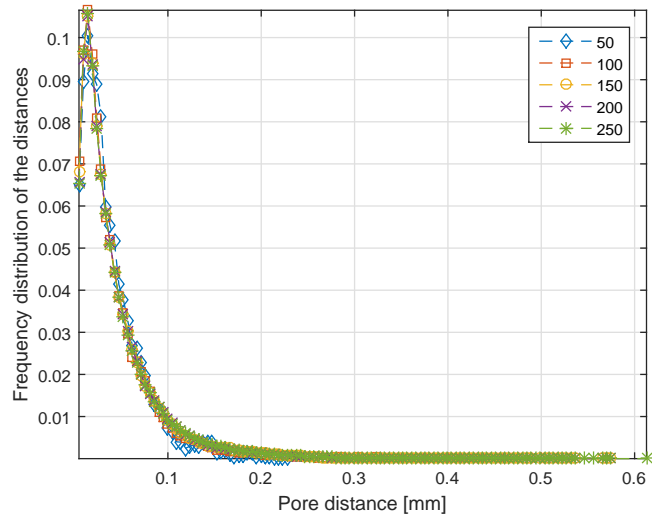
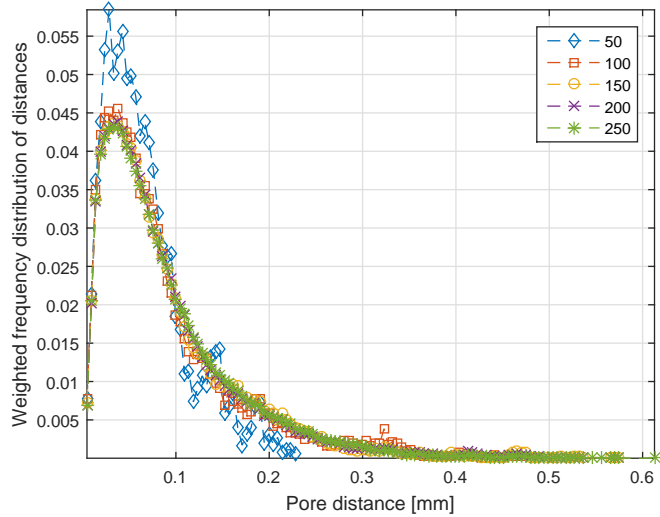


Figure 8.3: (a) Sketch of the method to compute the volume associated to each distance d_i ; (b) representation of distances between matrix voxels in x direction: d_a is the distance between face a and face b while d_b is the one spanning from face b to face a .

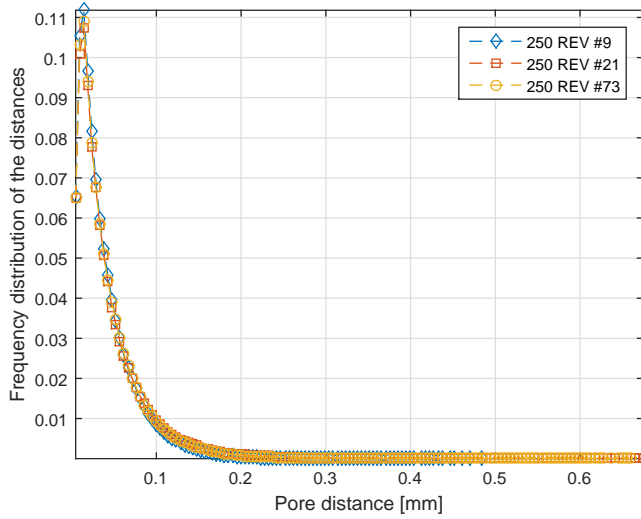


(a)

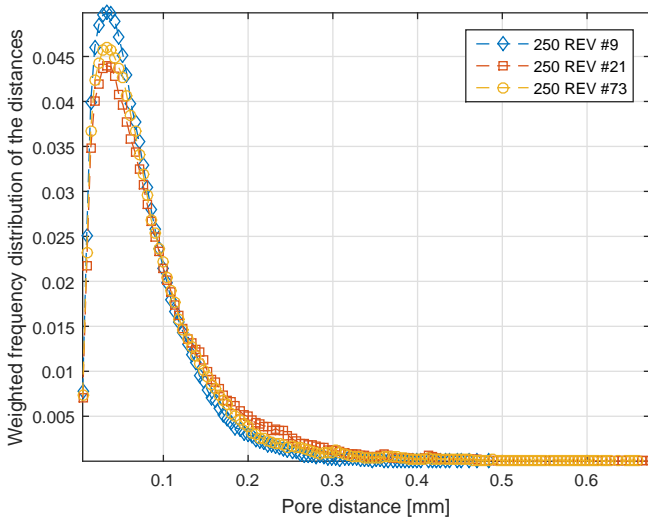


(b)

Figure 8.4: (a) Frequency distribution of the distances and (b) Weighted frequency distribution of the distances for EVs of 5 different sizes: 0.2375 mm (50 px), 0.4750 mm (100 px), 0.7125 mm (150 px), 0.9500 mm (200 px), 1.1875 mm (250 px).



(a)



(b)

Figure 8.5: (a) Frequency distribution of the distances and (b) Weighted frequency distribution of the distances for 3 different EVs of 1.1875 mm (250 px).

8.1.4 Average Mechanical Properties

The mechanical properties of a porous material REV can be evaluated in terms of the homogenized stiffness tensor

\mathbf{C}^{hom} and of Biot's tensor \mathbf{B} . If the behaviour of porous material at the macro-scale is isotropic, the Biot's tensor is spherical and it is possible to define it in terms of the Biot's coefficient b as $\mathbf{B} = b \mathbf{I}$, where \mathbf{I} is the identity matrix. The Biot's coefficient, and more generally the Biot's tensor \mathbf{B} , is evaluated in literature in an experimental or an analytical way. In particular, Biot (1962) gave a mechanically based expression to evaluate b (Eq. (2.42)), which relates the Biot's coefficient to the ratio of the bulk modulus of the porous material and the one of the solid matrix. It follows that the Biot's tensor is a function of the porosity and of the Poisson's coefficient of the solid matrix. Moreover, many experimental studies pointed out that the Biot's coefficient is strongly influenced by the pore shape of the considered material (Nur and Byerlee, 1971; Vlahinić et al., 2009; Walsh, 1965). Since the Biot's tensor depends on the overall porosity and on the different arrangements of the pore space, in this study it is chosen as an indicator to evaluate the representativeness of REV's mechanical properties.

8.2 CALCULATION OF THE BIOT'S TENSOR

Here, the procedure to compute the Biot's tensor starting from the real 3D geometry of a porous material obtained by X-ray μ CT images is detailed.

8.2.1 Theoretical framework

Referring to Figure 8.6, $\partial\Omega_{\text{REV}}$ is the external REV boundary and $\partial\Omega_{\text{p}}$ is the pore surface within the REV. We recall the following relations, which link the volumes of the pore space Ω_{p} and the one of the material matrix Ω_{m} to the overall porosity ϕ_0 :

$$|\Omega_{\text{p}}| = |\Omega_{\text{REV}}| \phi_0, \quad (8.3a)$$

$$|\Omega_{\text{m}}| = |\Omega_{\text{REV}}| (1 - \phi_0). \quad (8.3b)$$

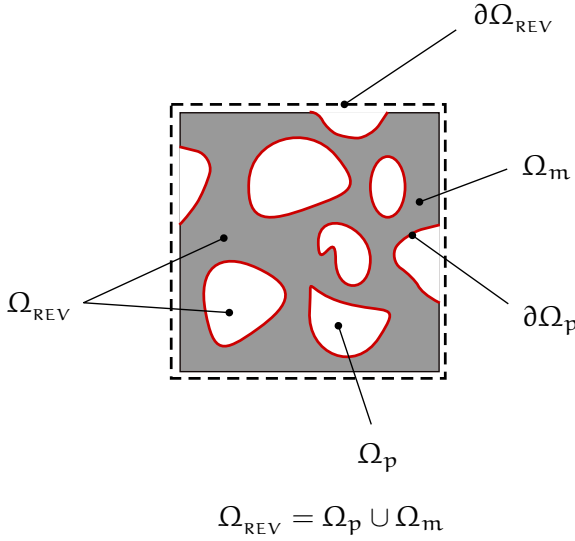


Figure 8.6: Notation in REV's definition: $\partial\Omega_{REV}$ is the external REV boundary (black dashed line) and $\partial\Omega_p$ is the pore surface within the REV (continuous red line).

The micromechanical boundary value problem for the calculation of the Biot's tensor can be written as follows:

$$\nabla \cdot \boldsymbol{\sigma} = \underline{\underline{0}} \quad \text{in } \Omega_m, \quad (8.4a)$$

$$\boldsymbol{\sigma} = \mathbf{C}_m : \boldsymbol{\varepsilon} \quad \text{in } \Omega_m, \quad (8.4b)$$

$$\boldsymbol{\varepsilon} = \text{sym}(\nabla \underline{\underline{u}}) \quad \text{in } \Omega_m, \quad (8.4c)$$

$$\underline{\underline{u}}(\underline{\underline{x}}) = \underline{\underline{0}} \quad \text{on } \partial\Omega_{REV}, \quad (8.4d)$$

$$\underline{\underline{T}} = -P \underline{\underline{n}}(\underline{\underline{x}}) \quad \text{on } \partial\Omega_p, \quad (8.4e)$$

where $\underline{\underline{u}}$ is the micro-scale displacement, $\underline{\underline{n}}(\underline{\underline{x}})$ is the outward unit normal to the boundary $\partial\Omega_p$, $\underline{\underline{T}}$ is the traction acting at the pore-matrix interface and \mathbf{C}_m is the local elasticity tensor. In particular, the solid skeleton is supposed to be homogeneous, linear elastic and isotropic, *i. e.* $\mathbf{C}_m(\nu_m, E_m)$, where ν_m and E_m are the Poisson's coefficient and the elastic modulus of the solid skeleton, respectively.

Eq. (8.4d) represents the linear displacement boundary condition (7.4) for $\mathbf{E} = \mathbf{0}$ and enforces that external boundaries

of the REV are clamped. According to the micromechanical boundary value problem (8.4), Eqs. (2.31) and (2.32) read:

$$\boldsymbol{\varepsilon}(\underline{x}) = -\mathbf{A}'(\underline{x})\mathbf{P}, \quad (8.5a)$$

$$\boldsymbol{\sigma}(\underline{x}) = -\mathbf{C}_m : \mathbf{A}'(\underline{x})\mathbf{P}. \quad (8.5b)$$

We derive the macroscopic stress tensor $\boldsymbol{\Sigma}$ from the microscopic stress field using the average rule (7.6), which is a consequence of the Hill's lemma:

$$\begin{aligned} \boldsymbol{\Sigma} &= \frac{(1 - \phi_0)}{|\Omega_m|} \int_{\Omega_m} \boldsymbol{\sigma}(\underline{x}) \, dV_m + \frac{\phi_0}{|\Omega_p|} \int_{\Omega_p} -\mathbf{P}\mathbf{I} \, dV_p \\ &= (1 - \phi_0)\langle \boldsymbol{\sigma} \rangle_m - \phi_0\mathbf{P}\mathbf{I}, \end{aligned} \quad (8.6)$$

being:

$$\langle \boldsymbol{\sigma} \rangle_m = \frac{1}{|\Omega_m|} \int_{\Omega_m} \boldsymbol{\sigma} \, dV_x. \quad (8.7)$$

Following the same path of Section 2.2.3.5 we get:

$$\boldsymbol{\Sigma} = -\boldsymbol{\Sigma}_{p,c} = -\mathbf{B}\mathbf{P}, \quad (8.8)$$

where the Biot tensor is defined in (2.34). Equating (8.6) with (8.8) yields:

$$\langle \boldsymbol{\sigma} \rangle_m = -\mathbf{C}_m : \langle \mathbf{A}' \rangle_m \mathbf{P}, \quad (8.9a)$$

$$\frac{\langle \boldsymbol{\sigma} \rangle_m}{\mathbf{P}} = -\mathbf{C}_m : \langle \mathbf{A}' \rangle_m = \mathbf{I} : \langle \mathbf{A} \rangle_m - \mathbf{I}. \quad (8.9b)$$

These relations show that eigenvalues of $\langle \boldsymbol{\sigma} \rangle_m$ are negative. Moreover, it is worth noting that, owing to the linear dependence of \mathbf{C}_m on \mathbf{E}_m , $\langle \boldsymbol{\sigma} \rangle_m/\mathbf{P}$, and hence $\langle \mathbf{A} \rangle_m$, does not depend on \mathbf{E}_m but only on the Poisson's coefficient of the matrix ν_m .

Combining (2.36) and (8.9b) the Biot's tensor can be written as a function of the overall porosity ϕ_0 and the average stress on the matrix $\langle \boldsymbol{\sigma} \rangle_m$ in the form :

$$\mathbf{B} = \phi_0\mathbf{I} - (1 - \phi_0) \frac{\langle \boldsymbol{\sigma} \rangle_m}{\mathbf{P}} \quad (8.10)$$

*The isotropic
case*

If the macroscopic behaviour is found isotropic, remembering (2.40), relation (8.9b) reduces:

$$\frac{\langle \boldsymbol{\sigma} \rangle_m}{P} = ((A_m)^v - 1) \mathbf{I}. \quad (8.11)$$

We can conclude that the tensor $\langle \boldsymbol{\sigma} \rangle_m$ is spherical, *i.e.* $\langle \boldsymbol{\sigma} \rangle_m = \bar{\sigma}_m \mathbf{I}$ with $\bar{\sigma}_m < 0$ and $(A_m)^v$ can be written as:

$$(A_m)^v = \frac{\bar{\sigma}_m}{P} + 1. \quad (8.12)$$

Therefore, the Biot's coefficient reads:

$$b = \phi_0 + (1 - \phi_0) \frac{|\bar{\sigma}_m|}{P}, \quad (8.13)$$

and on the base of 2.43 we can conclude:

$$0 \leq |\bar{\sigma}_m| \leq P. \quad (8.14)$$

In other words, if the macroscopic behaviour is found isotropic, $\langle \boldsymbol{\sigma} \rangle_m$ is spherical and the modulus of its associated scalar value $\bar{\sigma}_m$ spans from 0 to the value of P .

Assuming $P = 1$, the Biot's tensor can be computed from the solution of the above boundary value problem by means of Eq. (8.8) as

$$\mathbf{B} = \boldsymbol{\Sigma}_{p,c} = -\boldsymbol{\Sigma} = -\langle \boldsymbol{\sigma} \rangle. \quad (8.15)$$

It should be noted that the $\langle \boldsymbol{\sigma} \rangle$ involves the matrix contribution $\langle \boldsymbol{\sigma} \rangle_m$ and the the contribution of the phase inside the pores. Thus, Eq. (8.10) can be simplified as follows:

$$\mathbf{B} = \phi_0 \mathbf{I} - (1 - \phi_0) \langle \boldsymbol{\sigma} \rangle_m, \quad (8.16)$$

The quantity $\langle \boldsymbol{\sigma} \rangle_m$ can be calculated from a finite element analysis, as will be detailed in Section 8.2.2 . Thus, we can compute the Biot's tensor \mathbf{B} based on a micromechanical finite element analysis of the REV in which the pore surfaces are loaded with a unit pressure and all the external boundaries are clamped, as illustrated in Figure 8.7.

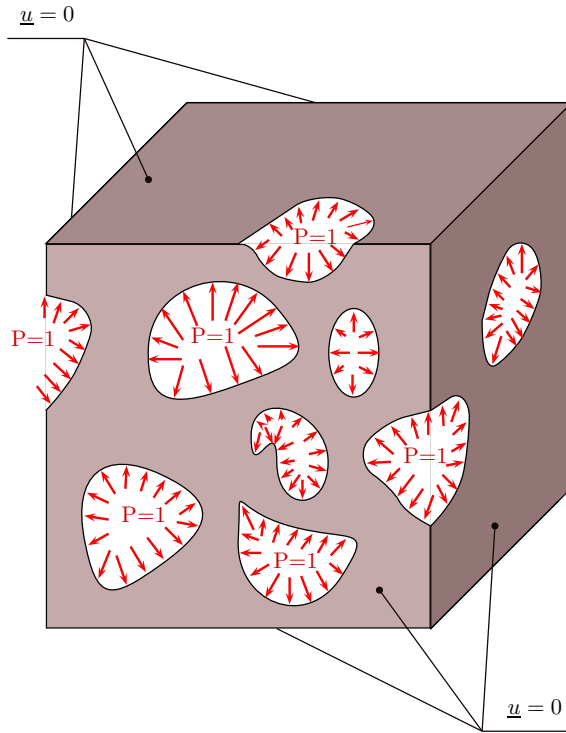


Figure 8.7: Boundary Conditions and loading scheme adopted for the numerical calculation of the Biot's Tensor.

8.2.2 The Finite Element Modelling

In order to calculate $\langle \sigma \rangle_m$, a finite element model is built by converting voxels representing the material matrix into hexahedral, 8-node finite elements, based on the idea recently proposed in Castellazzi et al. (2015a, 2017). The REV's chosen of 1.1875 mm consist in about 12M matrix voxels, which would result in 37 635 861 degrees of freedom for the finite element model. Therefore, the resolution of the images is decreased for computational cost reasons, passing from 250 images of 250×250 pixels with a resolution of $4.75 \mu\text{m}$ to 125 images of 125×125 pixels with a resolution of $9.5 \mu\text{m}$. An algorithm conserving the porosity is adopted for image scaling. The rescaled segmented images are labelled via Python's image libraries and all the pieces smaller than 3 voxels and the

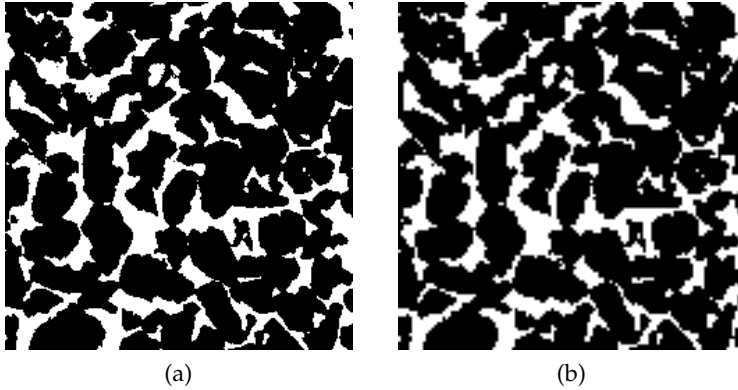


Figure 8.8: Comparison between the same slice of REV 73 before and after the rescaling and "cleaning procedure": (a) 4.75 μm (b) 9.5 μm cleaned

Table 8.2: Comparison between porosities before and after the rescaling and "cleaning procedure"

REV#	Porosity [%]	
	4.75 μm	9.50 μm cleaned
9	26.25	26.24
73	27.85	27.85
21	29.47	29.50

ones that do not belong to the REV boundary are erased. The aim is to delete small pieces which are not connected to the rest of the REV's matrix, and which would cause the presence of rigid body motions in the finite element model. These adjustments have a very low impact on the REV porosity, as shown in Table 8.2 and Figure 8.8. After the rescaling and "cleaning procedure", the REV consists in about 1.4M matrix voxels, which would result in 5 254 815 degrees of freedom for the finite element model.

In order to verify that the geometry of the pore space is conserved, the geometry indicator associated to the weighted distances $f_w(d_i)$, defined previously, is plotted and compared in Figure 8.9, showing that also the scaled REV repre-

sents the material micro-structure. The procedure adopted

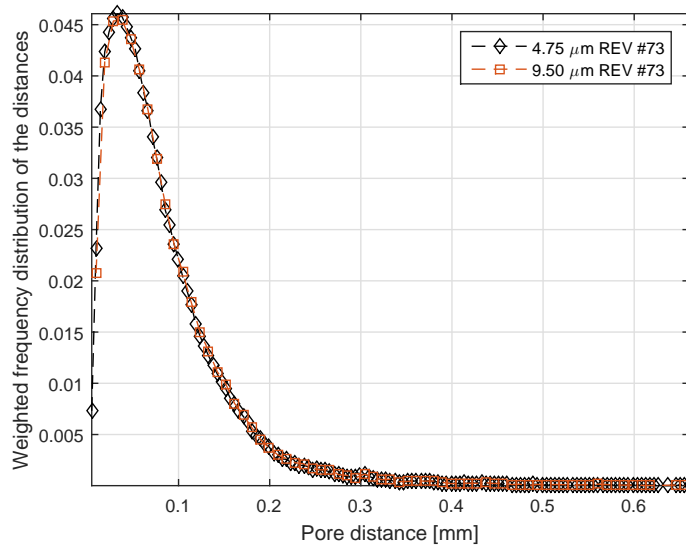


Figure 8.9: Comparison between the geometry indicators $f_w(d_i)$ computed for the two different resolution for REV #73.

to build the finite element model and to calculate the Biot's tensor \mathbf{B} is summarized in Figure 8.10. Starting from the set of segmented scaled X-ray μ CT images, the reconstruction of the original three-dimensional geometry is achieved by stacking all of its slices. Then, by using a common space-partitioning data structure (KD-TREE), the 3D image is transformed into the finite element mesh of the micro-structure, by simply generating the connectivity and the node matrices (Castellazzi et al., 2015a) of voxels representing the material. Next, clamped boundary conditions are imposed and all the pore surfaces are loaded with a unitary pressure $P = 1$ thanks to an automatic loading procedure. A static linear analysis allows to get the local stress maps, thus the average stress on the matrix $\langle \sigma \rangle_m$ is obtained through Eq. (8.7). Finally, the Biot's tensor is calculated by means of Eq. (8.16).

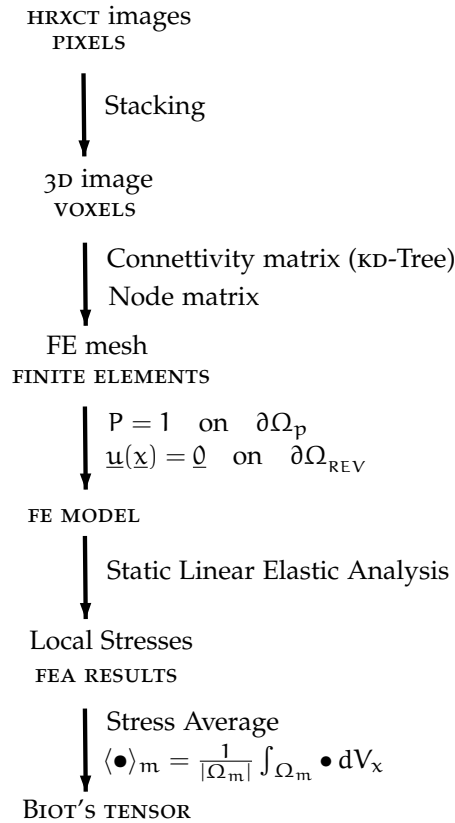


Figure 8.10: Workflow for calculation of Biot's tensor.

8.3 RESULTS AND DISCUSSION

In this section, we report the results of the estimation of Biot's tensors, according to the numerical procedure exposed in the previous sections. The Biot's tensor is calculated for the three samples of Prague sandstone reported in Table 8.2 with ν_m equal to 0.20 (no assumption is needed for E_m since the Biot's tensor does not depend on it). The resulting Biot's tensors are nearly spherical. This means that the material can be considered isotropic at the macro-scale: *i. e.* the pores can be considered randomly oriented. Therefore, it is possible to compute the Biot's coefficient b as the average of the Biot's tensor eigenvalues. The calculated Biot's coefficients are reported in Table 8.3. The difference between values of b

Table 8.3: Biot's coefficients

REV#	ϕ_0 [%]	b
9	26.24	0.6099
73	27.85	0.6340
21	29.50	0.6504

is due to the different porosity values of the three samples. It is worth noting that values in Table 8.3 are consistent with a Mori-Tanaka (MT) scheme with randomly oriented ellipsoidal inclusions (Benveniste, 1987; Berryman, 1980; Kuster and Toksöz, 1974; Mori and Tanaka, 1973; Wu, 1966), specialised for porous media in Section 7.2. In particular, they are in very good agreement with those of a MT scheme specialised for a porous medium having oblate pores with aspect ratio $r = 0.168$ (see Figure 8.11). Figure 8.11 proves that in this case the difference between the values of Biot's coefficient depends only on the overall porosity. In other words, for a chosen value of Poisson's coefficient of the material matrix, the variation of the average mechanical properties is only function of the porosity; this means that a REV of 1.1875 mm is also representative of the average mechanical properties. Therefore, we can conclude that 1.1875 mm is a good choice for the REV's size for this Prague sandstone specimen. For the further developments we will use only the REV #73 which has the average value of porosity among the EVs of 1.1875 mm.

8.4 CONCLUDING REMARKS

In this Chapter a general procedure to get the size of a porous medium Representative Elementary Volume (REV) starting from a X-ray Micro Computed Tomography dataset and to compute the related Biot's tensor have been illustrated. The proposed procedure have been applied to a Prague sandstone. The results in terms of Biot's tensor are used

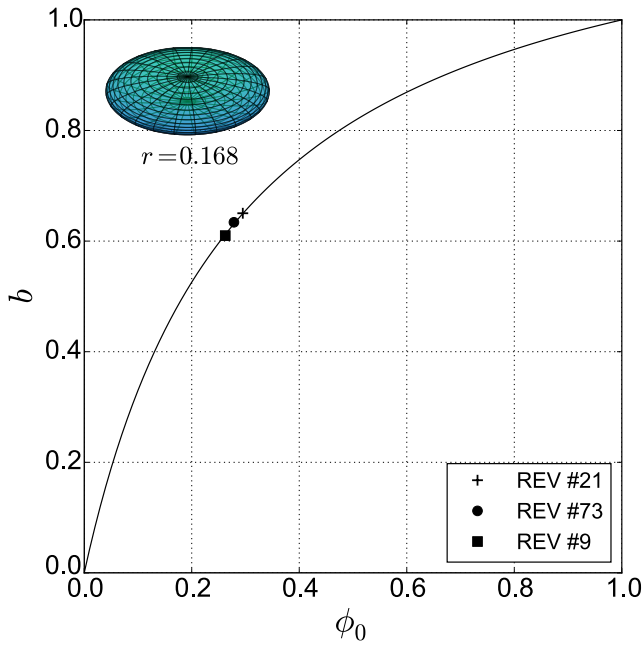


Figure 8.11: Calibration and validation of the Mori-Tanaka scheme with data of Table 8.3

to validate the size of the mechanical REV which is found 1.1875 mm.

DEFINITION OF SIMPLIFIED PORE GEOMETRIES

A procedure to obtain a simplified micro-mechanical model of a porous material is developed. A representative mechanical parameter is assessed (i) numerically for the real material, using the Finite Element model of the real porous material's micro-structure, and (ii) analytically by a micro-mechanical model with simplified geometry, making different assumptions about the shape of the pores. The comparison between the two evaluations make it possible defining the most suitable micro simplified geometry representing the real material. The proposed approach is general and applicable to any porous material. In order to prove its effectiveness, the developed approach is validated with an application on a Prague Sandstone.

9.1 THE PROCEDURE

The Chapter is aimed at the development of a procedure to obtain a simplified micro-mechanical model of a porous material which is able to reproduce the same macroscopic mechanical behaviour of the real one, taking into account the pore shape and their orientation.

The idea is to chose a representative mechanical parameter and to calibrate analytical homogenisation schemes, specialised for porous media, by making numerical simulations on the real material micro-structure.

The Biot's coefficient, and more generally the Biot's tensor, is selected as macroscopic mechanical property to compare the micro-mechanical model based on simplified geometries and the real material. Indeed, numerous experimental studies stress that the Biot's coefficient is strongly influenced by the pore shape of the material considered. Furthermore, it

is also a function of the material porosity and the Poisson's ratio of the soil skeleton, as remarked in Section 8.1.4.

The proposed procedure can be summarised as follows: the Biot coefficient is assessed (i) numerically for the real material, using the Finite Element model of the real porous material's micro-structure presented in Section 8.2.2, and (ii) analytically by a micro-mechanical model with simplified geometry (making different assumptions about the shape of the pores). The equivalence between the two evaluations made it possible to define the most suitable micro simplified geometry representing the real material. The proposed approach is general and applicable to any porous material. In order to prove its effectiveness, the developed approach is applied to the Prague Sandstone, for which the UGCT of Gent University provided the X-ray μ CT input dataset (see Section 8.1.1).

9.2 NUMERICAL EVALUATION

The numerical evaluation of Biot's tensors is performed according to the workflow depicted in Figure 8.10 (see Section 8.2.2). Biot's tensors are computed for REV #9 and #21 assuming $\nu_m = 0.2$, then for REV #73 for three different values of ν_m . The resulting Biot's tensors are nearly spherical. Therefore, it is possible to compute the Biot's coefficient b as the average of the Biot's tensor's eigenvalues. Computed Biot's coefficients are reported in Table 9.1. Moreover, since resulting Biot's tensors are nearly spherical, the material can be considered isotropic at the scale of the structure; it follows that we can think pores as randomly oriented.

9.3 CALIBRATION OF THE ANALYTICAL MODEL AND VALIDATION

As remarked in Section 7.2, the Biot's coefficient can be expressed as a function of the ratio between homogenised porous medium's bulk modulus and the one of solid matrix (See Eq. (7.24)). In order to get an analytical evaluation,

it is necessary to assess the homogenised porous medium's bulk modulus k^{hom} .

Homogenised bulk modulus' evaluation is conducted with a micromechanical model on the basis of the Mori-Tanaka scheme specialized for porous media, presented in Section 7.2. The model is calibrated using the results of numerical simulations in Table 9.1 for $\nu_m=0.2$, obtaining as pore ideal shape an oblate ellipsoid (see Table 7.1) having the aspect ratio r equal to 0.168. The model calibration is showed in Figure 9.1. It shows the trend of the Biot's coefficients b function of the aspect ratio r of pores for $\nu_m = 0.2$ and porosities values of REV # 9, 73 and 21 and the Biot's coefficients evaluated numerically. It is worth noting that for all the REV's the aspect ratio that ensures the equivalence between analytical and numerical evaluation is $r = 0.168$.

Next, the Mori-Tanaka model with randomly oriented pores having $r=0.168$ is validated with numerical results for different Poisson's ratios. In Figure 9.3 are depicted the predicted values of the analytical models and the ones computed by means of numerical simulations (Table 9.1), showing a very good agreement between numerical and analytical models. Figure 9.3 illustrates the surface representing the Biot's coefficient as a function of the porosity of the material ϕ_0 and Poisson's ratio ν_m for the aspect ratio derived from the calibration with numerical simulations.

Table 9.1: Numerical assessment of Biot's coefficients

REV #	b	ν_m		
		ϕ_0	0.1	0.2
9	26.24	-	0.6099	-
73	27.85	0.5804	0.6340	0.7084
21	29.50	-	0.6504	-

9.4 CONCLUDING REMARKS

A general procedure for the defining of micro-simplified geometries for a porous material, able to reproduce the same macroscopic mechanical behaviour of the real one, is developed. The comparison between results of numerical simulations with analytical schemes allows to quantify the pore aspect ratio of the analytical model that best describes the behaviour of the real porous media. In particular, we can conclude that Mori-Tanaka model with randomly oriented pores, presented in Section 7.2, is able to describe the trend of the Biot's coefficient for the Prague sandstone.

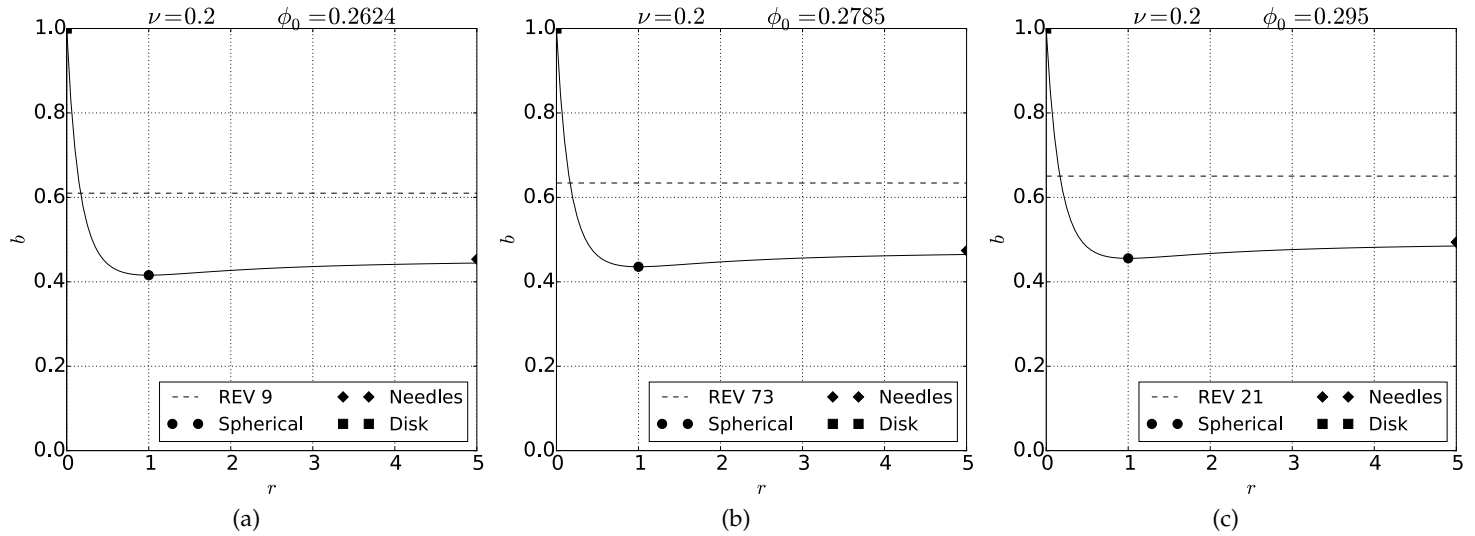


Figure 9.1: Calibration of the analytical model with simplified micro-geometries for Prague sandstone. Dashed lines represent numerical results for (a) REV #9; (b) REV #73; (c) REV #21. Biot's coefficients calculated with the analytical model based on the MT scheme function of the aspect ratio r are tracked using a continuous line.

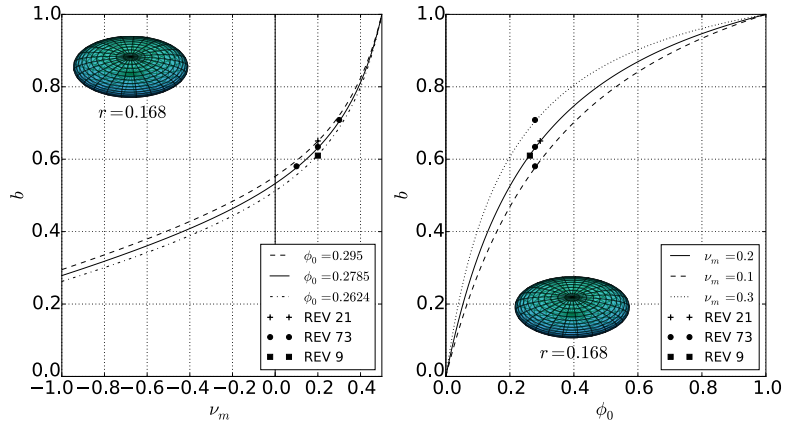


Figure 9.2: Validation of the analytical model with $r=0.168$: curves are the trends of Biot's coefficients varying matrix Poisson's coefficient and porosity; markers represent data of Table 9.1.

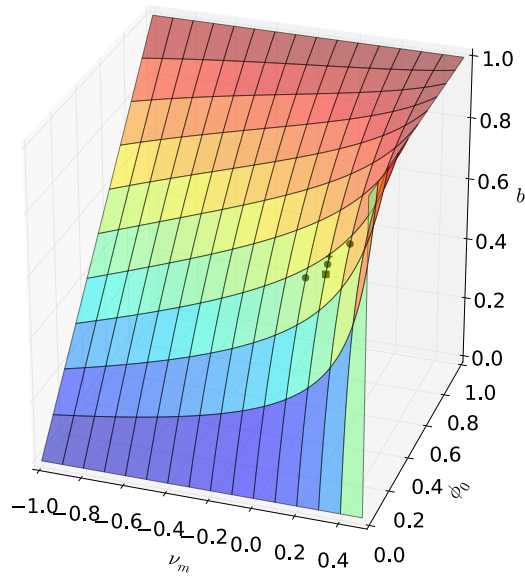


Figure 9.3: Surface representing the Biot's coefficient as a function of the porosity of the material ϕ_0 and Poisson's ratio ν_m for $r=0.168$. Black dots represent calculated values reported in Table 9.1.

POROUS MEDIA SATURATED WITH MULTIPLE SPECIES

A multi-scale approach for the analysis of mechanical effects induced by salt crystallisation in porous media is presented. The approach is based on numerical homogenisation and allows to predict the effects of salt crystallisation occurring at the scale of the structure, basing on the real 3D micro geometry of the porous material coming from Micro Computed Tomography images. Some hypotheses on the loading condition of the micro-mechanical model, accounting for different crystallisation physics, are introduced and their effects in terms of mechanical response at the macro-scale are compared. As case study, the proposed approach is applied to the Prague sandstone.

10.1 THE MODEL

Due to salt transport and crystallisation the porous medium can be saturated with different species α , *i. e.* air (a), water (w), salt (s), in three phases π , *i. e.* gaseous (g), liquid (l), solid (s). In this Chapter, the mechanical model for a porous medium saturated with different species is presented. The proposed formulation is based on homogenisation theories and it is an extension of the models presented in Coussy (2006); Dormieux et al. (2006). As case study, the proposed approach is applied to the Prague sandstone.

10.1.1 Hypotheses

We refer to a porous medium filled with a certain number of immiscible species α in π -phase (Figure 10.1), which occupies the whole pore volume. Each species α in π -phase occupies the domain Ω_{α}^{π} and it has its own pressure p_{α}^{π} .

Since the pressures p_α^π are different, there is no equilibrium at the interface between phases. In order to balance the system, surface tensions would be required. In the proposed formulation, for the sake of simplicity, all the surface tension effects are neglected.

The degree of saturation of a species α in π -phase, S_α^π , describes the pore volume fraction occupied by the phase:

$$S_\alpha^\pi = \frac{|\Omega_\alpha^\pi|}{|\Omega_p|}, \quad (10.1)$$

where $\Omega_p = \bigcup_{(\alpha,\pi)} \Omega_\alpha^\pi$.

In this dissertation, the attention is focused on the mechanical effects of salt that crystallises inside the pores, *i. e.* salt in solid phase. The passage from the salt in solution to the crystallised one involves a complex phase transition. Although the growing crystal is in a solid phase, it is modelled like a phase exerting a pressure on the pore surface without assuming a constitutive behaviour. Indeed, according to the literature on crystallisation presented in Section 2.1, in particular Scherer (1999, 2004); Steiger (2005a), it is reasonable to model the mechanical interaction between the growing crystal and the pore surface as a pressure acting on the surfaces of the material matrix in contact with the crystal.

10.1.2 Equations

Referring to Figure 10.1 the micromechanical boundary value problem can be written as:

$$\nabla \cdot \boldsymbol{\sigma} = 0 \quad \text{on} \quad \Omega_m, \quad (10.2a)$$

$$\boldsymbol{\sigma} = \mathbf{C}(\underline{\mathbf{x}}) : \boldsymbol{\varepsilon} \quad \text{on} \quad \Omega_m, \quad (10.2b)$$

$$\boldsymbol{\varepsilon} = \text{sym}(\nabla \underline{\mathbf{u}}) \quad \text{on} \quad \Omega_m, \quad (10.2c)$$

$$\underline{\mathbf{u}}(\underline{\mathbf{x}}) = \mathbf{E}(\underline{\mathbf{X}}) \cdot \underline{\mathbf{x}} \quad \text{on} \quad \partial\Omega_{\text{REV}}, \quad (10.2d)$$

$$\underline{\Gamma}_\alpha^\pi = -p_\alpha^\pi \underline{\mathbf{n}}(\underline{\mathbf{x}}) \quad \text{on} \quad \partial\Omega_\alpha^\pi, \quad (10.2e)$$

$$(10.2f)$$

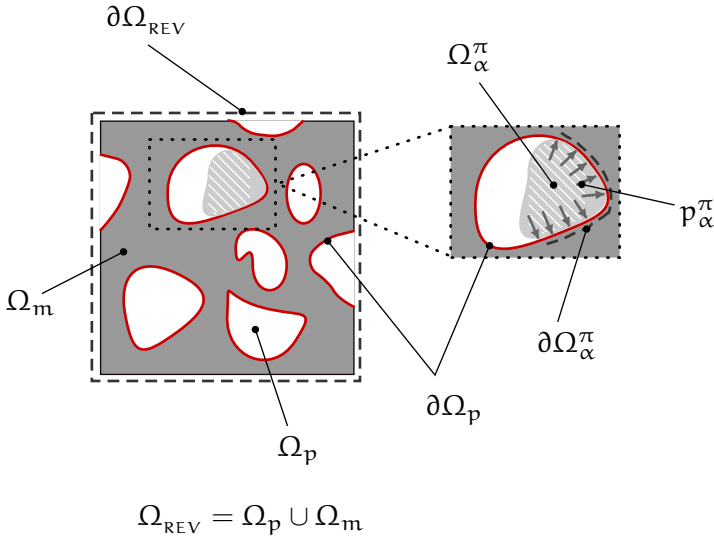


Figure 10.1: Notation in partially saturated REV: $\partial\Omega_p = \bigcup_{(\alpha,\pi)} \partial\Omega_\alpha^\pi$ is the pore surface within the REV (continuous red line).

where $\mathbf{C}(\underline{x}) = \mathbf{C}_m$ is the local elasticity tensor, supposed constant. Applying the Hill's lemma, we get the extension of Eq. (7.7) to unsaturated porous media:

$$\boldsymbol{\Sigma} = \mathbf{C}^{\text{hom}} : \mathbf{E} - \sum_{(\alpha,\pi)} \mathbf{B}_\alpha^\pi p_\alpha^\pi, \quad (10.3)$$

where \mathbf{B}_α^π is the partial Biot's tensor associated to the pressure p_α^π and domain Ω_α^π . The framework of linear microporomechanics allow to exploit the superposition principle: each phase can be treated separately, then the mechanical effect induced by each phase can be summed. Thanks to the superposition principle, it is possible to demonstrate that:

$$\sum_{(\alpha,\pi)} \mathbf{B}_\alpha^\pi = \mathbf{B}. \quad (10.4)$$

If we want to calculate one partial Biot's tensor using the geometry of a real micro-structure, we can suppose that only the partial pressures p_α^π associated to the one we want to compute is non-zero; it follows that Eq. (10.3) can be rewritten as:

$$\boldsymbol{\Sigma} = \mathbf{C}^{\text{hom}} : \mathbf{E} - \mathbf{B}_\alpha^\pi p_\alpha^\pi. \quad (10.5)$$

The micromechanical boundary value problem formulation for the calculation of \mathbf{B}_α^π can be written as follows:

$$\nabla \cdot \boldsymbol{\sigma} = \underline{0} \quad \text{in } \Omega_m, \quad (10.6a)$$

$$\boldsymbol{\sigma} = \mathbf{C}_m : \boldsymbol{\varepsilon} \quad \text{in } \Omega_m, \quad (10.6b)$$

$$\boldsymbol{\varepsilon} = \text{sym}(\nabla \underline{\mathbf{u}}) \quad \text{in } \Omega_m, \quad (10.6c)$$

$$\underline{\mathbf{u}}(\underline{\mathbf{x}}) = \underline{0} \quad \text{on } \partial\Omega_{\text{REV}}, \quad (10.6d)$$

$$\underline{\Gamma}_\alpha^\pi = -p_\alpha^\pi \underline{\mathbf{n}}(\underline{\mathbf{x}}) \quad \text{on } \partial\Omega_\alpha^\pi. \quad (10.6e)$$

Analogously to the case of porous medium saturated with one species, assuming $p_\alpha^\pi = 1$, the partial Biot's tensor can be computed as

$$\mathbf{B}_\alpha^\pi = \boldsymbol{\Sigma}_{p,c} = -\boldsymbol{\Sigma} = -\langle \boldsymbol{\sigma} \rangle, \quad (10.7)$$

where $\boldsymbol{\sigma}$ is the solution of the boundary value problem (10.6). Through mathematical passages, it is possible to write the partial Biot's tensor as a function of the overall porosity ϕ_0 and the average stress on the matrix $\langle \boldsymbol{\sigma} \rangle_m$:

$$\mathbf{B}_\alpha^\pi = \phi_0 S_\alpha^\pi \mathbf{I} - (1 - \phi_0) \langle \boldsymbol{\sigma} \rangle_m. \quad (10.8)$$

As in the case of porous medium saturated with one species, the quantity $\langle \boldsymbol{\sigma} \rangle_m$ can be calculated from a micromechanical finite element analysis. Thus, we can compute the partial Biot's tensor \mathbf{B}_α^π starting from the micro-structural geometry, loading a portion of pore surface $\partial\Omega_\alpha^\pi$ with a unit pressure and clamping all the external surfaces of the REV. Moreover, it is worth noting that $\mathbf{B}_\alpha^\pi(S_\alpha^\pi = 1) = \mathbf{B}$.

10.1.3 The law of partial pressures

Instead of Eq. (10.8) used in this work, in the literature (Dormieux et al., 2006; Flatt et al., 2014), it is often used a simple relation to compute the partial Biot's tensor. Here, it is briefly recalled since it will be compared with the proposed approach in the following:

$$\mathbf{B}_\alpha^\pi = S_\alpha^\pi \mathbf{B}. \quad (10.9)$$

According to Dormieux et al. (2006), Eq. (10.9) can be obtained assuming that there is not morphological difference between Ω_α^π and Ω_p . The physical meaning of Eq. (10.9) is that the contribute of each phase is distributed on the whole pore surface, as shown in Figure 10.2 considering a domain of only one pore and it is called "Law of Partial Pressures" (hereinafter denoted by LPP). In this case, \mathbf{B}_α^π results from

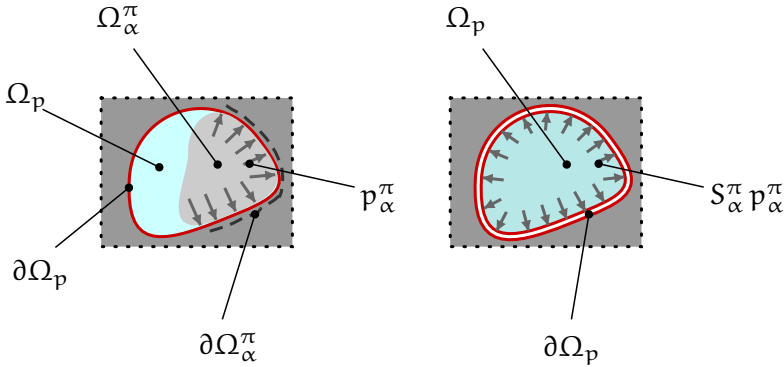


Figure 10.2: Comparison between the physical meaning of the proposed approach (on the left) and the one of Eq. (10.9), the "Law of Partial Pressures" (LPP) (on the right).

the computation of the boundary value problem (8.4), imposing $P = S_\alpha^\pi$ instead of $P = 1$. Indeed, substituting Eq. (10.9) in Eq. (10.3), we get:

$$\Sigma_{p,c} = \mathbf{B} \sum_{(\alpha,\pi)} S_\alpha^\pi p_\alpha^\pi. \tag{10.10}$$

If the Biot's tensor is spherical – *i.e.* $\mathbf{B} = b \mathbf{I}$ – then Eq. (10.9) can be rewritten as:

$$\mathbf{B}_\alpha^\pi = b_\alpha^\pi \mathbf{I}, \tag{10.11}$$

where b_α^π is the partial Biot's coefficient defined as:

$$b_\alpha^\pi = S_\alpha^\pi b. \tag{10.12}$$

Eq. (10.12) is used to describe the mechanical effect induced by salt crystallisation in Flatt et al. (2014). More refined analytical approaches, based on Self Consistent, Differential (Vlahinić et al., 2011) and the Mori-Tanaka (Coussy, 2006;

Vlahinić et al., 2011) schemes are proposed in literature. As proven in Vlahinić et al. (2011), the latter leads to Eq. (10.12).

10.2 COMPUTATION OF PARTIAL BIOT'S TENSORS

The procedure to compute the partial Biot's tensor \mathbf{B}_α^π is similar to the one described for the Biot's tensor in Section 8.2.2, but, in this case, the pore surfaces loaded with an unitary pressure depend on the degree of saturation (see Figure 10.3 for differences between the two procedures). For this reason, in order to build the micromechanical finite element model, we develop the following automatic loading procedure to implement the relationship between the degree of saturation S_α^π and loaded surfaces $\partial\Omega_\alpha^\pi$.

A distance d_i is associated to each face i of the finite element mesh as explained in Section 8.1.3 (see Figure 8.3b). The faces to be loaded are chosen on the basis of the value of the associated distance d_i . The first step consists in computing the pores distances. After that, a number of pore classes is defined, identifying surfaces where the pressure p_α^π is applied. For each pore class the corresponding value of degree of saturation is computed.

In order to establish a relationship between S_α^π and $\partial\Omega_\alpha^\pi$, we need firstly to link the volume occupied by a species $|\Omega_\alpha^\pi|$ to the loaded surface $\partial\Omega_\alpha^\pi$. Of course, in general, the link will depend on species α and phase π under consideration. As anticipated, in the present study we focus the attention on the crystallised salt (*i.e.* $\alpha = s$ and $\pi = s$) and, in this case, the aforementioned link depends on the choice of a crystal growth model; it can be implemented following the approach described in section 8.1.3, where each voxel can be split in six pyramids having a voxel's face as its base. This issue will be further detailed in the next Section.

10.2.1 From crystallisation's physics to the mechanical model

In order to evaluate the Biot's tensor associated to salt crystallisation according to the approach described in Section

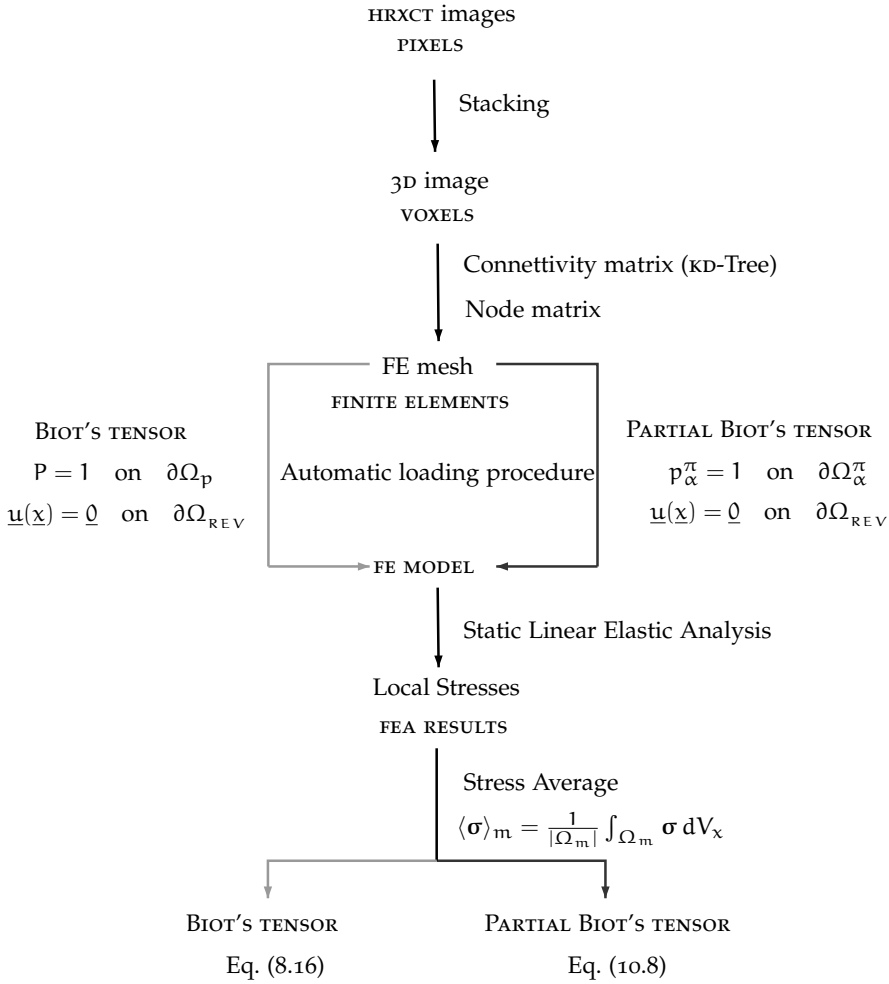


Figure 10.3: Workflow for calculation of Biot's tensor and of partial Biot's tensor.

10.1, it is necessary to translate the physical context and results on crystallisation's physics in a mechanical model. To provide the input data to calculate the pressure exerted by the crystal, p_s^s , and the degree of saturation S_s^s , the Hygro-Thermo-Chemical model presented in the first part of the dissertation, describing heat and mass transfer including salt transport and crystallisation at the macro-scale, can be used. For the Prague sandstone, we can quantify the crystallisation pressure, thus the crystal pressure, by means of

the expression proposed by Steiger for large crystals (Steiger, 2005a), since we expect that crystal sizes will be greater than about $0.1\text{-}1\ \mu\text{m}$ and, hence, that size effects are negligible.

Next, to solve the boundary value problem (10.6), some hypotheses on where the load is applied have to be made. Except in the most carefully controlled experiments (see for example Desarnaud et al. (2016a)), salt crystallisation occurs by heterogeneous nucleation (as shown in Desarnaud et al. (2015)), where a nucleating agent provides a surface with a relatively low interfacial energy with the crystal (Scherer, 1999). When the contact angle is low (less than 90°), concavities, such as cracks and pits, constitute particularly favorable nucleation substrate since they maximize contact between the substrate and crystal (Christian, 1975).

According to equilibrium thermodynamics salt precipitates preferentially in pores having a characteristic dimension $> 0.1\ \mu\text{m}$ (Espinosa-Marzal and Scherer, 2010a), *i.e.* all the pores that the X-ray μCT of Prague Sandstone under consideration is able to detect.

Considering the model for the crystal growth proposed in Espinosa et al. (2008a), nucleation and crystal growth take place equally in pores of different size. Thus, the contact between crystal and pore wall will occur firstly in smaller pores. The pore wall prevents growth in confined directions and the crystals can only keep on growing in the non-confined ones.

Finally, if we consider a real pore of a Prague sandstone, according to physical observation we may theorise that nucleation will take place in the pores' zones where concavities are present, *i.e.* we assume that crystallisation pressure will act firstly in places where distances between two opposite confining pore walls are smaller, as explained in Figure 10.4. We name this "Hypothesis of Small Pores first" (hereinafter denoted by HSP). Since the way crystal growth takes place in the pore network is still an open question, we are interested in testing also other loading schemes, *e.g.* the opposite situation: "Hypothesis of Large Pores first" (hereinafter denoted by HLP).

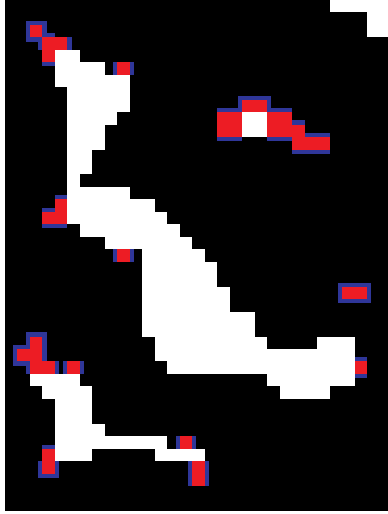


Figure 10.4: Exemplification of zones where it can be assumed that crystallisation pressure acts if the maximum distance between two opposite confining wall is assumed 2 pixels in a pore of Prague Sandstone: the boundaries in blue are assumed loaded by the crystallisation pressure.

In the case of HSP, it follows that the degree of saturation corresponding to the pore class comprehending all the pore surfaces for which is associated a distance $d_i \leq d$ is :

$$S_s^s(d) = \sum_{i=1}^{d/v} f_w(d_i). \quad (10.13)$$

where $f_w(d_i)$ is the geometry indicator associated to the weighted distances.

On the contrary, if we assume HLP, the degree of saturation corresponding to the pore class comprehending all the pore surfaces for which is associated a distance $d_i > d$ is :

$$S_s^s(d) = 1 - \sum_{i=1}^{d/v} f_w(d_i). \quad (10.14)$$

Figure 10.5 shows the degree of saturation of crystallised salt S_s^s as a function of the ratio between the pore distance and the maximum pore distance for a Prague sandstone according to the HSP.

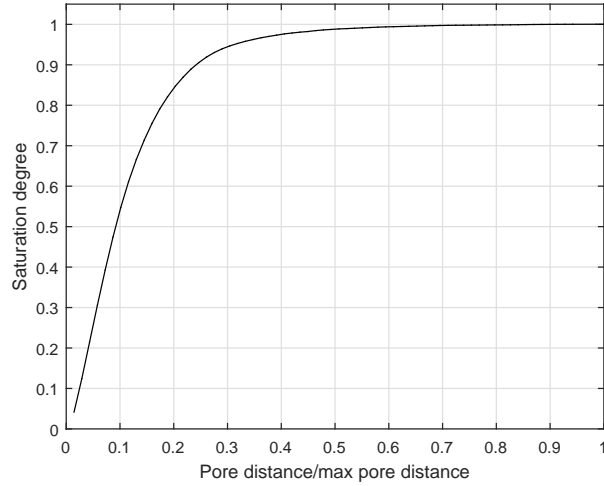


Figure 10.5: Saturation degree S_s^s according to the HSP REV #73 ($v = 9.5 \mu\text{m}$).

10.3 RESULTS AND DISCUSSION

In this section, we report the results of the computation of partial Biot's tensors, according to the numerical procedure exposed in the previous sections. In particular, in Section 10.3.1, results in terms of partial Biot's tensors related to the various hypotheses on the crystal growth model are presented and discussed. On the other hand, in Section 10.3.2 stress distributions at the micro-scale are shown and discussed.

10.3.1 *Partial Biot's tensor*

Here, we compute partial Biot's tensors for the REV #73 of Prague sandstone related to a crystallised salt at different levels of degree of saturation S_s^s .

The partial Biot's tensors are calculated according to the three models of crystal growth exposed in section 10.2.1, *i.e.* HSP, HLP and LPP, described by Eq. (10.9). The HSP and LPP partial Biot's tensors for different values of the degree of saturation are compared in Figure 10.6. As for the Biot's ten-

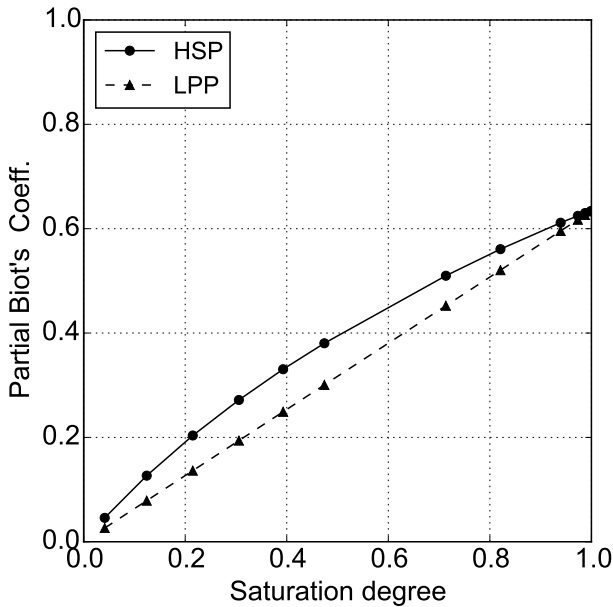


Figure 10.6: Partial Biot's coefficient function of degree of saturation assuming different crystal growth models: HSP vs. LPP.

sor of Section 8.3, also the partial ones are nearly spherical. Hence, results are given in terms of partial Biot's coefficient b_s^s , computed as the average of the partial Biot's tensors eigenvalues. As it can be noted, the relationship between the partial Biot's coefficient and the degree of saturation of crystallised salt is non linear, if the HSP is considered. Moreover, in this case the partial Biot's coefficient induced by salt crystallisation is higher than the one considering the law of partial pressure. This suggests that the law of partial pressures can be non conservative. For example, in the case of the Prague Sandstone it underestimates the partial Biot's coefficient up to 10%. On the contrary, if we assume that the larger pores are filled first (HLP), the law of partial pressures results conservative as shown in Figure 10.7. This means that the assumed loading scheme plays a crucial role in the estimation of the partial Biot's tensor in real porous media. They are computed also for different values of Poisson's co-

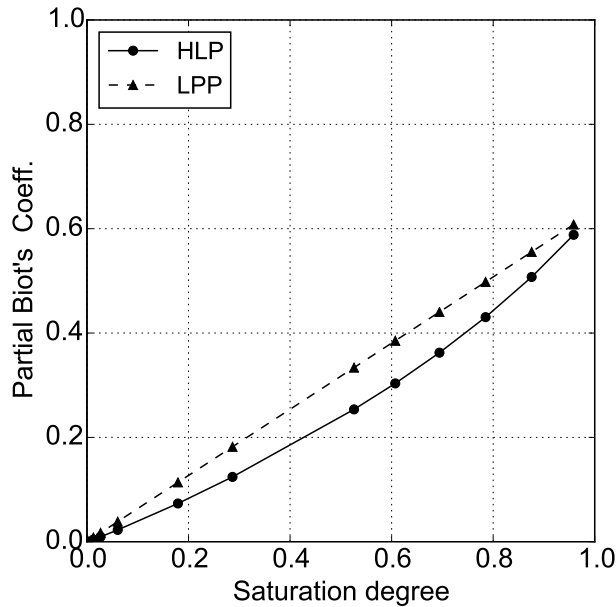


Figure 10.7: Partial Biot's coefficient function of degree of saturation assuming different crystal growth models: HSP vs. LPP.

efficient, as shown in Figure 10.8. Figure 10.8a illustrates partial Biot's tensors function of the saturation degree for ν_m equal to 0.10, 0.20 and 0.30, in the "Hypothesis of Small Pores first" (HSP). If the Poisson's coefficient of the material matrix increases, partial Biot's coefficients increases too. Normalising the curves reported in Figure 10.8a and defining the ratio between partial Biot's coefficients and Biot's coefficient $\chi = b_{\alpha}^{\pi}/b$, we get the trends depicted in Figure 10.8b. Results highlight that the values are different but the trend is the same; so, we can remark that the Poisson's coefficient of the material matrix has an influence only on the value of the Biot's coefficient. Therefore, we can write the partial Biot's tensor as:

$$b_{\alpha}^{\pi} = \chi b \quad (10.15)$$

where b is the Biot's coefficient which is function of (a) the porosity ϕ_0 , (b) the pore shape and (c) the Poisson's coeffi-

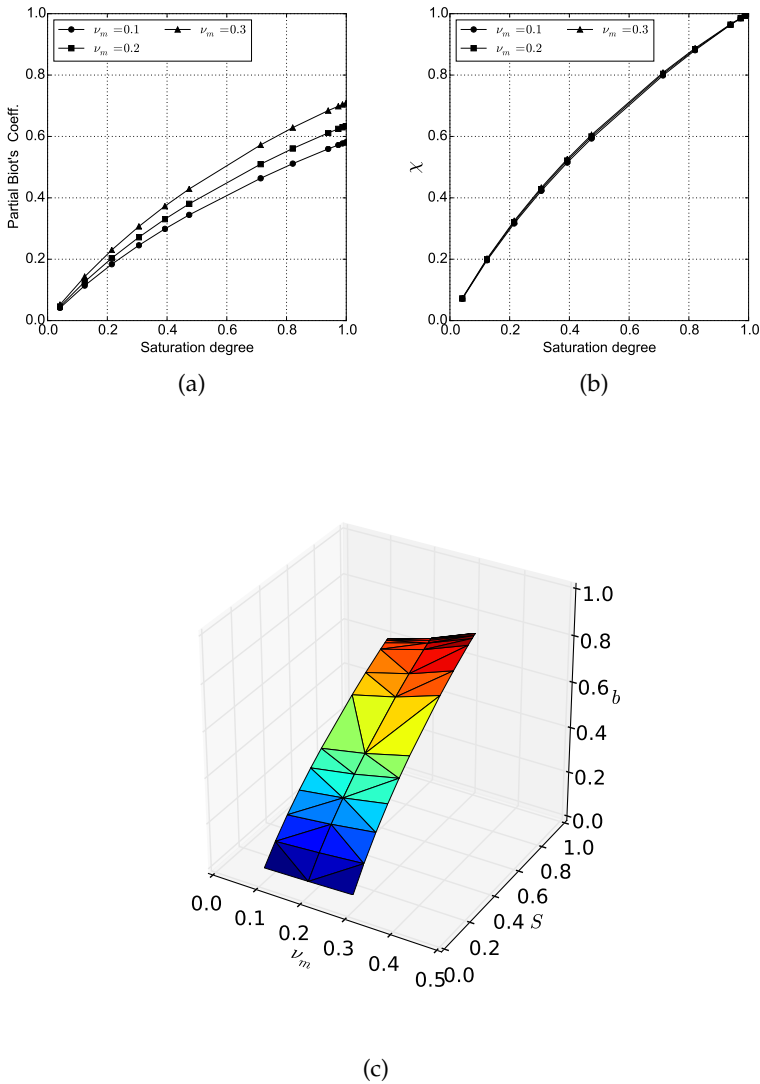


Figure 10.8: The influence of Poisson's coefficient of the material matrix on the partial Biot's coefficient: (a) partial Biot's coefficient function of degree of saturation assuming $\nu_m=0.10, 0.20, 0.30$; (b) normalised partial Biot's coefficient function of degree of saturation assuming $\nu_m=0.10, 0.20, 0.30$; (c) three dimensional representation.

cient of the material matrix ν_m and χ is a function of (a) the saturation degree S_α^π and (b) the loading scheme applied at the micro-scale. Here we will focus the attention only on results for $\nu_m = 0.20$.

10.3.2 *Stress distributions at the micro-scale*

We have shown in the previous section that the choice of the loading scheme influences the values of the partial Biot's tensor, that is the mechanical effect of salt crystallisation as seen at the macro-scale. The proposed approach allows also to inspect the effect of the loading scheme at the micro-scale. To this aim, we are going to show local stress maps in the case of HSP, since it seems the most reasonable hypothesis on the basis of the literature. In particular, we choose the maximum principal stress $\sigma_{III}(\underline{x})$ as an indicator, since it could be related to a Rankine-type criterion, which is appropriate for the prediction of failure of brittle rocks.

Figures 10.9 and 10.10 show the maps on a section of the REV of the maximum principal local stresses $\sigma_{III}(\underline{x})$ resulting from the static linear analysis to compute the partial Biot's tensor in the "Hypothesis of Small Pores first".

In particular, in these figures, the chosen colormap highlights the parts that are subjected to $0 \leq \sigma_{III}(\underline{x}) \leq p_\alpha^\pi = 1$: zones having $\sigma_{III}(\underline{x}) < 0$ are coloured in grey, since we do expect that the failure will occur in traction, while zones subjected to a positive maximum principal local stress $\sigma_{III}(\underline{x}) > p_\alpha^\pi = 1$ are coloured in dark red, being parts of the microstructure in which failure is most probably. As it can be noted, increasing the degree of saturation, the parts of the matrix that are subjected to tensile stress tend to diminish, while the stress' gradients increase. Moreover, positive maximum principal stresses tend to localise where grains are cemented. The REV's maximum and minimum values of principal stresses are reported in Figure 10.11 and compared with the law of partial pressures: it is worth noting that varying the degree of saturation, they does not follow

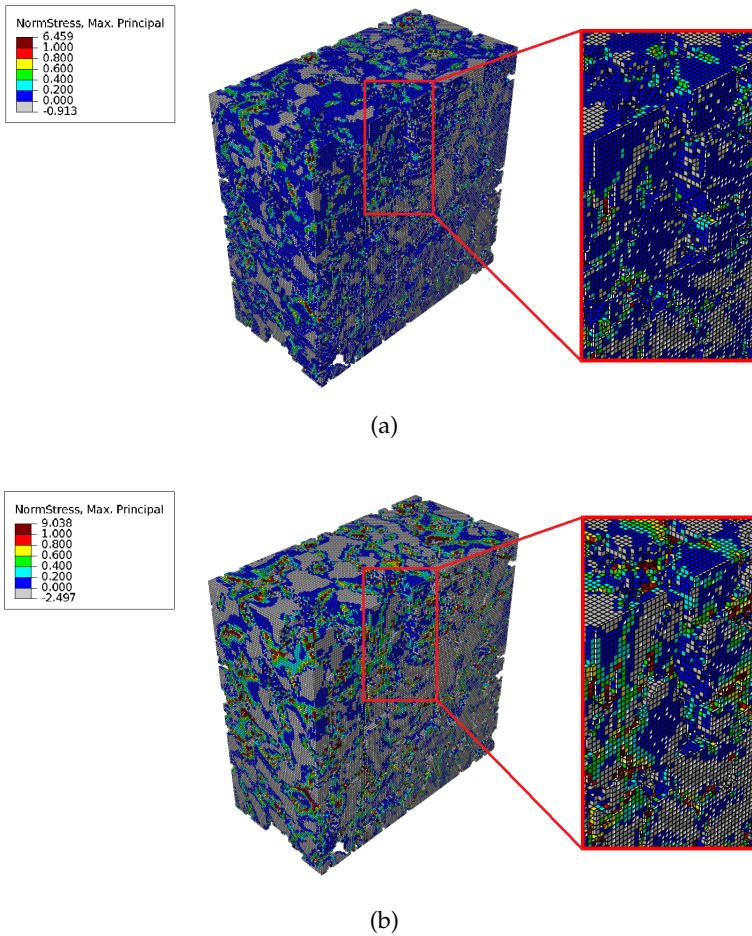


Figure 10.9: Hypothesis of smaller pores filled first: maximum principal local stresses $\sigma_{III}(\underline{x})$ at: (a) $S_\alpha^\pi = 4.15\%$, (b) $S_\alpha^\pi = 30.58\%$

a clear tendency, but they are an order of magnitude higher than the macroscopic values obtained with LPP.

10.4 CONCLUDING REMARKS

In this Chapter, we have presented a multi-scale approach for the analysis of the mechanical effects induced by salt

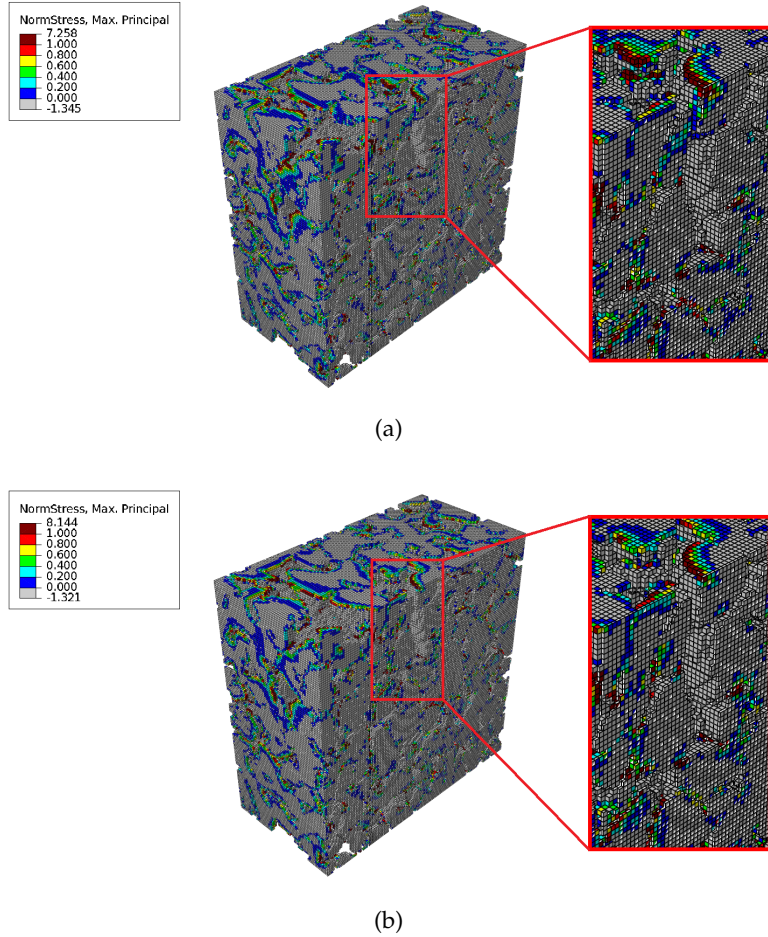


Figure 10.10: Hypothesis of smaller pores filled first: maximum principal local stresses $\sigma_{III}(\underline{x})$ at: (a) $S_{\alpha}^{\pi} = 71.34\%$, (b) $S_{\alpha}^{\pi} = 100.00\%$

crystallisation at the scale of the structure (*i.e.* the macro-scale) in porous materials saturated with different species, starting from its real 3D micro geometry obtained by X-ray Micro Computed Tomography images.

The proposed approach has been applied to the real porous medium's micro-structure of a Prague sandstone, computing the partial Biot's coefficient referred to the crystal pressure acting on the pore walls at different levels of saturation degree. The numerical procedure developed enabled us:

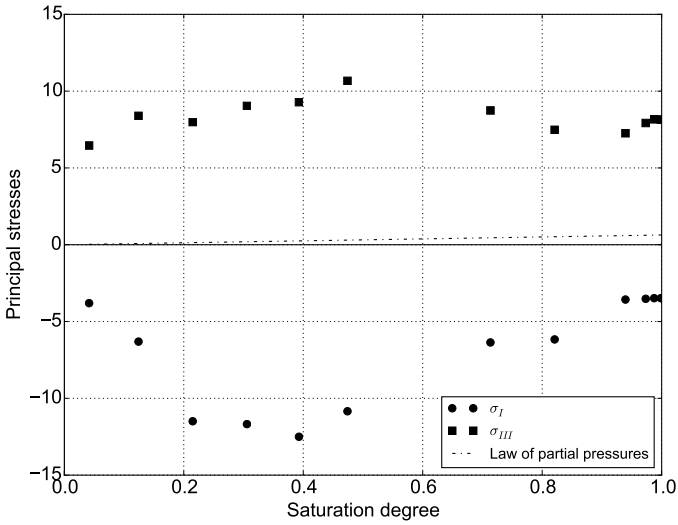


Figure 10.11: Comparison between the law of partial pressure and REV's maximum (σ_{III}) and minimum (σ_I) values of principal stresses for $\nu_m = 0.2$.

1. to establish a macroscopic relationship between partial Biot's tensors and degree of saturation for a real porous medium;
2. to test different loading schemes, deriving from some hypotheses on the way that crystals grow inside the porous medium;
3. to compare the achieved results with the simple relation often used in literature, *i.e.* "Law of Partial Pressures" (LPP);
4. to inspect maps of local stress, which can be used for a failure criteria or a damage model.

Results highlights that the loading scheme assumed plays a crucial role in the estimation of the partial Biot's tensor in real porous media. In particular, we have shown that changing the loading scheme the induced mechanical effects vary, both at the micro-scale and at the macro-scale, and that the law of partial pressures can be non conservative.

Part III

COUPLING HTC-MECHANICS

Results deriving from the first and second part of the dissertation are combined in a Hygro-Thermo-Chemo-Mechanical (HTCM) model. Moreover, they are incorporated in a structural computation with environmental-mechanical loadings to forecast the most probable damage scenarios.

THE HYGRO THERMO CHEMO MECHANICAL MODEL

A Hygro-Thermo-Chemo-Mechanical (HTCM) model, combining the hygro-thermo-chemical aspects – presented in Part I – and the mechanical ones – studied in Part II –, is developed. The proposed model is further specialised for sodium chloride solutions. The model considers an elastic porous material, isotropic at the macroscopic scale and described by the simplified micro-mechanical model developed in Chapter 9. Results presented in Chapter 10 are incorporated in the HTCM model. A structural computation with environmental and mechanical loadings is performed to forecast the most probable damage scenarios and to prove the effectiveness of the proposed approach.

11.1 INTRODUCTION

We develop here a Hygro-Thermo-Chemo-Mechanical (HTCM) model to describe the macroscopic behaviour of porous building materials contaminated with salts and subjected to environmental and structural loadings. Its formulation combines the HTC model presented in Chapter 3 and the macroscopic mechanical behaviour of porous materials saturated with multiple species, illustrated in Chapter 10.

We employ the concept of a Representative Elementary Volume (REV). The position of the centre of the REV in a global coordinate system is described by the position vector at macroscopic scale \underline{X} . While we treat the hygro-thermo-chemical aspects only from the macroscopic point of view, the mechanical ones have been studied in Part II with a multi-scale procedure illustrated in Figure 11.1. In order to combine these two aspects in a unique model the mechanical fundamental equation has to be appended to the system of equations of the HTC model. As regards the hygro-thermal-

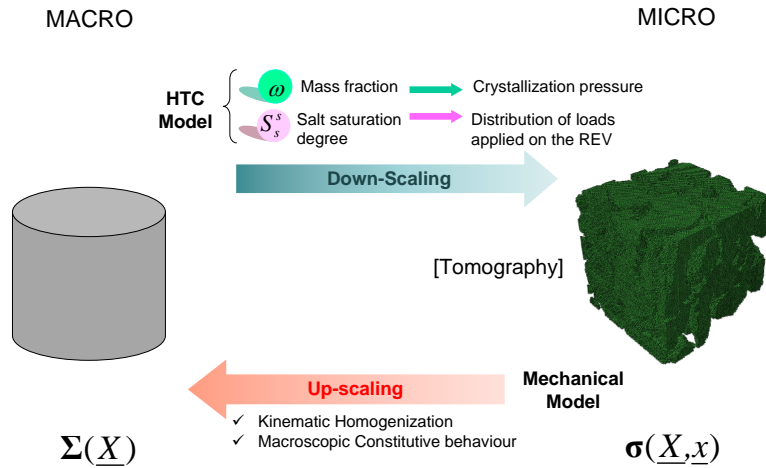


Figure 11.1: Multi-scale procedure for the evaluation of mechanical effects induced by salt crystallisation.

chemical aspects, a multiphase continuous porous medium (Gawin and Schrefler, 1996; Schrefler, 2002) is considered and the pores are considered cylindrical with isotropic distribution (Castellazzi et al., 2013a; Espinosa et al., 2008a), according to Chapter 3. As regards the mechanical part of the model we consider an elastic porous material, isotropic at the macroscopic scale and described by the simplified micro-mechanical model developed in Chapter 9. The equivalent relative humidity, the temperature, the concentration of the dissolved salt, the concentration of precipitated salts and the displacement field of the homogenized porous medium are assumed as independent variables. The governing equations are: moisture mass conservation, salt mass conservation, thermal energy balance, evolution equations of the kinetics of the crystallisation and the mechanical equation describing the momentum balance in terms of displacements at macroscopic scale. In the following the derivation of the latter will be presented.

11.2 MECHANICS

In this section we present the derivation of the momentum balance equation in terms of displacements, *i.e.* the one which includes compatibility, constitutive law and balance for the mechanical problem.

11.2.1 Momentum Balance Equation

The momentum balance equation at the macro-scale reads as:

$$\nabla \cdot \underline{\Sigma} + \underline{\mathbb{F}} = 0, \quad (11.1)$$

where $\underline{\Sigma} = \underline{\Sigma}^T$ is the macroscopic or total stress and $\underline{\mathbb{F}}$ are the macroscopic external body forces, which can be written as:

$$\underline{\mathbb{F}} = \underline{g} \rho_{eff}, \quad (11.2)$$

being \underline{g} the gravitational acceleration vector and ρ_{eff} the effective mass density defined in Eq. (3.17).

11.2.2 Strain-displacement Equation

Under the assumption of small displacements, the macroscopic strain-displacement equation reads as:

$$\underline{\mathbb{E}} = \text{sym}(\nabla \underline{\mathbb{U}}), \quad (11.3)$$

where $\underline{\mathbb{U}}$ is the macroscopic displacement field.

11.2.3 Constitutive Law

We are going to derive the constitutive law making the assumption of linear elastic, isotropic and homogeneous microscopical elasticity tensor. As detailed in Chapter 10 the constitutive relation for unsaturated porous media (see Eq. (10.3)) reads as:

$$\underline{\Sigma} = \underline{\mathbb{C}}^{\text{hom}} : \underline{\mathbb{E}} - \sum_{(\alpha, \pi)} \underline{\mathbb{B}}_{\alpha}^{\pi} p_{\alpha}^{\pi}. \quad (11.4)$$

Eq. (10.3) can be further generalised to account the thermal expansion or contraction of the porous material:

$$\boldsymbol{\Sigma} = \mathbf{C}^{\text{hom}} : (\mathbf{E} - \mathbf{E}_T) - \sum_{(\alpha, \pi)} \mathbf{B}_\alpha^\pi p_\alpha^\pi, \quad (11.5)$$

where $\mathbf{E}_T = \boldsymbol{\alpha} \Delta T$ is the thermal strain tensor, with $\boldsymbol{\alpha}$ the thermal expansion tensor of the porous material and ΔT the temperature variation respect to the thermal reference state. Equation (11.5) can be specialized considering species and phases illustrated in Table 3.1 as follows:

$$\boldsymbol{\Sigma} = \mathbf{C}^{\text{hom}} : (\mathbf{E} - \mathbf{E}_T) - \mathbf{B}_l p_l - \mathbf{B}_g p_g - \sum_{i=1}^N \mathbf{B}_{s_i}^s p_{s_i}^s, \quad (11.6)$$

where p_l , p_g and $p_{s_i}^s$ are the liquid, the reference atmospheric and the crystal pressure in its i -th form, respectively. According to Eq. (10.4) the following constraint holds:

$$\mathbf{B}_l + \mathbf{B}_g + \sum_{i=1}^N \mathbf{B}_{s_i}^s = \mathbf{B}. \quad (11.7)$$

Summing and subtracting $\mathbf{B}_l p_g$ to the second member of Eq. (11.6), we can write the constitutive relation as a function of the capillary pressure $p_c = p_l - p_g$:

$$\begin{aligned} \boldsymbol{\Sigma} = \mathbf{C}^{\text{hom}} : (\mathbf{E} - \mathbf{E}_T) - \mathbf{B}_l p_c + \\ - (\mathbf{B}_g + \mathbf{B}_l) p_g - \sum_{i=1}^N \mathbf{B}_{s_i}^s p_{s_i}^s, \end{aligned} \quad (11.8)$$

where p_g and p_c are defined in Equation (3.28), while pressure exerted by the crystal in its i -th form $p_{s_i}^s$ is defined as follows (Derluyn et al., 2014a; Steiger, 2005a):

$$p_{s_i}^s = \Delta p_i + p_l = \Delta p_i + p_g + p_c, \quad (11.9)$$

being Δp_i the crystallisation pressure of the i -th crystallised form. Substituting Eq. (11.9) in Eq. (11.8) we get:

$$\begin{aligned} \boldsymbol{\Sigma} = \mathbf{C}^{\text{hom}} : (\mathbf{E} - \mathbf{E}_T) - \left(\mathbf{B}_l + \sum_{i=1}^N \mathbf{B}_{s_i}^s \right) p_c + \\ - \mathbf{B} p_g - \sum_{i=1}^N \mathbf{B}_{s_i}^s \Delta p_i. \end{aligned} \quad (11.10)$$

11.2.3.1 Salts with one crystallised form

If we consider a salt with only one crystallised form, *e.g.* NaCl, we can write Eq. (11.10) as:

$$\Sigma = C^{\text{hom}} : (\mathbf{E} - \mathbf{E}_T) - (\mathbf{B}_l + \mathbf{B}_s^s) p_c - \mathbf{B} p_g - \mathbf{B}_s^s \Delta p. \tag{11.11}$$

The Biot’s tensor \mathbf{B} can be computed by means of the procedure illustrated in Section 8.2 and Section 8.2.2 or defining simplified pore geometries as shown in Chapter 9.

Assumptions on the constitutive law are summarised in

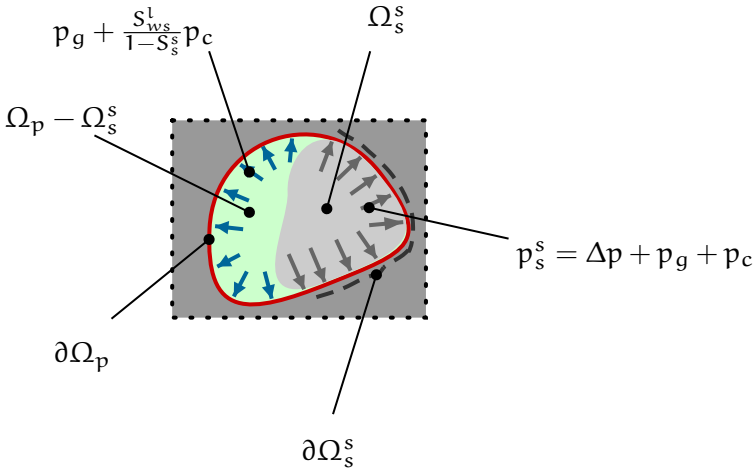


Figure 11.2: Assumptions made for the constitutive law in the case of salts with one crystallised form: representation of a pore.

Figure 11.2. The trend of partial Biot’s tensor for crystallised salt $\mathbf{B}_s^s(S_s^s)$ can be assessed choosing a suitable crystal growth model and applying the procedure presented in Chapter 10. Finally, the partial Biot’s tensor related to the liquid pressure \mathbf{B}_l and the one related to the vapour pressure \mathbf{B}_g can be evaluated making the assumption that the law of partial pressures expressed by (10.9) is valid in the portion of the domain occupied by the liquid and gaseous phase (see Figure 11.2) :

$$\mathbf{B}_l = \frac{S_{ws}^l}{1-S_s^s} (\mathbf{B} - \mathbf{B}_s^s), \quad \mathbf{B}_g = \frac{S_w^g}{1-S_s^s} (\mathbf{B} - \mathbf{B}_s^s), \tag{11.12}$$

being $1 - S_s^s = S_{ws}^l + S_w^g$, where S_{ws}^l is the degree of saturation of the salt solution and S_w^g is the one of the liquid water in gaseous phase (see Table 3.1).

Inserting Eqs. (11.12) in Eq. (11.11), it is possible the writing of the constitutive law as a function of \mathbf{B} and \mathbf{B}_s^s :

$$\begin{aligned} \boldsymbol{\Sigma} = & \mathbf{C}^{\text{hom}} : (\mathbf{E} - \mathbf{E}_T) - \mathbf{B}_s^s p_s^s + \\ & - \left(\frac{S_{ws}^l}{1 - S_s^s} (p_g + p_c) + \frac{S_w^g}{1 - S_s^s} p_g \right) (\mathbf{B} - \mathbf{B}_s^s), \end{aligned} \quad (11.13)$$

which can be reformulated as:

$$\begin{aligned} \boldsymbol{\Sigma} = & \mathbf{C}^{\text{hom}} : (\mathbf{E} - \mathbf{E}_T) - \mathbf{B}_s^s (\Delta p + p_g + p_c) + \\ & - \left(p_g + \frac{S_{ws}^l}{1 - S_s^s} p_c \right) (\mathbf{B} - \mathbf{B}_s^s). \end{aligned} \quad (11.14)$$

11.2.3.2 Isotropic macroscopic behaviour

Now, we are going to derive the constitutive law making the assumption of isotropic macroscopic behaviour of the porous material.

We have seen that the constitutive law consists in two terms:

1. $\mathbf{C}^{\text{hom}} : (\mathbf{E} - \mathbf{E}_T)$, which is the effective stress $\boldsymbol{\Sigma}'$ representing the elastic stress related to the elastic part of the deformation. It consists in $\mathbf{C}^{\text{hom}} : \mathbf{E}$, which takes into account the contributes of macroscopic deformations and $\mathbf{C}^{\text{hom}} : \mathbf{E}_T$, which takes into account the contributes of thermal deformations;
2. $\sum_{(\alpha, \pi)} \mathbf{B}_\alpha^\pi p_\alpha^\pi$, which takes into account the macroscopic stress induced by the presence of different species in various phases inside the porous medium for a material whose local deformation is prevented.

The term which takes into account the contributes of macroscopic deformations can be specialised as:

$$\mathbf{C}^{\text{hom}} : \mathbf{E} = \lambda^{\text{hom}} \nabla \cdot \underline{\underline{U}} \mathbf{I} + \mu^{\text{hom}} \left(\nabla \underline{\underline{U}} + (\nabla \underline{\underline{U}})^T \right), \quad (11.15)$$

where λ^{hom} and μ^{hom} are the homogenised Lamé constants. Thanks to the hypothesis of isotropic macroscopic behaviour, the thermal strain tensor can be written as $\mathbf{E}_T = \alpha \Delta T \mathbf{I}$. It follows that:

$$\begin{aligned} \mathbf{C}^{\text{hom}} : \mathbf{E}_T &= \lambda^{\text{hom}} \text{tr}(\mathbf{E}_T) \mathbf{I} + 2\mu^{\text{hom}}(\mathbf{E}_T) = \\ &= (3\lambda^{\text{hom}} + 2\mu^{\text{hom}}) \alpha \Delta T \mathbf{I} = \\ &= 3\kappa^{\text{hom}} \alpha \Delta T \mathbf{I}, \end{aligned} \quad (11.16)$$

being κ^{hom} the homogenised bulk modulus. Finally, the second term reduces to:

$$\sum_{(\alpha, \pi)} \mathbf{B}_\alpha^\pi p_\alpha^\pi = \left(\sum_{(\alpha, \pi)} b_\alpha^\pi p_\alpha^\pi \right) \mathbf{I}. \quad (11.17)$$

Therefore, total stress can be written as:

$$\begin{aligned} \boldsymbol{\Sigma} &= \lambda^{\text{hom}} \nabla \cdot \underline{\mathbf{u}} \mathbf{I} + \mu^{\text{hom}} \left(\nabla \underline{\mathbf{u}} + (\nabla \underline{\mathbf{u}})^T \right) + \\ &\quad - 3\kappa^{\text{hom}} \alpha \Delta T \mathbf{I} - \sum_{(\alpha, \pi)} b_\alpha^\pi p_\alpha^\pi \mathbf{I}. \end{aligned} \quad (11.18)$$

SALTS WITH ONE CRYSTALLISED FORM If we consider a salt with only one crystallised form, according to Section 11.2.3.1, we can write the third term as:

$$\begin{aligned} \sum_{(\alpha, \pi)} b_\alpha^\pi p_\alpha^\pi &= b_s^s (\Delta p + p_g + p_c) + \\ &\quad + \left(p_g + \frac{S_{ws}^l}{1 - S_s^s} p_c \right) (b - b_s^s). \end{aligned} \quad (11.19)$$

Exploiting the writing of the partial Biot's coefficient according to (10.15) $b_s^s = \chi_s^s b$ the equation can be simplified as:

$$\begin{aligned} \sum_{(\alpha, \pi)} b_\alpha^\pi p_\alpha^\pi &= b_s^s (\Delta p + p_g + p_c) + \\ &\quad + \left(p_g + \frac{S_{ws}^l}{1 - S_s^s} p_c \right) (1 - \chi_s^s) b. \end{aligned} \quad (11.20)$$

CRYSTALLISATION PRESSURE According to Steiger (2005a), the crystallisation pressure for large NaCl crystals can be written as:

$$\Delta p_{\text{NaCl}} \approx \frac{\nu RT}{V_s} \left(\ln \frac{\omega}{\omega_{\text{sat}}} + 0.56 \left(\frac{\omega}{\omega_{\text{sat}}} - 1 \right) \right), \quad (11.21)$$

being ν a factor of $\nu = 2$ in the case of 1-1 and 2-2 salts (e.g. NaCl). It is worth noting that Eq. (11.21) is valid for $1.0 \leq \frac{\omega}{\omega_{\text{sat}}} \leq 2.2$ (Steiger, 2005a). Figure 11.3 shows the trend of $\ln \frac{\omega}{\omega_{\text{sat}}} + 0.56 \left(\frac{\omega}{\omega_{\text{sat}}} - 1 \right)$ with respect to the supersaturation ratio for sodium chloride solutions.

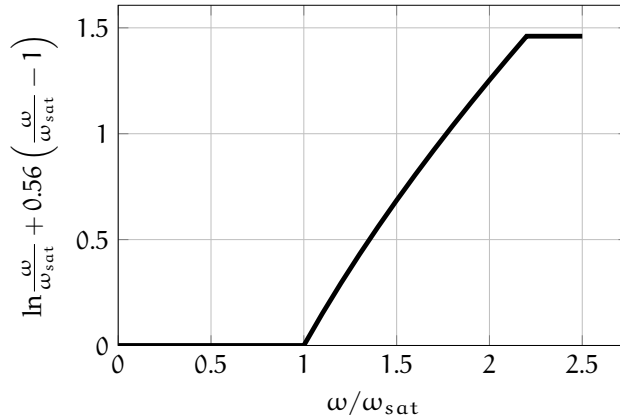


Figure 11.3: Trend of crystallisation pressure of Halite (NaCl) as a function of supersaturation ratio

11.2.4 Fundamental equation

Inserting the constitutive law (11.5) and the strain - displacement equation (11.3) in the momentum balance equation (11.1), we obtain the fundamental equation of the mechanical behaviour of the porous material saturated with multiple species, which represent the formulation of the momentum balance equation as a function of the macroscopic displacement field \underline{u} .

11.3 NUMERICAL APPLICATION

In this section, the potentialities of the HTCM model specialised for sodium chloride solutions are evaluated, simulating the drying behaviour of a piece of Prague sandstone saturated with an aqueous NaCl solution. In a particular, we simulate the drying behaviour of a piece of Prague sandstone having dimensions $25 \times 25 \times 25$ cm saturated with an aqueous NaCl solution with $\omega = 0.5\%$ and subjected to 50% RH at 20°C for 6 days. From the mechanical point of view, the specimen is simply supported on the bottom face. On the other edges we do not apply any load: it follows that the specimen is free to expand or shrink, since no deformation is restrained. The mechanical boundary conditions can be summarised as follows: $U_z = 0$ on the bottom face, with $\underline{U} = \underline{0}$ in a corner point in order to restrain the rigid body motions; $\underline{\Sigma} = \underline{0}$ on the other faces. The macroscopic external body force described by Eq. (11.2) is applied in the domain of the specimen. The material is modelled as a linear elastic solid. Only a quarter of the column is modelled thanks to the symmetries of the considered problem. The temperature is assumed constant in the domain during the simulations, thus the thermal strain tensor is null. These environmental conditions aim at the evaluation of damage scenarios applying plausible boundary and initial environmental conditions to larger specimens of Prague sandstone than the ones simulated in Chapter 6.

The model has been implemented by means of COMSOL Multiphysics (COMSOL, 2008). The non-linear system of equations is solved through a standard iterative strategy, based on Newton-Raphson method. The time discretisation is carried out by means of the backward finite difference method and the space discretisation is performed by the finite element method. Brick elements with standard Lagrangian quadratic shape functions are adopted. Each specimen has been spatially discretised with smaller finite elements in correspondence of the external surface and the vertical edge, since it is the area in which there are the most pronounced gradients. The typical size of the mesh spans from

15 mm in centre of the specimen to 3 mm at the corner, in which there are the most pronounced gradients. The finite element mesh is shown in Figure 11.4a, while the outer surfaces on which evaporation occurs are highlighted in blue in Figure 11.4b.

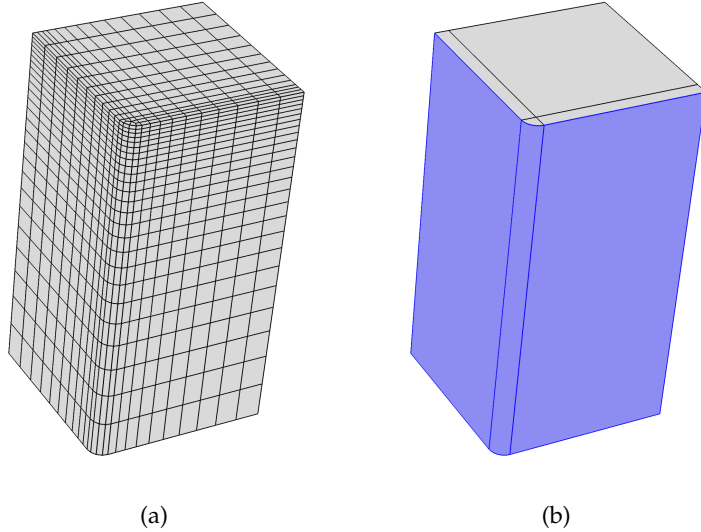


Figure 11.4: Geometry: (a) mesh; (b) evaporative surfaces.

Adopted parameters are shown in Table 11.1. It is worth noting that the supersaturation ratio threshold is assumed 1.6 according to Desarnaud et al. (2014). Homogenised mechanical properties of the porous medium – such as λ^{hom} , μ^{hom} and κ^{hom} – are calculated using the analytical model based on the Mori-Tanaka scheme, which has been calibrated and validated for the Prague sandstone in Chapter 9 and assuming $\nu_m = 0.10$ and $\kappa_m = 37000$ MPa. The Biot's coefficient results in 0.59. The trend of the partial Biot's coefficient function of the saturation degree of precipitated salt S_s^s is taken according to the "Hypothesis of Small Pores first" (HSP) model presented in Chapter 10. In particular, $\chi_s^s(S_s^s)$ is shown in Figure 11.5.

PAR.	VALUE	UNIT	DESCRIPTION
D_v	$1.9 \cdot 10^{-6}$	m^2/s	Vapour permeability
Φ_0	0.29	-	Porosity
A	1.68	$kg\ m^{-2}s^{-0.5}$	Water adsorption coefficient
r_p	$15 \cdot 10^{-6}$	m	Average pore radius
K_c	$1.08 \cdot 10^{-4}$	m/h	Growth rate coefficient
n	$7 \cdot 10^{12}$	$1/m^3$	Nuclei in solution
p	1	-	Crystallization process order
α_0	1.6	-	Crystallisation threshold
ω_{sat}	0.264	kg/kg	Mass fraction ω at saturation
K_s	$2.2 \cdot 10^{-9}$	m^2/h	Diffusion coefficient
ρ_s^s	2170	kg/m^3	Mass density of precipitated NaCl
Ψ	1.0028	-	Sorption isotherm parameter
κ^{hom}	15163	MPa	Homogenised bulk modulus
μ^{hom}	16353	MPa	Homogenised shear modulus
b	0.59	-	Biot's coefficient

Table 11.1: Parameters used in the simulations.

Figure 11.6 shows the maps of supersaturation ratio of ω/ω_{sat} every 24 hours. It can be remarked that the supersaturation threshold α_0 is exceeded after 5 days (120 hours). Inspecting the maps we observe that the concentration of the solution increases firstly at the edge. Consequently, it is observed that the salt begins to precipitate at first in correspondence of the edge. In Figure 11.7 the precipitated NaCl is depicted after 5 days (120 hours): at 120 hours, 128 hours, 136 hours and 144 hours (6 days).

Figure 11.8 shows the field of displacements induced by crystallisation of the salt on Prague sandstone at 120 hours, 128 hours, 136 hours and 144 hours (6 days). It can be noted how a bulge in correspondence of the areas in which the

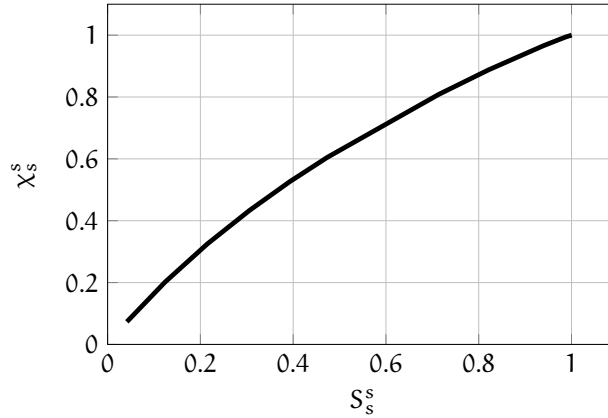


Figure 11.5: Trend of the partial Biot's coefficient as a function of the saturation degree of precipitated Halite

crystallisation takes place (the corner) grows: a particular showing the deformed and undeformed configurations is reported in Figure 11.9. Figure 11.10 represents the areas subjected to an spherical effective stress $\text{tr}(\Sigma')/3$ due to crystallisation exceeding the tensile strength of the material equal to 1.6 MPa (Pavlík et al., 2008) at 120 hours, 128 hours, 136 hours and 144 hours (6 days). It can be remarked that the tensile stress is exceeded, firstly, at the corner proceeding towards the edges of the specimen. In Figure 11.11 the trend of the maximum spherical effective stress as a function of time is reported. It is worth noting that this parameter increases when the quantity of crystallised salt arises. The choice of considering the macroscopic effective stress underlines the employing of a macroscopic failure or damage criteria to evaluate damage scenarios. Another option could consist in performing a re-localisation step (see Section 2.2.2) and evaluating the microscopic stress due to salt crystallisation and to the other applied loadings. In this case, the stress state should be compared with a microscopic failure or damage criteria, which should be obtained with microscopic mechanical tests.

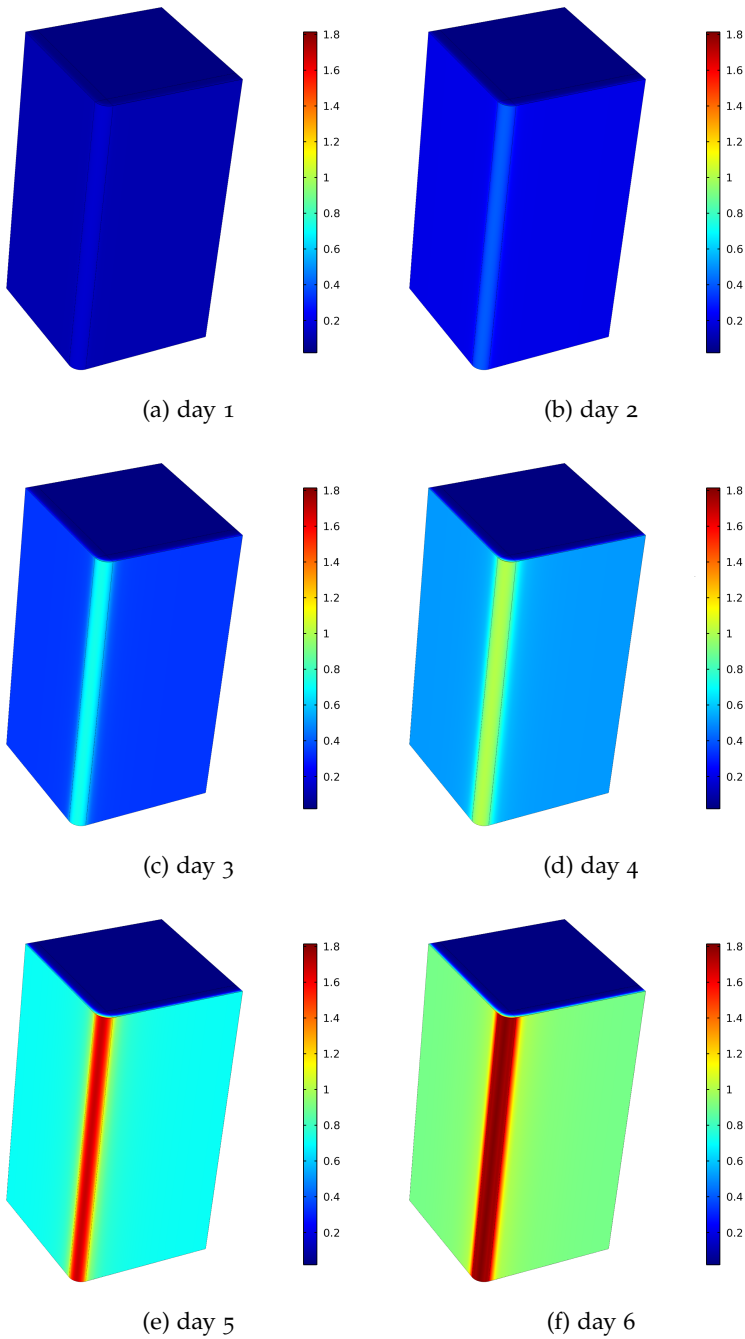


Figure 11.6: Supersaturation ratio $\omega/\omega_{\text{sat}}$ at 1 (a), 2 (b), 3 (c), 4 (d), 5 (e) and 6 (f) days.

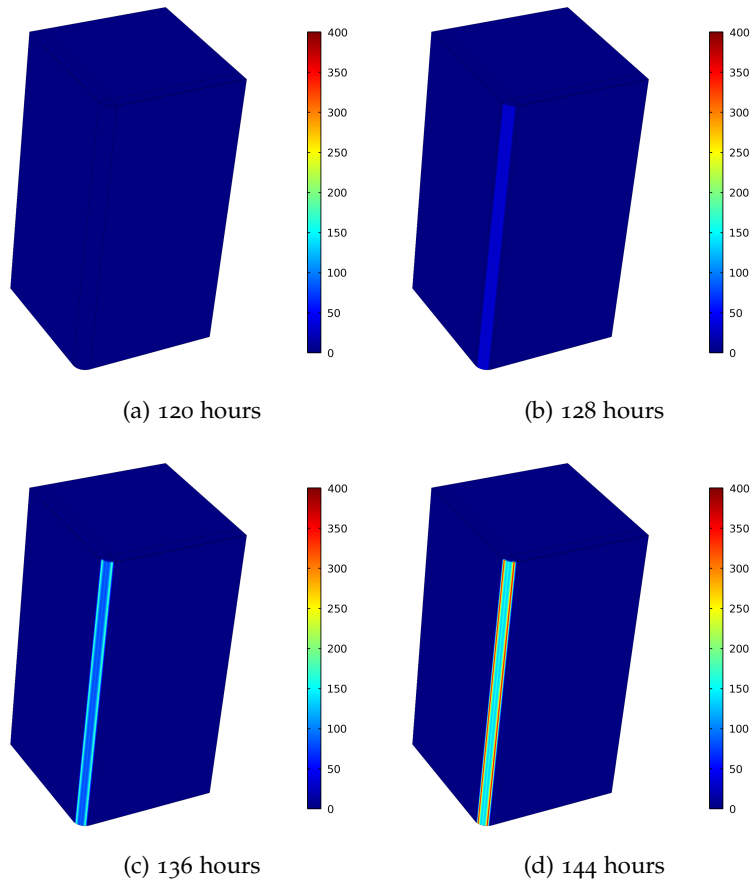


Figure 11.7: Precipitated NaCl (c_s^s) at (a) 120, (b) 128, (c) 136 and (d) 144 hours.

11.4 CONCLUDING REMARKS

In this chapter a Hygro-Thermo-Chemo-Mechanical (HTCM) model is proposed, adding the fundamental equation of mechanics to the HTC model presented in the first part of this dissertation. As constitutive law, a generalisation of the one derived in Chapter 10 is assumed. Then, it is specialised for materials having a macroscopic isotropic behaviour and a linear elastic, isotropic and homogeneous microscopic elasticity tensor. Finally, salts with one crystallised form, in particular NaCl, are considered. In order to show its potential-

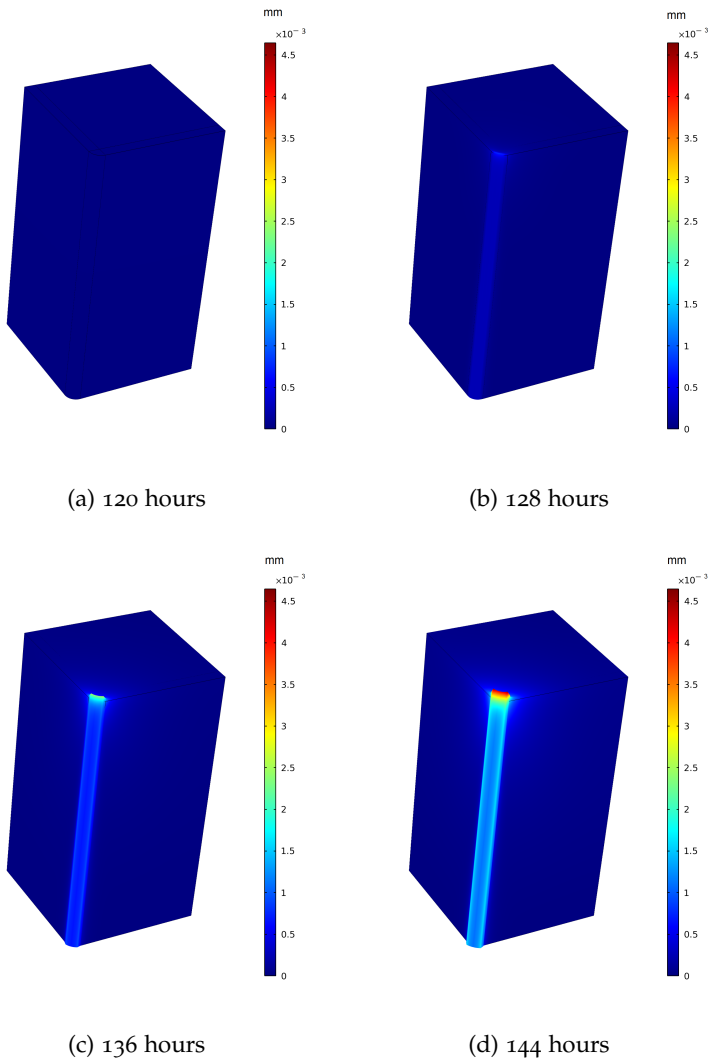


Figure 11.8: Magnitude of displacements at (a) 120, (b) 128, (c) 136 and (d) 144 hours.

ities, the HCM model specialised for sodium chloride solutions has been employed to simulate the first stages of the drying of a sodium chloride solution in a column made of Prague sandstone. The homogenised mechanical properties are computed by the Mori-Tanaka scheme considering the simplified pore geometries of the Prague sandstone ob-

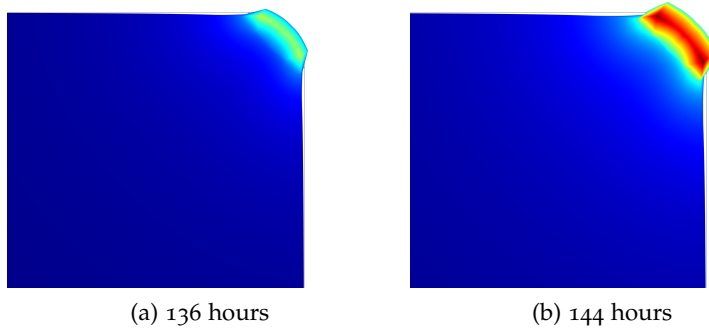


Figure 11.9: Magnitude of displacements (particular) at (a) 136 and (b) 144 hours.

tained in Chapter 9. The trend of the partial Biot's coefficient is taken according to the "Hypothesis of Small Pores first" discussed in Chapter 10. Results show that the salt begins to precipitate at first in correspondence of zones in which evaporation is faster (in this case the edge), causing the material swelling where the crystallisation takes place. This leads to the development of high effective stresses due to salt crystallisation that may exceed the tensile strength of the material, causing the beginning of weathering processes.

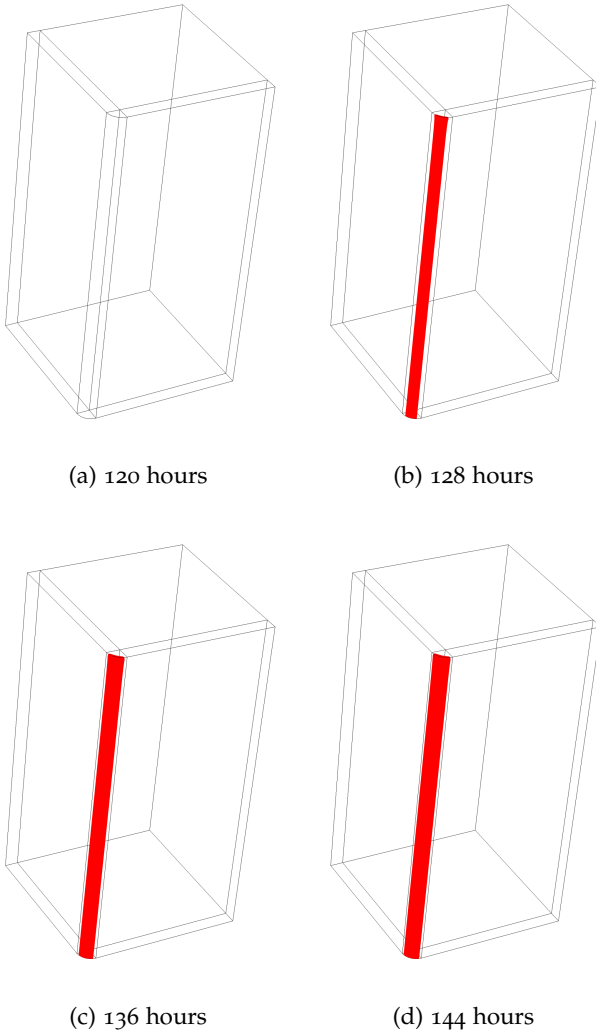


Figure 11.10: Areas subject to an spherical effective stress due to crystallisation exceeding the tensile strength of the material at (a) 120, (b) 128, (c) 136 and (d) 144 hours.

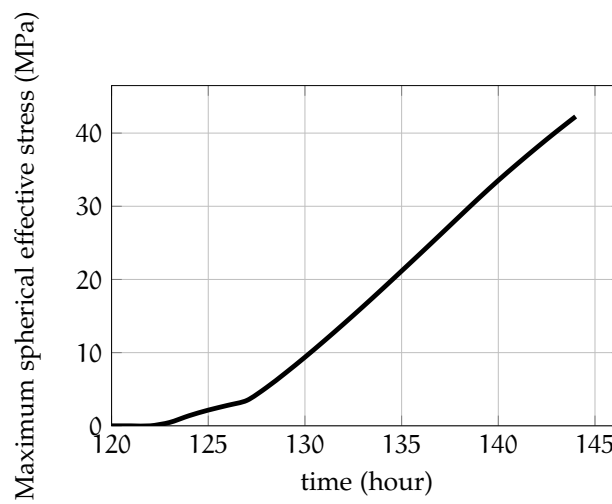


Figure 11.11: Trend of the maximum spherical effective stress as a function of time.

CONCLUSIONS AND PERSPECTIVES

In this dissertation the modelling and analysis of mechanical effects induced by salt crystallisation in porous building materials have been investigated employing a two-scale approach. To this aim, it has been necessary to study in advance the hygro-thermo-chemical aspects affecting the physical phenomenon.

In the first part of the dissertation, a new coupled multi-phase model for the hygrothermal analysis of porous building materials including salt crystallisation/dissolution and hydration/dehydration processes – HTC model – has been presented. The model describes the phenomenon at the scale of the structure, the macro-scale, and it is governed by three coupled, highly non-linear differential equations – moisture mass conservation, salt mass conservation and energy balance – completed by evolution equations that describe the kinetics of the salt precipitation. The HTC model has been specialised for Na_2SO_4 and NaCl solutions. As regards the former specialisation, the model has been validated through two benchmark tests taken from the literature, referred to sodium sulphate solutions and involving isothermal or isohygral conditions. Moreover, in order to show the potentialities of the model in more realistic cases, an example with non-isothermal and non-isohygral conditions has been discussed. As regards the latter specialisation, the influence of the thermal effects on salt transport and crystallisation in masonry structures has been investigated. A correlation between sorption/desorption curves at various temperatures has been presented and some model parameters depending on temperature have been analysed. Moreover, it has been employed to simulate the capillary rising of a sodium chloride solution in a masonry column in isothermal and non-

isothermal regime. Finally, the HTC model specialised for sodium chloride solutions has been extended to take into account the different kinetics of the drying process. The model is used to simulate two experimental campaigns carried out in the framework of the European project KISADAMA. In all, the numerical results demonstrate the effectiveness of the proposed HTC model to simulate salt transport and crystallisation at the macro-scale in a range of realistic cases involving different types of salts.

In the second part of the dissertation, mechanical aspects have been investigated. In particular, we have developed a multi-scale approach for the analysis of the mechanical effects induced by salt crystallisation at the macro-scale, starting from the real 3D micro geometry of a porous material obtained by X-ray Micro Computed Tomography images. The multi-scale approach is based on numerical homogenisation. The micro-mechanical model is obtained by automatically converting the images into a finite element mesh, specific loading conditions able to take into account the crystallisation process are implemented and, finally, the constitutive law at the macro-scale is retrieved through kinematic homogenisation. Much attention has been devoted to the choice of the mechanical REV on the basis of the overall porosity, the geometry of the pore space and the average mechanical properties in order to ensure its representativeness of the real micro-scale. The proposed approach has been applied to the real porous medium's micro-structure of a Prague sandstone, computing the partial Biot's coefficient referred to the crystal pressure acting on the pore walls at different levels of saturation degree. The numerical procedure developed enabled us: (i) to establish a macroscopic relationship between partial Biot's tensors and degree of saturation for a real porous medium; (ii) to test different loading schemes, deriving from some hypotheses on the way that crystals grow inside the porous medium; (iii) to compare the achieved results with the simple relation often used in literature, *i. e.* "Law of Partial Pressures"; (iv) to inspect maps of local stress, which can be used for a failure criteria or a damage model at micro-scale. Results highlight that the loading

scheme assumed plays a crucial role in the estimation of the partial Biot's tensor in real porous media. In particular, we have shown that changing the loading scheme the induced mechanical effects vary, both at the micro-scale and at the macro-scale, and that the law of partial pressures can be non-conservative. We can conclude that the proposed multi-scale approach for the analysis of the mechanical effect of salt crystallisation in porous media could shed some light on the still open issue of the relationship between the crystallisation physics and its mechanical effects. In addition, a general procedure for the defining of micro-simplified geometries for a porous material, able to reproduce the same macroscopic mechanical behaviour of the real one, has been developed. The comparison between results of numerical simulations with analytical schemes, in the case of a Prague sandstone, allowed to evaluate the pore aspect ratio of the analytical model that best describes the behaviour of the real porous media.

In the third part of the dissertation, hygro-thermo-chemical aspects have been combined with the mechanical ones to develop a Hygro-Thermo-Chemo-Mechanical (HTCM) model. Results of the numerical procedure proposed in the second part of the dissertation have been incorporated in a structural computation with environmental-mechanical loadings. Some numerical applications show its potentialities.

Perspectives

In view of assessing the mechanical effects induced by salt crystallisation in porous building materials, we developed a two-scale approach. This involves a numerical model that couples heat, water and salt transport, salt crystallization at the macroscopic scale – HTC model – and a mechanical part investigated employing a two-scale approach. However, several topics remain to be studied in the future.

As regards the HTC model, although it is general and it can be applied to electrolytic salts having different hydrous and anhydrous crystallised forms, to date it has been specialised only for sodium sulfate and sodium chloride aqueous solutions. This salt library should be extended with the properties of other salts and salt mixtures.

In Chapter 6, the HTC model has been enriched in order to describe the different drying kinetics, taking into account the different efflorescence formations, which can be observed in NaCl contaminated sandstones. It can be further improved to take into account the effects of different efflorescence formations on the deliquescence or dissolution processes. In particular, the modelling of these effects should be carried out also for other salts and different types of porous building material, performing ad hoc experimental campaigns. This could be helpful to model the effect of the micro-structural properties of the porous building material on the type of efflorescence formation.

As regards the mechanical effects induced by salt crystallisation it is evident that more knowledge is needed related to the nucleation and growth kinetics of salt crystals. In this dissertation a multi-scale approach for the analysis of mechanical effects induced by salt crystallisation in porous media has been presented, making some hypotheses on the loading condition of the micro-mechanical model. Experimental data related to the nucleation and growth kinetics of salt crystals at the microscopic scale would be required in order to refine and improve the proposed methodology. Moreover, maps of local stress obtained from numerical simulations could be used to express the microscopic stress-strain fields in terms of the macroscopic variables, through a re-localisation step, to forecast the most probable damage scenario.

The proposed two-scale approach could be exploited to develop a more sophisticated mechanical description, including the damage evolution as a function of the hygro-thermo-chemo-mechanical loading. In particular, the Hygro-Thermo-Chemo-Mechanical (HTCM) model could be improved with a suitable macroscopic damage law deriving from the micro-structural behaviour of the considered porous material subjected to salt crystallisation. Another option should be the implementation of a multilevel finite element approach, such as the FE² approach (Feyel, 2003), in order to take into account the non-linear behaviour and the micro-structure of the considered porous material. Nevertheless, this step it

is not trivial from a computational point of view, since the finite element analysis of real micro-structures is computational demanding, as shown in Chapter 8 and Chapter 10.

Part IV

APPENDIX

TABLES

Some useful data are reported in this section.

A.1 THERMAL CONDUCTIVITY OF THE LIQUID WATER FUNCTION OF TEMPERATURE

TEMPERATURE [K]	THERMAL CONDUCTIVITY OF LIQUID WATER [W/m/K]
275	0.5606
280	0.5715
285	0.5818
290	0.5917
295	0.6009
300	0.6096
305	0.6176
310	0.6252
315	0.6322
320	0.6387
325	0.6445
330	0.6499
335	0.6546

Table A.1: Thermal Conductivity of the liquid water function of temperature Ramires et al. (1995).

A.2 MOLAR DISSOLUTION ENTHALPY AT INFINITE DILUTION

SOLID SPECIES	a_{∞} [J/mol]	b_{∞} [J/mol/K]
NaCl	3799.7	-115.80
Na ₂ SO ₄	-1380.4	-302.09

Table A.2: Molar dissolution enthalpy at infinite dilution in J mol⁻¹ ($273.15 < T < 373.15$): $\overline{\Delta_{\text{sol}} H^{\infty}} = a_{\infty} + b_{\infty}(T - T_0)$ with $T_0 = 298.15$ K Marliacy et al. (2000).

A.3 MOLAR LATENT HEAT OF HYDRATION/ DEHYDRATION FOR H₂O-NA₂SO₄ SOLUTIONS

SOLID SPECIES	$h_{\text{hyd}}(T_0)$ [J/mol]	$\Delta_{\text{hyd}} C_p$ [J/mol/K]
Na ₂ SO ₄	-81 556	-687.91

Table A.3: Molar latent heat of hydration/ dehydration for H₂O-Na₂SO₄ solutions function temperature ($291.15 < T < 305.15$): $h_{\text{hyd}} = h_{\text{hyd}}(T_0) + \Delta_{\text{hyd}} C_p(T - T_0)$ with $T_0 = 298.15$ K Marliacy et al. (2000).

COEFFICIENTS OF THE HTC MODEL

Some useful expressions related to the HTC model are derived in this section.

B.1 LATENT HEAT OF CRYSTALLIZATION FOR AN ANHYDROUS SALT

Latent heat of crystallization for an anhydrous salt H_{cry_i} Marliacy et al. (2000):

$$H_{\text{cry}_j} = \frac{m_w^l \Delta_{\text{sol}} \hat{H}(m') - m_w^l \Delta_{\text{sol}} \hat{H}(m)}{\chi M_{s_j}^s} \quad (\text{B.1})$$

where:

$$\Delta_{\text{sol}} \hat{H}(m') = \hat{L}(m') + m' \overline{\Delta_{\text{sol}} H^\infty} \quad (\text{B.2})$$

$$\Delta_{\text{sol}} \hat{H}(m) = \hat{L}(m) + m \overline{\Delta_{\text{sol}} H^\infty} \quad (\text{B.3})$$

m' = molality of the electrolytic solution at the end of the crystallization process;

m = molality of the electrolytic solution at the beginning of the crystallization process;

$\hat{L}(m')$ and $\hat{L}(m)$ = excess enthalpy of a electrolytic solution containing 1 kg of water, calculated through the Pitzer's model as reported in Marliacy et al. (2000);

χ = number of moles of salt formed during the crystallization process.

$$\begin{aligned}
H_{\text{cryj}} &= \frac{m_w^l}{x M_{s_j}^s} (\hat{L}(m') + m' \overline{\Delta_{\text{sol}} H^\infty}) + \\
&\quad - \frac{m_w^l}{x M_{s_j}^s} (\hat{L}(m) + m \overline{\Delta_{\text{sol}} H^\infty}) = \\
&= \frac{1}{M_{s_j}^s} \left(-\overline{\Delta H^{\text{infly}}} + \Delta H_L \right), \tag{B.4}
\end{aligned}$$

Taking into account that $\frac{m_w^l}{x} \frac{m' - m}{m} = -1$ and defining ΔH_L as:

$$\Delta H_L = \frac{m_w^l}{x} \frac{\hat{L}(m') - \hat{L}(m)}{m}. \tag{B.5}$$

B.2 KINETIC HYDRATION/DEHYDRATION PARAMETER FOR SULPHATE SOLUTIONS

$$K_{H_{ij}} = \frac{K_{\text{esp}} M_{s_i}^s}{10 M_{\text{H}_2\text{O}} \rho_{s_i}^s \pi r_p^2} = \frac{K_{\text{esp}} (V_m)_{s_i}^s}{10 M_{\text{H}_2\text{O}} \pi r_p^2} \tag{B.6}$$

$$K_{H_{ji}} = \frac{K_{\text{esp}} M_{s_j}^s}{10 M_{\text{H}_2\text{O}} \rho_{s_j}^s \pi r_p^2} = \frac{K_{\text{esp}} (V_m)_{s_j}^s}{10 M_{\text{H}_2\text{O}} \pi r_p^2} \tag{B.7}$$

i= hydrated crystallised form;

j= dehydrated crystallised form;

$K_{\text{esp}} = 0.45\text{-}0.50$ mg/min experimental water absorption coefficient for sodium sulphate solutions Espinosa et al. (2008b).

B.3 COEFFICIENTS OF THE SYSTEM OF EQUATIONS

The coefficient of the equations of the model are reported in the following. In particular those related to Eq. (3.68) are:

$$\varphi_h = \frac{\partial c_w}{\partial h}, \tag{B.8}$$

$$\varphi_{h\omega} = \frac{\partial c_w}{\partial \omega}, \tag{B.9}$$

$$\varphi_{hT} = \frac{\partial c_w}{\partial T}, \quad (\text{B.10})$$

$$\varphi_{hs_i} = \frac{\partial c_w}{\partial c_{s_i}^s}, \quad (\text{B.11})$$

$$C_{hh} = \frac{D_v}{R_v T} p_{v,sat} + (1 - \omega) \frac{\rho_w^l R_v T K_l}{h}, \quad (\text{B.12})$$

$$C_{hT} = \frac{D_v h}{R_v T} \frac{\partial p_{v,sat}}{\partial T} + (1 - \omega) \rho_w^l R_v \ln(h) K_l, \quad (\text{B.13})$$

$$C_{h\omega} = \frac{D_v h}{R_v T} \frac{\partial p_{v,sat}}{\partial \omega} - \rho_{ws}^l K_s. \quad (\text{B.14})$$

Coefficients related to the equation (3.69) are:

$$\varphi_{\omega} = \frac{c_w}{(1 - \omega)^2} + \frac{\omega}{1 - \omega} \varphi_{h\omega}, \quad (\text{B.15})$$

$$\varphi_{\omega h} = \frac{\omega}{1 - \omega} \varphi_{h\omega}, \quad (\text{B.16})$$

$$\varphi_{\omega T} = \frac{\omega}{1 - \omega} \varphi_{hT}, \quad (\text{B.17})$$

$$\varphi_{s_i} = 1 + \frac{\omega}{1 - \omega} \varphi_{hs_i}, \quad (\text{B.18})$$

$$C_{\omega\omega} = \rho_{ws}^l K_s, \quad (\text{B.19})$$

$$C_{\omega h} = \omega \rho_w^l \frac{R_v T}{h} K_l, \quad (\text{B.20})$$

$$C_{\omega T} = \omega \rho_w^l R_v \ln(h) K_l. \quad (\text{B.21})$$

Coefficients related to the equation (3.70) are:

$$\begin{aligned} C_{TT} = & \lambda_{eff} + (\beta_w^g T + H_{eva}) \frac{D_v h}{R_v T} \frac{\partial p_{v,sat}}{\partial T} + \\ & + (\beta_w^l (1 - \omega) + \beta_s^l \omega) \rho_w^l R_v K_l \ln(h) T, \end{aligned} \quad (\text{B.22})$$

$$C_{Th} = (\beta_w^g T + H_{eva}) \frac{D_v}{R_v T} p_{v,sat} + \quad (B.23)$$

$$+ (\beta_w^l (1 - \omega) + \beta_s^l \omega) \frac{\rho_w^l R_v K_l T^2}{h},$$

$$C_{T\omega} = (\beta_w^g T + H_{eva}) \frac{D_v h}{R_v T} \frac{\partial p_{v,sat}}{\partial \omega} + \quad (B.24)$$

$$+ (\beta_s^l - \beta_w^l) \rho_{ws}^l K_s T,$$

$$B_w = (\beta_w^l - \beta_w^g) T + H_{eva}, \quad (B.25)$$

$$B_w^* = \beta_w^l T, \quad (B.26)$$

$$(\varphi_{T_{s_i}})_{cry} = (\beta_{s_i}^s - \beta_s^l) T + H_{cry_i}, \quad (B.27)$$

$$(\varphi_{T_{s_i}})_{hyd} = (\beta_{s_i}^s - \beta_s^l) T + H_{hyd_i}, \quad (B.28)$$

$$\varphi_T = \rho_{eff} \beta_{eff}, \quad (B.29)$$

Coefficients related to the equation (3.71) are:

$$C_{ss_i} = S_{ws}^l (n_i \phi_0 \rho_{s_i}^s \pi r_p^2) K_{C_i}, \quad (B.30)$$

$$C_{sh_i} = \frac{\pi r_p^2 \rho_{s_i}^s}{V_{tot}} K_{H_{ij}}. \quad (B.31)$$

COEFFICIENTS OF THE HTC MODEL FOR CHLORIDES

The expressions of coefficients φ_i , C_{ij} , B_i are detailed for the HTC model specialised for sodium chloride solutions in Chapter 5. In particular, those related to (5.2) are:

$$\varphi_h = \frac{\partial c_w}{\partial h}, \quad (C.1)$$

$$\varphi_{h\omega} = \frac{\partial c_w}{\partial \omega}, \quad (C.2)$$

$$\varphi_{hT} = \frac{\partial c_w}{\partial T}, \quad (C.3)$$

$$\varphi_{hs} = \frac{\partial c_w}{\partial c_s^s}, \quad (C.4)$$

$$C_{hh} = \frac{D_v}{R_v T} p_{v,sat} + (1 - \omega) \frac{\rho_w^l R_v T K_l}{h}, \quad (C.5)$$

$$C_{hT} = \frac{D_v h}{R_v T} \frac{\partial p_{v,sat}}{\partial T} + (1 - \omega) \rho_w^l R_v \ln(h) K_l, \quad (C.6)$$

$$C_{h\omega} = \frac{D_v h}{R_v T} \frac{\partial p_{v,sat}}{\partial \omega} - \rho_{ws}^l K_s. \quad (C.7)$$

Coefficients related to the equation (5.3) are:

$$\varphi_\omega = \frac{c_w}{(1 - \omega)^2} + \frac{\omega}{1 - \omega} \varphi_{h\omega}, \quad (C.8)$$

$$\varphi_{\omega h} = \frac{\omega}{1 - \omega} \varphi_h, \quad (C.9)$$

$$\varphi_{\omega T} = \frac{\omega}{1 - \omega} \varphi_{hT}, \quad (C.10)$$

$$\varphi_s = 1 + \frac{\omega}{1-\omega} \varphi_{hs}, \quad (\text{C.11})$$

$$C_{\omega\omega} = \rho_{ws}^l K_s, \quad (\text{C.12})$$

$$C_{\omega h} = \omega \rho_w^l \frac{R_v T}{h} K_l, \quad (\text{C.13})$$

$$C_{\omega T} = \omega \rho_w^l R_v \ln(h) K_l. \quad (\text{C.14})$$

Coefficients related to the equation (5.4) are:

$$C_{TT} = \lambda_{eff} + (\beta_w^g T + H_{eva}) \frac{D_v h}{R_v T} \frac{\partial p_{v,sat}}{\partial T} + (\beta_w^l (1-\omega) + \beta_s^l \omega) \rho_w^l R_v K_l \ln(h) T, \quad (\text{C.15})$$

$$C_{Th} = (\beta_w^g T + H_{eva}) \frac{D_v}{R_v T} p_{v,sat} + (\beta_w^l (1-\omega) + \beta_s^l \omega) \frac{\rho_w^l R_v K_l T^2}{h}, \quad (\text{C.16})$$

$$C_{T\omega} = (\beta_w^g T + H_{eva}) \frac{D_v h}{R_v T} \frac{\partial p_{v,sat}}{\partial \omega} + (\beta_s^l - \beta_w^l) \rho_{ws}^l K_s T, \quad (\text{C.17})$$

$$B_w = (\beta_w^l - \beta_w^g) T + H_{eva}, \quad (\text{C.18})$$

$$\varphi_{Ts} = (\beta_s^s - \beta_s^l) T + H_{cry}, \quad (\text{C.19})$$

$$\varphi_T = \rho_{eff} \beta_{eff}, \quad (\text{C.20})$$

Coefficients related to the equation (5.5) are:

$$C_{ss} = S_{ws}^l (n \phi_0 \rho_s^s \pi r_p^2) K_c. \quad (\text{C.21})$$

BIBLIOGRAPHY

- A. Abdulle and Y. Bai. Reduced basis finite element heterogeneous multi-scale method for high-order discretizations of elliptic homogenization problems. *Journal of Computational Physics*, 231(21):7014–7036, 2012. doi: 10.1016/j.jcp.2012.02.019.
- B.H. Abu Bakar, M.H. Wan Ibrahim, and M.A. Megat Johan. A review: Durability of fired clay brick masonry wall due to salt attack. *International Journal of Integrated Engineering*, 1, 2009.
- J. Ahl. Salt diffusion in brick structures part ii the effect of temperature, concentration and salt. *Journal of Materials Science*, 39(13):4247–4254, 2004. doi: 10.1023/B:JMSC.0000033406.40090.b4.
- I. Babuska. Homogenization approach in engineering. *Lecture Notes in Economics and Mathematical Systems*, 134(134):137–153, 1976. doi: 10.1007/978-3-642-85972-4_8.
- G.V. Barbosa-Canovas, Jr. A.J. Fontana, S.J. Schmidt, and T.P. Labuza, editors. *Water activity in foods: Fundamentals and Applications*. Blackwell Publishing, 1 edition, 2007.
- G.F. Becker and A.L. Day. The linear force of growing crystals. *Proceedings of the Washington Academy of Sciences*, 7:283–288, 1905.
- G.F. Becker and A.L. Day. Note on the linear force of growing crystals. *J. Geol.*, 24(4):313–333, 1916. doi: 10.1086/622342.
- Y. Benveniste. A new approach to the application of mori-tanaka’s theory in composite materials. *Mechanics of Materials*, 6(2):147–157, 1987. doi: 10.1016/0167-6636(87)90005-6.
- James G. Berryman. Long-wavelength propagation in composite elastic media - 2. ellipsoidal inclusions. *Journal of the Acoustical Society of America*, 68(6):1820–1831, 1980.
- M.A. Biot. General theory of three-dimensional consolidation. *Journal of Applied Physics*, 12(2):155–164, 1941. doi: 10.1063/1.1712886.
- M.A. Biot. Mechanics of deformation and acoustic propagation in porous media. *Journal of Applied Physics*, 33(4):1482–1498, 1962. doi: 10.1063/1.1728759.
- J.F.W. Bishop and R. Hill. Xlvi a theory of the plastic distortion of a polycrystalline aggregate under combined stresses. *London, Edinburgh, Dublin Philos. Mag. J. Sci*, 42(327):414–427, 1951. doi: 10.1080/14786445108561065.

- M. Boone, T. De Kock, T. Bultreys, G. De Schutter, P. Vontobel, L. Van Hoorebeke, and V. Cnudde. 3D mapping of water in oolitic limestone at atmospheric and vacuum saturation using X-ray micro-CT differential imaging. *Materials Characterization*, 97:150–160, 2014. doi: 10.1016/j.matchar.2014.09.010.
- M. Bornert, C. Stolz, and A. Zaoui. Morphologically representative pattern-based bounding in elasticity. *Journal of the Mechanics and Physics of Solids*, 44(3):307–330, 1996. doi: 10.1016/0022-5096(95)00083-6.
- L. Brabant, J. Vlassenbroeck, Y. De Witte, V. Cnudde, M.N. Boone, J. Dewanckele, and L. Van Hoorebeke. Three-dimensional analysis of high-resolution X-ray computed tomography data with morpho+. *Microscopy and Microanalysis*, 17(2):252–263, 2011. doi: 10.1017/S1431927610094389.
- Robert Bringhurst. *The Elements of Typographic Style*. Version 3.2. Hartley & Marks Publishers, Point Roberts, WA, USA, 2008.
- S. Brisard and L. Dormieux. FFT-based methods for the mechanics of composites: A general variational framework. *Computational Materials Science*, 49(3):663–671, 2010. doi: 10.1016/j.commatsci.2010.06.009.
- G. Castellazzi, C. Colla, S. de Miranda, G. Formica, E. Gabrielli, L. Molari, and F. Ubertini. A coupled multiphase model for hygrothermal analysis of masonry structures and prediction of stress induced by salt crystallization. *Construction and Building Materials*, 41:717–731, 2013a. doi: 10.1016/j.conbuildmat.2012.12.045.
- G. Castellazzi, S. de Miranda, L. Gremontieri, L. Molari, and F. Ubertini. Assessment of salt crystallization through numerical modelling. In A. Troi and E. Lucchi, editors, *Cultural Heritage Preservation: Proceedings; EWCHP-2013, 3rd European Workshop on Cultural Heritage Preservation*, pages 89–95. Bozen/Bolzano, Italy, 16th–18th September 2013b.
- G. Castellazzi, A. M. D’Altri, G. Bitelli, I. Selvaggi, and A. Lambertini. From laser scanning to finite element analysis of complex buildings by using a semi-automatic procedure. *Sensors (Switzerland)*, 15(8):18360–18380, 2015a. doi: 10.3390/s150818360.
- G. Castellazzi, S. de Miranda, G. Formica, L. Molari, and F. Ubertini. Coupled hygro-mechanical multiscale analysis of masonry walls. *Engineering Structures*, 84:266–278, 2015b. doi: 10.1016/j.engstruct.2014.11.034.
- G. Castellazzi, S. de Miranda, L. Gremontieri, L. Molari, and F. Ubertini. Modelling of non-isothermal salt transport and crystallization in historic masonry. *Key Engineering Materials*, 624:222–229, 2015c. doi: 10.4028/www.scientific.net/KEM.624.222.

- G. Castellazzi, S. de Miranda, L. Grementieri, L. Molari, and F. Ubertini. Multiphase model for hygrothermal analysis of porous media with salt crystallization and hydration. *Materials and Structures/Materiaux et Constructions*, 49(3):1039–1063, 2016. doi: 10.1617/s11527-015-0557-y.
- Giovanni Castellazzi, Antonio Maria D’Altri, Stefano de Miranda, and Francesco Ubertini. An innovative numerical modeling strategy for the structural analysis of historical monumental buildings. *Engineering Structures*, 132:229 – 248, 2017. ISSN 0141-0296. doi: <http://dx.doi.org/10.1016/j.engstruct.2016.11.032>.
- J.W. Christian. *The Theory of Transformations in Metals and Alloys*, volume Part I. Pergamon, New York, 1975. p. 451.
- COMSOL. *COMSOL Multiphysics Modeling Guide*, 2008. <http://math.nju.edu.cn/help/mathhpc/doc/comsol/modeling.pdf>.
- C.W. Correns. Über die erklärang der sogenannten kristallisationskraft. *Sitz Ber Preuss Akad Wiss*, 11:81–88, 1926.
- C.W. Correns. Growth and dissolution of crystals under linear pressure. *Discussions of the Faraday Society*, 5:267–271, 1949. doi: 10.1039/DF9490500267.
- C.W. Correns and W. Steinborn. Experimente zur messung und erklärang der sogenannten kristallisationskraft. *Zeitschrift für Kristallographie*, 101:117–133, 1939.
- O. Coussy. Deformation and stress from in-pore drying-induced crystallization of salt. *Journal of the Mechanics and Physics of Solids*, 54(8): 1517–1547, 2006. doi: 10.1016/j.jmps.2006.03.002.
- Olivier Coussy. *Poromechanics*. J. Wiley & sons, Chichester, 2004. ISBN 0-470-84920-7.
- S. de Miranda, K. Garikipati, L. Molari, and F. Ubertini. A simple solution strategy for coupled piezo-diffusion in elastic solids. *Computational Mechanics*, 44(2):191–203, 2009. doi: 10.1007/s00466-009-0366-7.
- S. de Miranda, L. Molari, V. Cnudde, N. Shahidzadeh, and F. Favaro. KISADAMA, kinetic of salt crystallization and mechanical damage in historic masonry. *Project financed in the JPI-Joint Heritage European Program Cultural Heritage*, 2013. www.kisadama.eu.
- S. de Miranda, L. Grementieri, L. Molari, V. Cnudde, H. Derluyn, J. Desarnaud, and N. Shahidzadeh. Drying of salt contaminated building sandstones: from experiments to numerical modelling. In *VI International Conference on Coupled Problems in Science and Engineering - COUPLED PROBLEMS 2015, Venice, Italy, May 18-20, 2015*.

- James J De Yoreo and Peter G Vekilov. Principles of crystal nucleation and growth. *Reviews in mineralogy and geochemistry*, 54(1):57–93, 2003.
- H. Derluyn. *Salt transport and crystallization in porous limestone: neutron-X-ray imaging and poromechanical modelling*. PhD thesis, ETH Zurich, ETH No, p. 20673., 2012.
- H. Derluyn. Private communication, 2017.
- H. Derluyn, P. Moonen, and J. Carmeliet. Deformation and damage due to drying-induced salt crystallization in porous limestone. *Journal of the Mechanics and Physics of Solids*, 63(1):242–255, 2014a. doi: 10.1016/j.jmps.2013.09.005.
- H. Derluyn, M.A. Boone, J. Desarnaud, L. Gremetieri, L. Molari, S. de Miranda, N. Shahidzadeh, and V. Cnudde. Quantifying salt crystallization dynamics in sandstone using 4D laboratory X-ray micro-CT. In *Science and Art: A Future for Stone: Proceedings of the 13th International Congress on the Deterioration and Conservation of Stone*, 2016.
- Hannelore Derluyn, Matthieu Boone, Tom Bultreys, Wesley De Boever, and Veerle Cnudde. Acquisition of the 3D geometries by pore network models. KISADAMA project report, Gent University, April 2014b. URL www.kisadama.eu.
- Hannelore Derluyn, Marijn Boone, Matthieu Boone, Tim De Kock, Julie Desarnaud, Steven Peetermans, Luisa Molari, Stefano de Miranda, Noushine Shahidzadeh, and Veerle Cnudde. Salt crystallization dynamics in building rocks: a 4D study using laboratory X-ray micro-CT. In Bernard Long, editor, *Tomography of Materials and Structures, 2nd International conference, Proceedings*, pages 565–568, 2015. ISBN 9782891468473.
- J. Desarnaud and N. Shahidzadeh-Bonn. Salt crystal purification by deliquescence/crystallization cycling. *EPL*, 95(4), 2011. doi: 10.1209/0295-5075/95/48002.
- J. Desarnaud, F. Bertrand, and N. Shahidzadeh-Bonn. Impact of the kinetics of salt crystallization on stone damage during rewetting/drying and humidity cycling. *Journal of Applied Mechanics, Transactions ASME*, 80(2), 2013. doi: 10.1115/1.4007924.
- J. Desarnaud, H. Derluyn, J. Carmeliet, D. Bonn, and N. Shahidzadeh. Metastability limit for the nucleation of nacl crystals in confinement. *Journal of Physical Chemistry Letters*, 5(5):890–895, 2014. doi: 10.1021/jz500090x.
- J. Desarnaud, H. Derluyn, L. Molari, S. de Miranda, V. Cnudde, and N. Shahidzadeh. Drying of salt contaminated porous media: Effect of primary and secondary nucleation. *Journal of Applied Physics*, 118(11), 2015. doi: 10.1063/1.4930292.

- J. Desarnaud, D. Bonn, and N. Shahidzadeh. The pressure induced by salt crystallization in confinement. *Scientific Reports*, 6, 2016a. doi: 10.1038/srep30856.
- J. Desarnaud, H. Derluyn, L. Grementieri, L. Molari, S. de Miranda, V. Cnudde, and N. Shahidzadeh. Salt weathering of sandstone during drying: Effect of primary and secondary crystallisation. In *Science and Art: A Future for Stone: Proceedings of the 13th International Congress on the Deterioration and Conservation of Stone*, page 299, 2016b.
- L. Dormieux, D. Kondo, and F.-J. Ulm. *Microporomechanics*. John Wiley and Sons., 1st edition, 2006. doi: 10.1002/0470032006.
- Luc Dormieux and Djimédo Kondo. *Micromechanics of Fracture and Damage*. Wiley-ISTE, 2016. doi: 10.1002/9781119292166.
- Luc Dormieux and Franz-Josef Ulm, editors. *Applied Micromechanics of Porous Materials*. Springer-Verlag Wien, 1st edition, 2005. doi: 10.1007/3-211-38046-9.
- W.J. Drugan and J.R. Willis. A micromechanics-based nonlocal constitutive equation and estimates of representative volume element size for elastic composites. *Journal of the Mechanics and Physics of Solids*, 44(4): 497–524, 1996. doi: 10.1016/0022-5096(96)00007-5.
- H. Eloukabi, N. Sghaier, S. Ben Nasrallah, and M. Prat. Experimental study of the effect of sodium chloride on drying of porous media: The crusty-patchy efflorescence transition. *International Journal of Heat and Mass Transfer*, 56(1-2):80–93, 2013. doi: 10.1016/j.ijheatmasstransfer.2012.09.045.
- J. D. Eshelby. The determination of the elastic field of an ellipsoidal inclusion, and related problems. *Proceedings of the Royal Society of London A: Mathematical, Physical and Engineering Sciences*, 241(1226):376–396, 1957. ISSN 0080-4630. doi: 10.1098/rspa.1957.0133.
- R.M. Espinosa, L. Franke, and G. Deckelmann. Model for the mechanical stress due to the salt crystallization in porous materials. *Construction and Building Materials*, 22(7):1350–1367, 2008a. doi: 10.1016/j.conbuildmat.2007.04.013.
- R.M. Espinosa, L. Franke, and G. Deckelmann. Phase changes of salts in porous materials: Crystallization, hydration and deliquescence. *Construction and Building Materials*, 22(8):1758–1773, 2008b. doi: 10.1016/j.conbuildmat.2007.05.005.
- R.M. Espinosa-Marzal and G.W. Scherer. Mechanisms of damage by salt. *Geological Society Special Publication*, 331:61–77, 2010a. doi: 10.1144/SP331.5.

- R.M. Espinosa-Marzal and G.W. Scherer. Advances in understanding damage by salt crystallization. *Accounts of Chemical Research*, 43(6): 897–905, 2010b. doi: 10.1021/ar9002224.
- F. Feyel. Multiscale FE² elastoviscoplastic analysis of composite structures. *Computational Materials Science*, 16(1-4):344–354, 1999. doi: 10.1016/S0927-0256(99)00077-4.
- F. Feyel. A multilevel finite element method (FE²) to describe the response of highly non-linear structures using generalized continua. *Computer Methods in Applied Mechanics and Engineering*, 192(28-30): 3233–3244, 2003. doi: 10.1016/S0045-7825(03)00348-7. cited By 0.
- F. Feyel and J.-L. Chaboche. FE² multiscale approach for modelling the elastoviscoplastic behaviour of long fibre sic/ti composite materials. *Computer Methods in Applied Mechanics and Engineering*, 183(3-4):309–330, 2000. doi: 10.1016/S0045-7825(99)00224-8.
- R.J. Flatt. Salt damage in porous materials: How high supersaturations are generated. *Journal of Crystal Growth*, 242(3-4):435–454, 2002. doi: 10.1016/S0022-0248(02)01429-X.
- R.J. Flatt, M. Steiger, and G.W. Scherer. A commented translation of the paper by c.w. correns and w. steinborn on crystallization pressure. *Environmental Geology*, 52(2):221–237, 2007. doi: 10.1007/s00254-006-0509-5.
- R.J. Flatt, F. Caruso, A.M.A. Sanchez, and G.W. Scherer. Chemo-mechanics of salt damage in stone. *Nature Communications*, 5, 2014. doi: 10.1038/ncomms5823.
- F. Fritzen and T. Böhlke. Influence of the type of boundary conditions on the numerical properties of unit cell problems. *Tech. Mech*, 30:354–363, 2010.
- H. Garrecht, H.K. Hilsdorf, and J. Kropp. Higrscopic salts–influence on the moisture behaviour of structural elements. In *Durability of building materials and components: proceedings of the fifth international conference*, Routledge, 2013.
- D. Gawin and B.A. Schrefler. Thermo-hydro-mechanical analysis of partially saturated porous materials. *Engineering Computations (Swansea, Wales)*, 13(7):113–143, 1996. doi: 10.1108/02644409610151584.
- M.G.D. Geers, E.W.C. Coenen, and V.G. Kouznetsova. Multi-scale computational homogenization of structured thin sheets. *Modelling and Simulation in Materials Science and Engineering*, 15(4):S393–S404, 2007. doi: 10.1088/0965-0393/15/4/S06.

- M.G.D. Geers, V.G. Kouznetsova, and W.A.M. Brekelmans. Multi-scale computational homogenization: Trends and challenges. *Journal of Computational and Applied Mathematics*, 234(7):2175–2182, 2010. doi: 10.1016/j.cam.2009.08.077.
- J. Geertsma. The effect of fluid pressure decline on volumetric changes of porous rocks. *Transactions of AIME*, 210:131, 1957.
- I.M. Gitman, H. Askes, and E.C. Aifantis. The representative volume size in static and dynamic micro-macro transitions. *International Journal of Fracture*, 135(1-4):L3–L9, 2005. doi: 10.1007/s10704-005-4389-6.
- A.S. Goudies and H.A. Viles. *Salt Weathering Hazard*. Wiley, London, 1997.
- L. Gremontieri, F. Daghia, L. Molari, G. Castellazzi, H. Derluyn, V. Cnudde, and S. de Miranda. A multi-scale approach for the analysis of the mechanical effects of salt crystallisation in porous media. 2017. Submitted.
- J. Grunewald, P. Häupl, and M. Bomberg. Towards an engineering model of material characteristics for input to ham transport simulations - part 1: An approach. *Journal of Thermal Envelope and Building Science*, 26(4): 343–366, 2003. doi: 10.1177/1097196303026004002.
- S. Gupta, H.P. Huinink, M. Prat, L. Pel, and K. Kopinga. Paradoxical drying of a fired-clay brick due to salt crystallization. *Chemical Engineering Science*, 109:204–211, 2014. doi: 10.1016/j.ces.2014.01.023.
- K.K. Hansen. Sorption isotherms catalogue. Technical report, Technical University of Denmark, 1986. Technical report 162/86.
- Z. Hashin. Analysis of composite materials - a survey. *Journal of Applied Mechanics, Transactions ASME*, 50(3):481–505, 1983. doi: 10.1115/1.3167081.
- Z. Hashin and S. Shtrikman. A variational approach to the theory of the elastic behaviour of multiphase materials. *Journal of the Mechanics and Physics of Solids*, 11(2):127–140, 1963. doi: 10.1016/0022-5096(63)90060-7.
- P. Häupl, J. Grunewald, H. Fechner, and H. Stopp. Coupled heat air and moisture transfer in building structures. *International Journal of Heat and Mass Transfer*, 40(7):1633–1642, 1997. doi: 10.1016/s0017-9310(96)00245-1.
- W.M. Haynes, editor. *CRC handbook of chemistry and physics*. CRC Press, 93rd edition, 2012-2013. Internet Version 2013.
- R. Hill. The elastic behaviour of a crystalline aggregate. *Proceedings of the Physical Society. Section A*, 65(5):349–354, 1952. doi: 10.1088/0370-1298/65/5/307.

- R. Hill. Elastic properties of reinforced solids: Some theoretical principles. *Journal of the Mechanics and Physics of Solids*, 11(5):357–372, 1963. doi: 10.1016/0022-5096(63)90036-x.
- R. Hill. A self-consistent mechanics of composite materials. *Journal of the Mechanics and Physics of Solids*, 13(4):213–222, 1965. doi: 10.1016/0022-5096(65)90010-4.
- R. Hill. The essential structure of constitutive laws for metal composites and polycrystals. *Journal of the Mechanics and Physics of Solids*, 15(2): 79–95, 1967. doi: 10.1016/0022-5096(67)90018-x.
- R. Hill. On constitutive macro-variables for heterogeneous solids at finite strain. *Proc. R. Soc. London A*, 326(1565):131–147, 1972. doi: 10.1098/rspa.1972.0001.
- M. Hori and S. Nemat-Nasser. Double-inclusion model and overall moduli of multi-phase composites. *Mechanics of Materials*, 14(3):189–206, 1993. doi: 10.1016/0167-6636(93)90066-Z.
- Y. Huang, K.X. Hu, X. Wei, and A. Chandra. A generalized self-consistent mechanics method for composite materials with multiphase inclusions. *Journal of the Mechanics and Physics of Solids*, 42(3):491–504, 1994. doi: 10.1016/0022-5096(94)90028-0.
- T. Kanit, S. Forest, I. Galliet, V. Mounoury, and D. Jeulin. Determination of the size of the representative volume element for random composites: Statistical and numerical approach. *International Journal of Solids and Structures*, 40(13-14):3647–3679, 2003. doi: 10.1016/S0020-7683(03)00143-4.
- P. Kanouté, D.P. Boso, J.L. Chaboche, and B.A. Schrefler. Multiscale methods for composites: A review. *Archives of Computational Methods in Engineering*, 16(1):31–75, 2009. doi: 10.1007/s11831-008-9028-8.
- M. Karoglou, A. Moropoulou, Z.B. Maroulis, and M.K. Krokida. Water sorption isotherms of some building materials. *Drying Technology*, 23 (1-2 SPEC. ISS.):289–303, 2005. doi: 10.1081/DRT-200047948.
- M. Koniorczyk and D. Gawin. Heat and moisture transport in porous building materials containing salt. *Journal of Building Physics*, 31(4): 279–300, 2008. doi: 10.1177/1744259107088003.
- M. Koniorczyk and D. Gawin. Numerical modeling of salt transport and precipitation in non-isothermal partially saturated porous media considering kinetics of salt phase changes. *Transport in Porous Media*, 87(1):57–76, 2011. doi: 10.1007/s11242-010-9668-7.
- M. Koniorczyk and D. Gawin. Modelling of salt crystallization in building materials with microstructure - poromechanical approach. *Construction and Building Materials*, 36:860–873, 2012. doi: 10.1016/j.conbuildmat.2012.06.035.

- M. Koniorczyk and P. Konca. Experimental and numerical investigation of sodium sulphate crystallization in porous materials. *Heat and Mass Transfer/Waerme- und Stoffuebertragung*, 49(3):437–449, 2013. doi: 10.1007/s00231-012-1093-8.
- M. Koniorczyk and M. Wojciechowski. Influence of salt on desorption isotherm and hygral state of cement mortar - modelling using neural networks. *Construction and Building Materials*, 23(9):2988–2996, 2009. doi: 10.1016/j.conbuildmat.2009.05.001.
- M. Koniorczyk, D. Gawin, P. Konca, and D. Bednarska. Modeling damage of building materials induced by sodium sulphate crystallization [Modellierung von Schäden an durch Natriumsulfat-kristallisation]. *Bauphysik*, 38(6):366–371, 2016. doi: 10.1002/bapi.201610041.
- V. Kouznetsova, M.G.D. Geers, and W.A.M. Brekelmans. Multi-scale constitutive modelling of heterogeneous materials with a gradient-enhanced computational homogenization scheme. *International Journal for Numerical Methods in Engineering*, 54(8):1235–1260, 2002. doi: 10.1002/nme.541.
- V.G. Kouznetsova, M.G.D. Geers, and W.A.M. Brekelmans. Multi-scale second-order computational homogenization of multi-phase materials: A nested finite element solution strategy. *Computer Methods in Applied Mechanics and Engineering*, 193(48-51):5525–5550, 2004. doi: 10.1016/j.cma.2003.12.073.
- E. Kröner. Berechnung der elastischen konstanten des vielkristalls aus den konstanten des einkristalls. *Zeitschrift für Physik*, 151(4):504–518, 1958. doi: 10.1007/BF01337948.
- Guy T. Kuster and M.Nafi Toksöz. Velocity and attenuation of seismic waves in two-phase media - 1, 2. *Geophysics*, 39(5):587–618, 1974.
- J. Lavallo. Recherche sur la formation des cristaux à la température ordinaire. *Comptes Rendus de l'Académie des Sciences*, 36:493–495, 1853.
- R.W. Lewis and B.A. Schrefler. *The finite element method in the static and dynamic deformation and consolidation of porous media*. Wiley, Chichester, 1998.
- J.Y. Li and M.L. Dunn. Variational bounds for the effective moduli of heterogeneous piezoelectric solids. *Philosophical Magazine A: Physics of Condensed Matter, Structure, Defects and Mechanical Properties*, 81(4):903–926, 2001. doi: 10.1080/01418610151133357.
- N. Lindström, N. Heitmann, K. Linnow, and M. Steiger. Crystallization behavior of $\text{NaNO}_3\text{-Na}_2\text{SO}_4$ salt mixtures in sandstone and comparison to single salt behavior. *Applied Geochemistry*, 63:116–132, 2015. doi: 10.1016/j.apgeochem.2015.07.007.

- N. Lindström, T. Talreja, K. Linnow, A. Stahlbuhk, and M. Steiger. Crystallization behavior of Na_2SO_4 - MgSO_4 salt mixtures in sandstone and comparison to single salt behavior. *Applied Geochemistry*, 69:50–70, 2016. doi: 10.1016/j.apgeochem.2016.04.005.
- B. Lubelli, R.P.J. van Hees, and C.J.W.P. Groot. Sodium chloride crystallization in a "salt transporting" restoration plaster. *Cement and Concrete Research*, 36(8):1467–1474, 2006. doi: 10.1016/j.cemconres.2006.03.027.
- S. Majid Hassanizadeh and A. Leijnse. A non-linear theory of high-concentration-gradient dispersion in porous media. *Advances in Water Resources*, 18(4):203–215, 1995. doi: 10.1016/0309-1708(95)00012-8.
- J. Mandel. *Plasticité Classique, Viscoplasticité (CISM Courses and Lectures)*, volume 97. Springer-Verlag, New York., 1972.
- P. Marliacy, R. Solimando, M. Bouroukba, and L. Schuffenecker. Thermodynamics of crystallization of sodium sulfate decahydrate in H_2O - NaCl - Na_2SO_4 : Application to H_2O - NaCl - Na_2SO_4 -based latent heat storage materials. *Thermochimica Acta*, 344(1-2):85–94, 2000.
- B. Masschaele, M. Dierick, D.V. Loo, M.N. Boone, L. Brabant, E. Pauwels, V. Cnudde, and L.V. Hoorebeke. HECTOR: A 240kV micro-CT setup optimized for research. *Journal of Physics: Conference Series*, 463(1), 2013. doi: 10.1088/1742-6596/463/1/012012.
- R. McLaughlin. A study of the differential scheme for composite materials. *International Journal of Engineering Science*, 15(4):237–244, 1977. doi: 10.1016/0020-7225(77)90058-1.
- J.C. Michel, H. Moulinec, and P. Suquet. Effective properties of composite materials with periodic microstructure: A computational approach. *Computer Methods in Applied Mechanics and Engineering*, 172(1-4):109–143, 1999. doi: 10.1016/S0045-7825(98)00227-8.
- J.C. Michel, H. Moulinec, and P. Suquet. A computational method based on augmented lagrangians and fast fourier transforms for composites with high contrast. *CMES - Computer Modeling in Engineering and Sciences*, 1(2):79–88, 2000.
- G.W. Milton and R.V. Kohn. Variational bounds on the effective moduli of anisotropic composites. *Journal of the Mechanics and Physics of Solids*, 36(6):597–629, 1988. doi: 10.1016/0022-5096(88)90001-4.
- V. Monchiet and G. Bonnet. A polarization-based FFT iterative scheme for computing the effective properties of elastic composites with arbitrary contrast. *International Journal for Numerical Methods in Engineering*, 89(11):1419–1436, 2012. doi: 10.1002/nme.3295.

- T. Mori and K. Tanaka. Average stress in matrix and average elastic energy of materials with misfitting inclusions. *Acta Metallurgica*, 21(5): 571–574, 1973. doi: 10.1016/0001-6160(73)90064-3.
- M. Mosby and K. Matouš. Hierarchically parallel coupled finite strain multiscale solver for modeling heterogeneous layers. *Internat. J. Numer. Methods Engrg.*, 102(3-4):748–765, 2015.
- H. Moulinec and P. Suquet. A numerical method for computing the overall response of nonlinear composites with complex microstructure. *Computer Methods in Applied Mechanics and Engineering*, 157(1-2):69–94, 1998. doi: 10.1016/S0045-7825(97)00218-1.
- J. W. Mullin. *Crystallization*. Butterworths-Heinemann, 4th edition, 2001.
- T. Mura, H.M. Shodja, and Y. Hirose. Inclusion problems. *Applied Mechanics Reviews*, 49(10 PART 2):S118–S127, 1996. doi: 10.1115/1.3101963.
- S. Nemat-Nasser, N. Yu, and M. Hori. Bounds and estimates of overall moduli of composites with periodic microstructure. *Mechanics of Materials*, 15(3):163–181, 1993. doi: 10.1016/0167-6636(93)90016-K.
- Sia Nemat-Nasser and Muneo Hori. Universal bounds for overall properties of linear and nonlinear heterogeneous solids. *Journal of Engineering Materials and Technology, Transactions of the ASME*, 117(4):412–432, 1995.
- T.Q. Nguyen, J. Petković, P. Dangla, and V. Baroghel-Bouny. Modelling of coupled ion and moisture transport in porous building materials. *Construction and Building Materials*, 22(11):2185–2195, 2008. doi: 10.1016/j.conbuildmat.2007.08.013.
- V.-D. Nguyen, G. Becker, and L. Noels. Multiscale computational homogenization methods with a gradient enhanced scheme based on the discontinuous galerkin formulation. *Computer Methods in Applied Mechanics and Engineering*, 260:63–77, 2013. doi: 10.1016/j.cma.2013.03.024.
- V.P. Nguyen, M. Stroeven, and L.J. Sluys. Multiscale continuous and discontinuous modelling of heterogeneous materials: A review on recent developments. *J. Multiscale Modell*, 3(4):229–270, 2011.
- A. Nicolai. *Modeling and numerical simulation of salt transport and phase transitions in unsaturated porous building materials*. PhD thesis, Syracuse University, New York, 2007.
- A.N. Norris. A differential scheme for the effective moduli of composites. *Mechanics of Materials*, 4(1):1–16, 1985. doi: 10.1016/0167-6636(85)90002-X.
- Amos Nur and J. D. Byerlee. An exact effective stress law for elastic deformation of rock with fluids. *Journal of Geophysical Research*, 76(26): 6414–6419, 1971. ISSN 2156-2202. doi: 10.1029/JB076i026p06414.

- R.W. Ogden. On the overall moduli of non-linear elastic composite materials. *Journal of the Mechanics and Physics of Solids*, 22(6):541–553, 1974. doi: 10.1016/0022-5096(74)90033-7.
- M. Ostoja-Starzewski. Random field models of heterogeneous materials. *International Journal of Solids and Structures*, 35(19):2429–2455, 1998.
- Martin Ostoja-Starzewski. *Microstructural Randomness and Scaling in Mechanics of Materials*. Chapman and Hall/CRC, Boca Raton, FL., i edition, 2007.
- F. Otero, X. Martinez, S. Oller, and O. Salomón. An efficient multi-scale method for non-linear analysis of composite structures. *Composite Structures*, 131:707–719, 2015. doi: 10.1016/j.compstruct.2015.06.006.
- Z. Pavlík, P. Michálek, M. Pavlíková, I. Kopecká, I. Maxová, and R. Černý. Water and salt transport and storage properties of mšené sandstone. *Construction and Building Materials*, 22(8):1736–1748, 2008. doi: 10.1016/j.conbuildmat.2007.05.010.
- S. Pecullan, L.V. Gibiansky, and S. Torquato. Scale effects on the elastic behavior of periodic and hierarchical two-dimensional composites. *Journal of the Mechanics and Physics of Solids*, 47(7):1509–1542, 1999. doi: 10.1016/S0022-5096(98)00111-2.
- L. Pel. *Moisture transport in porous building materials*. PhD thesis, Technische Universiteit Eindhoven, 1995.
- D. Perić, E.A. De Souza Neto, R.A. Feijóo, M. Partovi, and A.J.C. Molina. On micro-to-macro transitions for multi-scale analysis of non-linear heterogeneous materials: Unified variational basis and finite element implementation. *International Journal for Numerical Methods in Engineering*, 87(1-5):149–170, 2011. doi: 10.1002/nme.3014.
- O. Pierard, C. Friebel, and I. Doghri. Mean-field homogenization of multi-phase thermo-elastic composites: A general framework and its validation. *Composites Science and Technology*, 64(10-11):1587–1603, 2004. doi: 10.1016/j.compscitech.2003.11.009. cited By 0.
- M.L.V. Ramires, C.A. Nieto Castro, Y. Nagasaka, A. Nagashima, M.J. Asael, and W.A. Wakeham. Standard reference data for the thermal conductivity of water. *Journal of Physical and Chemical Reference Data*, 24(3):1377–1381, 1995. doi: 10.1063/1.555963.
- J. Renard and M.F. Marmonier. Etude de l’initiation de l’endommagement dans la matrice d’un matériau composite par une méthode d’homogénéisation. *Aerosp. Sci. Technol*, 6:37–51, 1987.
- A. Reuss. Berechnung der fließgrenze von mischkristallen auf grund der plastizitätsbedingung für einkristalle. *ZAMM - Journal of Applied Mathematics and Mechanics / Zeitschrift für Angewandte Mathematik und Mechanik*, 9(1):49–58, 1929. doi: 10.1002/zamm.19290090104.

- C. Rodriguez-Navarro and E. Doehne. Salt weathering: Influence of evaporation rate, supersaturation and crystallization pattern. *Earth Surface Processes and Landforms*, 24(2-3):191–209, 1999. doi: 10.1002/(sici)1096-9837(199903)24:3<191::aid-esp942>3.0.co;2-g.
- K. Sab. On the homogenization and the simulation of random materials. *European Journal of Mechanics, A/Solids*, 11(5):585–607, 1992.
- G. Sachs. Zur ableitung einer fließbedingung. *Z. Ver. Dtsch. Ing.*, 72: 734–736, 1928. doi: 10.1007/978-3-642-92045-5_12.
- S. Saeb, P. Steinmann, and A. Javili. Aspects of computational homogenization at finite deformations: A unifying review from reuss' to voigt's bound. *Applied Mechanics Reviews*, 68(5), 2016. doi: 10.1115/1.4034024.
- G.A. Scheffler and R. Plagge. A whole range hygric material model: Modelling liquid and vapour transport properties in porous media. *International Journal of Heat and Mass Transfer*, 53(1-3):286–296, 2010. doi: 10.1016/j.ijheatmasstransfer.2009.09.030.
- G.W. Scherer. Crystallization in pores. *Cement and Concrete Research*, 29(8):1347–1358, 1999. doi: 10.1016/S0008-8846(99)00002-2.
- G.W. Scherer. Stress from crystallization of salt. *Cement and Concrete Research*, 34(9):1613–1624, 2004. doi: 10.1016/j.cemconres.2003.12.034.
- G.W. Scherer, R. Flatt, and G. Wheeler. Materials science research for the conservation of sculpture and monuments. *MRS Bulletin*, 26(1):44–50, 2001. doi: 10.1557/mrs2001.18.
- B.A. Schrefler. Mechanics and thermodynamics of saturated/unsaturated porous materials and quantitative solutions. *Applied Mechanics Reviews*, 55(4):351–388, 2002. doi: 10.1115/1.1484107.
- N. Shahidzadeh-Bonn, S. Rafai, D. Bonn, and G. Wegdam. Salt crystallization during evaporation: Impact of interfacial properties. *Langmuir*, 24(16):8599–8605, 2008. doi: 10.1021/la8005629.
- H. Shen and L.C. Brinson. A numerical investigation of the effect of boundary conditions and representative volume element size for porous titanium. *J. Mech. Mater. Struct*, 1(7):1179–1204, 2006.
- N. Shokri. Pore-scale dynamics of salt transport and distribution in drying porous media. *Physics of Fluids*, 26(1), 2014. doi: 10.1063/1.4861755.
- D.D. Somer, E.A. de Souza Neto, W.G. Dettmer, and D. Perić. A substepping scheme for multi-scale analysis of solids. *Computer Methods in Applied Mechanics and Engineering*, 198(9-12):1006–1016, 2009. doi: 10.1016/j.cma.2008.11.013.

- M. Steiger. Crystal growth in porous materials - I: The crystallization pressure of large crystals. *Journal of Crystal Growth*, 282(3-4):455-469, 2005a. doi: 10.1016/j.jcrysgro.2005.05.007.
- M. Steiger. Crystal growth in porous materials - ii: Influence of crystal size on the crystallization pressure. *Journal of Crystal Growth*, 282(3-4):470-481, 2005b. doi: 10.1016/j.jcrysgro.2005.05.008.
- M. Steiger and S. Asmussen. Crystallization of sodium sulfate phases in porous materials: The phase diagram $\text{Na}_2\text{SO}_4 - \text{H}_2\text{O}$ and the generation of stress. *Geochimica et Cosmochimica Acta*, 72(17):4291-4306, 2008. doi: 10.1016/j.gca.2008.05.053.
- M. Steiger, J. Kiebusch, and A. Nicolai. An improved model incorporating pitzer's equations for calculation of thermodynamic properties of pore solutions implemented into an efficient program code. *Construction and Building Materials*, 22(8):1841-1850, 2008. doi: 10.1016/j.conbuildmat.2007.04.020.
- J. Sýkora, T. Krejčí, J. Kruis, and M. Šejnoha. Computational homogenization of non-stationary transport processes in masonry structures. *Journal of Computational and Applied Mathematics*, 236(18):4745-4755, 2012. doi: 10.1016/j.cam.2012.02.031.
- S. Taber. The growth of crystals under external pressure. *American Journal of Science*, 41(246):532-556, 1916.
- F. Tariku, K. Kumaran, and P. Fazio. Transient model for coupled heat, air and moisture transfer through multilayered porous media. *International Journal of Heat and Mass Transfer*, 53(15-16):3035-3044, 2010. doi: 10.1016/j.ijheatmasstransfer.2010.03.024.
- G.I. Taylor. Plastic strain in metals. *J. Inst. Metals*, 62:307-324, 1938.
- K. Terada, I. Saiki, K. Matsui, and Y. Yamakawa. Two-scale kinematics and linearization for simultaneous two-scale analysis of periodic heterogeneous solids at finite strain. *Computer Methods in Applied Mechanics and Engineering*, 192(31-32):3531-3563, 2003. doi: 10.1016/S0045-7825(03)00365-7.
- K.v. Terzaghi. Die berechnung der durchlässigkeitsziffer des tones aus dem verlauf der hydrodynamischen spannungserscheinungen. *Sitzungsberichte der Akademie der Wissenschaften Wien*, 132(125), 1923.
- H.R. Treschler. Moisture analysis and condensation control in building envelopes. Technical report, (ed), American Society for Testing and Materials, West Conshohocken, 2001.
- J.F. Unger. An $\text{FE}^2\text{-X}^1$ approach for multiscale localization phenomena. *Journal of the Mechanics and Physics of Solids*, 61(4):928-948, 2013. doi: 10.1016/j.jmps.2012.12.010.

- U. Šolinc and J. Korelc. A simple way to improved formulation of fe2 analysis. *Computational Mechanics*, 56(5):905–915, 2015. doi: 10.1007/s00466-015-1208-4.
- O. Van Der Sluis, P.J.G. Schreurs, W.A.M. Brekelmans, and H.E.H. Meijer. Overall behaviour of heterogeneous elastoviscoplastic materials: Effect of microstructural modelling. *Mechanics of Materials*, 32(8):449–462, 2000. doi: 10.1016/S0167-6636(00)00019-3.
- I. Vlahinić, H.M. Jennings, and J.J. Thomas. A constitutive model for drying of a partially saturated porous material. *Mechanics of Materials*, 41(3):319–328, 2009. doi: 10.1016/j.mechmat.2008.10.011.
- I. Vlahinić, H.M. Jennings, J.E. Andrade, and J.J. Thomas. A novel and general form of effective stress in a partially saturated porous material: The influence of microstructure. *Mechanics of Materials*, 43(1):25–35, 2011. doi: 10.1016/j.mechmat.2010.09.007.
- J. Vlassenbroeck, M. Dierick, B. Masschaele, V. Cnudde, L. Van Hoorebeke, and P. Jacobs. Software tools for quantification of X-ray microtomography. *Nuclear Instruments and Methods in Physics Research, Section A: Accelerators, Spectrometers, Detectors and Associated Equipment*, 580(1 SPEC. ISS.):442–445, 2007. doi: 10.1016/j.nima.2007.05.073.
- W. Voigt. Über die beziehung zwischen den beiden elastizitätskonstanten isotroper körper. *Wied. Ann*, 38:573–587, 1889. doi: 10.1002/andp.18892741206.
- L.J. Walpole. On bounds for the overall elastic moduli of inhomogeneous systems-ii. *Journal of the Mechanics and Physics of Solids*, 14(5):289–301, 1966.
- L.J. Walpole. On the overall elastic moduli of composite materials. *Journal of the Mechanics and Physics of Solids*, 17(4):235–251, 1969. doi: 10.1016/0022-5096(69)90014-3.
- J. B. Walsh. The effect of cracks on the compressibility of rock. *Journal of Geophysical Research*, 70(2):381–389, 1965. ISSN 2156-2202. doi: 10.1029/JZ070i002p00381.
- J.B. Walsh. New analysis of attenuation in partially melted rock. *J Geophys Res*, 74(17):4333–4337, 1969. doi: 10.1029/jb074i017p04333.
- J.R. Willis. The overall response of nonlinear composite media. *Eur. J. Mech.-A/Solids*, 19:165–184, 2000. cited By 0.
- F. Willot, B. Abdallah, and Y.-P. Pellegrini. Fourier-based schemes with modified green operator for computing the electrical response of heterogeneous media with accurate local fields. *International Journal for Numerical Methods in Engineering*, 98(7):518–533, 2014. doi: 10.1002/nme.4641.

- Tai Te Wu. The effect of inclusion shape on the elastic moduli of a two-phase material. *International Journal of Solids and Structures*, 2(1):1–8, 1966. doi: 10.1016/0020-7683(66)90002-3.
- R.A.J. Wüst and J. McLane. Rock derioration in the royal tomb of seti i, valley of the kings, luxor, egypt. *Engineering Geology*, 58(2):163–190, 2000. doi: 10.1016/S0013-7952(00)00057-0.
- S. Yadegari, S. Turteltaub, and A.S.J. Suiker. Generalized grain cluster method for multiscale response of multiphase materials. *Computational Mechanics*, 56(2):193–219, 2015. doi: 10.1007/s00466-015-1167-9.
- R.W. Zimmerman. Hashin-shtrikman bounds on the poisson ratio of a composite material. *Mechanics Research Communications*, 19(6):563–569, 1992. doi: 10.1016/0093-6413(92)90085-O.
- T.I. Zohdi and P. Wriggers. Computational micro-macro material testing. *Archives of Computational Methods in Engineering*, 8(2):131–228, 2001. doi: 10.1007/bfo2897871.

COLOPHON

This document was typeset using the typographical look-and-feel `classicthesis` developed by André Miede. The style was inspired by Robert Bringhurst's seminal book on typography "*The Elements of Typographic Style*" (Bringhurst, 2008).

Final Version as of March 30, 2017 (`classicthesis` version 4.0).